



Defect Localization Capabilities of a Global Detection Scheme: Spatial Pattern Recognition Using Full-Field Vibration Test Data in Plates

A.F. Saleeb and M. Prabhu
University of Akron, Akron, Ohio

The NASA STI Program Office . . . in Profile

Since its founding, NASA has been dedicated to the advancement of aeronautics and space science. The NASA Scientific and Technical Information (STI) Program Office plays a key part in helping NASA maintain this important role.

The NASA STI Program Office is operated by Langley Research Center, the Lead Center for NASA's scientific and technical information. The NASA STI Program Office provides access to the NASA STI Database, the largest collection of aeronautical and space science STI in the world. The Program Office is also NASA's institutional mechanism for disseminating the results of its research and development activities. These results are published by NASA in the NASA STI Report Series, which includes the following report types:

- **TECHNICAL PUBLICATION.** Reports of completed research or a major significant phase of research that present the results of NASA programs and include extensive data or theoretical analysis. Includes compilations of significant scientific and technical data and information deemed to be of continuing reference value. NASA's counterpart of peer-reviewed formal professional papers but has less stringent limitations on manuscript length and extent of graphic presentations.
- **TECHNICAL MEMORANDUM.** Scientific and technical findings that are preliminary or of specialized interest, e.g., quick release reports, working papers, and bibliographies that contain minimal annotation. Does not contain extensive analysis.
- **CONTRACTOR REPORT.** Scientific and technical findings by NASA-sponsored contractors and grantees.

- **CONFERENCE PUBLICATION.** Collected papers from scientific and technical conferences, symposia, seminars, or other meetings sponsored or cosponsored by NASA.
- **SPECIAL PUBLICATION.** Scientific, technical, or historical information from NASA programs, projects, and missions, often concerned with subjects having substantial public interest.
- **TECHNICAL TRANSLATION.** English-language translations of foreign scientific and technical material pertinent to NASA's mission.

Specialized services that complement the STI Program Office's diverse offerings include creating custom thesauri, building customized data bases, organizing and publishing research results . . . even providing videos.

For more information about the NASA STI Program Office, see the following:

- Access the NASA STI Program Home Page at <http://www.sti.nasa.gov>
- E-mail your question via the Internet to help@sti.nasa.gov
- Fax your question to the NASA Access Help Desk at 301-621-0134
- Telephone the NASA Access Help Desk at 301-621-0390
- Write to:
NASA Access Help Desk
NASA Center for Aerospace Information
7121 Standard Drive
Hanover, MD 21076



Defect Localization Capabilities of a Global Detection Scheme: Spatial Pattern Recognition Using Full-Field Vibration Test Data in Plates

A.F. Saleeb and M. Prabhu
University of Akron, Akron, Ohio

Prepared under Cooperative Agreement NCC3-808

National Aeronautics and
Space Administration

Glenn Research Center

Acknowledgments

The financial support provided for this work by NASA Glenn Research Center NCC3-808 to the University of Akron is gratefully acknowledged. We would like to also thank both Dr. S.M. Arnold (Life Prediction Branch) and Mr. S. Samorezov (Structural Dynamics Laboratory) for their extensive cooperation and help in carrying out and summarizing all the results on conventional modal tests reported in Chapter IV.

The Aerospace Propulsion and Power Program at
NASA Glenn Research Center sponsored this work.

Available from

NASA Center for Aerospace Information
7121 Standard Drive
Hanover, MD 21076

National Technical Information Service
5285 Port Royal Road
Springfield, VA 22100

Available electronically at <http://gltrs.grc.nasa.gov/GLTRS>

TABLE OF CONTENTS

	Page
LIST OF TABLES.....	v
LIST OF FIGURES	vii
ABSTRACT	xiii
1.0 INTRODUCTION	1
1.1 General.....	1
1.2 Problem Statement.....	3
1.3 Objective of the current research	4
2.0 BACKGROUND AND LITERATURE REVIEW	5
2.1 Background	5
2.2 Material Properties at Damage	6
2.3 Signature Analysis or Pattern Recognition Approaches.....	7
2.4 Modal Updating and System Identification Process.....	10
2.5 System identification using Neural Network Techniques	14
2.6 Concluding Remarks	15
3.0 THEORETICAL DEVELOPMENTS AND SIMULATION RESULTS	15
3.1 Introduction.....	15
3.2 Governing equations for Flexural Vibration of Shear-Flexible Plates	17
3.3 The Detection Parameter Specialization.....	18
3.4 Generalizations	21
3.5 Background on Simulation	21
3.6 Outlines for Shell Modeling in Numerical Simulations	22
3.7 Damage Scenario	23
3.8 Overall simulation case study	24
3.8.1 Dynamic Loading Case (Modal Analysis)	24
3.8.2 Static Loading Case	60
3.9 Conclusion	61
4.0 EXPERIMENTAL VERIFICATION—CONVENTIONAL MEASURING MODAL TESTING WITH ACCELEROMETER IN A COARSE-SENSOR NETWORK	62
4.1 Introduction.....	62
4.2 Background about the Experiments.....	63
4.3 Experimental Setup.....	66
4.4 Processing the Data.....	69
4.5 Processing the Results and Observations	71
4.6 Conclusions of the Experimental Verification	88

5.0	FULL FIELD EXPERIMENTAL INVESTIGATIONS—THE USE OF ELECTRONIC SPECKLE INTERFEROMETRY TECHNOLOGY AND EXTENSIVE PATTERN RECOGNITION TECHNIQUES FOR DEFECT LOCALIZATION.....	89
5.1	Introduction.....	89
5.2	Principles of the Method – Fringe formulation in ESPI and ESPI.....	91
5.3	General Experimental Set-up and Measurements.....	93
5.4	Specimen description and results.....	95
5.5	Conclusion	124
6.0	SUMMARY, CONCLUSION AND FUTURE WORK	124
6.1	Summary.....	124
6.2	Conclusion	125
6.3	Future Work.....	126
	APPENDIX A	127
	REFERENCES	145

LIST OF TABLES

3.1	Frequencies of free vibration of various mode shapes for a “Healthy (undamaged Plate) for various mesh size	29
3.2	Frequencies of the Dynamic Case Damaged Plate with reduced Modulus of Elasticity (0.8E).....	58
3.3	Summary of the Frequencies of the Dynamic Case Damaged Plate with increased Modulus of Elasticity (1.2 E)	59
4.1	Exact frequencies and Eigenvalues of the fixed – fixed plate	72
4.2	Frequencies and Eigenvalues of Set 1	72
4.3	Frequencies and Eigenvalues of Set 2	73
4.4	Frequencies and Eigenvalues of Set 3	74
5.1	Comparison of the Frequencies for the first 10 resonant modes by AF-ESPI, FEM and DDC	99

LIST OF FIGURES

3.1	Geometric Dimensions and Material Properties of the Plate.....	27
3.2	Mode Shapes for Fixed – Fixed Plate.....	27
3.3	Mode Shapes for Simply Supported Plate	28
3.4	Schematic Diagram of the location of the patch or patch group for the single or multiple damage cases with the opposite edges either fixed – fixed or simply supported	30
3.5	Organization chart of the various mesh sizes and case scenarios of damage	31
3.6	Organization of the case scenarios having the positive false alarm (increase in stiffness)	31
3.7	Case I: – Spatial Distribution of the Defect Energy Force Parameter showing (for each mode) the F_1 , F_2 and F (resultant) Force Diagrams (columns 1, 2 and 3) for single patch damage with fixed – fixed boundary conditions.....	32
3.8	Case I: – Energy Vector Field Diagram for the damaged plate with overall and zoomed plots for single patch damaged with fixed – fixed boundary conditions.....	33
3.9	Case II: – Spatial Distribution of the Defect Energy Force Parameter showing (for each mode) the F_1 , F_2 and F (resultant) Force Diagrams (columns 1, 2 and 3) for multiple patch damage with fixed – fixed boundary condition	34
3.10	Case II: – Energy Vector Field Diagram for the damaged plate with overall and zoomed plots for multiple patch damage with fixed – fixed boundary condition	35
3.11	Case III: – Spatial Distribution of the Defect Energy Force Parameter showing (for each mode) the F_1 , F_2 and F (resultant) Force Diagrams (columns 1, 2 and 3) for single location of patch group damage with fixed – fixed boundary condition.....	36
3.12	Case III: – Energy Vector Field Diagram for the damaged plate with overall and zoomed plots for single location of patch group damage with fixed – fixed boundary condition.....	37

3.13 Case IV: – Spatial Distribution of the Defect Energy Force Parameter showing (for each mode) the F_1 , F_2 and F (resultant) Force Diagrams (columns 1, 2 and 3) for multiple blocks damaged with fixed – fixed boundary condition	38
3.14 Case IV: – Energy Vector Field Diagram for the damaged plate with plots for multiple location of patch group damaged with fixed – fixed boundary condition	39
3.15 Case V: – Spatial Distribution of the Defect Energy Force Parameter showing (for each mode) the F_1 , F_2 and F (resultant) Force Diagrams (columns 1, 2 and 3) for single patch damage with simply supported boundary conditions.....	40
3.16 Case V: – Energy Vector Field Diagram for the damaged plate with overall and zoomed plots for single patch damage with simply supported boundary conditions.....	41
3.17 Case VI: – Spatial Distribution of the Defect Energy Force Parameter showing (for each mode) the F_1 , F_2 and F (resultant) Force Diagrams (columns 1, 2 and 3) for multiple location of patch damages with simply supported boundary condition	42
3.18 Case VI: – Energy Vector Field Diagram for the damaged plate with overall and zoomed plots for multiple location of patch damages with simply supported boundary condition.	43
3.19 Case VII: – Spatial Distribution of the Defect Energy Force Parameter showing (for each mode) the F_1 , F_2 and F (resultant) Force Diagrams (columns 1, 2 and 3) for single location of patch group damage with simply supported boundary condition	44
3.20 Case VII: – Energy Vector Field Diagram for the damaged plate with overall and zoomed plots for single location of patch damage with simply supported boundary condition	45
3.21 Case VIII: – Spatial Distribution of the Defect Energy Force Parameter showing (for each mode) the F_1 , F_2 and F (resultant) Force Diagrams (columns 1, and 3) for multiple locations of patch group damaged with simply supported boundary condition	46
3.22 Case VIII: – Energy Vector Field Diagram for the damaged plate with plots for multiple locations of patch group damage with simply supported boundary condition	47

3.23	Case IX: – Spatial Distribution of the Defect Energy Force Parameter showing (for each mode) the F_1 , F_2 and F (resultant) Force Diagrams (columns 1, 2 and 3) for single location of patch with increased stiffness (strengthening) for fixed – fixed boundary condition.....	48
3.24	Case IX: – Energy Vector Field Diagram for the strengthened plate with plots for single location of patch damaged with fixed – fixed boundary conditions.....	49
3.25	Case X: – Spatial Distribution of the Defect Energy Force Parameter showing (for each mode) the F_1 , F_2 and F (resultant) Force Diagrams (columns 1, 2 and 3) for single location of patch group with increased stiffness (strengthening) for fixed – fixed boundary condition.	50
3.26	Case X: – Energy Vector Field Diagram for the strengthened plate with plots for single location of patch group with fixed – fixed boundary condition	51
3.27	Case XI: – Spatial Distribution of the Defect Energy Force Parameter showing (for each mode) the F_1 , F_2 and F (resultant) Force Diagrams (columns 1, 2 and 3) for single location of patch with increased stiffness (strengthening) for simply supported boundary condition	52
3.28	Case XI: – Energy Vector Field Diagram for the strengthened plate with plots for single location of patch with simply supported boundary conditions.....	53
3.29	Case XII: – Spatial Distribution of the Defect Energy force Parameter showing (for each mode) the F_1 , F_2 and F (resultant) Force Diagrams (columns 1, 2 and 3) for single location of patch with increased stiffness (strengthening) for simply supported boundary condition	54
3.30	Case XII: – Energy Vector Field Diagram for the strengthened plate with plots for single location of patch group with simply supported boundary conditions.....	55
3.31	Spatial Distribution of the Defect Energy Force Parameter showing (for each mode) the F_1 , F_2 and F (resultant) Force Diagrams (columns 1, 2 and 3) for single location of patch group damage with fixed – fixed boundary condition and incomplete data.....	56
3.32	Energy Vector Field Diagram for the damaged plate with overall plots for single location of patch group damage with fixed – fixed boundary condition and incomplete data	57

3.33	Energy Vector Field Diagram for the damaged plate with overall and zoomed plots for single element statical loading damaged with fixed – fixed boundary conditions.....	60
3.34	Energy Vector Field Diagram for the damaged plate with overall and zoomed plots for Large (block) area of elements with statical loading damaged with fixed – fixed boundary conditions.....	61
3.35	Energy Vector Field Diagram for the damaged plate with overall and zoomed plots for single element damaged with statical loading, increased modulus of elasticity and fixed – fixed boundary conditions.....	61
4.1	Experimental Plate at NASA showing the clamping, the location of the accelerometer and geometry of the plate	64
4.2	Organization chart of the experiments conducted in the laboratory	65
4.3	Undamaged Plate with the accelerometers attached in the NASA Glenn laboratory	67
4.4	Side view of the support conditions with the plate and the accelerometers attached	67
4.5	(a) 1.125-inch diameter hole (b) 1.375-inch diameter hole (c) 1.6875-inch diameter hole (d) overall view of the damaged plate with the accelerometer attached	68
4.6	Flowchart of the automated damage detection process	70
4.7	“Set 1” – Spatial distribution of the defect energy force parameter for modes 1 to 3 showing the F_1 , F_2 and F (resultant) Force Diagrams (columns 1, 2 and 3) for the raw spatial distribution of states “X” and “Y” experiments	75
4.8	Energy Vector Field Diagrams for “Set 1”, modes 1 to 3 for “X” and “Y”	76
4.9	Schematic Descriptive Block diagram for the “Set 1” experiment after processing with the color scheme	77
4.10	“Set 2” – Spatial distribution of the defect energy force parameter for modes 1 to 3 showing the F_1 , F_2 and F (resultant) Force Diagrams (columns 1, 2 and 3) for the raw spatial distribution of states “X” “Y” and “Z” experiments	78

4.11	Energy Vector Field Diagrams for “Set 2”, modes 1 to 3 for states “X”, “Y” and “Z” experiments	81
4.12	Schematic Block diagram for the “Set 2” experiment after processing with the color scheme (The actual location of the damage is shown in dotted circles)	82
4.13	“Set 3” – Spatial distribution of the defect energy force parameter for modes 1 to 3 showing the F_1 , F_2 and F (resultant) Force Diagrams for (columns 1, 2 and 3) the raw spatial distribution of states “X”, “Y” and “Z” experiments	83
4.14	Energy Vector Field Diagrams for “Set 3”, modes 1 to 3 for states “X”, “Y” and “Z” experiments	86
4.15	Schematic Block diagram for the “Set 3” experiment after processing with the color scheme (The actual location of the damage is shown in dotted circles).....	87
5.1	Schematic Diagram of ESPI Experimental setup for out-of-plane measurement	94
5.2	Geometric dimensions and configurations of cracked rectangular plate	95
5.3	Showing the 3D mesh plot of the first 10 mode shapes for boundary crack problem	100
5.4	Mode Shape contour plots using various methods for $a = 20$ mm crack.....	105
5.5	Mode Shape contour plots using various methods for $a = 35$ mm crack.....	108
5.6	Mode Shape contour plots using various methods for $a = 50$ mm crack.....	111
5.7	Energy vector field plot, nodal damage intensity and damage defect Energy Parameter contour intensity for 20 mm boundary crack versus the 35 mm boundary crack	114
5.8	Energy vector field plot, nodal damage intensity and damage defect Energy Parameter contour intensity for 20 mm boundary crack versus the 50 mm boundary crack	119
A.1	Linear Regression analysis of errors versus average magnitude	130
A.2	Non-Linear Regression analysis of errors versus average magnitude.....	131

A.3	Regression analysis of error versus distance from fixed end Left Distance from Fixed End – Linear Equation	133
A.4	Regression analysis of error versus distance from fixed end Right Distance from Fixed End – Linear Equation	134
A.5	Regression analysis of error versus distance from fixed end Combined Distance from Fixed End – Linear Equation	135
A.6	Regression analysis of error versus distance from fixed end Left Distance from Fixed End – Quadratic Equation	137
A.7	Regression analysis of error versus distance from fixed end Right Distance from Fixed End – Quadratic Equation	138
A.8	Regression analysis of error versus distance from fixed end Combined Distance from Fixed End – Quadratic Equation	139
A.9	Regression analysis of difference (in absolute values) in errors versus distance for each point Left Distance from Fixed End.....	141
A.10	Regression analysis of difference (in absolute values) in errors versus distance for each point Right Distance from Fixed End.....	142
A.11	Regression analysis of difference (in absolute values) in errors versus distance for each point Combined Distance from Fixed End.....	143

ABSTRACT

Methods for health monitoring and damage detection have traditionally focused on finding differences between the intact/undamaged and the damaged structure; e.g. differences between vibration frequencies, differences in mode shapes, in deformed shape derivatives, or in flexibility (time domain) or transmissibilities (frequency – domain) arrays, etc. The likelihood of success in any of the approaches holds then a strong relationship to the ability of the corresponding damage detection indices utilized to locate the damage sites (through clear and persistent patterns) based on these measured differences. However, a careful examination of the existing literature indicates many serious limitations in this regard. For example, many of the techniques are heuristic, being conceived for particular types of simple structures. Indeed, almost exclusively, only one-dimensional trusses and beams are used in the applications. Also, few of the methods can operate with multiple damage scenarios, and they can be easily confused by “false” alarm (e.g., changes due to operational/environmental variability or increased stiffness as opposed to the actual damages).

More recently, a conceptually simple approach, based on the notion of defect energy in material space by Saleeb and coworkers, has been developed and extensively studied (from the theoretical and computational standpoints). The present study focuses on its evaluation from the viewpoint of damage localization capabilities in case of two-dimensional plates; i.e., spatial pattern recognition on surfaces.

To this end, two different experimental modal test results are utilized; i.e., (i) conventional modal testing using (white noise) excitation and accelerometer - type sensors and (ii) pattern recognition using Electronic speckle pattern interferometry (ESPI), a full field method capable of analyzing the mechanical vibration of complex structures. Unlike the conventional modal testing technique (using contacting accelerometers), these emerging ESPI technologies operate in a non-contacting mode, can be used even under hazardous conditions with minimal or no presence of noise and can simultaneously provide measurements for both translations and rotations.

Detailed documentations of the results obtained in the course of the above two studies have clearly demonstrated the robustness and versatility of the global NDE scheme developed. This stems from the vectorial character of the indices used, which enabled the extraction of distinct patterns for localizing damages. In the context of the targeted pattern recognition paradigm, two algorithms were developed for the interrogation of test measurements; i.e., intensity contour maps for the damaged index, and the associated defect energy vector field plots. With this dual representation, excellent results were obtained. In particular, they provided “fine - grained” visibility for clear discrimination of the damage single/multiple locations, in any of the vibration modes considered, and they were capable of distinguishing false-alarm tests from the case of true damage.

Defect Localization Capabilities of a Global Detection Scheme: Spatial Pattern Recognition Using Full-Field Vibration Test Data in Plates

A.F. Saleeb and M. Prabhu
University of Akron
Akron, Ohio

1.0 INTRODUCTION

1.1 General

Many aerospace, civil and mechanical engineering systems are used continuously despite aging and the associated potential for deterioration and damage accumulation. Therefore, the ability to monitor the structural health of these systems is becoming increasingly important, from the viewpoints of both economy and life safety. As a result, structural health monitoring has received considerable attention in the technical literature. In this, there has been a concerted effort to develop a firm mathematical and physical foundation, and the related experimental procedures, to advance the technology of health monitoring and damage detection.

Structural damage is considered as a weakening of the structure that negatively affects its performance. Damage may also be defined as any deviation in the structures original geometric or material properties that may cause undesirable stresses, displacements, or vibrations on the structure. This weakening and deviation may be due to cracks, loose bolts, broken welds, corrosion, fatigue, etc. Any crack or localized damage in a structure reduces the stiffness and increases the damping in the structure. Reduction in stiffness is associated with decreases in the natural frequencies and modification of the modes of vibration of the structure. Many researchers have used one or more of the above characteristics to detect and locate a crack. Most of the emphasis has been on using the decrease in frequency or the increase in damping to detect the crack.

Visual inspection has been and still is the most common method used in detecting damage on a structure. The increased size and complexity of today's structures can reduce the efficiency of the visual inspections. Conventional visual inspection can be costly and time consuming, especially when disassembly is necessary to provide access to the area being inspected. In addition, these visual inspection techniques are often inadequate for identifying the status of a structure where the damage is invisible to the human eye. Examples of Nondestructive damage detection techniques such are:

- Ultrasonic and eddy current scanning.
- Acoustic emission.
- X-ray inspection, etc., provide options to detect the occurrence of damage.

These methods are considered as “local” inspection approaches. Structural damage identification through changes in dynamic characteristics, on the other hand, provides a “global” way to evaluate the structural state. Dynamic-based damage detection has drawn worldwide attention due to their infra-structural role.

Despite significant research efforts in the area of nondestructive damage localization in structures, several problems remain to be solved before damage detection in real structures becomes a routine activity. A need remains for robust theories of damage detection to simultaneously include changes in all modal parameters. There is also a necessity to circumvent the reality of being capable of measuring only a few modes, particularly in large structures. In addition, we also have to be able to take into account the experimental errors in measured modal parameters. Furthermore, even if these types of damage detection theories were available, and experimental errors were insignificant, the need still exists to account for the uncertainty associated with modeling the properties and boundary conditions of real structures.

Normally the mode based damage detection technique cannot be directly used for real measurements. There are still some practical aspects that should be considered such as,

- System identification
- Finite element modeling and model updating
- Mode shape expansion
- Mode orthonormalization with respect to the mass matrix
- Applicability to real noise or measurement errors.

The dynamic characteristics of a structural system, i.e., eigen-frequencies, damping ratios and mode shapes can be extracted from dynamic measurements. These are done by system identification. The main problem is to match the experimental and analytical mode shapes. In practice, it is impossible to measure all the DOF's of a FEM model due to a limited number of sensors. Therefore, mode shape expansion plays an important role in structural damage identification algorithms based on changes in modal properties.

Many of the techniques are time intensive and may not be suited for routine inspection, as results often do not yield quantifiable results. As such a “global” damage detection method with attributes including economy, efficiency, and ease of operation is desired. Methods based on observed differences in dynamic behavior of structures, before and after damage, have been found to be a promising approach. Damage changes the performance of structures, i.e., it results in a loss of functionality. A structural system loss of functionality means, within this context a reduction in load carrying capacity or a reduction in its ability to control motion under imposed forces. That is, the regional material properties such as Young's modulus, moment of inertia, mass, local stiffness and damping will be affected. Such property changes will result in a variation in the system response, as well as eigen-parameters (eigen-values and the

corresponding eigenvectors). Variation of these quantities can be used as a tool to detect damage by means of modal analysis and modal testing. To carryout the experimental modal analysis, external excitation has to be used, e.g., using an impact load produced by hammer blows, a vibration generator or a shaking table. For large-scale civil structures, a natural random excitation is preferred, and mimics wind gusts, traffic vibration, earthquakes and tides which are available everywhere at any time.

Much attention has focused on the problem of detecting, locating and sizing damage in structures using modal parameters. The majority of the previous work has detected and localized damage using theories from modal analysis or from dynamic response measurements. Present NDE methods only modestly succeed in the prediction of damage in structures from limited amount of modal information.

1.2 Problem Statement

Damage detection using NDE techniques has prompted a lot of conceptual, theoretical and computational work, as well as experimental challenges concerning the difficulties and problems in obtaining measurements. The most suitable NDE method would no doubt lead to saving of lives, reduction in human suffering, protection of property, increased reliability, increased productivity of operations and a reduction in maintenance cost and time.

There are a number of factors that influence the choice and effective use of any suitable NDE method. Among them are:

- Input Signal requirement
- Output signal requirement
- Suitability of the Test structure
- Response – signature – analysis
- Implementation issues

With respect to the input signal the excitation (static vs. dynamic) its type (forced vs. ambient vibration) as well as the extent (low vs. higher order modes makes the decision quite tricky. Depending on the application and details of the NDE algorithm, output-signature measurements (i.e., their type, their qualitative/quantitative information content, as well as the associated sensor/instrumentation network required) will significantly impact the overall performance. The use of any NDE technique is indeed dependent on its ability to handle incomplete, noisy, measurements. With regard to test structures, their topology and configurations, the great variety of materials in construction and associated failure/damage modes, as well as their level of deterioration, are important in designing suitable NDE techniques.

There are three main parts of the overall process; i.e., detection of localized faults or “presence,” estimation of the damage location, and sizing or estimation of the extent of damage. The first is, of course, the most critical, whereas the other two phases would generally require additional, more detailed measurements. There are basically two alternative approaches for implementation of these global techniques, i.e., system-identification and direct post processing of measurement data. The two approaches differ mainly in the amount of data and type of information sets utilized. In one extreme, the system identification approach is typically based on a complete analytical model that is fitted optimally to the measured response. On the other hand, direct detection schemes do not require a priori identification of an analytical model. Instead, the key ingredient is the selection of an appropriate “measure” or damage parameter that is sufficiently sensitive to slight perturbation in system properties. The implementation simply reduces to the processing of “raw” experimental data with the objective being pattern-recognition, using the notion of comparison of processed signatures, i.e., the present (damage) versus the base/reference (intact) states.

To judge the correctness of any NDE method under consideration, the following steps are necessary:

- Theoretical and computational studies along with simulation of the model
- Laboratory studies for validation of the model
- Full scale Field demonstration or testing

For a sound and robust technique, all the above criteria have to be full-filled. In addition, carrying out extensive numerical and experimental studies under both ideal and noisy data conditions that could be computer generated. A full field demonstration of the method is an essential step to clear all the necessary obstacles in the method devised.

1.3 Objective of the Current Research

Professor Saleeb and coworkers in an ongoing research program funded by the NASA Glenn Research Center have successfully developed a direct type global damage detection technique. The present work is an extension of damage detection to new types of structures such as plate, shells and disks. Over the years, various researchers have proven, with experimental investigation and theoretical developments detection schemes for beam and frame type structures.

This research presents the overall work of damage to plates subjected to flexure bending (out-of-plane) for a variety of cases of damage. The damage is simulated as heterogeneity in the structure or a sudden change in the Young’s Modulus of Elasticity, and is measured using a newly proposed damage index, i.e., defect energy parameter. A few experimental investigations were carried out and are shown in the chapter for experimental verification. This method proved very versatile, far beyond anyone’s

imagination, in the detection of the location of damage. Though not exact, the location of damage was very close to the actual case. This was attributed to the very noisy measurement data from the accelerometers and environmental noise such as thermal and climatic effects. Also, the special contribution of Full Field Investigation is explained. This experimental investigation technique is powerful in terms of giving the slope and modal displacement of the entire structure. Most importantly, there is no human intervention and the measured output is absolutely free of all environmental noise.

2.0 BACKGROUND AND LITERATURE REVIEW

2.1 Background

Damage detection is a challenging problem that is under vigorous investigation by numerous research groups using a variety of analytical and experimental techniques. Health monitoring techniques may be classified as global or local. Global methods attempt to simultaneously assess the condition of the whole structure, whereas local methods provide information about a relatively small region of the system by using local measurements. The choice of the type of sensors effects the measurements and their spatial resolution, nature of the instrumentations used and the degree of noise in the measurement. Finally, the damage detection procedure for the structure concerned depends upon the level of damage and deterioration of concern, the available knowledge concerning the ambient dynamic environment, sophistication of the available computing resources, complexity of the detection scheme, selected threshold level for detecting perturbations in the system condition and the depth of knowledge concerning the failure modes of the structure and many more.

The difficult challenge in formulating damage parameters possessing all these and other desirable attributes (e.g., applicability to different materials, multiple damage sites various support condition, different vibration modes etc.) is demonstrated by the numerous proposals made over the years (e.g., natural frequencies, mode shapes, influence flexibility coefficients, strain mode shape, curvature mode shapes, as well as ratios, differences and fractions obtained from them). Basically, the performances of these methods were found to be heavily problem-dependent. With several conflicting conclusions often reached when using the same measure under different conditions. As such, there are three main parts involved in the overall process for damage detection

- a) Detection of localized damage/fault “presence.”
- b) Estimation of damage location.
- c) Sizing or estimation of the extent of damage.

The first is of course the most critical, whereas the other two phases would generally require additional, more detailed measurements. There are two alternative approaches for mathematical representation and implementation of these global detection techniques, i.e., system-identification and direct post processing of measurement data. The two approaches mainly differ in the amount and type of information sets utilized. The system-identification approach is typically based on a complete analytical model that is fitted to the measured response. For the most part the approach has been restricted to numerical simulations of linear systems. In addition to the intense computational demands, another main disadvantage is the need to treat the ‘inherent non-uniqueness’ caused by incompleteness of measured data with noise. More recently, artificial neural networking has been used as an attempt to remedy some of these problems, but they still remain computationally intensive. But the direct detection scheme requires a key ingredient for the selection of the appropriate ‘measure’ or damage parameter, which is sufficiently sensitive to any slight perturbation in system properties. The whole implementation simply reduces to processing of raw experimental data, the objective being pattern-recognition, using the notion of comprised processed signatures, i.e., present (damage) verses the base/reference (intact) states. Sharper resolution will be obtain if there is more distinct differences between two signatures. The presence of noisy data and consistency of distinctive patterns under different excitations (i.e., different vibration modes or different static load intensities) reflects on the robustness of NDE technique.

We have seen the basic idea behind understanding and developing a damage detection technique for structures. The next article summarizes the various contributions by researcher over the years to the field of NDE technology for damage detection. Emphasis will be put on the direct-type global methods similar to the present parametric investigation of damage in disk type structures.

2.2 Material Properties at Damage

The term damage refers to the degradation or failure of a material. Damage can originate from diverse phenomena such as oxidation, carbonation, mechanical work, or any type of disintegration or weakening from aging or mechanical processes. Within the framework of damage mechanics, only that which causes the loss of area, associated with change in local material properties such as Young’s modulus E , moment of inertia I , stiffness and flexibility and energy dissipation, is considered. When such changes occur there is a change of the entire physical system. This change leads a to change in vibration characteristics in physical space and also in material space

In physical space, when abrupt reductions in the cross section of a beam are considered, the properties have been changed, especially for the relationships between geometry and the centerline deflection curves. For free vibration behavior, such a beam results in a noticeable error in natural frequencies because of the overestimation of the bending stiffness. It was found that resonant frequency and vibration amplitudes were

considerably affected by the presence of cracks. A change in energy with respect to damage is also important. Damage to engineering materials essentially results in a decrease in the free energy stored in a body with consequent degradation of the material stiffness.

In material space, damage creates heterogeneity in a homogenous body, with consequent reduction of material properties including Young's modulus, stiffness and moment of inertia. So in both cases, damage affects the Young's modulus, stiffness and moment of inertia.

2.3 Signature Analysis or Pattern Recognition Approaches

The signature of a structure is related to its dynamic characteristics and is one of most widely used damage detection techniques. The observed changes in the structure, for example, like modal parameters, are compared to a database of possible changes and the most likely change is selected for detecting damage and locating its position.

Stubbs and Oseguda [1,2] applied a finite difference to the homogeneous equations of motion of an undamaged structure to yield expressions for the changes in modal stiffness in terms of modal masses, modal damping, eigen-frequencies, eigenvectors and their respective changes. Using matrix structural analysis, expressions relating variations in stiffnesses of structural elements to the variations in modal stiffness were generated resulting in a system of algebraic equations with a known load vector of fractional changes in modal stiffness and unknown fractional changes in member stiffnesses. Experimental evidence, obtained from their controlled laboratory experiments provided support to their damage detection technique. Dynamic responses of the damaged and undamaged frequencies were obtained from a cantilevered specimen. Using experimental frequency responses of the specimen and the numerically generated sensitivity matrix, they predicted the location and magnitude of the damage on the specimen.

Biswas et al. [3] studied several dynamic parameters for damage detection using full scale modal testing. A probable failure due to a large fatigue crack was simulated by unfastening a set of high-strength bolts in a splice connection of a steel highway bridge. Experimental modal testing was performed for the intact case as well as the cracked case. Results indicate the presence of detectable changes in some of the response data to a simulated physical failure. Non-parametric information, i.e., time records, frequency spectra, transfer functions as well as parametric information, i.e., modal frequencies and mode shapes had been examined. The modal Assurance Criteria (MAC) and modal frequencies can detect the damage in higher modes; otherwise the modal frequencies were not sensitive.

Modal curvature method was used by Wahab et al. [4] to detect damage in a prestressed concrete bridge. To establish their method they used simulated data from simply supported and continuous beams containing damaged parts at different locations. A damage indicator called a “curvature damage factor” was introduced which is the difference in curvature mode shapes for all modes and could be summarized by one number for each measured point. For several damage locations in the structure, all modes should be carefully examined. The lower modes are, in general, more accurate than the higher modes. When more than one fault exists in the structure, it is not possible to locate damage in all positions from the result of only one mode.

Gattulli and Romeo [5] proposed an integrated procedure based on a direct adaptive control algorithm and was applied to structural systems for both vibration suppression and damage detection. This is accomplished by tracking a reference output of an arbitrary model with desired damping characteristics and by detecting on-line mechanical parameters variations. A large number of mechanical parameters are shown to be identifiable in non-collocated configurations. Using full-state feedback, these capabilities are effectively exploited for oscillation reduction and health monitoring of uncertain multi-degree-of-freedom (MDOF) shear-type structures.

Hajemstad et al. [6] developed an algorithm for damage detection and assessment based on system identification using a finite element model and the measured modal response of a structure. A change in an element constitutive property from a baseline value is taken as indicative of damage. A Monte Carlo simulation was used to determine the threshold values that distinguished damage from the measured experimental noisy values. However, identification of geometric features of a solid body, in general, is inherently more difficult than identification of constitutive parameters.

Ultrasonic non-destructive testing is widely used method to find various kinds of defects in structures. This method is especially useful in material components that are isotropic. The method is also useful in the inspection of composite materials although the anisotropy induces several complications in interpreting the results obtained at the examination. Grahn [7] demonstrated the 2-D scattering problem of an internal crack in a layered anisotropic plate. He showed a complete ultrasonic simulation model (i.e., the output from the receiving probe is modeled) of a layered anisotropic plate that can be compared to a layered composite plate. He solved his problem by deriving the Green function for the layered plate and then using the integral representation for the total field to obtain an integral equation for the crack opening displacement. The integral equation is solved by expanding the crack opening displacement (COD) in Chebyshev functions.

Laser ultrasonic techniques were used by Dokun et al. [8] to monitor ultrasonic property-frequency-dependant Rayleigh wave velocity (material dispersion) and then relates changes in this acoustic property to material properties (such as stiffness) that characterize damage. The experimental procedure consists of measuring a series of transient elastic waveforms in a thick FRP (Fiber Reinforced Plastic) specimen and then

operating on these waveforms with 2D fast Fourier transformation to develop the dispersion relationship for that specimen. Material degradation (damage) is introduced into these specimens with environmental aging, and the dispersion curves are used to quantitatively track changes in material properties.

Sampaio et al. [9] tried to develop a method that covers all four steps of the process of damage detection – existence, localization, extent and prediction. They developed with the frequency – response – function - curvature method, encompassing the first three of the above methods and based only on the measured data without the need for any modal identification. This method performed well in detecting, locating and quantifying damage, although, the last item still needed to be further developed and better characterized. The main advantage of this method was its simplicity and no need for performing a modal analysis for the identification of mode shapes or resonant frequencies, as in the case of other methods.

Thyagarajan et al. [10], in their paper used the FRF (frequency – response – function) data and optimization to diagnose damage in a structure using a minimum number of sensors. Their technique did not use modal analysis, modal reduction or a training step but used all the information contained in the FRF data (not just the information around the peaks), the modal connectivity and the bounds on the structural stiffness values to diagnose the damage. They suggested detecting damage in large structures, scanning sections of the model to detect and diagnose damage. This scanning was based on the nodal connectivity patterns of the elements and running a separate optimization. The only drawback of their technique was that it required a lot of computation and was restricted to small models. To overcome the second limitation of the FRFs not being exactly repeatable due to variations in temperature which changes the elastic modulus and causes boundary conditions to change, a technique that shifts the frequency to remove global structural changes due to the environment was used.

DiPasquale et al. [11], proposed as early as 1989 that the global damage indices based on equivalent modal parameters are defined using the vibrational parameters of an equivalent linear structure. Damage to engineering materials essentially results in a decrease of the free energy stored in the body with consequent degradation of the material stiffness. They showed that the parameter based global damage indices can be related to the local damage variables through operations of averaging over the body volume.

Ray et al. [12] used a method of enhancing modal frequency sensitivity to damage using feedback control. The method was intended for smart structures, which embodied self actuation and self-sensing capabilities. Using state feedback, closed – loop modal frequencies are placed at locations in the complex plane that enhance sensitivity to particular types of damage.

A wavelet-based approach for Structural Health Monitoring (SHM) and damage detection was used by Z. Hou et al. [13]. The method is applied to simulation data

generated from a simple structural model subjected to a harmonic excitation. Spikes in details of the wavelet decomposition may detect changes in system stiffness, and the locations of these spikes indicate the moment when structural damage occurred.

2.4 Modal Updating and System Identification Approaches

Stubbs and Garcia [14] showed the use of pattern recognition to localize damage in structures in general and bridge structures in particular. In the physical world data are transduced into the so-called pattern space. Using techniques of dimensionality reduction, the pattern space is reduced to a smaller dimension known as the feature space. Data in the feature space are introduced to a decision algorithm, and the elements of the feature space are classified into a finite number of clusters. They developed a theory of damage localization to identify a feature space that can be defined entirely from measurable parameters and then propose several classification algorithms to aid in identifying a given portion of the structure as damaged or undamaged. This theory was then applied to the localization of damage in a three dimensional finite element model of a real bridge structural element.

Ren and De Roeck [15, 16], proposed a damage identification technique based on a change in frequencies and mode shapes of vibration, for predicting damage location and severity. The method is applied at an element level with a conventional finite element model. The element damage equations have been established through the eigen-value equations that characterize the dynamic behavior. The influence of noise was also shown and they verified their method by a number of damage scenarios for simulated beams and found the exact location and severity of damage. They demonstrated that multiplying the damage eigen-value equations with the undamaged or damaged mode shapes provides more equations and guarantees the damage localization.

Stubbs and Topole [17], proposed a formulation that localizes and determines the sizes changes in the stiffness of the structure. Generally such changes are a reduction in stiffness and are associated with some type of structural damage. Serious damage will change the stiffness locally and globally. Thus, in this study, a reduction in stiffness is generally interpreted as damage. However, reductions in stiffness do not necessarily relate to damage. Therefore, the algorithm is a conservative method to determine potential locations of damage.

Sohn and Law [18, 19] demonstrated the use of load-dependent ritz vectors from vibration data along with Bayesian probabilistic approach for damage detection. As applied to multistory frame structures. The approach is applied to identify multiple damage locations using estimated modal parameters when (1) the measurement data are potentially corrupted with noise, (2) only a small number of degrees of freedom are measured and (3) a few fundamental modes are estimated. They also proposed a branch-and-bound search scheme and a simplified approach for modeling a multistory frame structure. As an alternative to modal vectors, load-dependent Ritz vectors have

been shown useful in various areas of structural dynamics such as model reduction and damage detection. They also presented a procedure to extract these load-dependent Ritz vectors using a complete flexibility matrix constructed from measured vibration test data. The method shows the construction of the Ritz vectors corresponding to both the actual load pattern employed in the vibration test and from arbitrary load patterns. An experimental study on the use of Ritz vectors was described [20, 21] for damage detection of a grid-type bridge model. A procedure for extraction of the Ritz vector from experimental modal analysis and then used for the damage detection of the test structure using a Bayesian probabilistic approach.

F. Vestroni and D. Capecchi [22] found damage by frequency measurement. A linear behavior was assumed, before and after the damage. The method was described and used when frequencies are the observed quantities. The procedure is generalized by assuming finite-element interpretative models and an automatic algorithm of modal updating, which is used to determine the best stiffness distribution for an assigned location of damage. A minimum amount of frequencies are necessary to obtain a unique solution. This is important, because the problem is often over determined. A quantity of measured data is important to reach an acceptable solution.

Gawronski and Sawicki [23] used modal and sensor norms to determine damage locations in flexible structures. It provided information about the impact of the damage on the natural modes of the damaged structures. As the norm is determined from the system natural frequencies, modal damping ratios, and the input and output gains, they depend neither on the input time history nor the actual system deformation.

Hung-Liang et al. [24] presented a nondestructive evaluation method to identify the structural stiffness of ceramic candle filters. All filters were subjected to an excitation force, and the response was picked up by an accelerometer in a free-free boundary condition. The frequency response function and vibration mode shapes of each filter were evaluated. Beam vibration equations and finite element models were built to calculate the filter's dynamic response. The results indicated that the vibration signatures could be used as an index to quantify the structural properties. The results also estimate the overall bending stiffness values for four different types of candle filters. The used filters showed stiffness degradation. The location and the size of the damaged section were identified using the measured modified model modal strain energy procedure.

The dynamic bending stiffness was used by Maeck et al. [25] to detect damage. Different techniques are discussed and compared to derivations from experimentally determined modal characteristics of a reinforced concrete beam from its dynamic bending stiffness. The degradation of stiffness, due to cracking of the reinforced concrete, gives information on the position and severity of the damage that has occurred. The direct stiffness calculation needs the experimental mode shapes in deriving the dynamic stiffness through the curvature calculations. The advantage of this method is that no numerical model is needed to obtain the dynamic stiffness

distribution. However, a rather dense measurement grid is necessary to be able to identify accurately the higher mode shapes for curvature calculations.

Yuen [26] presented a systematic study of the relationship between damage location and size, and the change in the eigenvalues and eigenvectors of a cantilever beam by introducing damage to each element and also by varying the degree of damage for the case of a fixed damage location. Damage was modeled as a modulus reduction in an element of the beam. Two eigen parameters were studied, i.e., translation and rotation. Both showed a sudden change at the damaged region along the beam coordinate. However, the rotation eigen-parameter was not detected for higher modes.

Cracked rotating shafts exhibit a certain particular dynamic response due to the local flexibility of the cracked section. Dimarogonas and Papadopoulos [27] found the local flexibility of a cracked section of a cylindrical shaft by using the Paris energy equation. Computation of the local flexibility was based on a plane strain assumption for the strip. Such a factor is not available for the transverse crack on a cylinder. Nevertheless, the experimental results show that approach to be quite adequate. The uncoupled bending vibration of a rotor and a transverse surface crack were also investigated.

Akgun and Ju [28, 29] evaluated damage by using an electrical analogy method. Based on modal frequencies, they formulated damage functions. Investigation was made on multiple cracks in a beam structure. The multiple cracks were not closely spaced and cannot be determined. Later, a similar approach was extended to the evaluation of frame structures. The optimum excitation, location and frequency and the optimum location for response measurement were determined.

Another method, developed by C.-P. Fritzen et al. [30] is based upon a mathematical model representing the undamaged vibrating structure and a local description of the damage, e.g., a finite element for a cracked beam. The problem of modeling errors and their influence to damage localization accuracy and an approach to obtain reliable results is presented. The method was demonstrated through application to laboratory structures in the frequency domain using frequency response functions in the time domain. But the accuracy of the original model was found to be of great importance.

Time domain analysis can also be used for the same purpose. Tsai et al. [31] formulated the cross-random decrement method in a time domain. The free decay responses contain many structural modes. The modal frequencies, damping and the complex amplitudes were resolved by curve fitting. These parameters were used for damage detection. The discretization time interval and the number of sampled data points were found to be important factors affecting numerical accuracy. This technique was also applied to an offshore structure by Yang et al. [32] to detect damage. It only requires the measurement of the dynamic response of the structure. Here, an initial series of tests was conducted to establish baseline data so as to advocate a physical

description of the platform prior to any damage and against which the data from the damaged mode could be compared. They were very successful in the detection of small fatigue cracks but detecting the location of such a damage was not developed.

Rioz et al. [33] developed a method that can be used to identify cracks in structures by measuring its modal characteristics. They measured the flexural vibrations of a cantilever beam with a rectangular cross-section having a transverse crack extending uniformly along the width of the beam and analytical results were used to relate the measured vibration modes to the crack location and depth. From the measured amplitudes at two points of the structure vibrating at one of its natural modes, the respective vibration frequency and an analytical solution of the dynamic response, the crack location was found and depth estimated with ease. The main advantage of the method is that it could be carried out on the site with rather simple equipment and modest calculations. The drawbacks of the method was that it was possible for only a one dimensional structure (structures with analytical descriptions) or can be modeled with finite element method or some other conventional discretization method.

Pandey et al. [34] investigated the parameter called curvature-mode shapes for identifying and locating damage in a structure. They showed that by using the absolute change in this parameter is located in the region of damage, and hence can be used to detect damage in a structure. The changes in the curvature mode shape increases with increasing damage. The difference in modal curvature between the intact and the damaged beam showed not only a high peak at the fault position, but also some small peaks at different undamaged locations for higher modes.

Pai et al. [35, 36] presented a method of pinpointing structural damage locations using operational deflection shapes (ODSs) measured by a scanning laser vibrometer. This method initially assumes a form for the ODSs to match with the experimental data using a sliding-window-least-squares method to determine the four coefficients of the initially assumed equation. Each of these coefficients represented the central solution of displacement, boundary layer solution of displacement caused by boundary constraints, central solution of slope and boundary-layer solution of slope. They also developed the boundary effect detection (BED) method for finding damage locations. This method requires no model or historical data for locating structural damage. At the damage location the boundary layer solution of slope changes sign, and the boundary layer solution of displacement peaks up or dimples down. They showed the effect of noise and different types of damage and how they affect the damage locating curves. Experimental results showed that this damage detection method is sensitive and reliable for locating small damages in beams.

2.5 System Identification Using Neural Network Techniques

Sohn et al. [37], posed the process of structural health monitoring in the context of a statistical pattern recognition paradigm. They focused on applying a statistical process control (SPC) technique known as an “X-bar control chart” to vibration-based damage diagnosis. Basically, a control chart provides a statistical framework for monitoring future measurements and for identifying new data that are inconsistent with past data. A unique aspect of their study was the coupling of various projection techniques such as principal component analysis and linear and quadratic discrimination operators with SPC in an effort to enhance the discrimination between features from the undamaged and damaged structures. This approach was applied to a concrete bridge column as it was progressively damaged. The coupled approach gave a clearer distinction between undamaged and damaged vibration responses than by applying an SPC alone.

Among the nonparametric identification approaches that have been receiving growing attention, are neural networks; e.g., see [38, 39] by Agbabian et al. and Masri et al. Research is aimed at developing an automatic monitoring method of detection of structural damage. A study by Wu et al., [40] on the feasibility of self-organization and learning capabilities of neural networks was carried out. They trained a neural network onto a computer system to recognize the behavior of undamaged structures as well as behavior of possible damaged states. This idea applied to a simple structure, when carried out with experimental data, gave very promising results.

Masri et al. [41] trained a network with vibration measurements from a healthy structure and a structure under different episodes of response in order to monitor the health of the structure. The method was useful in assessing intricate mechanical systems whose internal states are not accessible for measurements. Their proposed method, a nonparametric structural damage detection methodology based on nonlinear system identification was very robust.

G. Garcia et al. [42] used a neural network with statistical pattern recognition for nondestructive damage detection (NDD). There he compared the capabilities of neural networks and statistical pattern recognition to detect localized damage in three-dimensional structures. Manning [41] used a neural network in conjunction with an active member transferring function data to evaluate structural damage detection. He suggested that the key for making the problem tractable for large problems was to adequately identify members at high risk for damage and including enough pole / zero information in the training of the neural network.

Extended system identification concepts were reviewed and discussed by Yao and Natke [43]. Application of tests and computer aided modeling (TACAM) to reliability evaluation of existing structures remains to be investigated. Finally, Aktan et al. [44, 45] reported a comprehensive application to bridge field-testing of the

combined system identification approach, with flexibility coefficient charts for pattern recognition.

2.6 Concluding Remarks

A great deal of research in the past thirty years has been aimed at establishing an effective method for health monitoring in civil, mechanical, and aerospace structures. The ultimate goal is to determine the existence, location and degree of damage in a structure. The development of a successful technology for structural health monitoring has enormous potential for application in evaluation of offshore structures and bridges subject to fatigue, corrosion, impact and earthquakes as well as buildings and aerospace structures subject to severe loads or structural deterioration. A variety of methods for evaluating damage in structural systems have emerged and evolved. All of these methods require a parameter estimation algorithm to drive them; i.e., the selection of an appropriate “measure” or suitable candidate for the damage parameters, that is sufficiently sensitive to slight perturbation in system properties. To this end, recent work by Saleeb et al. [46] has been directed toward the development of appropriate global indices of this type, based on a more fundamental approach in structural mechanics.

The novelty of this approach stems from the use of an alternative formulation in material (vs. physical) space. These dual balance laws are revealing in that the resulting force/source terms are directly and explicitly driven by increased heterogeneity due to deterioration. It thus provides an ideal candidate for the damage detection parameter. Such a damage parameter is easily computed from the measured raw data (e.g., strains, deflections, and rotations). A large number of numerical simulations and comparison to data have clearly demonstrated the power of this formulation under different test conditions [47, 48]. The focus of this study is to provide further validation for the feasibility and effectiveness of this new algorithm under realistic conditions.

3.0 THEORETICAL DEVELOPMENTS AND SIMULATION RESULTS

3.1 Introduction

The overall objective in this chapter is three-fold:

- i. To exploit the underlying mathematical structure of the damage index used in the detection scheme.
- ii. To investigate various methods to extract its damage - sensitive features for visualization in the context of pattern – recognition paradigm, and
- iii. To present the results of validation tests (through numerical / simulations) of these features – extraction / visualization procedures.

Thus providing the necessary background and insights needed to carry out the applications in Chapters IV and Chapters V dealing with actual measurements from experimental vibration recordings. With regard to items (i) and (ii) it will be gathered from subsequent discussions that, despite its conceptual simplicity and theoretical tractability, the damage index possess a rather intricate vectorial / tensorial character, and as a result, it is best to approach the pattern recognition strategy from the viewpoints of both intensity (magnitude) as well as directional properties. For instance, the magnitude of various components of damage tensorial index are shown to exhibit large and abrupt changes (spikes / peaks) in the presence of “true” defects. However, taken in isolation, this representation alone is not sufficient, since also vibration response changes due to environmental and/or operational variability (i.e., the so-called false alarm tests, which are known to pose extreme difficulties for many existing detection schemes) can trigger spurious patterns of this type.

In this regard, it is opportune that the complementing directional property of the index is quite unique; i.e., the vector flow fields evaluated from the projection of the tensor component on a (variationally - consistent C° – field of) position vectors perturbations will always be pointing in the direction of increased dissipations (or equivalently the direction of decreased total stored energy). Consequently, for a true defect case (irrespective of the underlying physical mechanism leading to the defect / deterioration) the discrete set of arrows representing these vector fields on the boundaries of the regions enclosing the defects will be directed outward. This will persist in a consistent manner, irrespective of the mechanical response signature being interrogated (i.e., any vibration mode or any static – load testing). On the contrary, this position will be completely or partially lost in case of false - alarm test, e.g., all vectors will no be reversed, for extreme case of increase stiffness in a small localized region in the structure, to point inwardly (relative to an observer situated inside the enhanced stiffness region).

Considering the numerical studies performed in conjunction with item (iii) above, an effort was made here to incorporate many of the complications that are anticipated in actual experimental applications (as in later chapters IV and V). For example, in the majority of the cases we have employed very small amounts of simulated localized damages using relatively coarse (non-optimized) meshes in the simulations; i.e., in a sense the inaccuracies involved in the vibration responses obtained will be reminiscent to the effects of noise in experiments. Furthermore, realizing that typical experimental results will be essentially incomplete; e.g., in data content when lacking the measurements of rotational degrees-of-freedom (DOF), or in space when only a restricted small size network or sensors are utilized, several simulations were obtained on the basis of vertical displacements only at few discrete points (sensor locations). This has enabled us to investigate the extent of deterioration in the accuracy of the detection scheme in such cases. Finally, extensive testing of false – alarm cases was also included.

3.2 Governing equations for Flexural Vibration of Shear-Flexible Plates

Consider the case of dynamic response of a homogenous, isotropic plate (with no thermal effects, etc.). With no defects, subject to free vibration in flexure. Adopting the well-known approach of treating free vibration, we consider for one typical mode; i.e., the n^{th} mode with frequency $\omega \equiv \omega_n$ and mode shapes $(w, \psi_1, \psi_2) \equiv (w_n, \psi_{1n}, \psi_{2n})$. Here, (w, ψ_1, ψ_2) represent the displacement in z - direction and the rotations in the x - and y - directions respectively. Note, that for convenience, we will drop the subscript "n" in all the subsequent derivations. For plate flexure, we utilize a shear flexible theory developed by Mindlin/Reissner [49] in which both bending and transverse shear effects as well as lateral (linear) and rotary inertia are accounted for. In addition, the following notation is introduced.

The Kinematical Quantities, namely, the curvatures and the transverse shear may be expressed as,

- Curvatures: $\kappa_x = \frac{\partial^2 \psi_1}{\partial x^2}$, $\kappa_y = \frac{\partial^2 \psi_2}{\partial y^2}$, $\kappa_{xy} = \frac{\partial \psi_1}{\partial y} + \frac{\partial \psi_2}{\partial x}$
- Transverse Shears: $\tau_{xz} = \frac{\partial w}{\partial x} + \psi_1$, $\tau_{yz} = \frac{\partial w}{\partial y} + \psi_2$

The Statical Quantities, i.e., the Stress Resultants per unit width which taken from the moments are expressed as,

- Moments:
- $$M_x \equiv M_{11} = \int_{-\frac{h}{2}}^{\frac{h}{2}} \frac{h}{2} \sigma_{xx} z \, dz$$
- $$M_y \equiv M_{22} = \int_{-\frac{h}{2}}^{\frac{h}{2}} \frac{h}{2} \sigma_{yy} z \, dz$$
- $$M_{xy} \equiv M_{12} \equiv M_{21} = \int_{-\frac{h}{2}}^{\frac{h}{2}} \frac{h}{2} \sigma_{xy} z \, dz$$

The Constitutive Relationships for the plate isotropy and with the assumptions of linear-elastic response take the following form,

$$M_{11} = D_b \left(\frac{d\psi_1}{dx} + \nu \frac{d\psi_2}{dy} \right) \quad M_{22} = D_b \left(\frac{d\psi_2}{dy} + \nu \frac{d\psi_1}{dx} \right)$$

$$M_{12} = M_{21} = D_b \left(\frac{1-\nu}{2} \right) \left(\frac{d\psi_1}{dy} + \frac{d\psi_2}{dx} \right)$$

$$Q_1 = k^2 Gh \left(\frac{d\psi_1}{dx} + \psi_1 \right) \quad Q_2 = k^2 Gh \left(\frac{d\psi_2}{dy} + \psi_2 \right)$$

$$\text{where } D_b = \frac{Eh^3}{12(1-\nu^2)}$$

Finally in what follows are the well-known Conservation expressions in physical space. That is, the balance of the linear and angular momentum in the form of first order differential equations are given as,

$$\frac{dM_{11}}{dx} + \frac{dM_{12}}{dy} - Q_1 + \rho I \omega^2 \psi_1 \equiv 0 \quad (3.1)$$

$$\frac{dM_{12}}{dx} + \frac{dM_{22}}{dy} - Q_2 + \rho I \omega^2 \psi_2 \equiv 0 \quad (3.2)$$

$$\frac{dQ_1}{dx} + \frac{dQ_2}{dy} + \rho h \omega^2 w \equiv 0 \quad (3.3)$$

The following section presents step-by-step procedure from which we can show that the equations (3.1), (3.2) and (3.3) are the basic equations for Defect Energy Parameter.

3.3 The Detection Parameter Specialization

The total strain energy, W, for a thin plate can be defined as

$$W(w, \psi_1, \psi_2) = \frac{1}{2} \left[M_{11} \frac{d\psi_1}{dx} + M_{22} \frac{d\psi_2}{dy} + M_{12} \left(\frac{d\psi_1}{dy} + \frac{d\psi_2}{dx} \right) + Q_1 \left(\frac{dw}{dx} + \psi_1 \right) + Q_2 \left(\frac{dw}{dy} + \psi_2 \right) \right] \quad (3.4)$$

After substituting the expressions for M_{11} , M_{22} , M_{12} , Q_1 and Q_2 from equations (3.4) the following expression for W is obtained

$$\begin{aligned}
W(w, \psi_1, \psi_2) = & \frac{1}{2} G h k^2 \psi_1^2 + \frac{1}{2} G h k^2 \psi_2^2 + G h k^2 \psi_2 \left(\frac{\partial w}{\partial y} \right)^2 + \frac{1}{2} G h k^2 \left(\frac{\partial w}{\partial y} \right)^2 + \frac{1}{4} D_b \left(\frac{\partial \psi_1}{\partial y} \right)^2 \\
& - \frac{1}{4} D_b v \left(\frac{\partial \psi_1}{\partial y} \right)^2 + \frac{1}{2} D_b \left(\frac{\partial \psi_2}{\partial y} \right)^2 + G h k^2 \psi_1 \left(\frac{\partial w}{\partial x} \right) + \frac{1}{2} G h k^2 \left(\frac{\partial w}{\partial x} \right)^2 + D_b v \left(\frac{\partial \psi_2}{\partial y} \right) \left(\frac{\partial \psi_1}{\partial x} \right) \\
& + \frac{1}{2} D_b \left(\frac{\partial \psi_1}{\partial x} \right)^2 + \frac{1}{2} D_b \left(\frac{\partial \psi_1}{\partial y} \right) \left(\frac{\partial \psi_2}{\partial x} \right) - \frac{1}{2} D_b v \left(\frac{\partial \psi_1}{\partial y} \right) \left(\frac{\partial \psi_2}{\partial x} \right) + \frac{1}{4} D_b \left(\frac{\partial \psi_2}{\partial x} \right)^2 - \frac{1}{4} D_b v \left(\frac{\partial \psi_2}{\partial x} \right)^2
\end{aligned}$$

The kinetic energy per unit area, T, which is defined as

$$T = \int_{-\frac{h}{2}}^{\frac{h}{2}} \frac{1}{2} \rho \mathbf{v}^T \mathbf{v} dz \quad (3.5)$$

in which the velocity vector, \mathbf{V} is, $\mathbf{V} = \left[x_3 \frac{d\psi_2}{dt}, x_3 \frac{d\psi_1}{dt}, \frac{dw}{dt} \right]$

For the special case of free vibrations: i.e., over one natural period of vibration for mode number “n” and integrating over the thickness of the plate, T reduces to

$$T = \frac{1}{2} \rho \omega_n \left[\frac{1}{12} h^3 (\psi_1^2 + \psi_2^2) + h w^2 \right] \quad (3.6)$$

The first term in equation (3.6) represents the rotary inertia due to the rotations ψ_1 and ψ_2 along the x and y-axes, and the second term is the translation / transverse inertia due to the displacement w along the z-axis.

The defect energy parameter for detection can then be formed as two components of “forces”; i.e.,

$$\left. \begin{aligned} F_x &\equiv F_1 = \int_s (P_{11} l + P_{21} m) ds \\ F_y &\equiv F_2 = \int_s (P_{12} l + P_{22} m) ds \end{aligned} \right\} \quad (3.7)$$

Where l and m are the direction cosines of the unit normal to “ds”, and S is the length of the perimeter curve surrounding an area of the plate middle surface, the terms P_{11} , P_{12} , P_{21} and P_{22} are given as,

$$\begin{aligned}
P_{11} &= (W - T) - (M_{11} \frac{d\psi_1}{dx} + M_{12} \frac{d\psi_2}{dx} + Q_1 \frac{dw}{dx}) \\
P_{21} &= - (M_{12} \frac{d\psi_1}{dx} + M_{22} \frac{d\psi_2}{dx} + Q_2 \frac{dw}{dx}) \\
P_{12} &= - (M_{11} \frac{d\psi_1}{dy} + M_{12} \frac{d\psi_2}{dy} + Q_1 \frac{dw}{dy}) \\
P_{22} &= (W - T) - (M_{12} \frac{d\psi_1}{dy} + M_{22} \frac{d\psi_2}{dy} + Q_2 \frac{dw}{dy})
\end{aligned}
\tag{3.8}$$

In the absence of any “defects” in the plate structure, the associated forces in Eq. (3.7) must be zero and equivalently this will lead to the following condition:

$$\text{Divergence of tensor } \mathbf{P} = \mathbf{0} \tag{3.9}$$

The above “proof” will serve to facilitate the understanding of the abstract, “mathematically-intriguing” nature of the damage parameter components. Note that, the formal derivation of the proper expression for such damage parameters requires the study of the variational symmetry of complex structures governed by coupled systems of partial differential equations. Using the language of “finite-strain” analysis, one then considers the inverse motion of the structure i.e., variations in material space while the present deformed state remain unchanged.

Note, from Eqs. (3.7) to (3.9), that all fields (i.e., displacements, rotations, strains and curvatures) are the basic parameters that convey damage information. According to the defect energy point of view, these parameters are correlated and contribution from each one of them makes the information about damage complete and clear. One can certainly envision several reductions/changes in response due to the defect energy equation, e.g., to give changes in natural frequency or some other single/isolated quantities (related to the corresponding mode shapes) by making some assumptions and approximations. Though useful in some cases, the ensuing detection indices will certainly be limited in their scope for general applications. However, if there are no approximations, all the individual contributions, such as natural frequency, stresses, strains, deformations, bending and shear forces, etc. interact in a very complex manner with their respective different weights and degrees of participation on a particular excitation to produce the final damage index. It is this latter, more comprehensive, viewpoint that is adopted here.

3.4 Generalizations

With the above in mind, one can obtain the necessary expressions required for the analysis of other structural vibration modes; e.g. the membrane/in plane counterpart. In fact, a more effective approach is to consider the combined flexure/membrane formulation as in the case of general, spatially curved shells. This indeed was the case considered in the implementation completed for the purpose of the feasibility study for the damage-detection-scheme.

In particular, the details of the formulation utilized here as a basis for the numerical simulations are given in [54]; i.e., for general mixed-type, shell finite elements. In the sequel, only a very brief outline of the schemes will be given. As to the simulation of damage scenarios, the simplest types of defects have been considered; i.e., in the form of “elastic” material-stiffness-degradation. Note that this approach has also been the most popular approach in the existing literature on fault detection. Of course, further generalization to more complex types of dissipative damage/defect phenomena should be straightforward, both conceptually as well as mathematically.

3.5 Background on Simulation

Theoretical development of the damage index is based on the shear flexible theory of Mindlin / Reissner [49]. This theory includes rotary inertia and shear in the same manner as Timoshenko’s [51] one-dimensional theory of bars.

Depending upon the treatment of the effect of transverse shear deformation, the existing plate bending elements may be divided into two groups: one based on Kirchhoff plate theory and the other on Mindlin Plate theory. In the formulation according to Kirchhoff, finite elements derived from the principle of virtual work or the principle of minimum total potential energy must satisfy the C^1 compatibility across element boundaries. On the other hand, the Mindlin plate formulation, that includes the effect of transverse shear deformation, the C^1 compatibility is not required, even an element derived from the principle of minimum total potential energy. In addition, a Mindlin plate-bending element can be easily extended to a degenerate type shell element, with curved geometry. But unfortunately Mindlin plate bending elements have a tendency to lock as the thickness of the plate becomes very small. Therefore, in formulating a Mindlin plate-bending element, special care must be taken to eliminate locking. A similar locking effect has been discussed by Hinton et al. [52].

The development of suitable finite element models for linear and nonlinear analysis of plates and shells has always presented a major challenge, due to the many theoretical intricacies involved. To overcome such intricacies, Saleeb et al. [53] developed a simple, shear flexible, quadrilateral plate element, designated as HMPL5. To predict the capabilities of the damage index, this quadrilateral plate element has been used for the present computer simulations. This element has five nodes, with three

displacements and two rotations at each node. The interior fifth node is located at the geometrical centroid of the element. As Mindlin plate theory accounts for transverse shear in addition to bending deformation, this shear flexible quadrilateral plate element is valid for thin as well as thick plates.

3.6 Outlines for Shell Modeling in Numerical Simulations

Based on a modified Hellinger-Reissner variational principle, where both displacement and strain fields are assumed independent, Saleeb et al. [50, 53, 54] developed an effective 5-node shell element, designated as HMSH5. HMSH5 is primarily used for damage numerical simulation. Five degrees of freedom are defined at each nodal point, that is, three translations (u, v, w) along the Cartesian global axes and two rotations (θ_1, θ_2) about mutually-perpendicular lamina coordinates. In total the HMSH5 element has 25 DOF. In finite element discretizations using element type HMSH5, the displacements are interpolated in terms of nodal degrees of freedom and can be written as

$$\mathbf{u} = \mathbf{N} \mathbf{q} \quad (3.10)$$

where \mathbf{N} is the interpolation matrix and \mathbf{q} is the vector of nodal displacements of the element where

$$\mathbf{q} = [u_1, v_1, w_1, \theta_1^{(1)}, \theta_2^{(1)}, \dots, u_5, v_5, w_5, \theta_1^{(5)}, \theta_2^{(5)}]^T \quad (3.11)$$

in which the superscript T denotes transpose of a matrix. Consequently, the acceleration field, $\ddot{\mathbf{u}}$, within the element is interpolated in terms of nodal acceleration as

$$\ddot{\mathbf{u}} = \mathbf{N} \ddot{\mathbf{q}} \quad (3.12)$$

While strains $\boldsymbol{\varepsilon}$ are approximated in terms of a strain parameter $\boldsymbol{\beta}$, as

$$\boldsymbol{\varepsilon} = \mathbf{P} \boldsymbol{\beta} \quad (3.13)$$

where $\boldsymbol{\beta}$ has 19 terms, among which seven terms that belong to the ‘membrane’ lamina strains (constant through thickness) and 12 terms are included in the combined bending part. In the combined bending portion, five terms are the transverse shear strain components. \mathbf{P} is a (5×19) strain-interpolation matrix for element lamina strains. In general, the entries in \mathbf{P} are polynomial functions of natural coordinates. By utilizing Eqs. (3.10) and (3.13), the Hellinger-Reissner functional π_R can be written as

$$\pi_R = \mathbf{q}^T \mathbf{M} \ddot{\mathbf{q}} - \frac{1}{2} \boldsymbol{\beta}^T \mathbf{H} \boldsymbol{\beta} + \boldsymbol{\beta}^T \mathbf{G} \mathbf{q} - W_{\text{ext}} \quad (3.14)$$

where

$$\mathbf{H} = \int_v \mathbf{P}^T \mathbf{D} \mathbf{P} \, dv, \quad \mathbf{G} = \int_v \mathbf{P}^T \mathbf{D} \mathbf{B}^l \, dv, \quad \mathbf{M} = \int_v \mathbf{N}^T \rho \mathbf{N} \, dv$$

In the above, \mathbf{D} is the elastic stiffness matrix, \mathbf{B}^l is local strain displacement matrix and W_{ext} is the external work done. Invoking the stationarity of Eq. (3.14) with respect to strain yields $\boldsymbol{\beta}$ in terms of \mathbf{q}

$$\boldsymbol{\beta} = \mathbf{H}^{-1} \mathbf{G} \mathbf{q} \quad (3.15)$$

which is used to eliminate the strain parameters on the element level. Finally substituting Eq. (3.15) into (3.14) results in

$$\pi_R = \mathbf{q}^T \mathbf{M} \ddot{\mathbf{q}} + \frac{1}{2} \mathbf{q}^T \mathbf{K} \mathbf{q} - W_{\text{ext}} \quad (3.16)$$

where the stiffness matrix for the hybrid/mixed element is given by

$$\mathbf{K} = \mathbf{G}^T \mathbf{H}^{-1} \mathbf{G} \quad (3.17)$$

Once the stiffness and mass matrices are assembled for the entire shell, the equilibrium equation can be obtained as

$$\mathbf{M} \ddot{\mathbf{q}} + \mathbf{K} \mathbf{q} = \mathbf{0} \quad (3.18)$$

which leads to the standard generalized eigen-problem to be solved for, ω and the corresponding eigen-vector, ϕ ; e.g., subspace iteration (Bathe [55])

$$(\mathbf{K} - \omega^2 \mathbf{M}) \boldsymbol{\phi} = \mathbf{0} \quad (3.19)$$

3.7 Damage Scenario

When damage develops, the effective properties of the material in the damaged area of the structure are changed. Changes in the material properties may take the form of the modification of the elastic stiffness as well as the damping coefficient damaged region, when considering the vibration behavior. Here a thin plate was chosen to provide the flexural vibration signatures required in the presented simulations for damage detection using the defect energy parameter.

For each plate, several damage scenarios are imposed. These can be a single or multiple damage locations that may be imposed at points inside (or on the boundaries)

the domain in the plate. For each damage location, different levels severities of severity may be imposed. Damage severity is represented by the percentage reduction of the plate bending rigidities, as well as shear rigidities. Throughout this report, the percent of damage is defined as that specific percent reduction of Young's modulus (E) at the specified damage inflicted regions. Other material properties, such as cross-section, thickness, mass and density remain intact.

3.8 Overall Simulation Case Study

As alluded to previously, only cases involving flexural responses of the simulated plates are considered here. Both dynamic (free vibrations) and static loading cases are treated. For the inflicted damage scenarios, we have considered two basic configurations of stiffness reductions, for both single and multiple locations. The first corresponds to a case of localized (point-like) defect in one small element of the mesh utilized, whereas in the second configuration we studies the effect of a more "distributed" type of damage at each site; i.e., reduced elastic modulus in a patch of elements.

For the presentation of results in each case, we have adopted the following formats, for visualizations and subsequent pattern recognitions. That is we show, spatial distribution on the two dimensional space of plate surface of both intensity (magnitude of components) as well as vector-type flow fields associated with the utilized damage detection parameter. To this end, we employ the nodal points of the finite element mesh/grid as the counterparts of sensor (experimental measurement) locations, e.g., leading to the very dense case when full field experiments are available (as in results of Chapter V) or the relative coarse case (as in results of Chapter IV). In addition, when interpreting the plots of vector fields, the convention is adopted that the observer is situated inside the element concerned, i.e., for a true damage in this latter element, the vectors at the boundary nodes of this element will all point outward implying that if allowed to relocate these boundary nodes moving in the direction of the respective (outward) force vectors will lead to increased defect areas; i.e., direction of more dissipations.

3.8.1 Dynamic Loading Case (Modal Analysis)

The material properties, geometric dimensions and location of the boundary conditions of the plate are shown in Fig. 3.1. The mode shapes for a square plate for a fixed – fixed and simply supported condition are shown in Fig. 3.2 and Fig. 3.3 respectively. The comparison of the change in frequencies "healthy"/undamaged structure for the various mode shapes and mesh dimensions are shown in Table 3.1. Figure 3.4 shows the location of the patch or the patch group that has undergone damage. An organization chart illustrating the different cases that were first attempted and thereon continued is shown in Fig. 3.5 for the plate damage (decrease in stiffness). For the cases that were considered for the increased stiffness (denoted in the following

as the positive “false alarm”), Fig. 3.6, only the case with the 32×32 case is presented in detailed here. Associated results for all the dynamic cases reported are shown in Figs. 3.7 to 3.32.

Some important remarks regarding the above program selected for this present study are in order here. First Fig. 3.5, (the organization chart for the simulation cases), the mesh-sizes chosen; i.e., starting from an 8×8 , going to 16×16 and finally to a 32×32 mesh, was mainly inspired by the experimental setting adopted in the in-house tests conducted by the sponsoring agency, NASA Glenn Research Center. In these latter experiments, only a coarse sensor network with 8×8 grids was utilized because of the physical limitations on the test object size and the overlapping of accelerometers attached. Therefore, all the mesh sizes considered were in order of a multiple of the 8×8 mesh such that once the data from the experiments were obtained they could be easily superimposed / mapped to the finer mesh (32×32) nodal points for plotting purpose.

Various case studies showing the locations of the “patch” (defect / damage zones) are shown for “idealized” experimental data, i.e., assuming that all the response values (e.g., vertical deflection and two rotations at each point) of the structure are being measured. As regards to the infliction of damage, a reduction of the elastic modulus E by 20%, for various locations on the plate, consists of four cases for each of the boundary conditions was considered. The term “patch” in the following case would mean a single element from a 32×32 mesh being damaged. A “patch group” would mean a number of elements adjacent to each other being damaged in a 32×32 element mesh forming a block which is equivalent to the single element in the 8×8 mesh (Fig. 3.4). Cases such as a single or a multiple patch and a single or a multiple patch group have been simulated to understand the effects on the corresponding damage pattern. The damage pattern was displayed using two basic viewing techniques, the unsmoothed (raw) spatial distribution of the intensity (magnitudes) of the components of defect energy parameter and the energy vector flow field plots. These are shown from Figs. 3.7 – 3.22 where the mesh plots show the intensity (scalar magnitudes) of defect energy force parameter in terms of individual F_1 , F_2 components and their resultant F component formats as the first, second and the third column plots.

Included along with the above mesh plots, the energy vector fields showing the overall distributions and a “zoomed” detailing near the precise the damage location in each example are also presented for each of the cases. The energy vector field flow phenomenon basically illustrates how the energy that is stored in a body is dissipated due to increased damages / defects. It is always found that these vectors point from a lower energy / weaker region to a higher energy / stronger region. Here the weaker and stronger descriptions refer to the damaged (cracked / loss of stiffness) and the “healthy” intact part of the plate. It is therefore, observed that there is always an outward flow of vectors away from the region of true damage towards the healthier portion. Indeed, it is

only with such dual viewing techniques, i.e., spatial distribution of damage parameter, energy vector fields and the contour intensity plots, that one is able to extract useful damage-sensitive features with an eye towards establishing a pattern recognition paradigm.

In this connection, a vivid case to the point concerns the “false alarm” test case included in the chart of Fig. 3.6. Here, referring to the associated plots in Figs. 3.23 – 3.30, it is seen that reliance only on the intensity (magnitude) plots can be misleading in that spurious spikes (similar to those in the true damage cases of Figs. 3.7 to 3.22) are still obtained here. However, combined with the vector field directional plots in Figs. 3.24, 3.26 and 3.28, one can easily see that the directions of these vectors are all opposite to those pertinent to the true damage cases (e.g., compare with Figs. 3.8, 3.10, 3.12, 3.16, 3.18, 3.20 and 3.22).

Finally, as a prelude to the studies reported in the next chapter (Chapter IV) we have also included a case simulating the effect of incompleteness in the experimental data. In this case, we consider a single patch group being damaged in a 32×32 mesh (Fig. 3.4) with the frequency, modal displacements and rotations being calculated as in the idealized case (refined mesh). The modal frequency and displacements only for a “healthy” and the damaged (with loss of stiffness) structures corresponding to 8×8 mesh were then extracted from these previous results and subsequently applied as measurements, i.e., as if no rotations and no displacements at the other intermediate points were supplied. This is similar to the NASA experimental set-up using only vertical displacement accelerometers at only 49, as shown in Figs. 3.31 to 3.32. Although some deterioration in accuracy is certainly obvious in the results of the present damage—detection—code (DDC), the results are still quantitatively good. Considering the rather incomplete (both in content and space) nature of the data supplied here. On the other hand (although not shown here), a similar exercise, but only lacking in rotational DOF measurements; i.e., employing full field displacements as in the Electronic speckle pattern interferometry (ESPI) of Chapter V, indicated very favorable results; i.e., with no discernable decrease in accuracy.

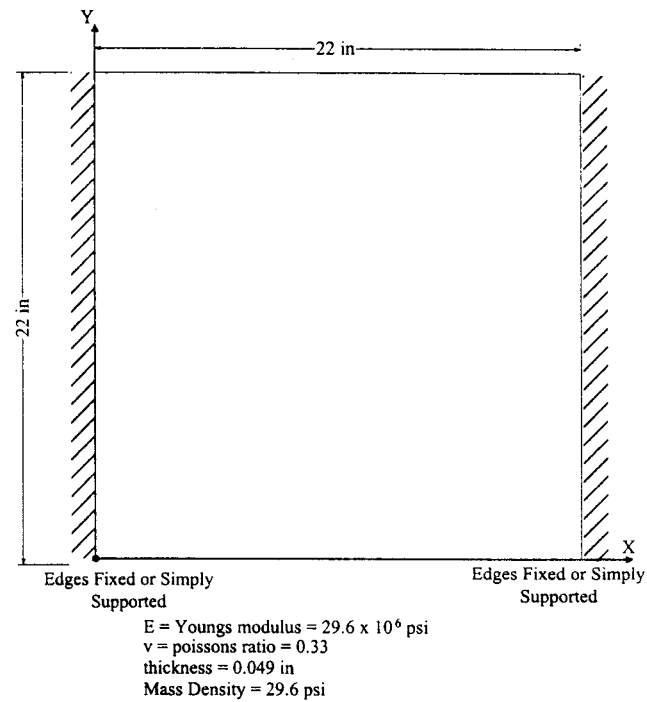


Fig. 3.1: Geometric Dimensions and Material Properties of the Plate

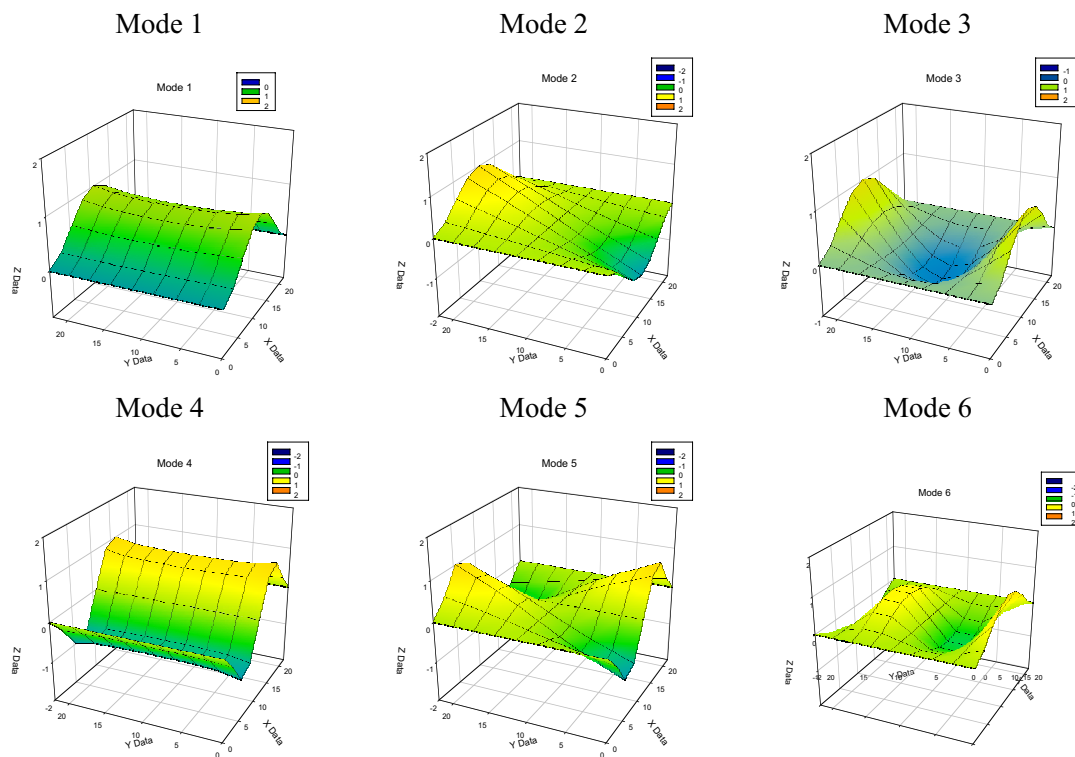


Fig. 3.2: Mode Shapes for Fixed - Fixed Plate

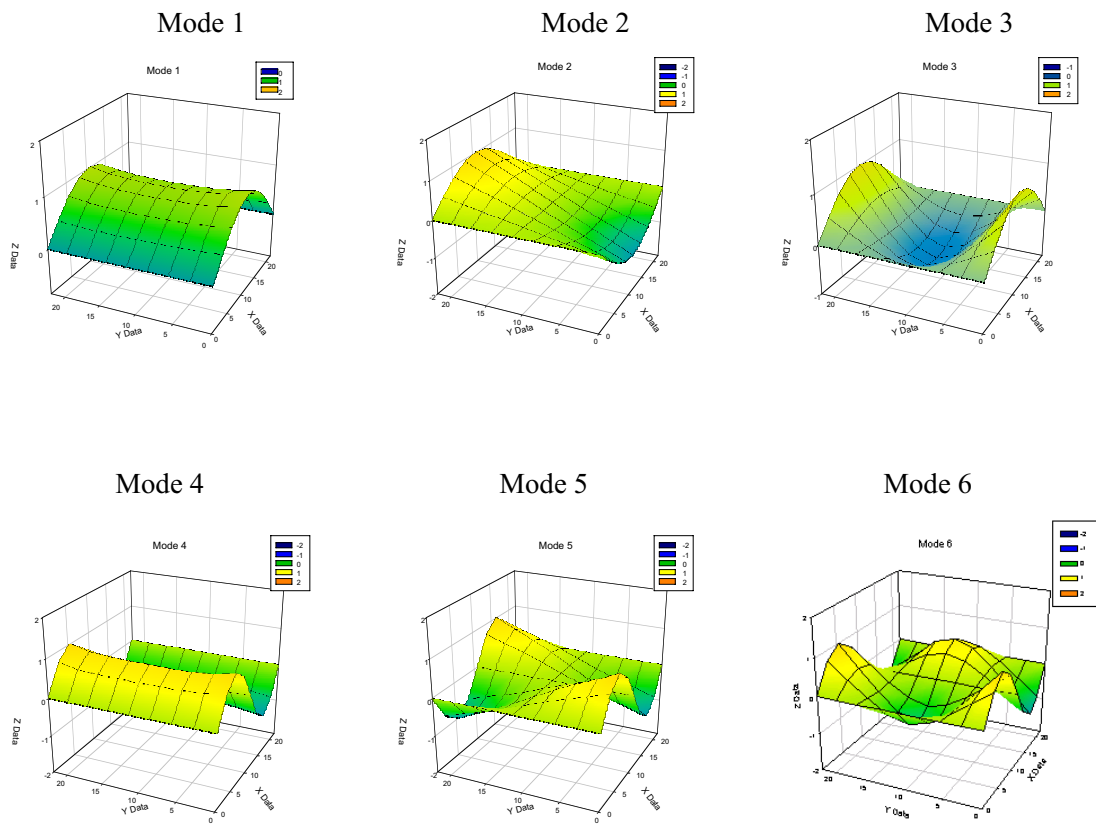
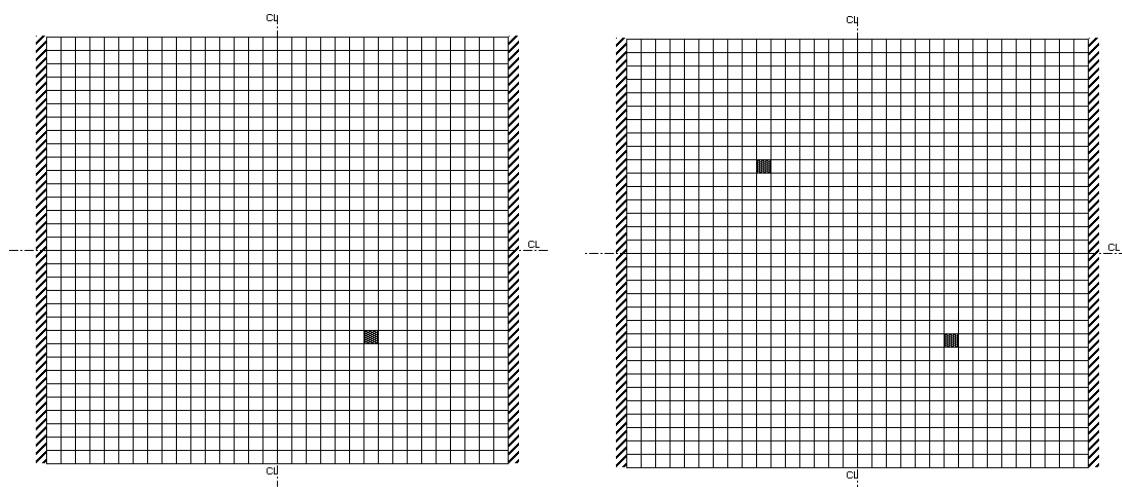


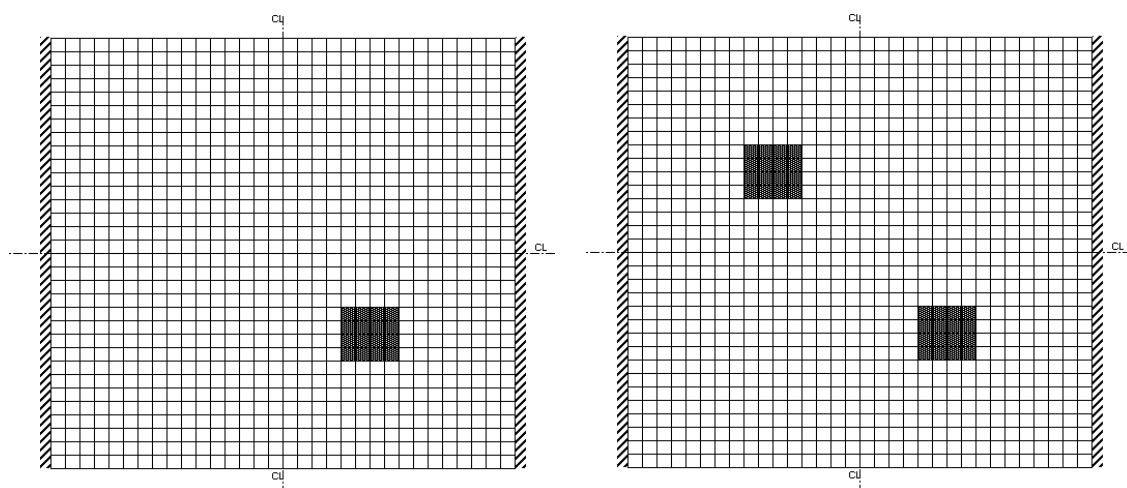
Fig. 3.3: Mode Shapes for Simply Supported Plate

Table 3.1: Frequencies of free vibration of various mode shapes for a healthy (undamaged plate) for various mesh size

	Fixed - Fixed Plate			Simply - Supported Plate		
	8 × 8	16 × 16	32 × 32	8 × 8	16 × 16	32 × 32
Eigenvalues						
Mode 1	1.78E+04	1.79E+04	1.82E+04	3.41E+03	3.37E+03	3.36E+03
Mode 2	2.52E+04	2.54E+04	2.67E+04	9.53E+03	9.44E+03	9.43E+03
Mode 3	6.86E+04	6.88E+04	7.03E+04	4.94E+04	4.89E+04	4.88E+04
Mode 4	1.36E+05	1.98E+05	1.45E+05	5.82E+04	5.57E+04	5.51E+04
Mode 5	1.64E+05	1.67E+05	1.94E+05	8.53E+04	8.01E+04	7.93E+04
Mode 6	2.31E+05	2.32E+05	2.46E+05	1.87E+05	1.82E+05	1.81E+05
Frequency (in rad/sec)						
Mode 1	133.51	133.78	134.81	58.41	58.08	58.00
Mode 2	158.87	159.28	163.25	97.63	97.14	97.09
Mode 3	262.01	262.31	265.09	222.17	221.03	220.92
Mode 4	368.98	444.65	380.40	241.14	236.09	234.83
Mode 5	404.73	408.88	440.52	291.98	282.98	281.52
Mode 6	480.19	482.12	495.93	432.74	426.58	425.39
Frequency in (Hz)						
Mode 1	21.46	21.29	21.25	9.30	9.24	9.23
Mode 2	25.98	25.36	25.29	15.54	15.46	15.45
Mode 3	42.19	41.76	41.70	35.36	35.18	35.16
Mode 4	60.54	59.10	58.72	38.38	37.58	37.37
Mode 5	70.11	65.10	64.41	46.47	45.04	44.80
Mode 6	78.93	76.79	76.42	68.87	67.89	67.70



Patch location of a single and multiple damage sites



Patch group locations of a single and multiple damage sites corresponding to an 8×8 mesh

Fig. 3.4: Schematic Diagram of the location of the patch or patch group for the single or multiple damage cases with the opposite edges either fixed – fixed or simply supported.

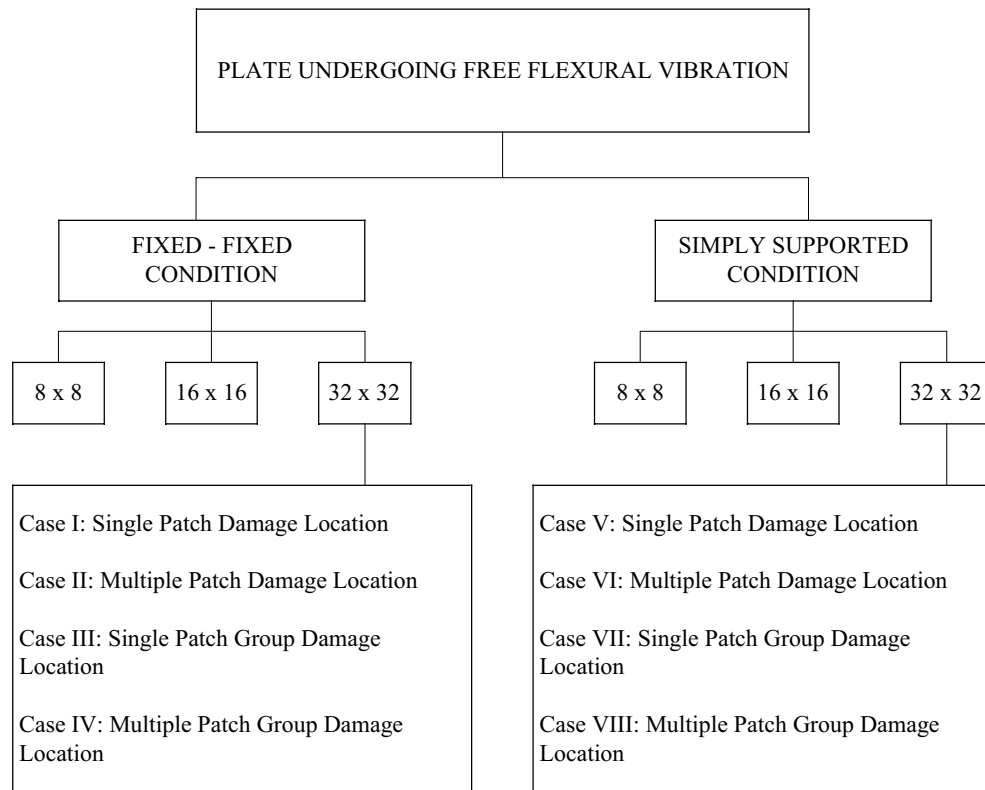


Fig. 3.5 Organization chart of the various mesh sizes and case scenarios of damage

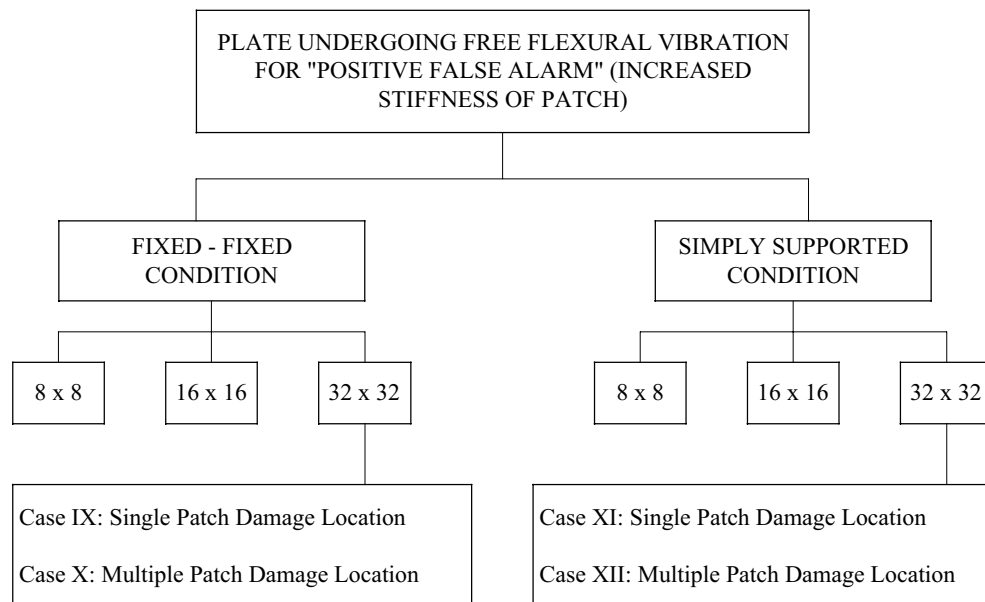


Fig. 3.6: Organization of the case scenarios having the positive false alarm (increase in stiffness)

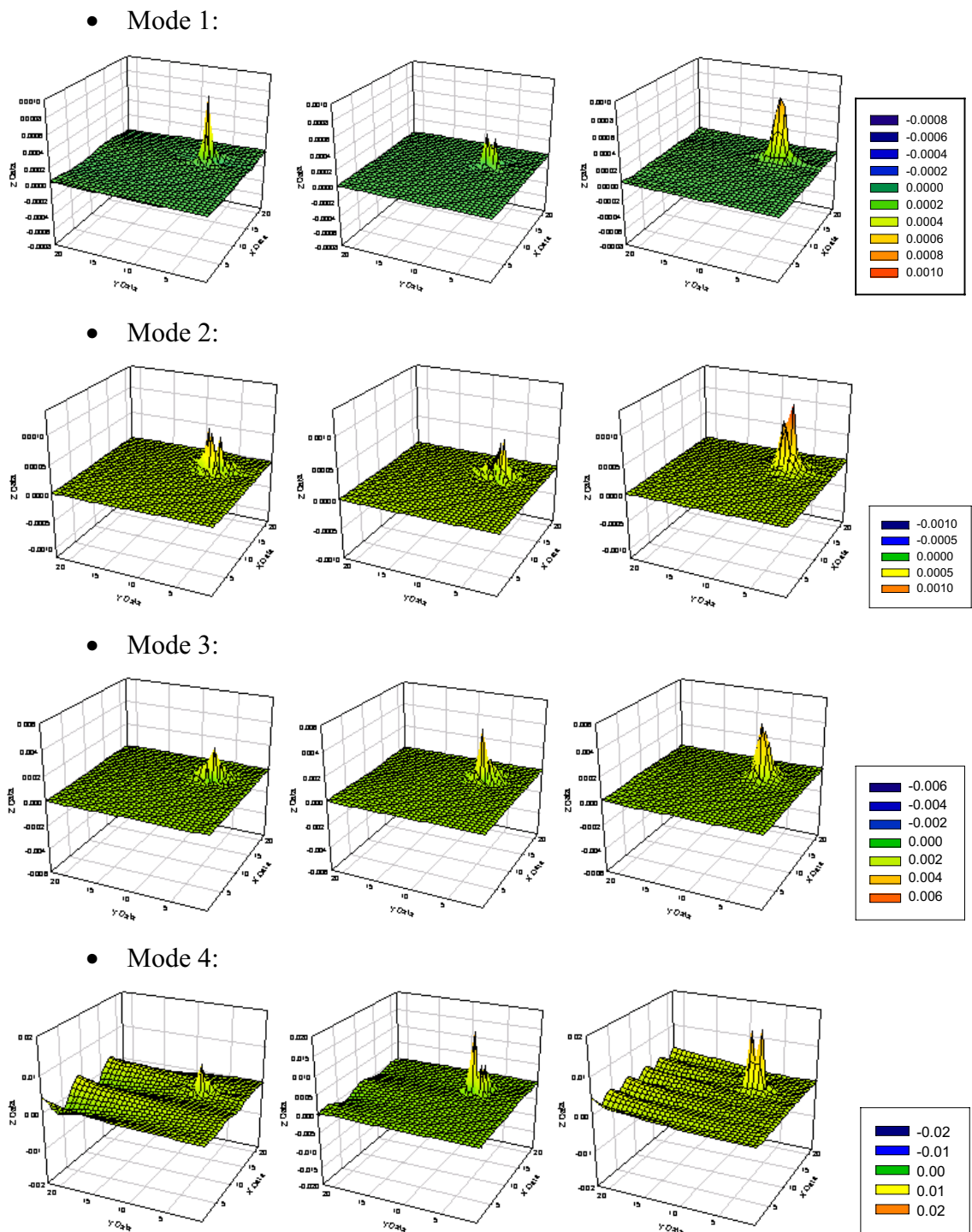
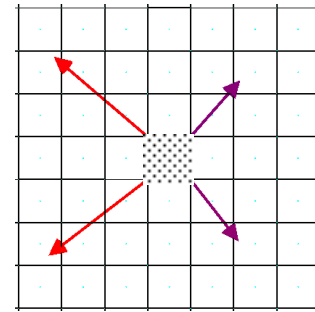
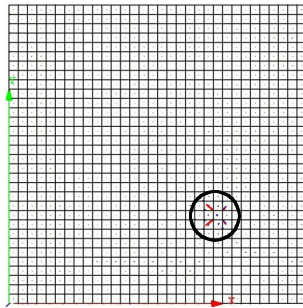
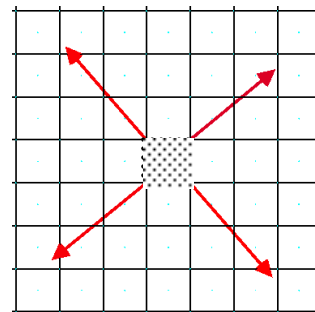
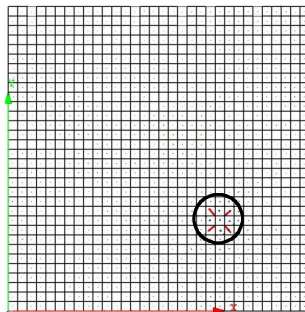


Fig. 3.7: Case I: - Spatial Distribution of the Defect Energy Force Parameter showing (for each mode) the F_1 , F_2 and F (resultant) Force Diagrams (columns 1, 2 and 3) for single patch damage with fixed – fixed boundary conditions.

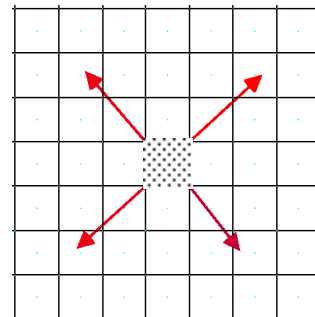
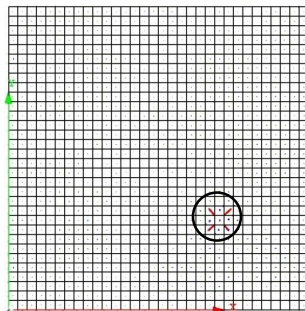
- Mode 1:



- Mode 2:



- Mode 3:



- Mode 4:

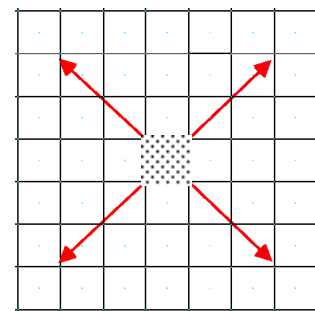
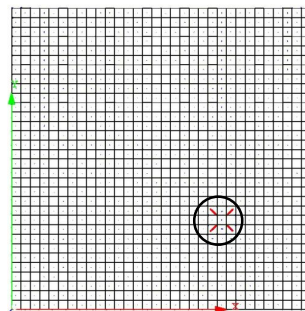


Fig. 3.8: Case I: - Energy Vector Field Diagram for the damaged plate with overall and zoomed plots for single patch damaged with fixed - fixed boundary conditions.

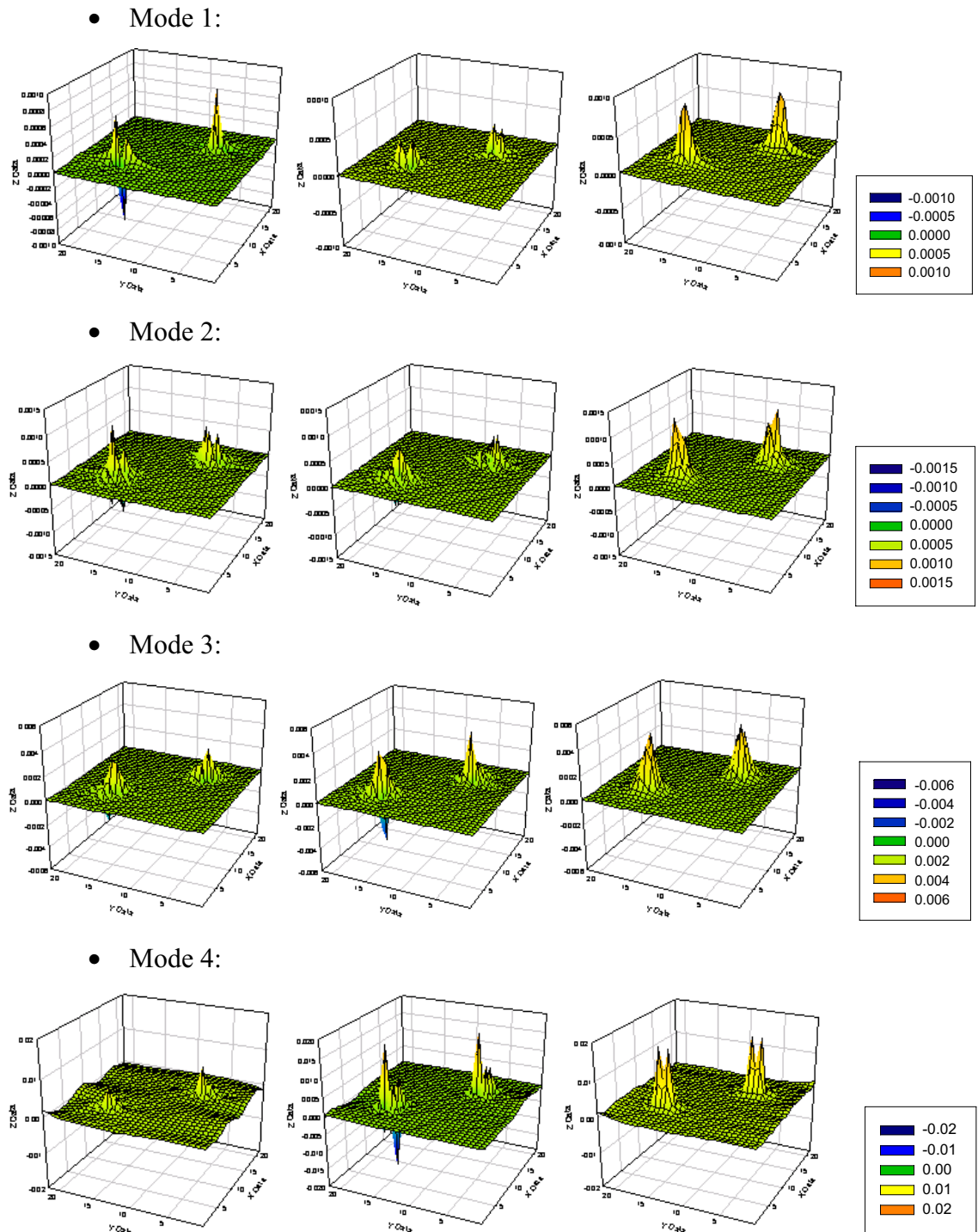
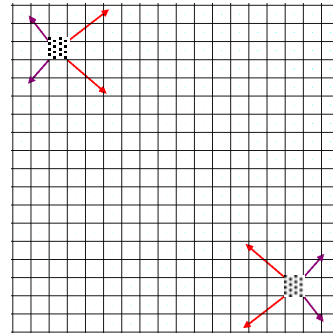
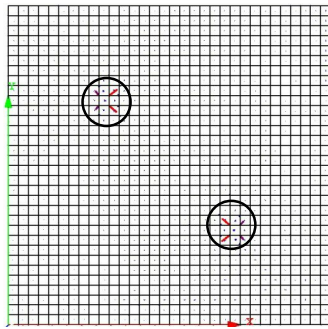
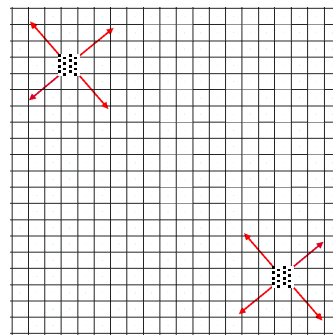
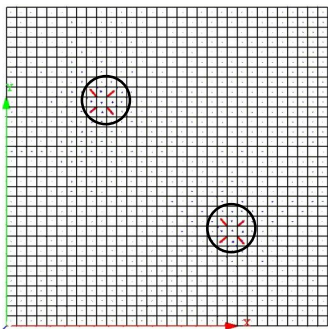


Fig. 3.9: Case II: - Spatial Distribution of the Defect Energy Force Parameter showing (for each mode) the F_1 , F_2 and F (resultant) Force Diagrams (columns 1, 2 and 3) for multiple patch damage with fixed – fixed boundary condition.

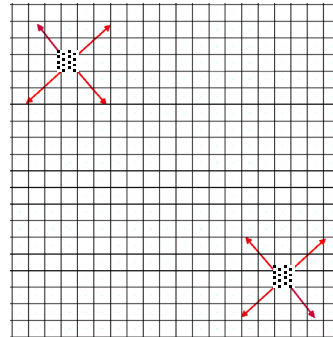
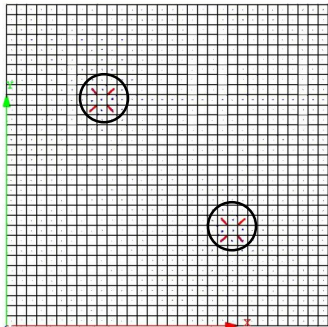
- Mode 1:



- Mode 2:



- Mode 3:



- Mode 4:

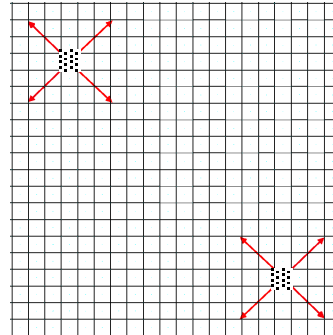
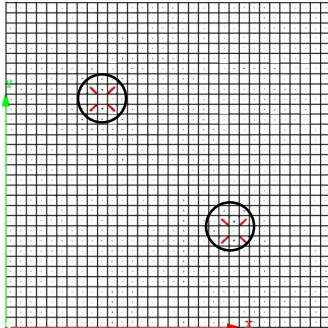
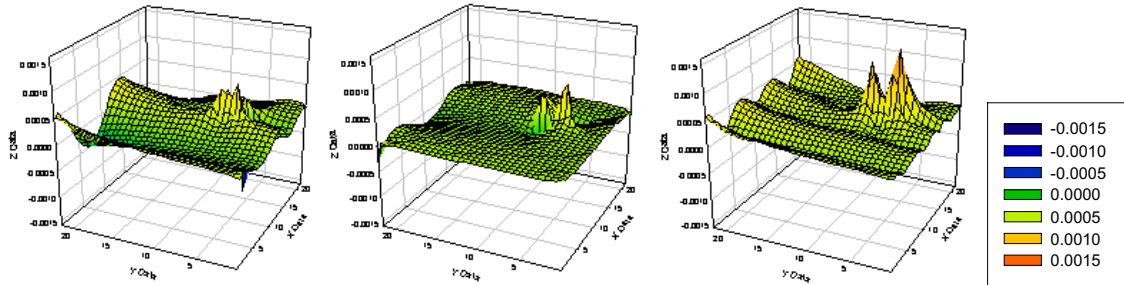
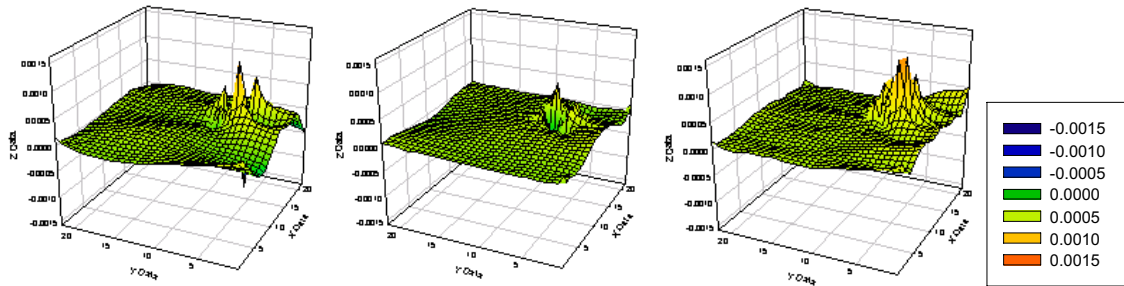


Fig. 3.10: Case II: - Energy Vector Field Diagram for the damaged plate with overall and zoomed plots for multiple patch damage with fixed – fixed boundary condition.

- Mode 1:



- Mode 2:



- Mode 3:

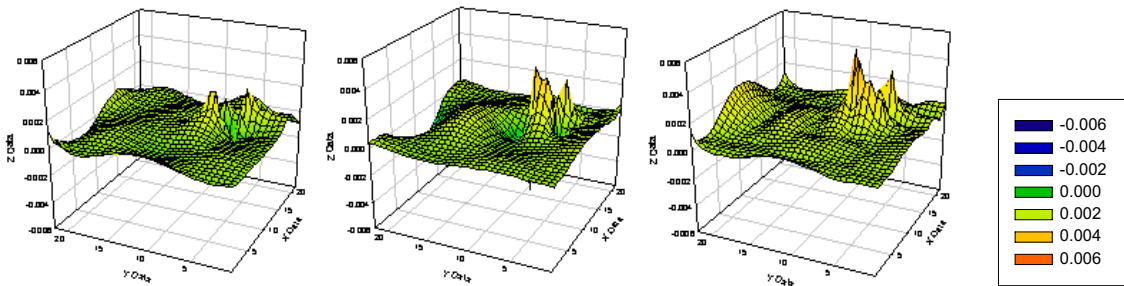
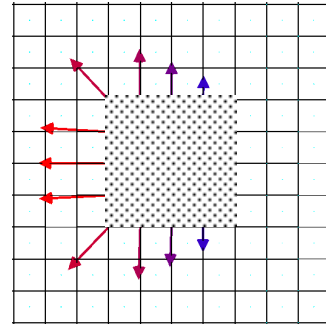
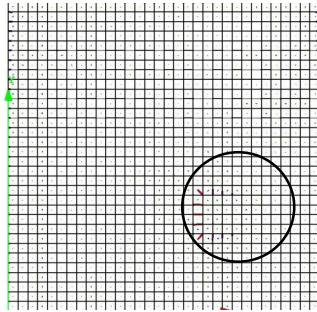
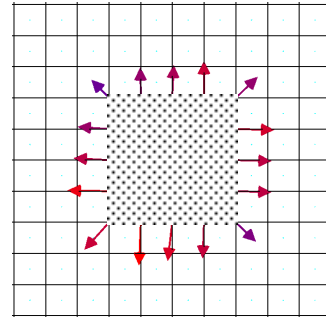
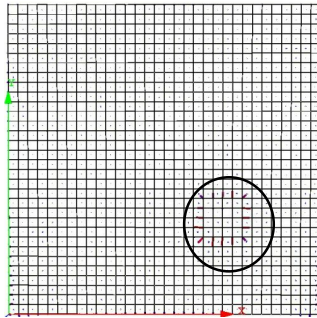


Fig. 3.11: Case III: - Spatial Distribution of the Defect Energy Force Parameter showing (for each mode) the F_1 , F_2 and F (resultant) Force Diagrams (columns 1, 2 and 3) for single location of patch group damage with fixed – fixed boundary condition.

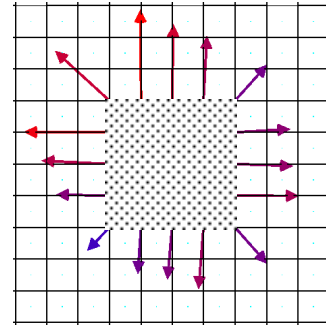
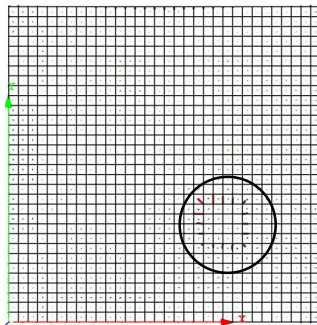
- Mode 1:



- Mode 2:



- Mode 3:



- Mode 4:

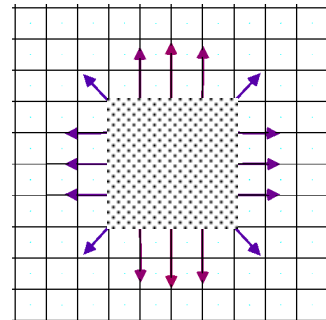
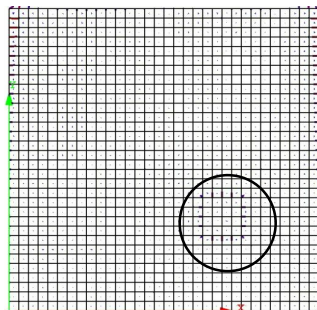


Fig. 3.12: Case III: - Energy Vector Field Diagram for the damaged plate with overall and zoomed plots for single location of patch group damage with fixed – fixed boundary condition.

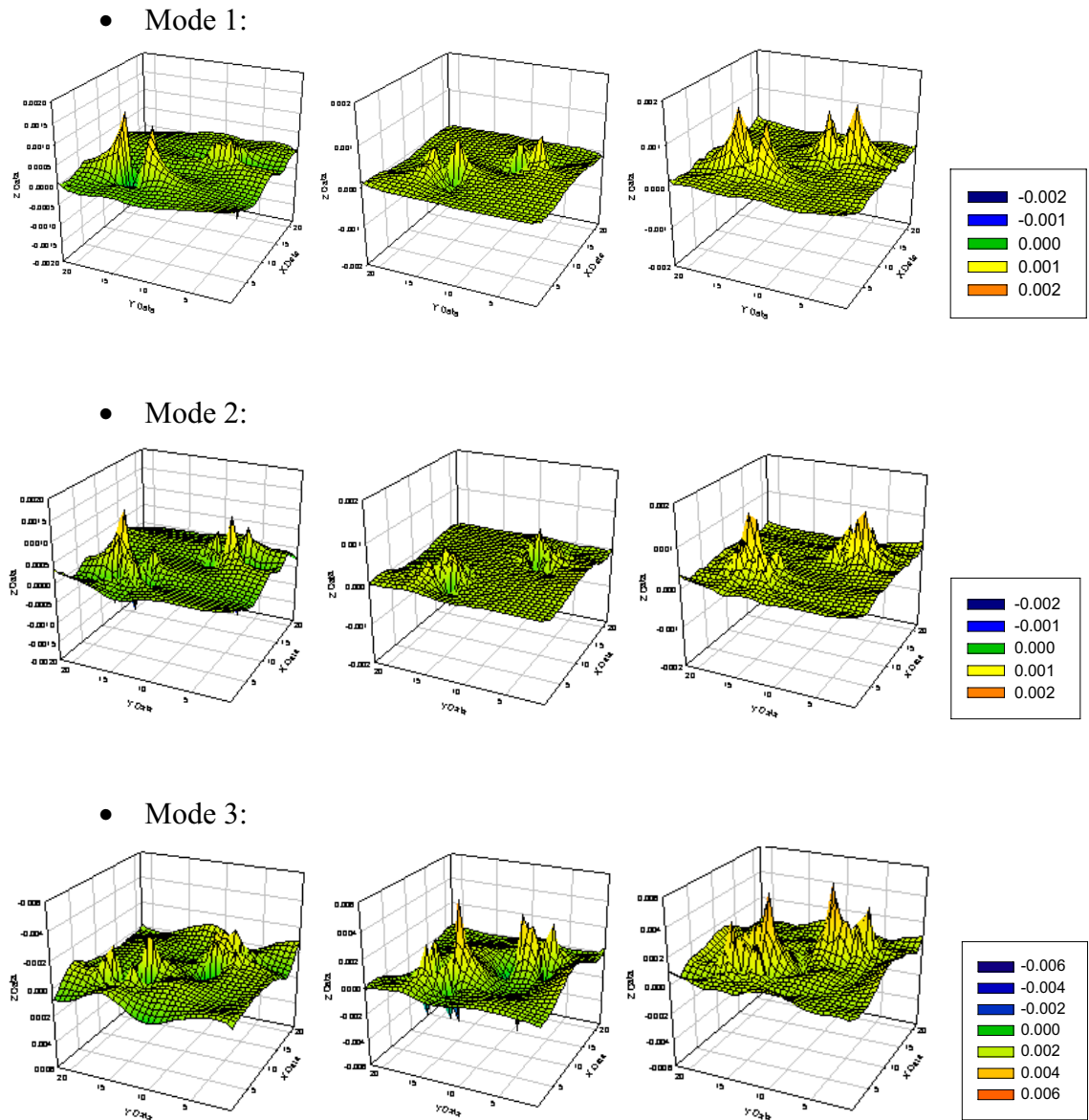
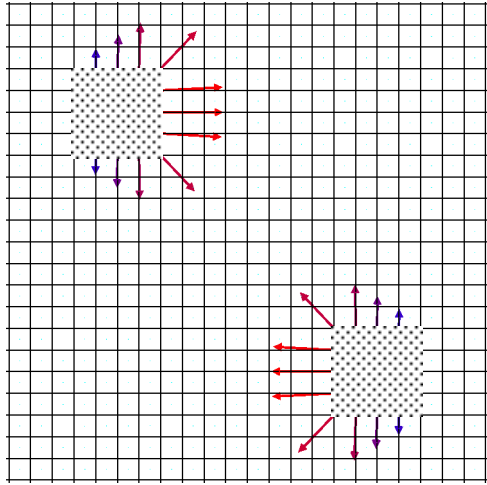
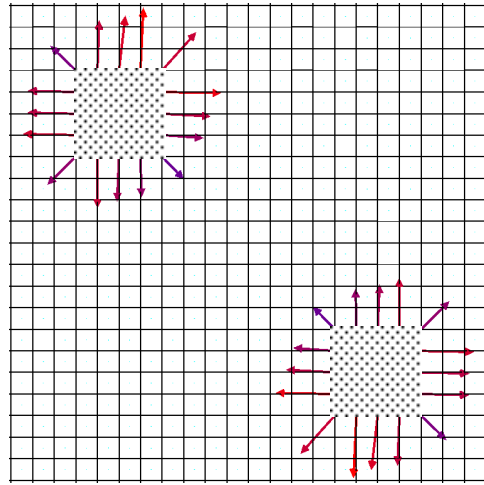


Fig. 3.13: Case IV: - Spatial Distribution of the Defect Energy Force Parameter showing (for each mode) the F_1 , F_2 and F (resultant) Force Diagrams (columns 1, 2 and 3) for multiple blocks damaged with fixed – fixed boundary condition.

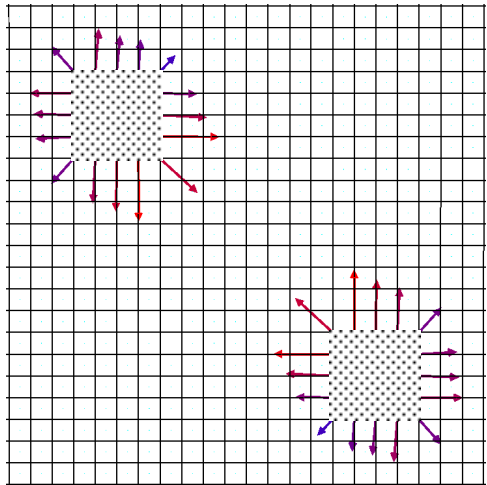
- Mode 1:



- Mode 2:



- Mode 3:



- Mode 4:

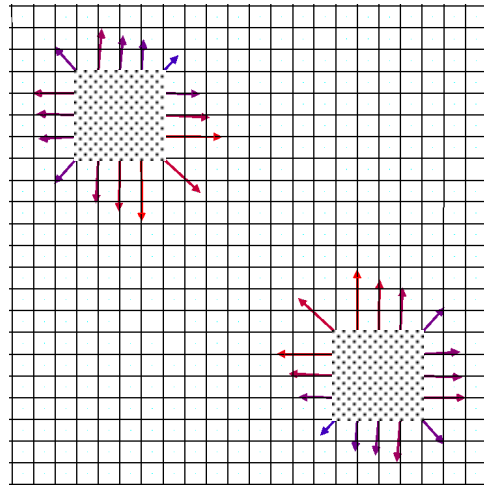
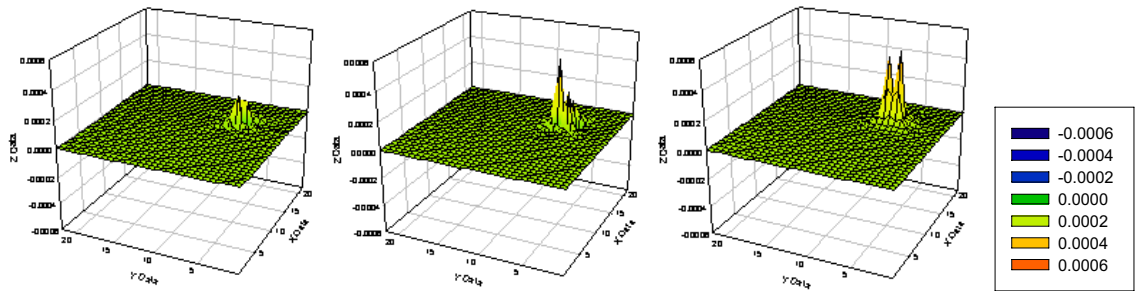
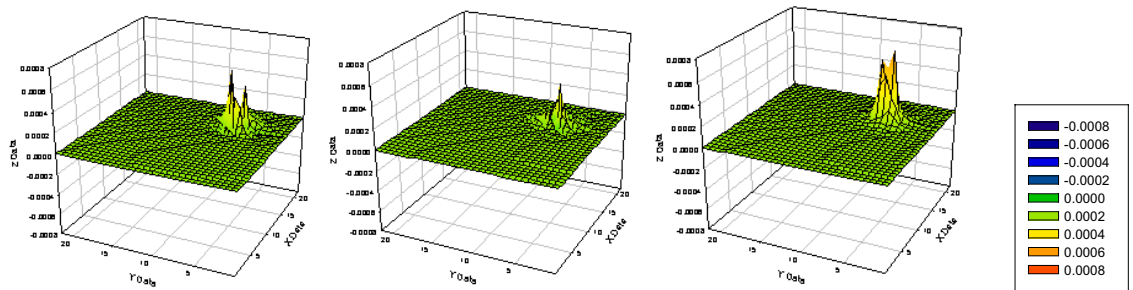


Fig. 3.14: Case IV: - Energy Vector Field Diagram for the damaged plate with plots for multiple location of patch group damaged with fixed – fixed boundary condition.

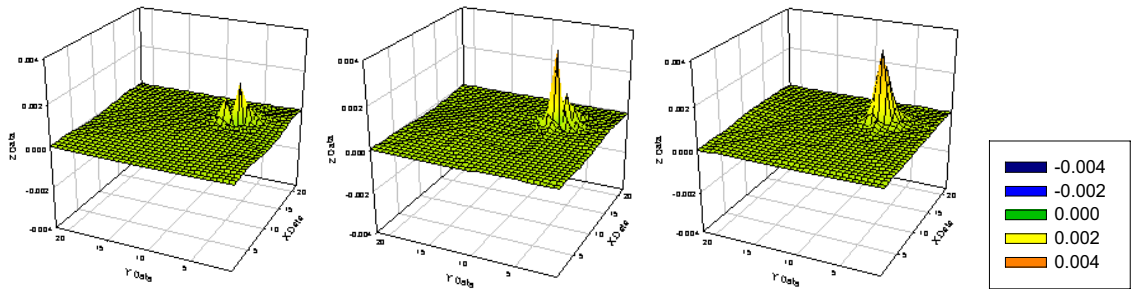
- Mode 1:



- Mode 2:



- Mode 3



- Mode 4

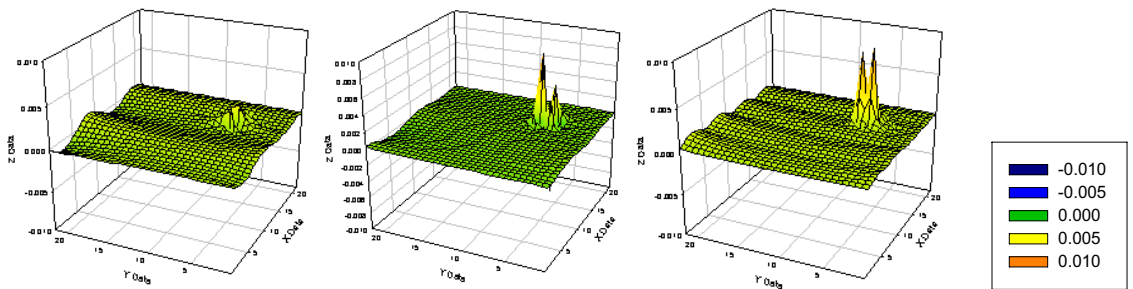
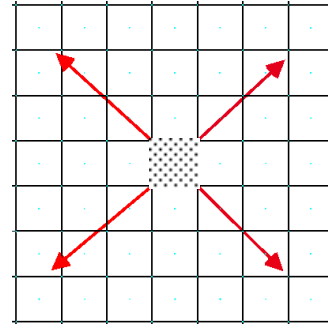
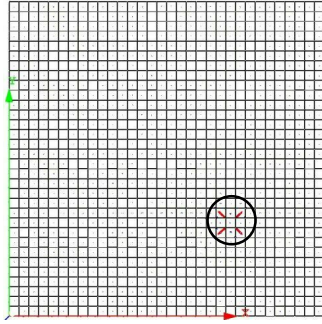
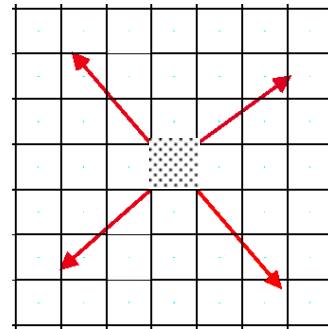
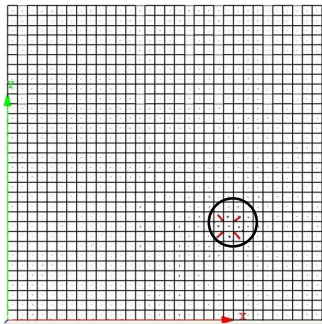


Fig. 3.15: Case V: - Spatial Distribution of the Defect Energy Force Parameter showing (for each mode) the F_1 , F_2 and F (resultant) Force Diagrams (columns 1, 2 and 3) for single patch damage with simply supported boundary conditions.

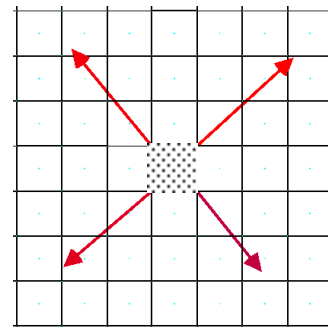
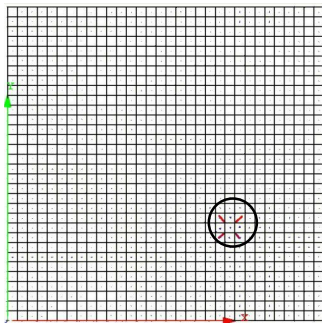
- Mode 1:



- Mode 2:



- Mode 3:



- Mode 4:

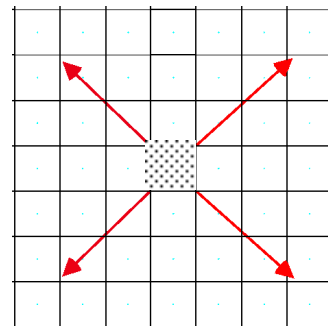
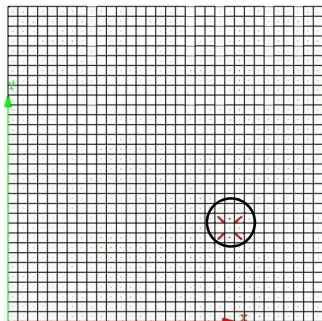


Fig. 3.16: Case V: - Energy Vector Field Diagram for the damaged plate with overall and zoomed plots for single patch damage with simply supported boundary conditions.

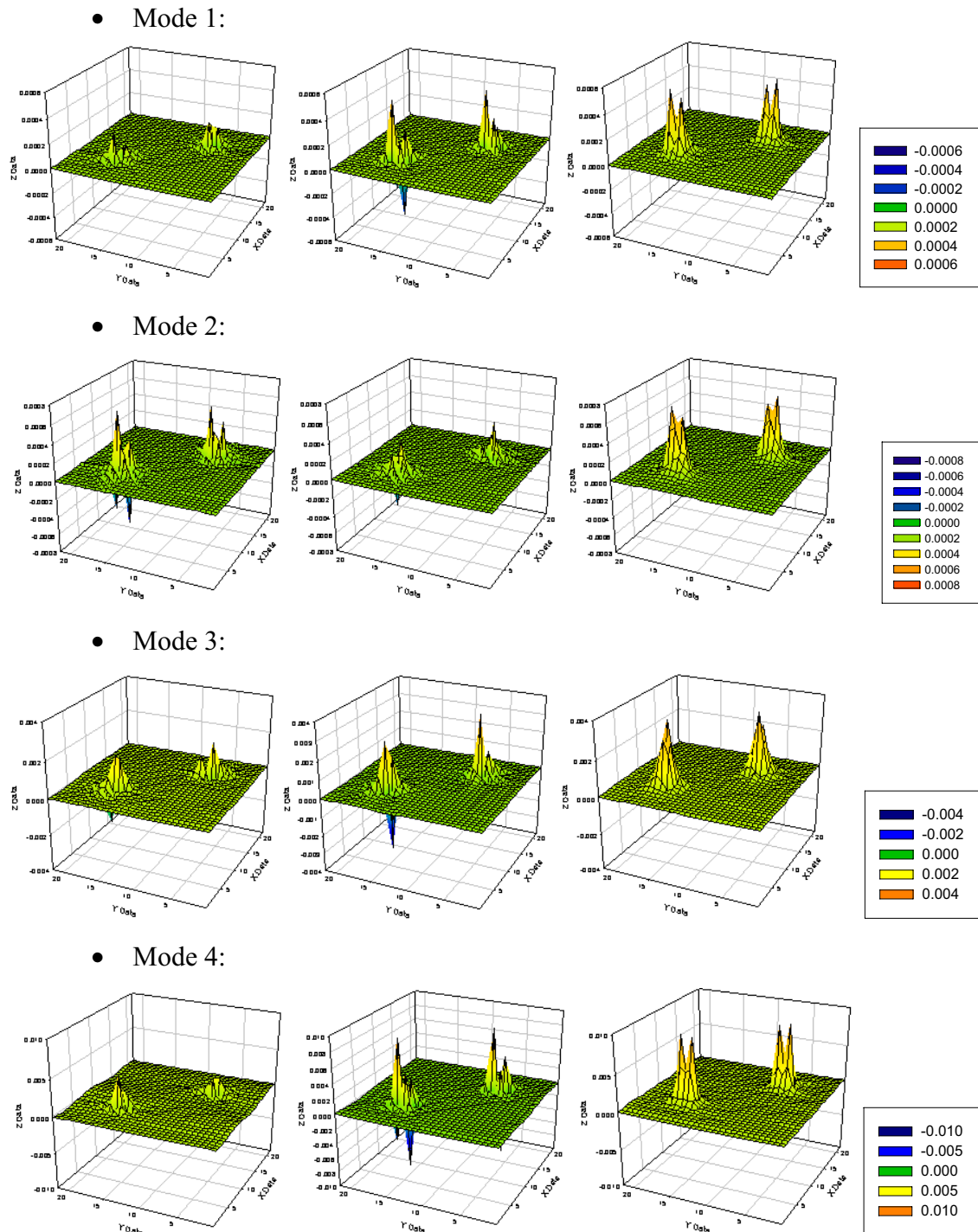
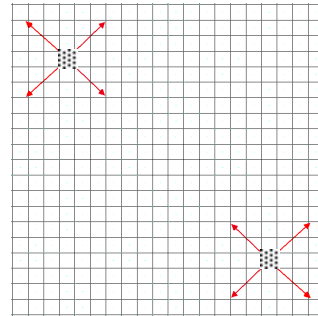
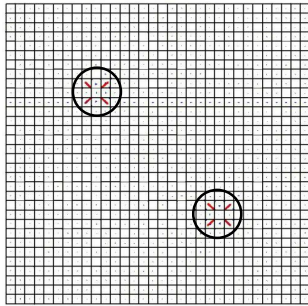
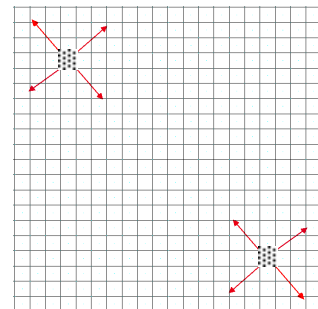
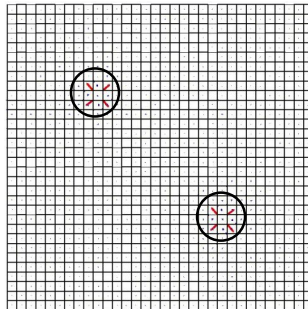


Fig. 3.17: Case VI: - Spatial Distribution of the Defect Energy Force Parameter showing (for each mode) the F_1 , F_2 and F (resultant) Force Diagrams (columns 1, 2 and 3) for multiple location of patch damages with simply supported boundary condition.

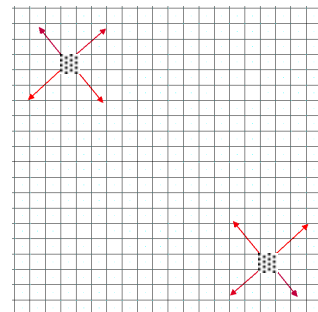
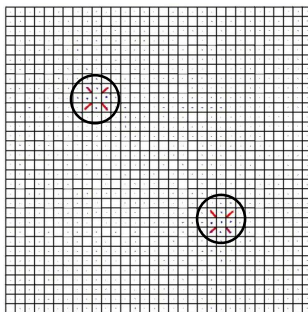
- Mode 1:



- Mode 2:



- Mode 3:



- Mode 4:

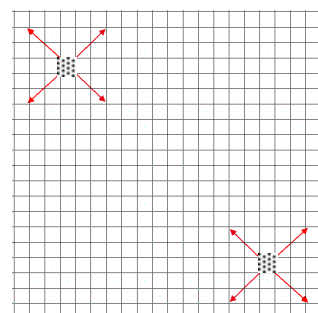
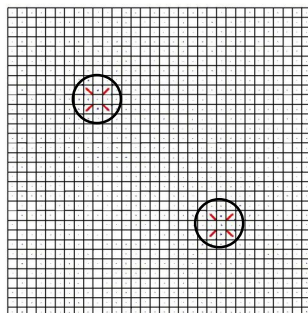


Fig. 3.18: Case VI: - Energy Vector Field Diagram for the damaged plate with overall and zoomed plots for multiple location of patch damages with simply supported boundary condition.

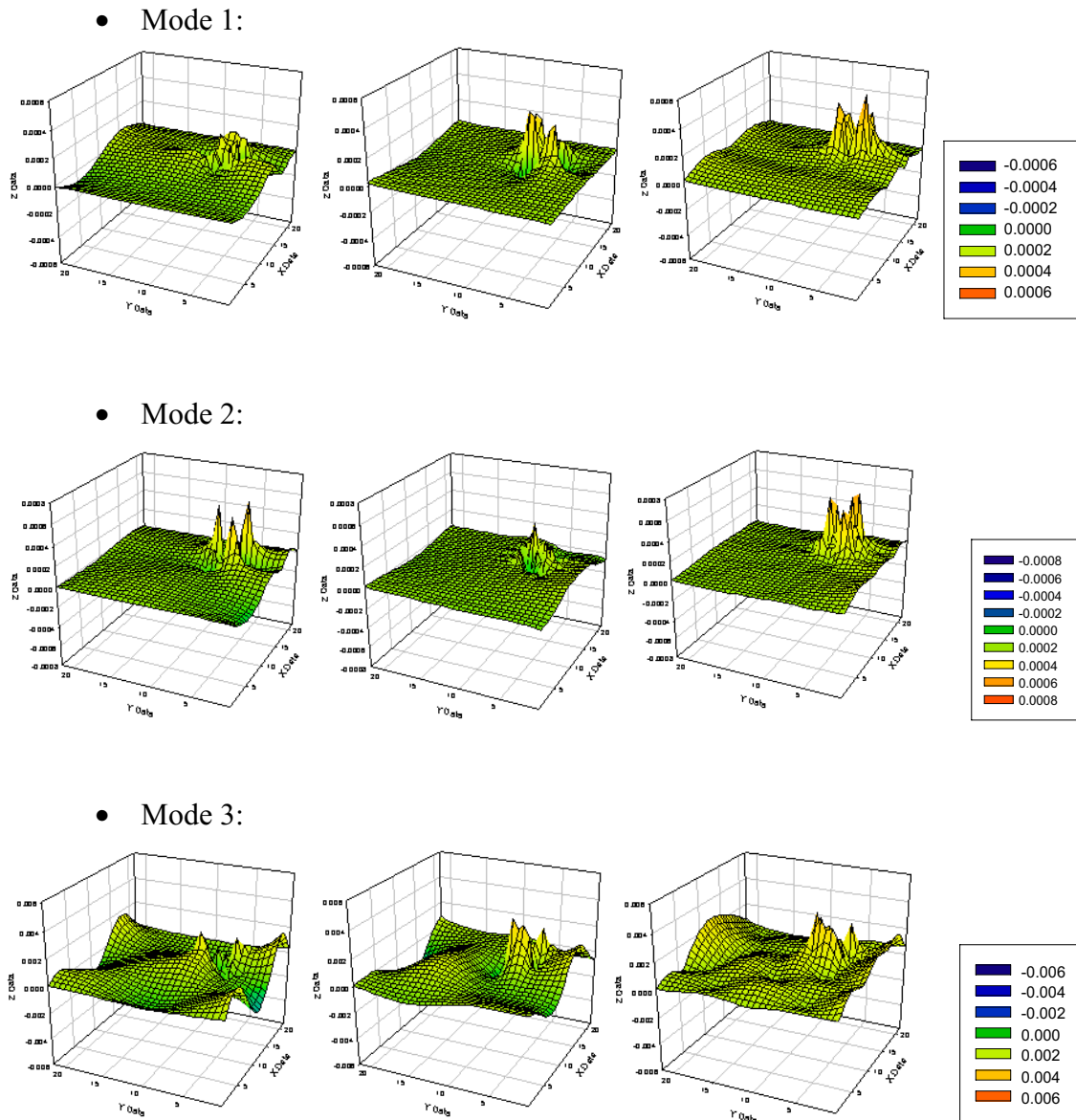
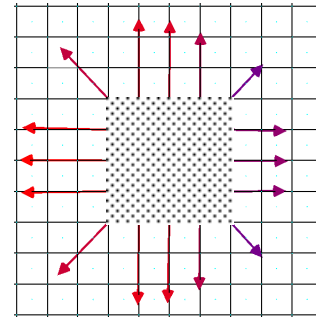
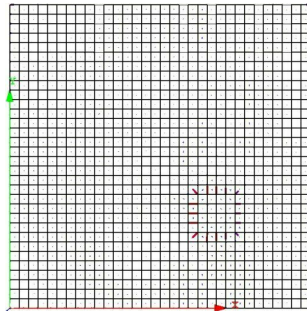
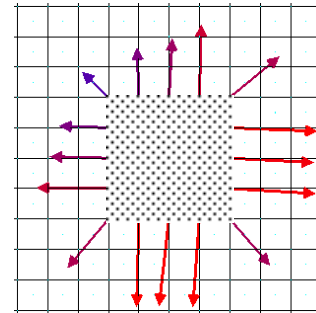
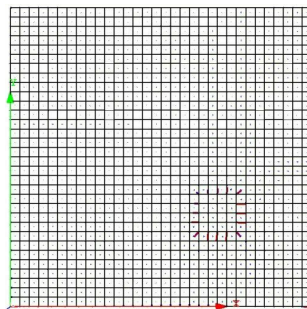


Fig. 3.19: Case VII: - Spatial Distribution of the Defect Energy Force Parameter showing (for each mode) the F_1 , F_2 and F (resultant) Force Diagrams (columns 1, 2 and 3) for single location of patch group damage with simply supported boundary condition.

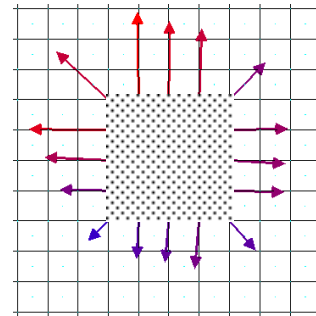
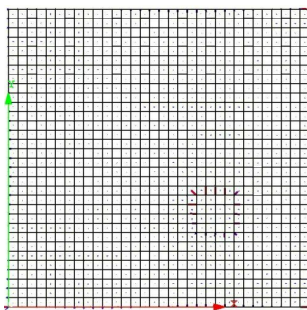
- Mode 1:



- Mode 2:



- Mode 3:



- Mode 4:

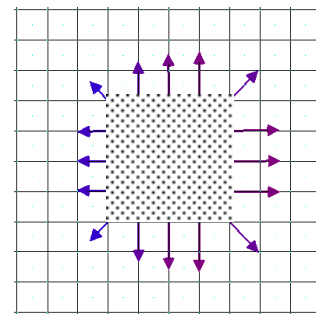
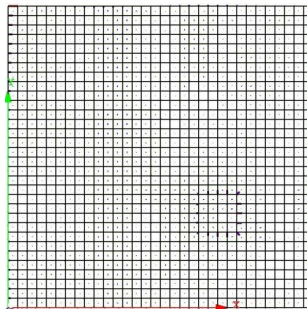
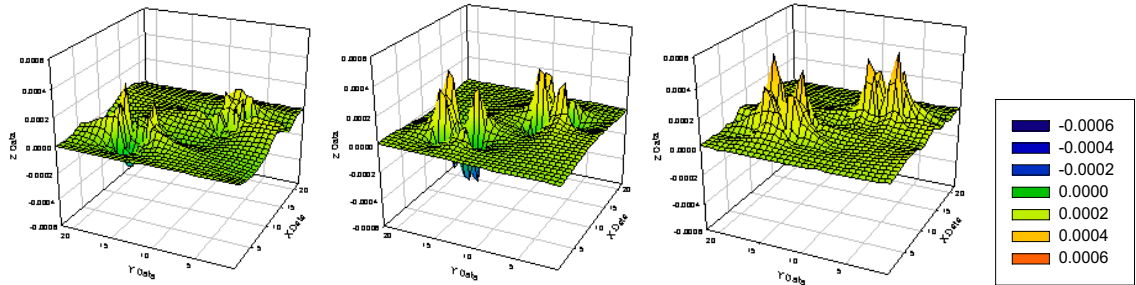
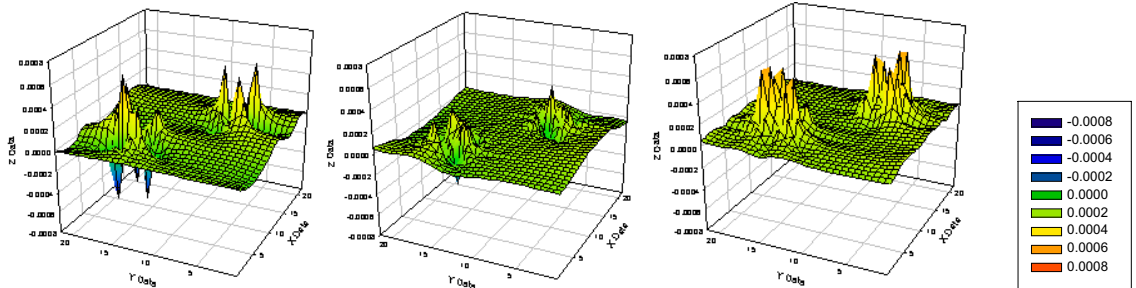


Fig. 3.20: Case VII: - Energy Vector Field Diagram for the damaged plate with overall and zoomed plots for single location of patch damage with simply supported boundary condition.

- Mode 1:



- Mode 2:



- Mode 3:

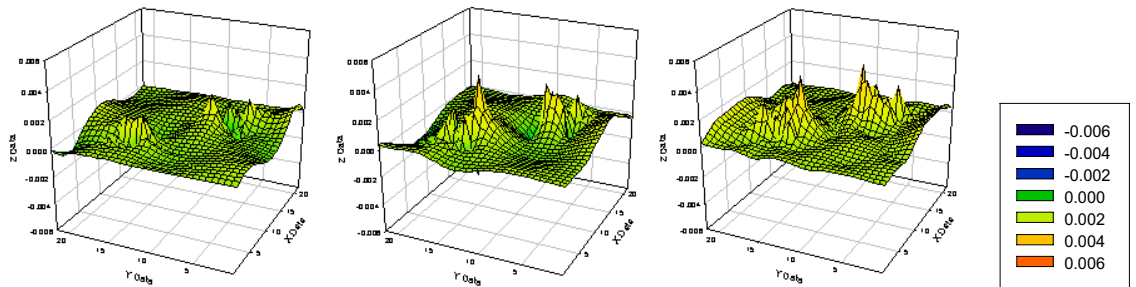
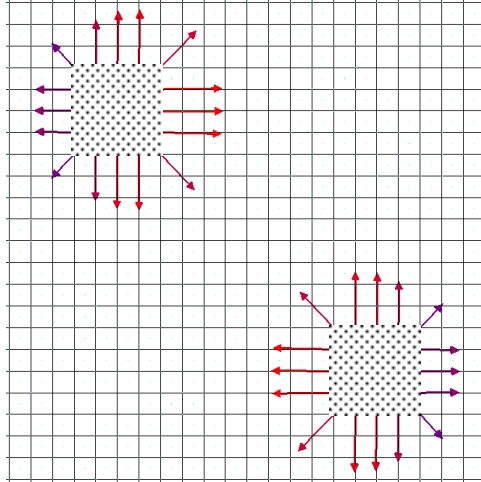
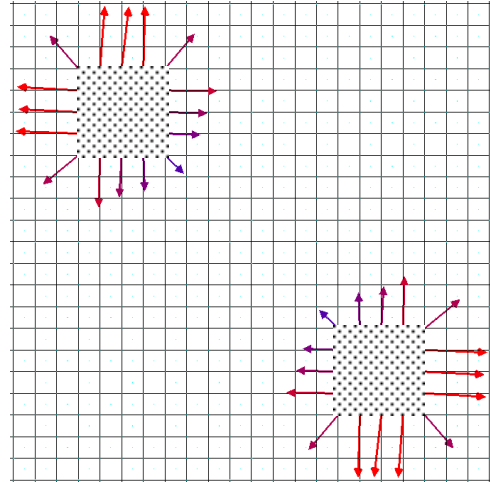


Fig. 3.21: Case VIII: - Spatial Distribution of the Defect Energy Force Parameter showing (for each mode) the F_1 , F_2 and F (resultant) Force Diagrams (columns 1, 2 and 3) for multiple locations of patch group damaged with simply supported boundary condition.

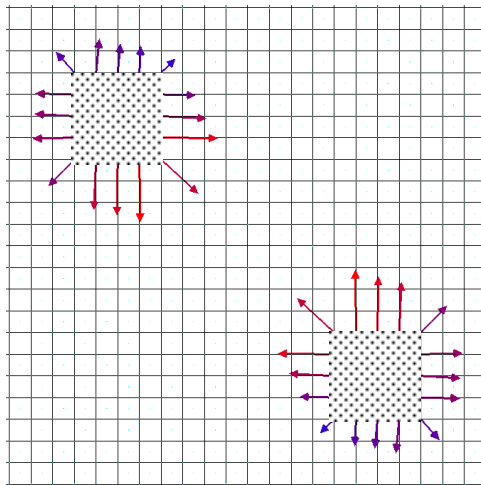
- Mode 1:



- Mode 2:



- Mode 3:



- Mode 4

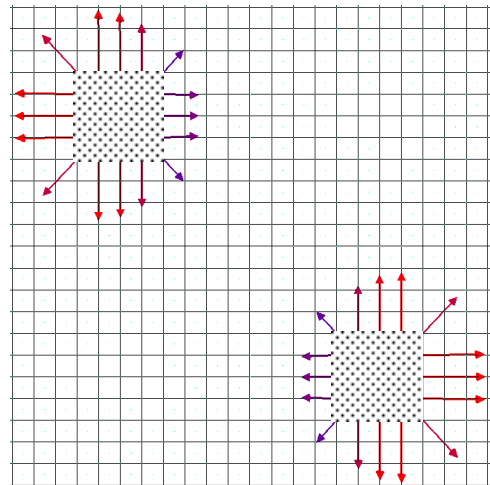
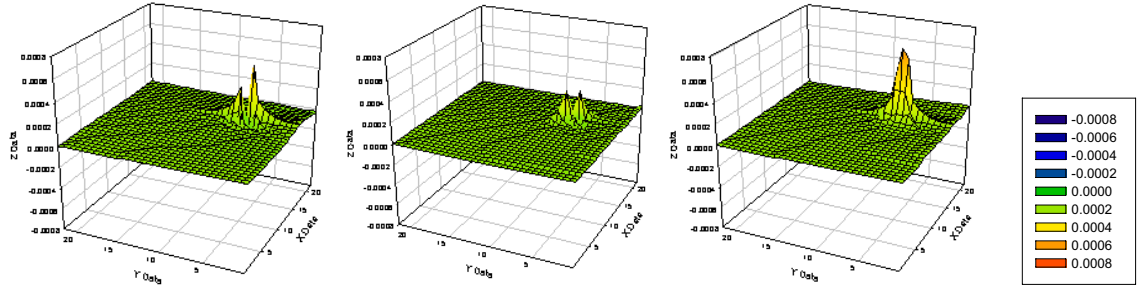
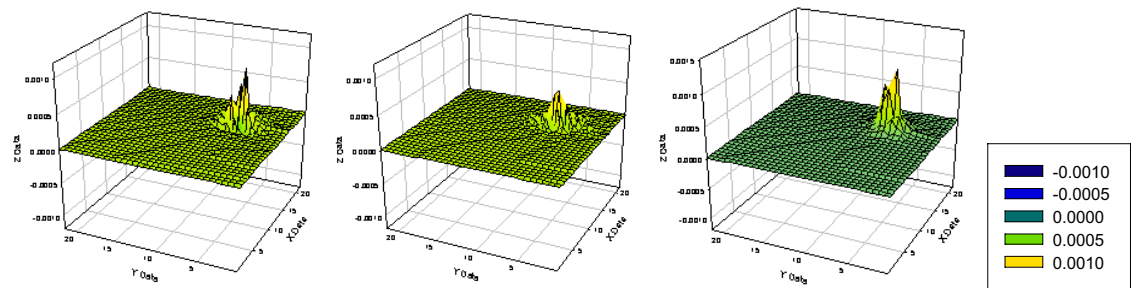


Fig. 3.22: Case VIII: - Energy Vector Field Diagram for the damaged plate with plots for multiple locations of patch group damage with simply supported boundary condition.

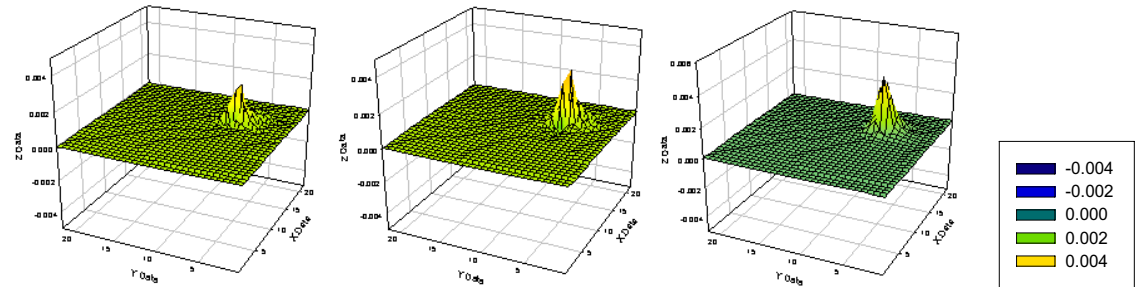
- Mode 1:



- Mode 2:



- Mode 3:



- Mode 4:

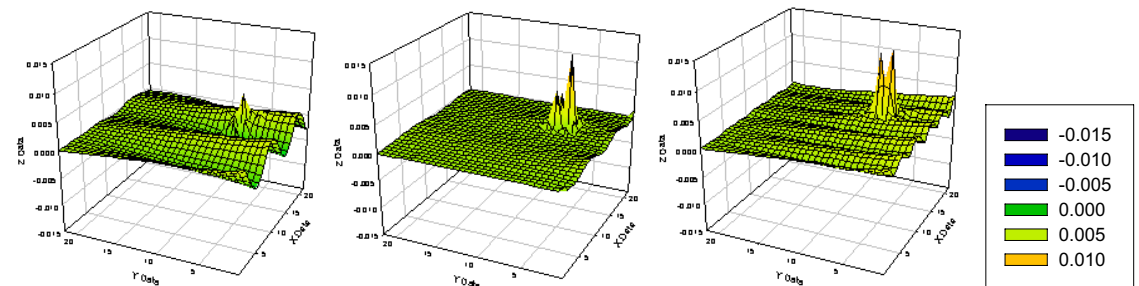
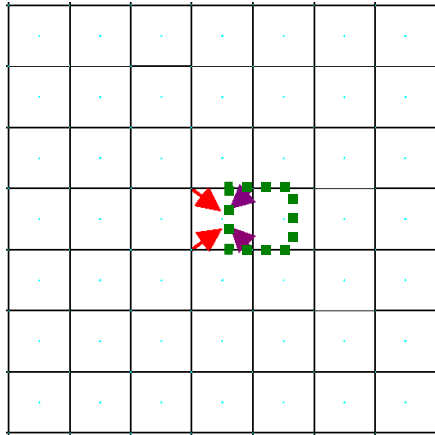
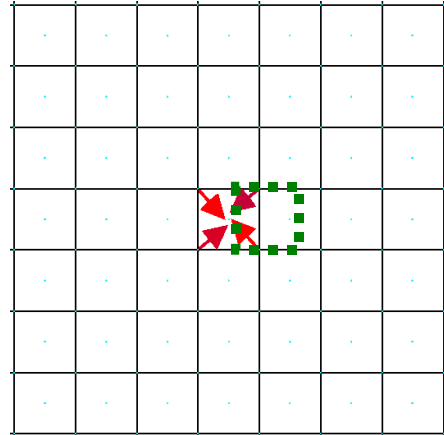


Fig. 3.23: Case IX: - Spatial Distribution of the Defect Energy Force Parameter showing (for each mode) the F_1 , F_2 and F (resultant) Force Diagrams (columns 1, 2 and 3) for single location of patch with increased stiffness (strengthening) for fixed – fixed boundary condition.

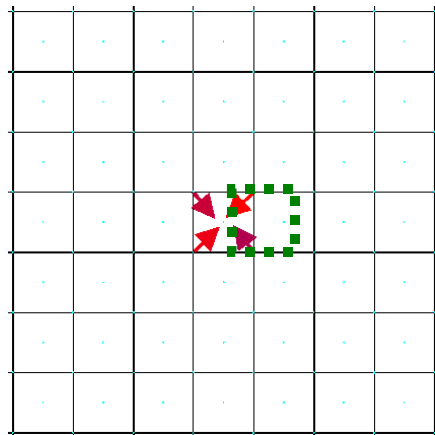
- Mode 1:



- Mode 2:



- Mode 3:



- Mode 4:

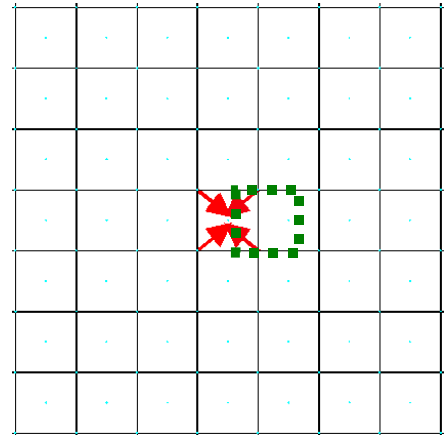


Fig. 3.24: Case IX: - Energy Vector Field Diagram for the strengthened plate with plots for single location of patch damaged with fixed - fixed boundary conditions.

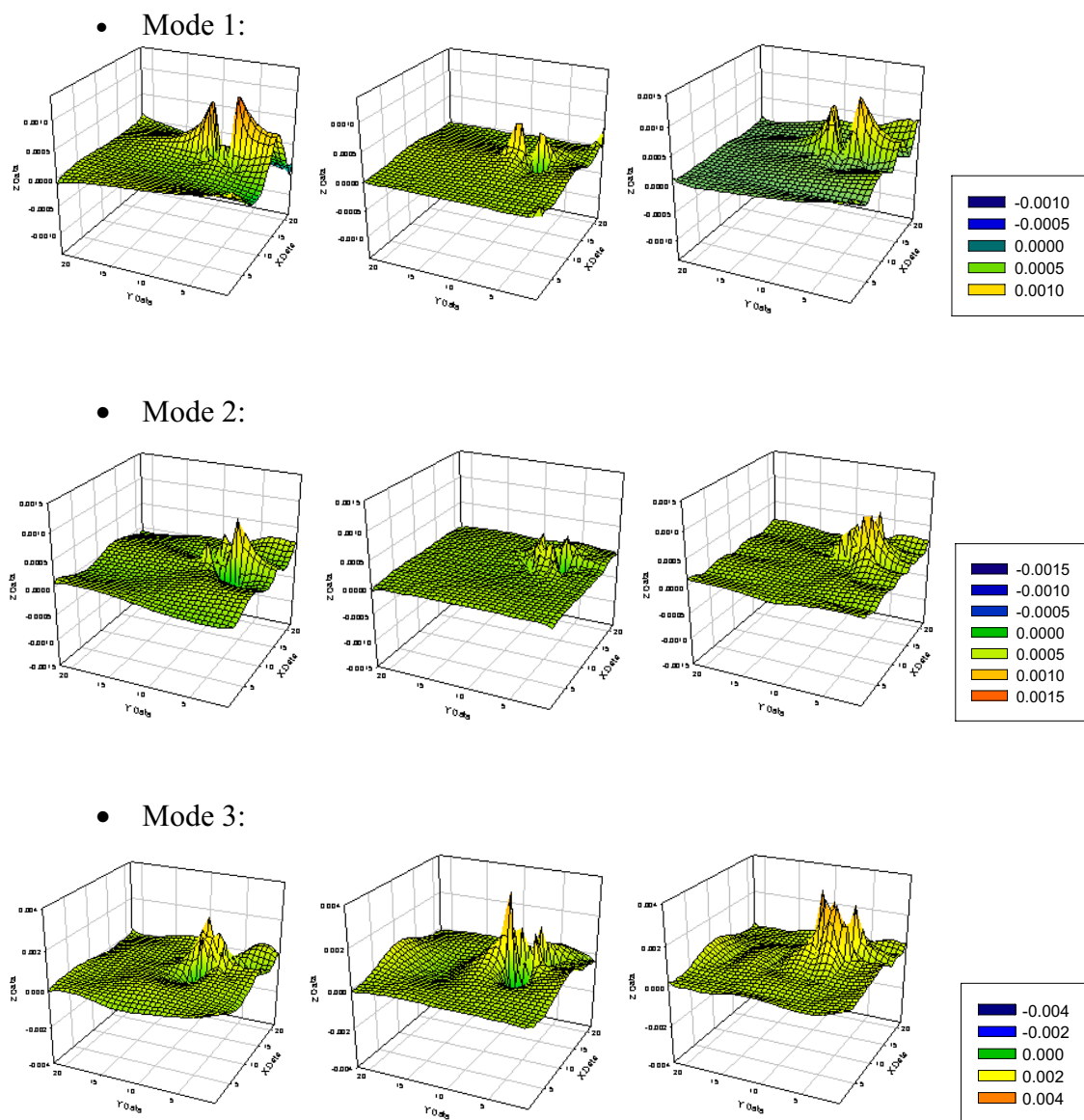
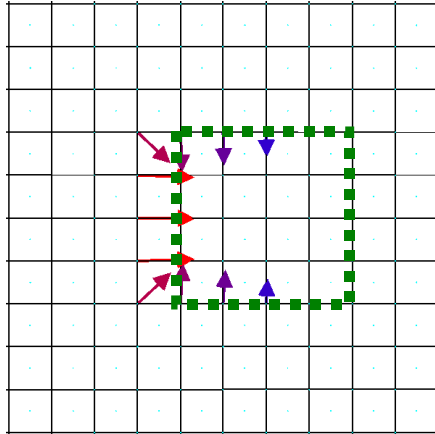
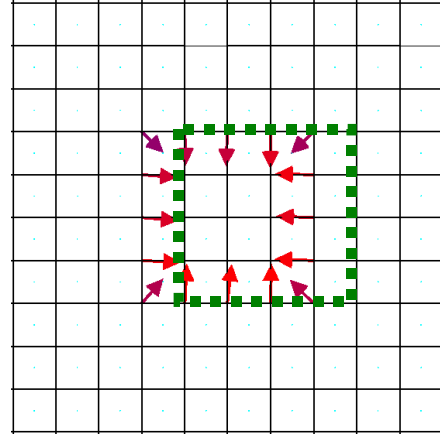


Fig. 3.25: Case X: - Spatial Distribution of the Defect Energy Force Parameter showing (for each mode) the F_1 , F_2 and F (resultant) Force Diagrams (columns 1, 2 and 3) for single location of patch group with increased stiffness (strengthening) for fixed – fixed boundary condition.

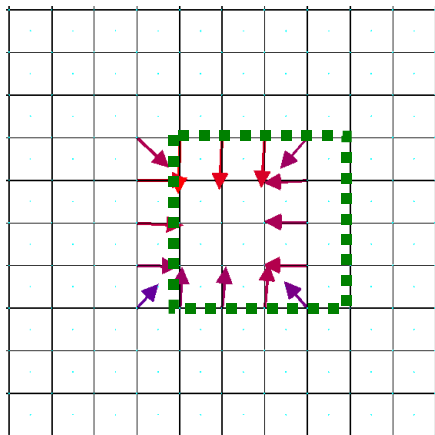
- Mode 1:



- Mode 2:



- Mode 3:



- Mode 4:

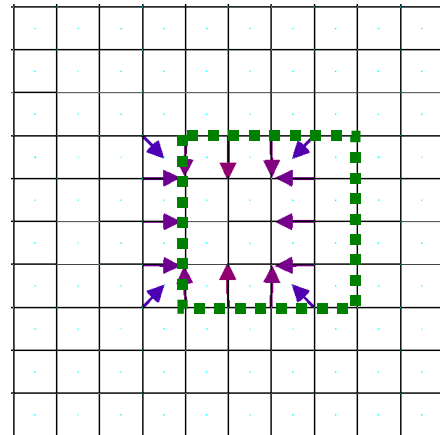


Fig. 3.26: Case X: - Energy Vector Field Diagram for the strengthened plate with plots for single location of patch group with fixed – fixed boundary condition.

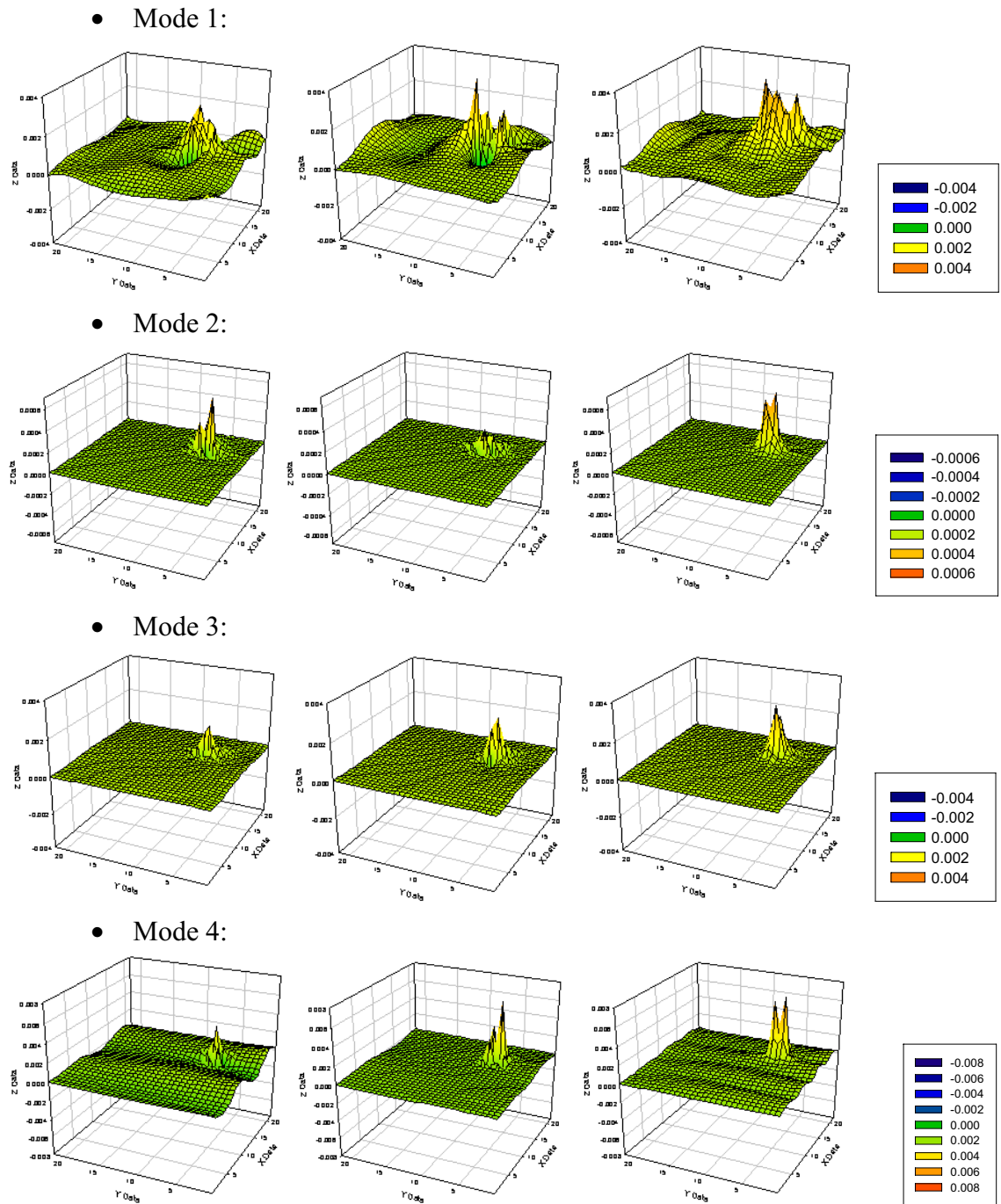
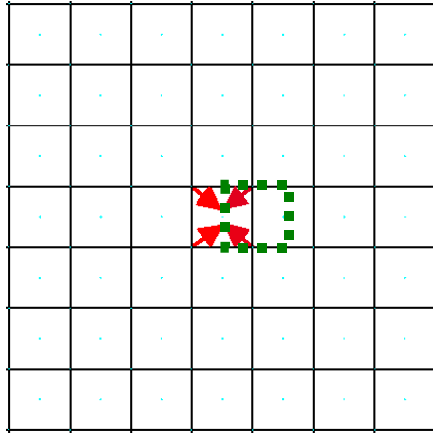
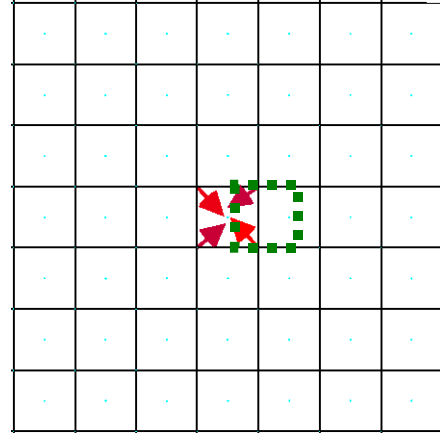


Fig. 3.27: Case XI: - Spatial Distribution of the Defect Energy Force Parameter showing (for each mode) the F_1 , F_2 and F (resultant) Force Diagrams (columns 1, 2 and 3) for single location of patch with increased stiffness (strengthening) for simply supported boundary condition.

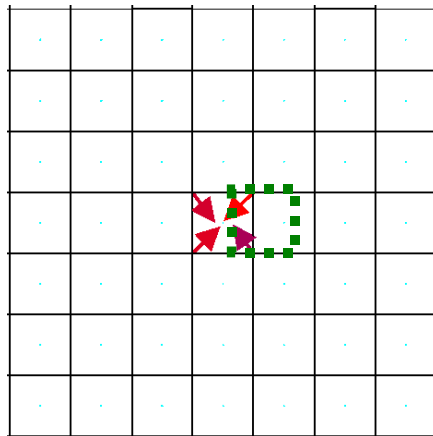
- Mode 1:



- Mode 2:



- Mode 3:



- Mode 4:

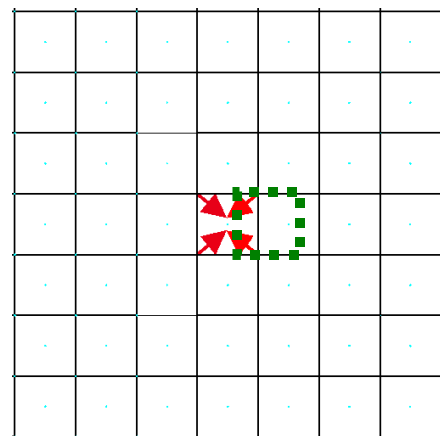
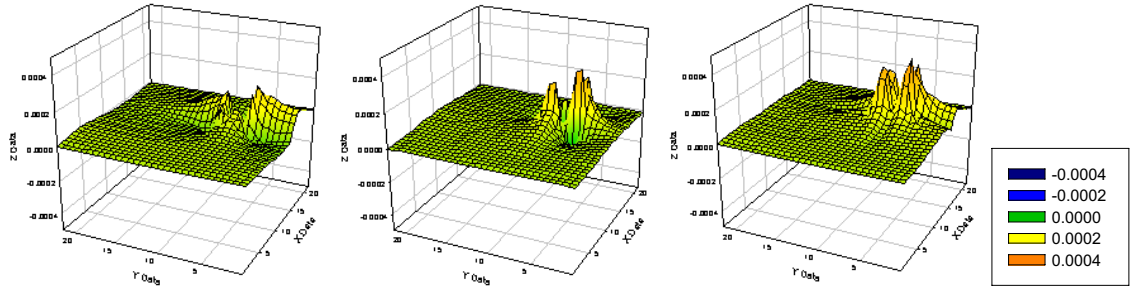
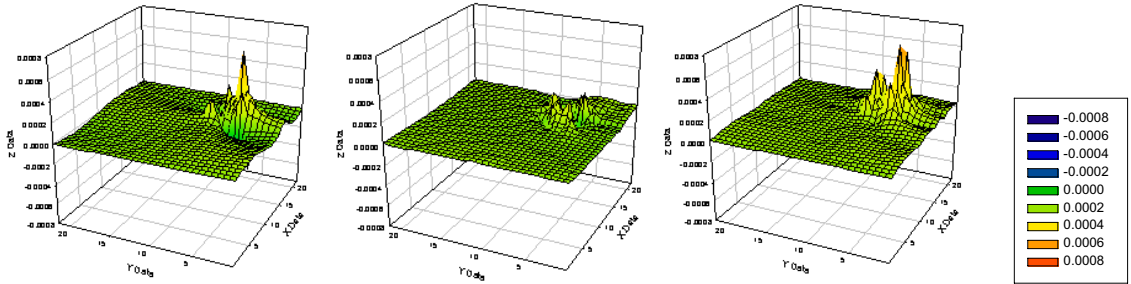


Fig. 3.28: Case XI: - Energy Vector Field Diagram for the strengthened plate with plots for single location of patch with simply supported boundary conditions.

- Mode 1:



- Mode 2:



- Mode 3:

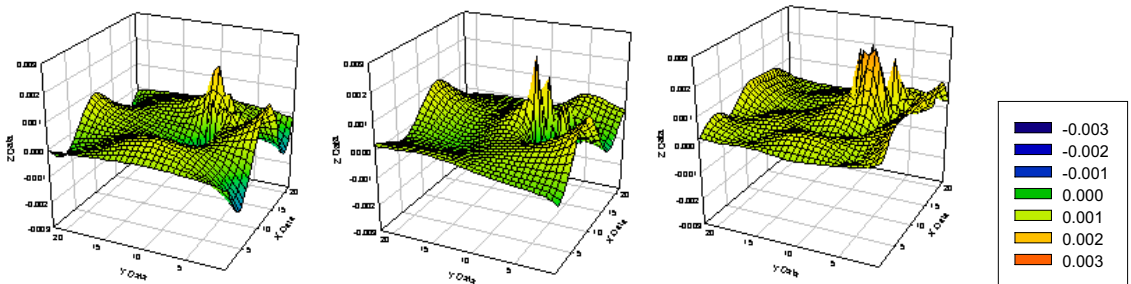
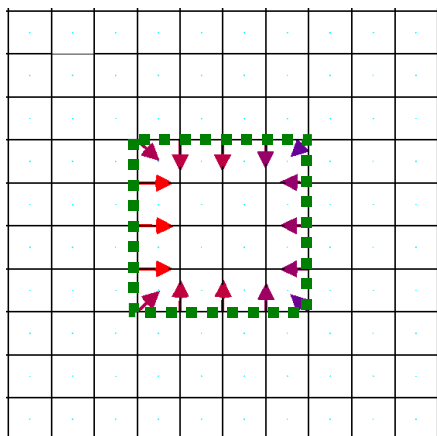
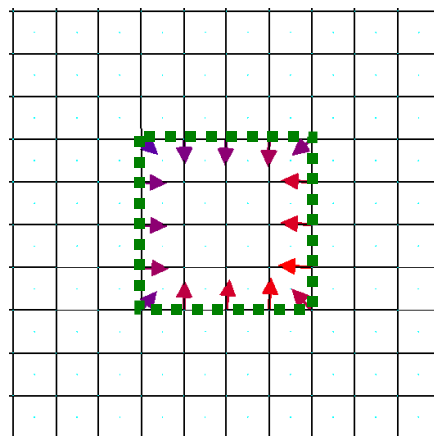


Fig. 3.29: Case XII: - Spatial Distribution of the Defect Energy Force Parameter showing (for each mode) the F_1 , F_2 and F (resultant) Force Diagrams (columns 1, 2 and 3) for single location of patch with increased stiffness (strengthening) for simply supported boundary condition.

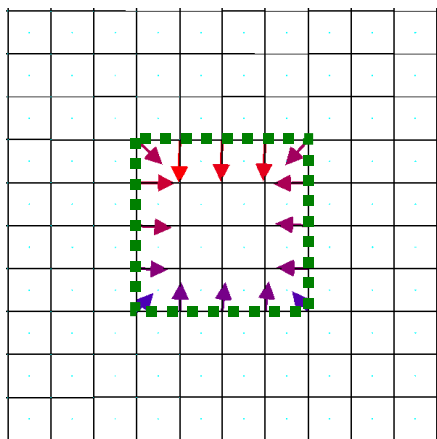
- Mode 1:



- Mode 2:



- Mode 3:



- Mode 4:

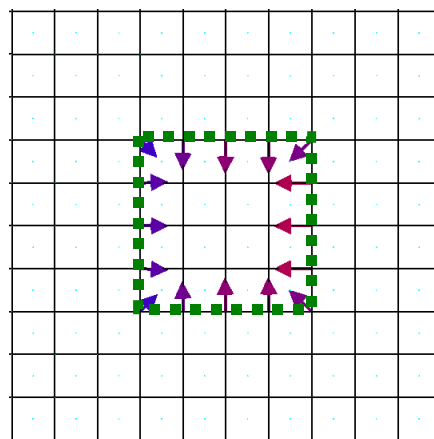
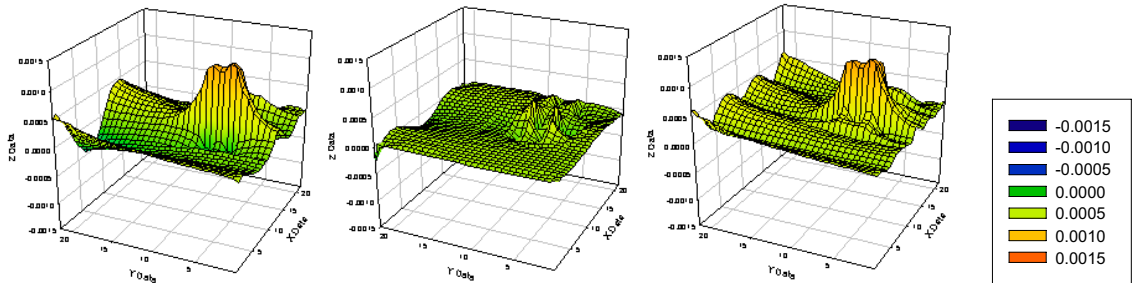
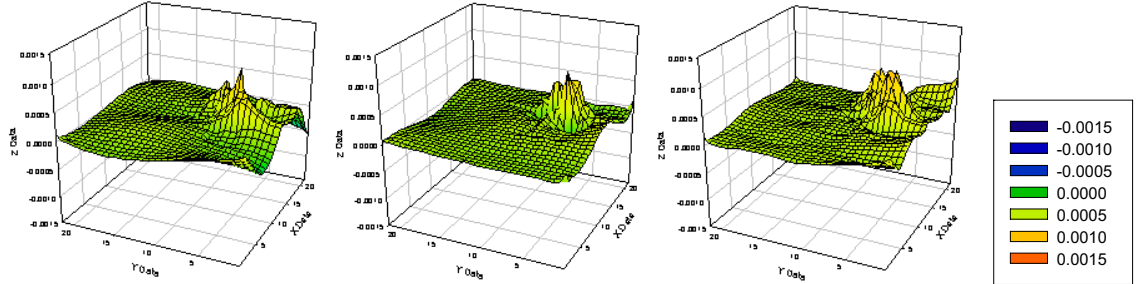


Fig. 3.30: Case XII: - Energy Vector Field Diagram for the strengthened plate with plots for single location of patch group with simply supported boundary conditions.

- Mode 1:



- Mode 2:



- Mode 3:

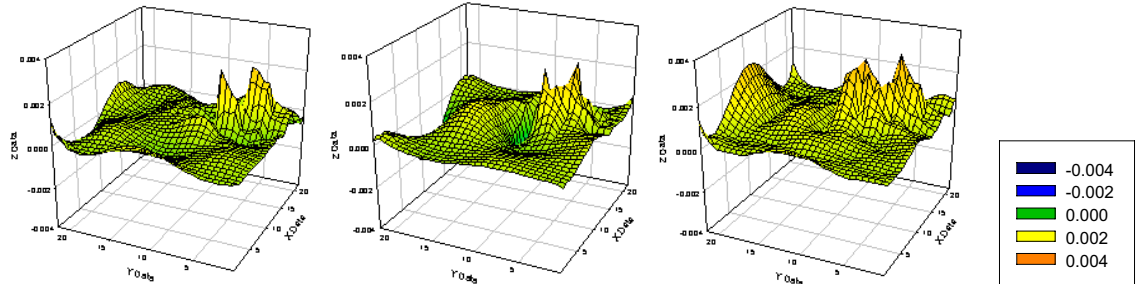
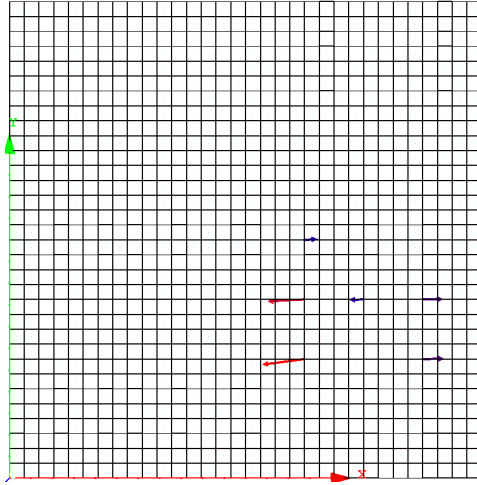
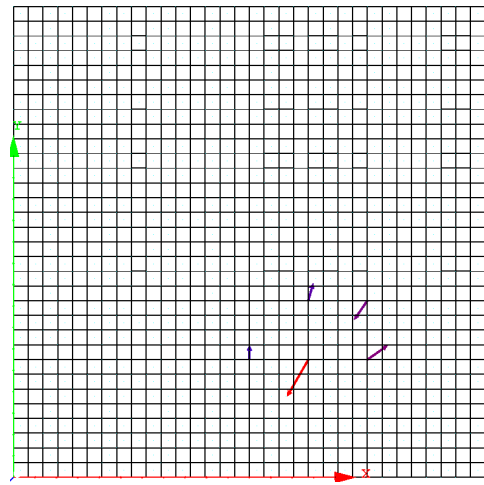


Fig. 3.31: Spatial Distribution of the Defect Energy Force Parameter showing (for each mode) the F_1 , F_2 and F (resultant) Force Diagrams (columns 1, 2 and 3) for single location of patch group damage with fixed – fixed boundary condition and incomplete data.

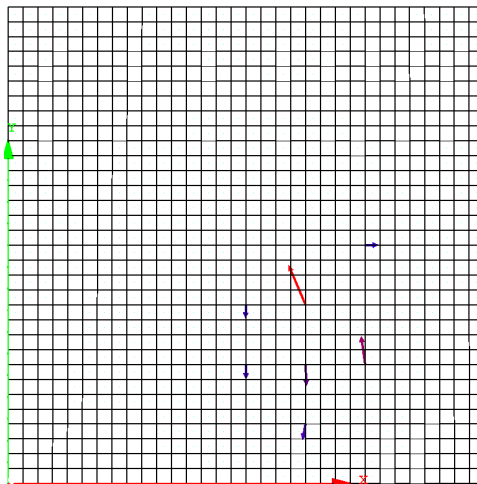
- Mode 1:



- Mode 2:



- Mode 3:



- Mode 4:

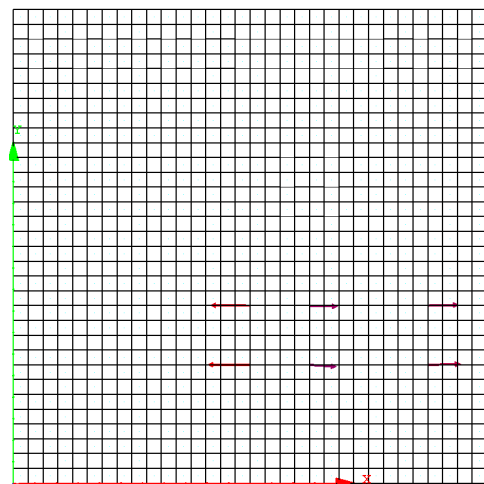


Fig. 3.32: Energy Vector Field Diagram for the damaged plate with overall plots for single location of patch group damage with fixed – fixed boundary condition and incomplete data.

Table 3.2: Frequencies of the Dynamic Case Damaged Plate with reduced modulus of elasticity (0.8 E).

	Fixed - Fixed Boundary Condition				Simply - Supported Boundary Condition			
	Case 1	Case 2	Case 3	Case 4	Case 5	Case 6	Case 7	Case 8
Modulus of Elasticity	2.3680E+07	2.3680E+07	2.3680E+07	2.3680E+07	2.3680E+07	2.3680E+07	2.3680E+07	2.3680E+07
(psi)								
Eigenvalues								
Mode 1	1.7825E+04	1.7780E+04	1.7803E+04	1.7824E+04	3.3634E+03	3.3626E+03	3.3494E+03	3.3347E+03
Mode 2	2.5237E+04	2.5147E+04	2.5194E+04	2.5234E+04	9.4253E+03	9.4239E+03	9.4055E+03	9.3842E+03
Mode 3	6.8633E+04	6.8173E+04	6.8409E+04	6.8620E+04	4.8795E+04	4.8786E+04	4.8628E+04	4.8455E+04
Mode 4	1.3610E+05	1.3475E+05	1.3544E+05	1.3605E+05	5.5127E+04	5.5107E+04	5.4859E+04	5.4572E+04
Mode 5	1.6377E+05	1.6297E+05	1.6339E+05	1.6374E+05	7.9237E+04	7.9223E+04	7.9054E+04	7.8855E+04
Mode 6	2.3048E+05	2.2726E+05	2.2892E+05	2.3038E+05	1.8094E+05	1.8092E+05	1.8049E+05	1.7999E+05
Frequency (in rad/sec)								
Mode 1	133.5105	133.3404	133.4269	133.5069	57.9950	57.9875	57.8741	57.7467
Mode 2	158.8629	158.5786	158.7255	158.8537	97.0841	97.0767	96.9821	96.8719
Mode 3	261.9799	261.0992	261.5510	261.9537	220.8966	220.8752	220.5178	220.1255
Mode 4	368.9135	367.0875	368.0224	368.8504	234.7911	234.7486	234.2207	233.6071
Mode 5	404.6907	403.6931	404.2200	404.6534	281.4904	281.4652	281.1657	280.8112
Mode 6	480.0841	476.7189	478.4509	479.9799	425.3702	425.3465	424.8378	424.2543
Frequency in (Hz)								
Mode 1	21.2489	21.2218	21.2356	21.2483	9.2302	9.2290	9.2110	9.1907
Mode 2	25.2838	25.2386	25.2620	25.2824	15.4514	15.4502	15.4352	15.4176
Mode 3	41.6954	41.5552	41.6271	41.6912	35.1568	35.1534	35.0965	35.0341
Mode 4	58.7144	58.4238	58.5726	58.7044	37.3682	37.3614	37.2774	37.1797
Mode 5	64.4085	64.2497	64.3336	64.4026	44.8006	44.7966	44.7489	44.6925
Mode 6	76.4078	75.8722	76.1478	76.3912	67.6998	67.6960	67.6150	67.5222

Table 3.2: Summary of the Frequencies of the Dynamic Case Damaged Plate with increased Modulus of Elasticity (1.2 E).

	Fixed - Fixed Condition			Simply - Supported Condition		
	Case 9	Case 10	Case 11	Case 12	Case 12	Case 12
Modulus of Elasticity (psi)	3.5520E+07	3.5520E+07	3.5520E+07	3.5520E+07	3.5520E+07	3.5520E+07
Eigenvalues						
Mode 1	1.7827E+04	1.7845E+04	3.3650E+03	3.3768E+03		
Mode 2	2.5243E+04	2.5282E+04	9.4281E+03	9.4455E+03		
Mode 3	6.8659E+04	6.8849E+04	4.8813E+04	4.8948E+04		
Mode 4	1.3618E+05	1.3672E+05	5.5164E+04	5.5387E+04		
Mode 5	1.6383E+05	1.6416E+05	7.9263E+04	7.9419E+04		
Mode 6	2.3066E+05	2.3193E+05	1.8098E+05	1.8132E+05		
Frequency (in rad/sec)						
Mode 1	133.5171	133.5861	58.0088	58.1099		
Mode 2	158.8807	159.0041	97.0982	97.1882		
Mode 3	262.0295	262.3906	220.9366	221.2428		
Mode 4	369.0300	369.7533	234.8696	235.3448		
Mode 5	404.7590	405.1627	281.5367	281.8137		
Mode 6	480.2745	481.5861	425.4134	425.8223		
Frequency in (Hz)						
Mode 1	21.2499	21.2609	9.2324	9.2485		
Mode 2	25.2866	25.3063	15.4537	15.4680		
Mode 3	41.7033	41.7608	35.1632	35.2119		
Mode 4	58.7330	58.8481	37.3807	37.4563		
Mode 5	64.4194	64.4836	44.8080	44.8520		
Mode 6	76.4381	76.6468	67.7066	67.7717		

3.8.2 Static Loading Case

Referring to the same boundary conditions, material properties and geometric dimensions of the plate as given in Fig. 3.1, concentrated loads were applied and the Energy Vector Field Diagrams were plotted for the various statical test cases studied for both the reduced and increased modulus of elasticity. These include the following examples:

- **Case I:** Fixed – Fixed Plate with small area of single damage location at (15.47, 6.53) from the origin. Fig. 3.28 shows the plot for the mesh for the damaged plate with 1000 unit concentrated loading.
- **Case II:** Fixed – Fixed Plate with large (block) area of single damage location at (15.125, 6.875) from the origin. Fig. 3.29 shows the plot for the mesh for the damaged plate with 1000 unit concentrated loading.
- **Case III:** Fixed – Fixed Plate with small area of single damage location at (15.47, 6.53) from the origin. Fig. 3.30 shows the plot for the mesh for the damaged plate with 1000 unit concentrated loading and increased modulus of elasticity.

As can be seen in Figs. 3.33 – 3.35, similar patterns as shown in the dynamics case, also exist here. In particular, only near the inflicted regions are the magnitudes of damage parameters significant, and directions for the false – alarm cases are opposite to the true damage scenarios.

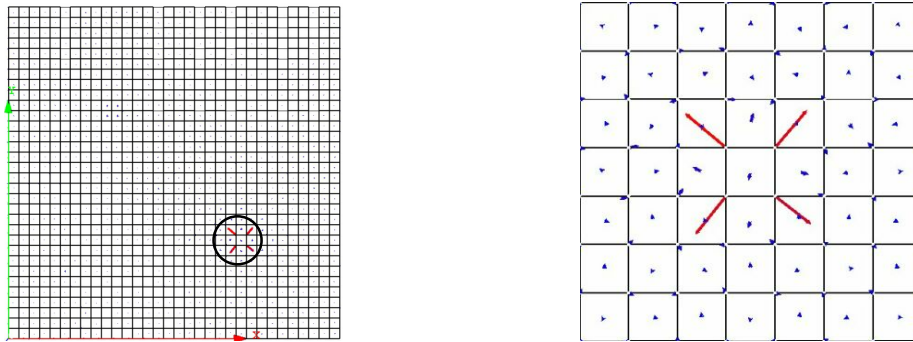


Fig. 3.33: Energy Vector Field Diagram for the damaged plate with overall and zoomed plots for single element statical loading damaged with fixed - fixed boundary conditions

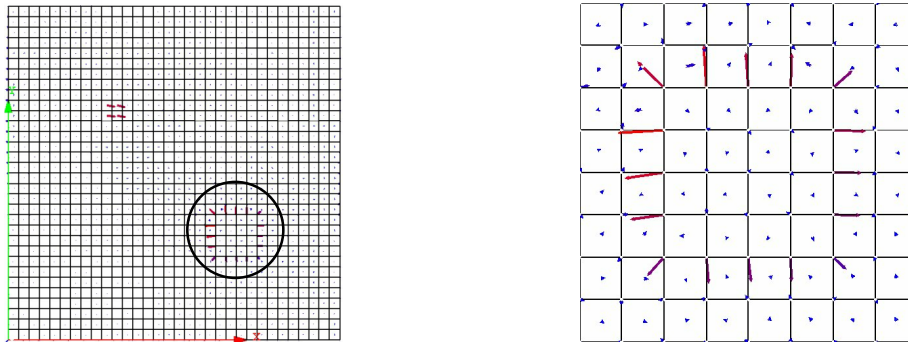


Fig. 3.34: Energy Vector Field Diagram for the damaged plate with overall and zoomed plots for Large (block) area of elements with statical loading damaged with fixed - fixed boundary conditions

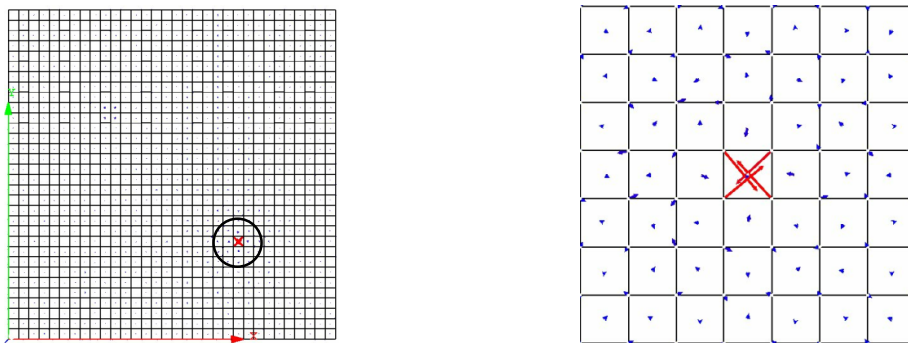


Fig. 3.35: Energy Vector Field Diagram for the damaged plate with overall and zoomed plots for single element damaged with statical loading, increased modulus of elasticity and fixed - fixed boundary conditions

3.9 Conclusion

Considering the cases for true inflected damages in the dynamics of free vibration, the defect energy force intensity plots were consistent with the Energy Vector Field Diagrams for the first three modes. As the mode numbers increased, the accuracy of mesh diagram showing the spatial distribution of the intensity of the defect energy force somewhat deteriorated exhibiting results are a bit noisy. This was in total contrast when compared with the energy vector field diagrams, wherein the energy flow pin - pointed exactly the area of the damage. However, when considering also the possibility of false – alarm testing, it has been clearly demonstrated that only the simultaneous use of the dual representation in tandems, i.e., both magnitudes and directional properties, will lend to a successful damage detection and localization strategy. This will confirm further for the statical loading cases where excellent results were again obtained from the vector field plots.

It has been emphasized that there is always an inherent directional property for the flow of energy dissipation in the system. In other words, a crack leading to a deterioration/reduction in the material properties, will result in vectors flowing from the weaker (cracked) region to the stronger (undamaged) part. Similarly, a false – alarm in the form of a thickening or stiffening of the structure would cause these vector directions to completely reverse. Therefore, the severe limitations of many existing detection schemes of scalar type (relying only on intensity/magnitudes) will be eliminated entirely.

Finally, anticipating the incompleteness of the experimental data (e.g., as provided from the experiments conducted at NASA Glenn Research Center), the DDC was modified. To operate with a truncated set of data having no rotational DOF and with only a rather coarse network of sensors for the vertical translations. Even in these more difficult cases, the alternative dual representations of intensity and vector field plots have proved quite robust, i.e., in predicting quite accurately the locations of inflected damages.

4.0 EXPERIMENTAL VERIFICATION—CONVENTIONAL MEASURING MODAL TESTING WITH ACCELEROMETER IN A COARSE – SENSOR NETWORK

4.1 Introduction

Damage detection is a challenging problem that is under vigorous investigation by numerous research groups using a variety of analytical and experimental techniques. The structural geometry, material properties, boundary conditions and topology of the test structure, etc. all influence the choice of a suitable method for damage detection. The damage detection procedure for a structure depends upon the level and extent of damage, available knowledge concerning the ambient dynamic environment, sophistication of available computing resources, complexity of the detection scheme, selected threshold level for detecting perturbations in the system condition and depth of knowledge concerning the failure modes of the structure.

One of the most important criterion to be fulfilled in any damage detection method based on a theoretical/computational model is the robustness of the method to a real life laboratory setup. The effectiveness of the method in consideration will be assessed based on its ability to determine the location of damage when provided with the experimental measurements (e.g., strains, deflections and rotations) and accounting for the various environmental factors and human errors.

4.2 Background About the Experiments

The experimental results reported here were obtained by NASA (National Aeronautics and Space Administration) Glenn Research Center, as a part of a test program aiming at the assessment of merits and/or limitations of various experimental alternatives used in conjunction with global detection based on mechanical response measurements. This part was conducted under the supervision of S.M. Arnold, Life Prediction Branch and Sergey Samorezov, Structural Dynamics Laboratory. More specifically, three experiments with varying degree of damage were provided. These experiments were of the free vibration mode type with the boundary conditions of the structure (square plate) being fixed (clamped) and free on each of its two opposite sides. The “fixed” boundary conditions were experimentally approximated by high-tension bolted connections, see Fig. 4.1. The data for each test specimen is termed a “Set”, i.e., data for the first, second and third experiments were termed “Set1”, “Set 2” and “Set3” respectively.

Each set as shown in Fig. 4.2, was divided into states “X”, “Y” and “Z” each of these states is represented by a pair of experiments assessing the structural condition of the specimen at a given time. Two experiments for each state were conducted to minimize the effect of data noise caused by environmental, machine and human factors. As provided to us, the unknown “damage” state in a given specimen may or may not have changed between states. Each state “X” contains data for experiment “Xa” and “Xb”, “Y” contains data for experiment “Ya” and “Yb”, “Z” contains the data for experiment “Za” and “Zb”, note that there was absolutely no change in the specimen during the same sub-set of a given state. Damage may or may not have been inflicted on the specimen between states “X” and “Y” and between states “Y” and “Z”. The “X” state of an experimental set was the baseline or the “healthy” plate experiment. The Damage Detection Code (DDC) was always executed with the “X” versus the “Y” state and the “X” versus the “Z” state. The main objective in the present exercise is to predict the potential sites of inflected damage (if any).

Date, time and the temperature of the laboratory were all recorded during each of the experiments. Subsequent to submittal of our “predictions”, further details on the experiments were provided to us for more detailed reporting purposes. This includes the size of damage (holes drilled through the plate) and some of their respective locations was all measured and are shown in Fig. 4.5.

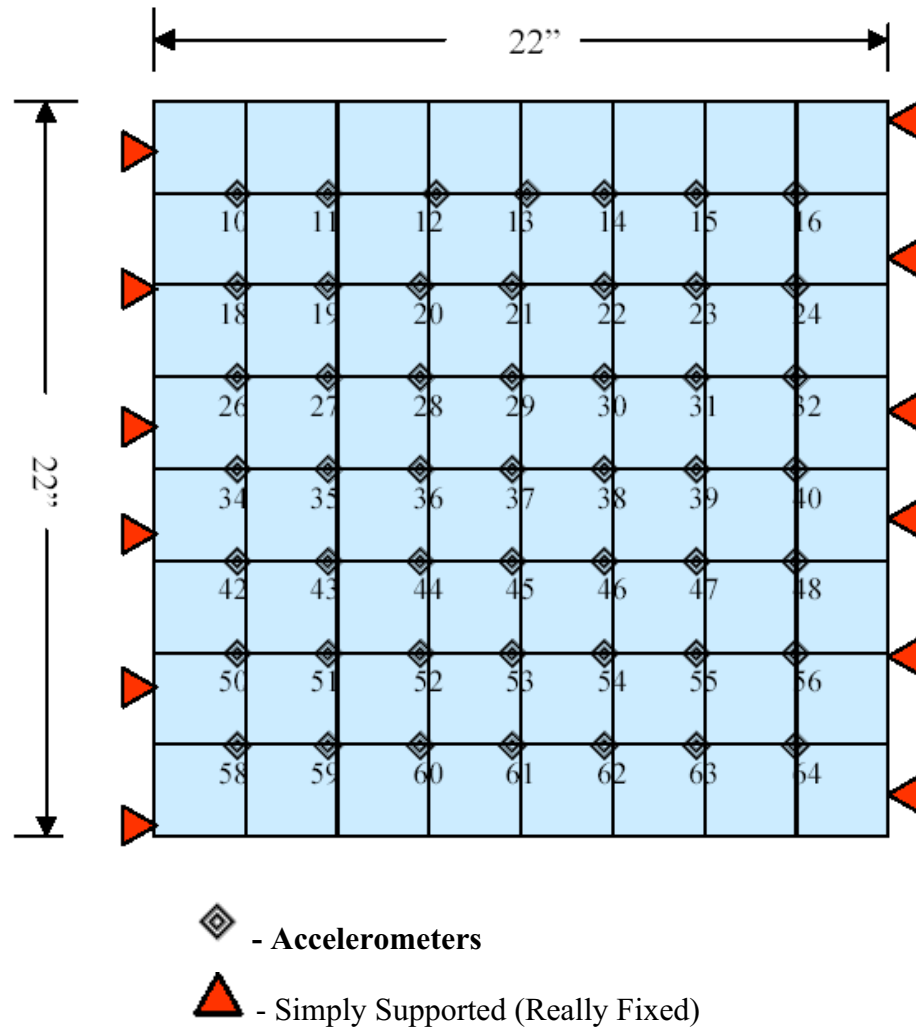


Fig. 4.1: Experimental Plate at NASA Glenn showing the clamping, the location of the accelerometer and geometry of the plate.

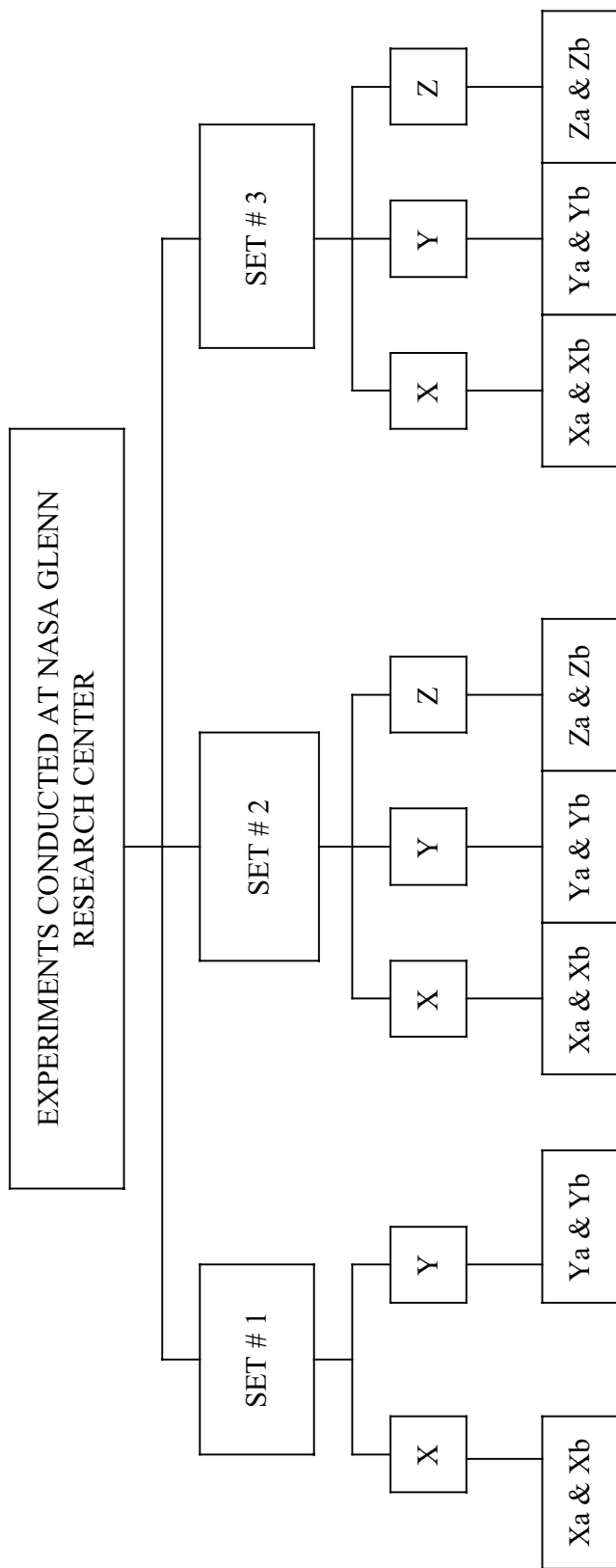


Fig. 4.2: Organization chart of the experiments conducted in the laboratory

4.3 Experimental Setup

A 22-inch (in nominal size) square, INCONEL 718, plate supported on two opposite edges and free on the other edges was subjected to a random excitation of 0.032g RMS (root mean square) with a frequency content of 10 – 500 Hz. Forty-nine PCB 333A32 accelerometers were used to measure the vertical displacement of the plate and no rotations. These accelerometers were all within standard calibration marked and numbered as shown in Fig. 4.1. The origin of all measuring points being taken at the lower left hand corner of the plate. Fig. 4.3 shows a close up view of the undamaged plate with all the accelerometers attached. Initially, the fixture was designed to be with simple support conditions but due to the thinness of the plate it experienced more like a fixed boundary condition.

All data was acquired using the software package IDEAS developed by SDRC (Structural Dynamics Research Corporation). Random excitation was imposed via an electro-dynamic shaker table (LING 4022) with 0.032g RMS force. Time response data was collected and then post processed using IDEAS to obtain the frequency response functions (FRF) per location and the corresponding mode shapes. Repeated measurements were taken using the undamaged plate during a series of loosening and retightening of the supports in an effort to achieve some repeatability of results. There was always a drift in the frequency and mode shape measurements and this was never specifically determined.

The damage inflicted to the plate was in the form of holes of varying sizes from 0.125 in. to 1.6875 in. diameter with the smaller ones achieved through the use of a standard metal drill bit and the larger sized holes were obtained using a screw-punch device. Due to the excessive levels of variability/noise in the measurement of data (as documented in the forthcoming report [61]) only the results of 1.125 in. and 1.6875 in. diameter hole damage test results were provided. In all there were 48 gages that were placed on the plate such that they formed an 8×8 mesh to only measure the modal vertical displacements (no rotations). These points were then superimposed/mapped to the nodal points on a refined 32×32 finite element mesh for processing the results.

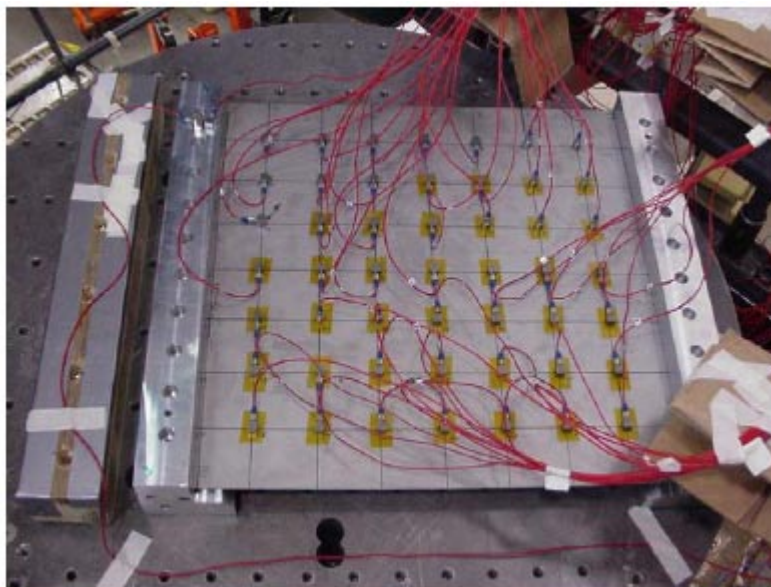


Fig. 4.3: Undamaged Plate with the accelerometers attached in the NASA Glenn laboratory.

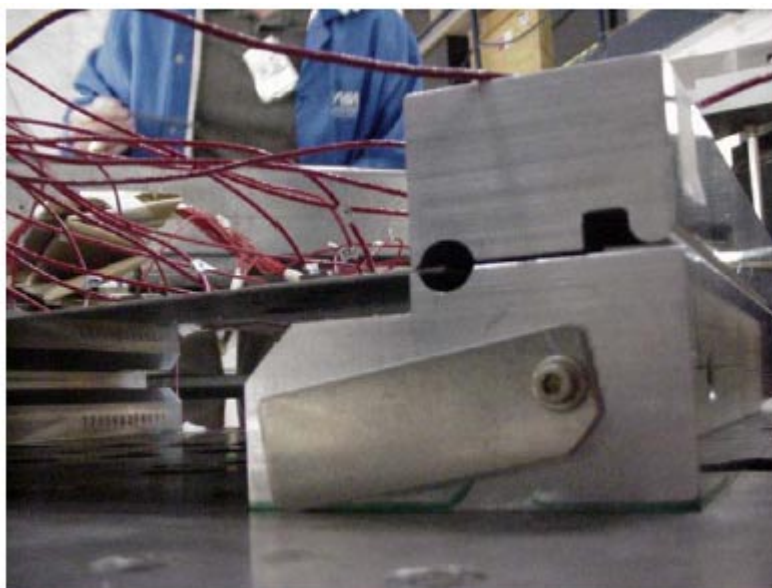
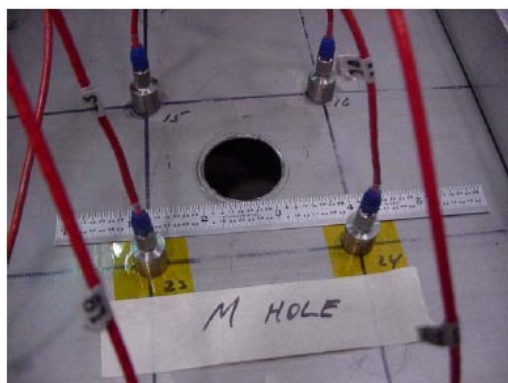
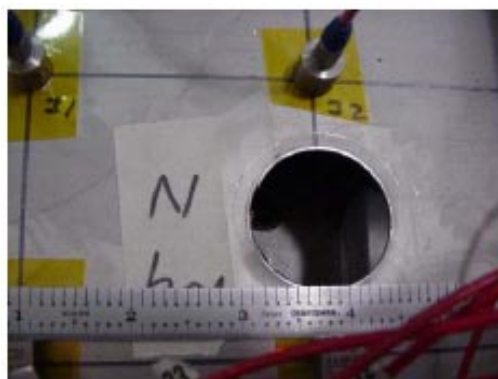


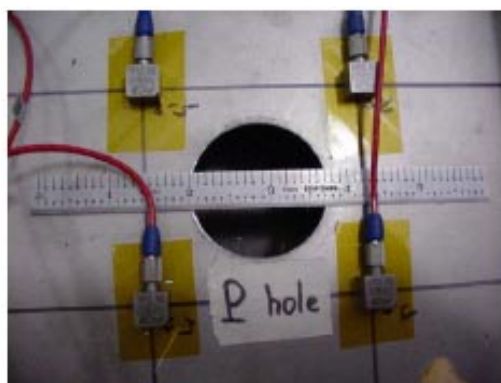
Fig. 4.4: Side view of the support conditions with the plate and the accelerometers attached.



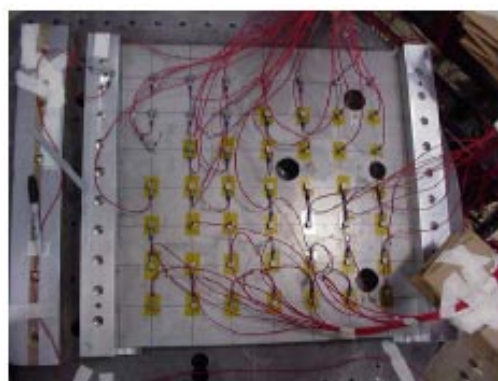
(a)



(b)



(c)



(d)

Fig. 4.5: (a) 1.125-in. diameter hole (b) 1.375-in. diameter hole (c) 1.6875-in. diameter hole (d) overall view of the damaged plate with the accelerometer attached.

4.4 Processing the Data

The experimental data as obtained from NASA Glenn contained the modal displacement, frequency, damping coefficient, etc., from the accelerometers attached to the plate as shown in Fig. 4.1. The experiments were a first attempt to pave the way for in-house capabilities of measurement and data analysis for modal parameters, displacements, frequencies, slopes, etc., at NASA Glenn. For the damage detection code (DDC), only the eigenvalue (frequency) and the normalized modal displacements were used. The entire process of calculating and running the DDC was automated using the UNIX scripting language and dynamic file editing. A flow-chart of the process is shown in Fig. 4.2.

The raw experimental data sets for a given specimen state (e.g., “Xa” or “Xb”) were searched for the missing accelerometer data. This is to ensure that all the data for the points shown in Fig. 4.1 present in “Xa” had to be present in “Xb” and vice versa. If, due to some high noise or an error, the measurement data is deleted for a node, it will also be deleted from the other file, this maintains consistency in finding the threshold value as discussed below. The pair of resulting data files were then normalized to the maximum value of each file (Master). Each file is also normalized based on the value at the location of the maximum value in the other file of the pair (Slave). This results in four new files, for example, “Xa – master” and “Xb – Slave” and “Xb – master” and “Xa – Slave” combinations.

The “Varsub” (variable substitution) routine uses these normalized files and builds the boundary condition files and two DDC input files. The DDC input files with (“Xa – master” and “Xb – slave”) and (“Xb – master” and “Xa – slave”) combinations prepared in this process were run through the DDC to obtain a threshold value from the nodal damage forces. The threshold value is the difference between the nodal damage force values of the (“Xa – master and Xb – slave”) and (“Xb – master & Xa – slave”) run of the DDC. A file containing the average normalized accelerometer data is then prepared from the normalized unique grid points of each master “Xa” and “Xb” such that one experimental for state “X” file was obtained. This file is then renormalized to its maximum value.

The same steps as mentioned above were repeated for state “Y” (“Ya” and “Yb”) and state “Z” (“Za” and “Zb”) resulting in a file containing averaged normalized accelerometer data for states and their respective threshold values. Since it was known state “X” represented the “healthy” plate and the “Y” or “Z” states were possibly damaged, the DDC was executed such that state “X” was considered as the reference state. The results obtained were then processed and are shown in the next article to predict the damage. This automated process was carried out for only the first three modes since, as stated earlier; it was observed that the higher modes gave prohibitively noisy results.

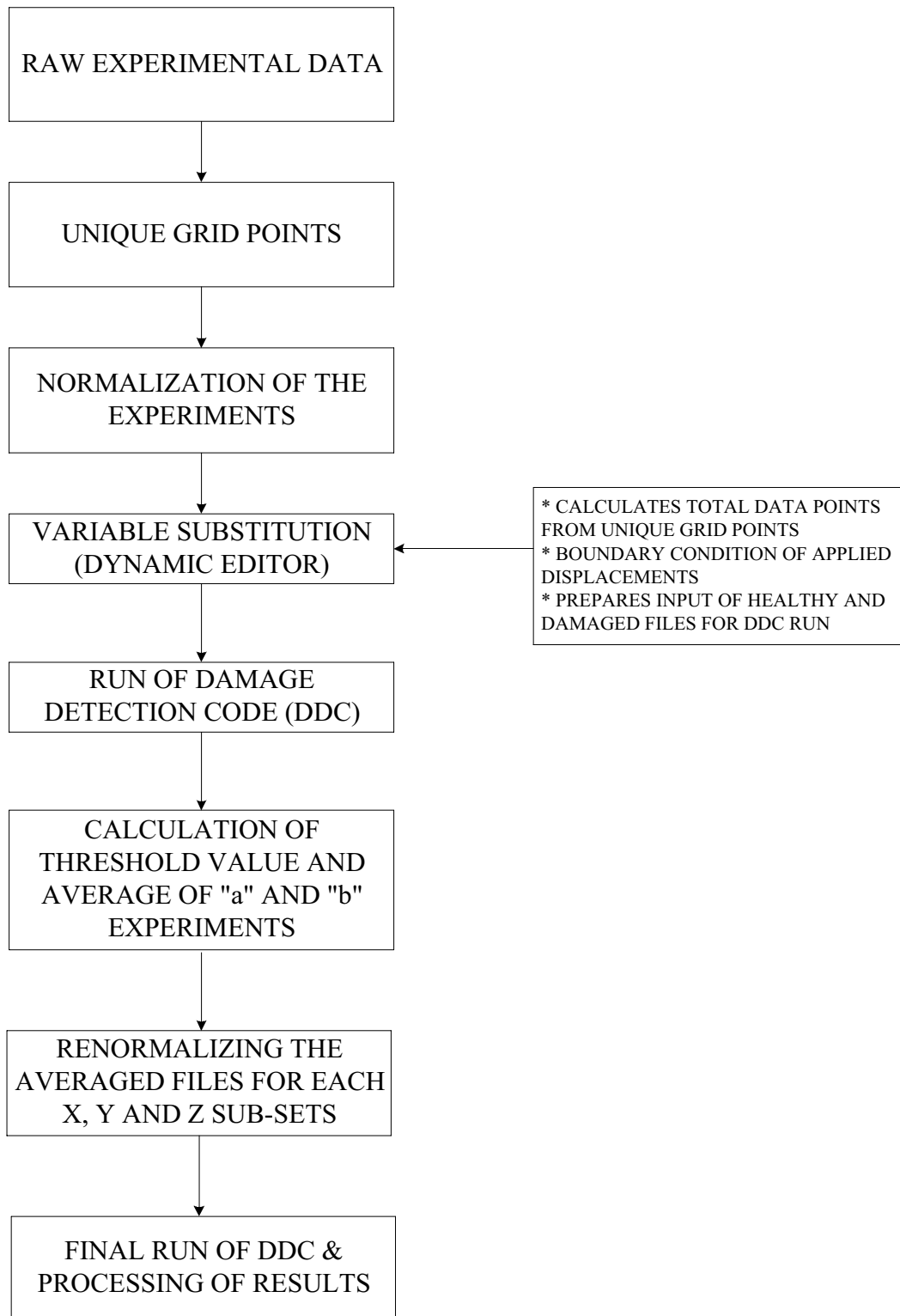


Fig. 4.6: Flowchart of the automated damage detection process.

4.5 Processing the Results and Observations

The observations herein are of a descriptive nature as opposed to being precise and quantitative. This is due to the fact there is a lot of variability/noise in the measured data. The Tables 4.1, 4.2, 4.3 and 4.4 provides a summary of the data obtained for the exact fixed-fixed plate and the different experimental sets that were conducted. Adopting the methods detailed in Chapter III, the spatial distribution of the defect energy force parameter and the energy vector field diagrams were plotted for each of the experimental sets. Conclusions were made after comparing both the energy vector field diagrams and the spatial distribution of the defect energy parameter. These are summarized in the form of a schematic block diagram summarizing the level of certainty and sites for possible damage. For each individual Set I, II and III, assessment of the level of noise was based on a restricted comparison of the two repeats of reference measurements (e.g., “Xa” and “Xb”).

To provide some feel for the rather severe levels of variabilities and noises in the above experimental results, we refer to some of the comparisons in Tables 4.2 to 4.4. For instance, as it turns out Set I corresponds to a false alarm test but all the cases indicated sizable reductions in the vibration frequencies in all the five vibration modes reported. Such a consistent and relatively – large reduction may certainly cause some of the conventional detection schemes, using frequency data alone, to be trapped into falsely detecting “damage”. On the other hand, for the true damage in Set II for “Y” and “Z” measurements relative to the reference in X of the same Set II, the artificial *increases* in frequencies for readings of mode 4 and 5 in all columns Set II “Ya”, “Yb”, “Za” and “Zb” will certainly prove very perplexing for these scalar (frequency-only) detection methods. The same confusing trends also existed in the readings of the true multiple location damage cases of Table 4.4. Furthermore, although certainly lacking in terms of the size of experimental samples for any rational statistical analysis to be of great value, some simple (regression/statistical noises) analyses of these data are given in Appendix A.

At the end of processing each experimental Set, a conclusion with regard to the damage location and amount was given and submitted to the NASA Glenn Research Center. The feedbacks received from them provided confirmation to the results and observations. For “Set I”, it was observed that there was no exact damage to the plate and was clearly seen of a case of false – alarm test case. For Set II and Set III, the predicted damage location was in very close proximity to the true location of inflicted damages in each case. Note that Set III actually uses a reference state “X” that by itself included initial damage from the end of damage scenarios in Set II. It has been shown that the damage detection code, even with very noisy data, consistently predicted the location of damage.

Table 4.1: Exact frequencies and eigenvalues of the fixed - fixed plate.

Fixed - Fixed Plate			
	Frequency		Eigenvalue
	(Hz)	(rad/sec)	
Mode 1	21.25	133.57	1.7840E+04
Mode 2	25.29	158.94	2.5261E+04
Mode 3	41.70	262.11	6.8702E+04
Mode 4	58.72	369.13	1.3625E+05
Mode 5	64.41	404.89	1.6394E+05

Table 4.2: Frequencies and eigenvalues of “Set 1”

	Set 1 Xa			Set 1 Xb		
	Frequency		Eigenvalue	Frequency		Eigenvalue
	(Hz)	(rad/sec)		(Hz)	(rad/sec)	
Mode 1	23.73	149.16	2.2249E+04	23.15	145.51	2.1174E+04
Mode 2	29.27	183.98	3.3850E+04	29.02	182.41	3.3274E+04
Mode 3	43.11	270.98	7.3429E+04	43.00	270.29	7.3054E+04
Mode 4	55.21	347.03	1.2043E+05	55.07	346.15	1.1982E+05
Mode 5	57.55	361.74	1.3086E+05	57.03	358.47	1.2850E+05

	Set 1 Ya			Set 1 Yb		
	Frequency		Eigenvalue	Frequency		Eigenvalue
	(Hz)	(rad/sec)		(Hz)	(rad/sec)	
Mode 1	22.67	142.50	2.0305E+04	22.38	140.67	1.9789E+04
Mode 2	28.36	178.26	3.1778E+04	28.28	177.76	3.1599E+04
Mode 3	42.79	268.97	7.2343E+04	42.71	268.46	7.2072E+04
Mode 4	54.08	339.93	1.1555E+05	53.72	337.67	1.1402E+05
Mode 5	56.69	356.34	1.2698E+05	56.58	355.65	1.2648E+05

Table 4.3: Frequencies and eigenvalues of “Set 2”

	Set 2 Xa			Set 2 Xb		
	Frequency		Eigenvalue	Frequency		Eigenvalue
	(Hz)	(rad/sec)		(Hz)	(rad/sec)	
Mode 1	24.51	154.06	2.3735E+04	23.87	150.04	2.2512E+04
Mode 2	30.42	191.21	3.6562E+04	30.91	194.29	3.7749E+04
Mode 3	43.91	276.01	7.6179E+04	44.23	278.02	7.7294E+04
Mode 4	51.98	326.73	1.0675E+05	51.16	321.58	1.0341E+05
Mode 5	54.87	344.90	1.1895E+05	53.66	337.29	1.1377E+05

	Set 2 Ya			Set 2 Yb		
	Frequency		Eigenvalue	Frequency		Eigenvalue
	(Hz)	(rad/sec)		(Hz)	(rad/sec)	
Mode 1	23.26	146.21	2.1376E+04	23.25	146.14	2.1358E+04
Mode 2	29.71	186.75	3.4875E+04	29.74	186.94	3.4945E+04
Mode 3	43.70	274.69	7.5452E+04	43.73	274.87	7.5556E+04
Mode 4	52.94	332.77	1.1073E+05	52.88	332.39	1.1048E+05
Mode 5	55.26	347.35	1.2065E+05	55.12	346.47	1.2004E+05

	Set 2 Za			Set 2 Zb		
	Frequency		Eigenvalue	Frequency		Eigenvalue
	(Hz)	(rad/sec)		(Hz)	(rad/sec)	
Mode 1	23.73	149.16	2.2249E+04	23.15	145.51	2.1174E+04
Mode 2	29.27	183.98	3.3850E+04	29.02	182.41	3.3274E+04
Mode 3	43.11	270.98	7.3429E+04	43.00	270.29	7.3054E+04
Mode 4	55.21	347.03	1.2043E+05	55.07	346.15	1.1982E+05
Mode 5	57.55	361.74	1.3086E+05	57.03	358.47	1.2850E+05

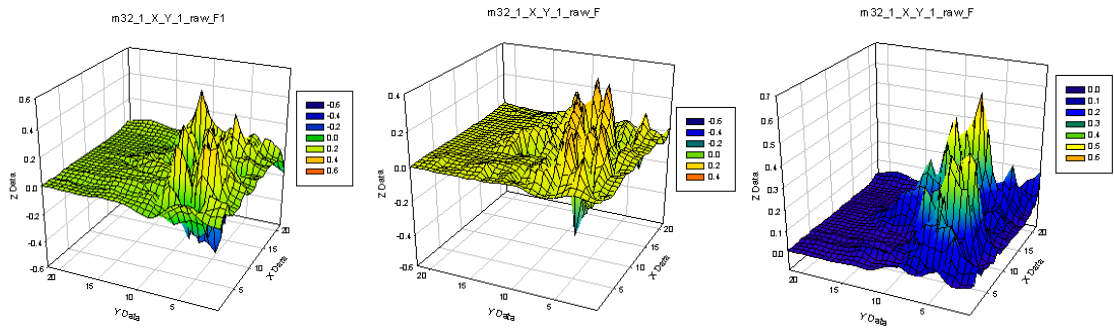
Table 4.4: Frequencies and eigenvalues of “Set 3”

	Set 3 Xa			Set 3 Xb		
	Frequency		Eigenvalue	Frequency		Eigenvalue
	(Hz)	(rad/sec)		(Hz)	(rad/sec)	
Mode 1	22.67	142.50	2.0305E+04	22.38	140.67	1.9789E+04
Mode 2	28.36	178.26	3.1778E+04	28.28	177.76	3.1599E+04
Mode 3	42.79	268.97	7.2343E+04	42.71	268.46	7.2072E+04
Mode 4	54.08	339.93	1.1555E+05	53.72	337.67	1.1402E+05
Mode 5	56.69	356.34	1.2698E+05	56.58	355.65	1.2648E+05

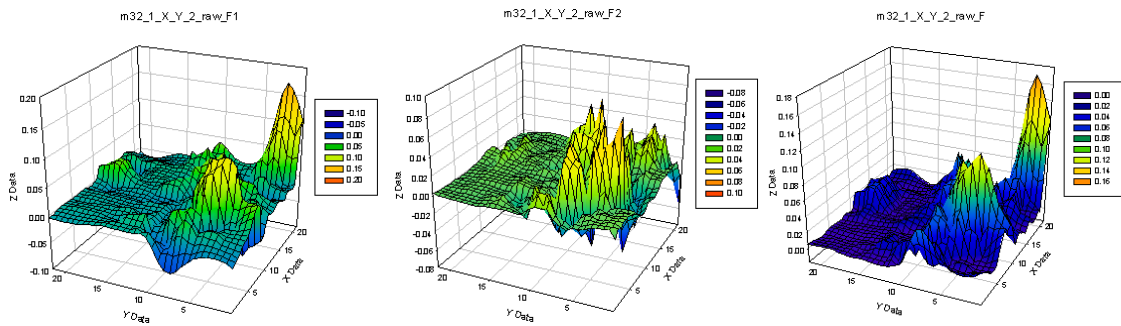
	Set 3 Ya			Set 3 Yb		
	Frequency		Eigenvalue	Frequency		Eigenvalue
	(Hz)	(rad/sec)		(Hz)	(rad/sec)	
Mode 1	23.49	147.65	2.1801E+04	23.42	147.21	2.1671E+04
Mode 2	28.33	178.07	3.1710E+04	28.24	177.51	3.1509E+04
Mode 3	41.39	260.17	6.7686E+04	41.30	259.60	6.7392E+04
Mode 4	54.34	341.57	1.1667E+05	54.83	344.65	1.1878E+05
Mode 5	55.42	348.35	1.2135E+05	56.05	352.31	1.2413E+05

	Set 3 Za			Set 3 Zb		
	Frequency		Eigenvalue	Frequency		Eigenvalue
	(Hz)	(rad/sec)		(Hz)	(rad/sec)	
Mode 1	24.56	154.38	2.3832E+04	24.31	152.81	2.3350E+04
Mode 2	28.76	180.78	3.2680E+04	28.70	180.40	3.2544E+04
Mode 3	42.06	264.38	6.9895E+04	41.94	263.62	6.9497E+04
Mode 4	55.40	348.23	1.2126E+05	55.25	347.29	1.2061E+05
Mode 5	59.04	371.11	1.3772E+05	58.51	367.78	1.3526E+05

- Mode 1:



- Mode 2:



- Mode 3:

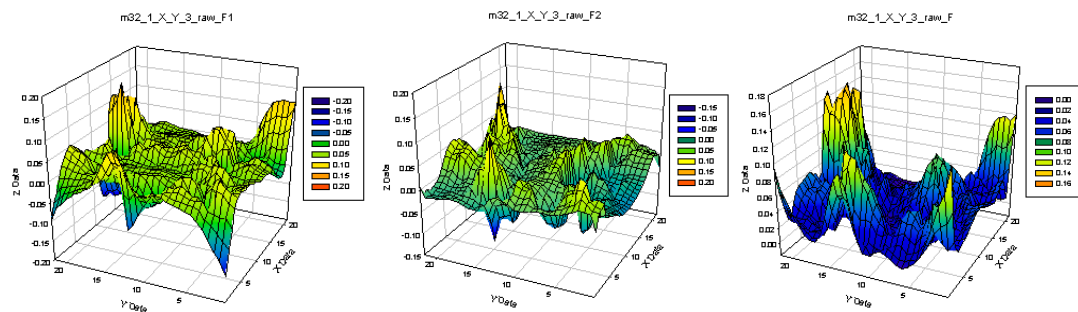
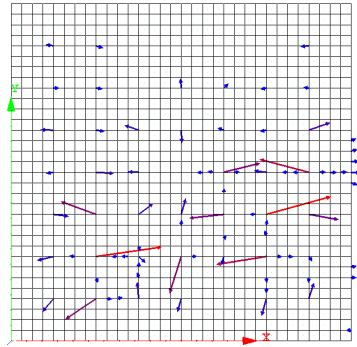
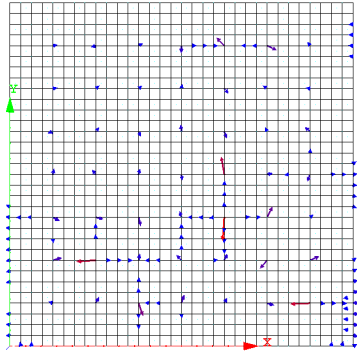


Fig. 4.7: “Set 1” – Spatial distribution of the defect energy force parameter for modes 1 to 3 showing the F_1 , F_2 and F (resultant) Force Diagrams (columns 1, 2 and 3) for the raw spatial distribution of states “X” and “Y” experiments.

- **Mode 1:**



- **Mode 2:**



- **Mode 3:**

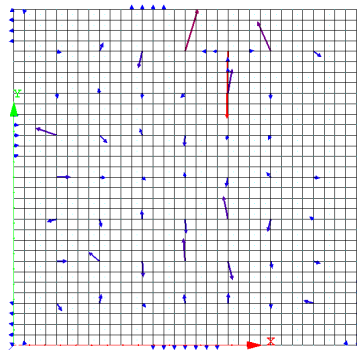
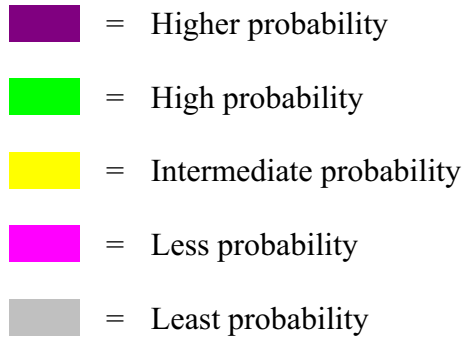


Fig. 4.8: Energy Vector Field Diagrams for “Set 1”, modes 1 to 3 for “X” and “Y”.

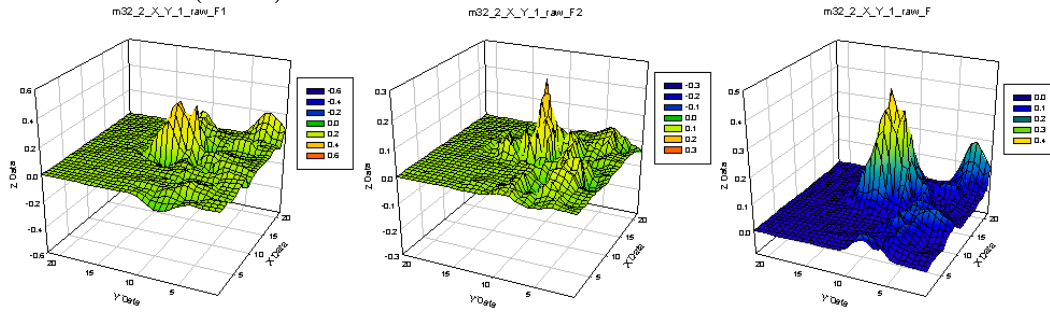


(At most 5% certainty relative to Set I (“Xa”, “Xb”) noise level)

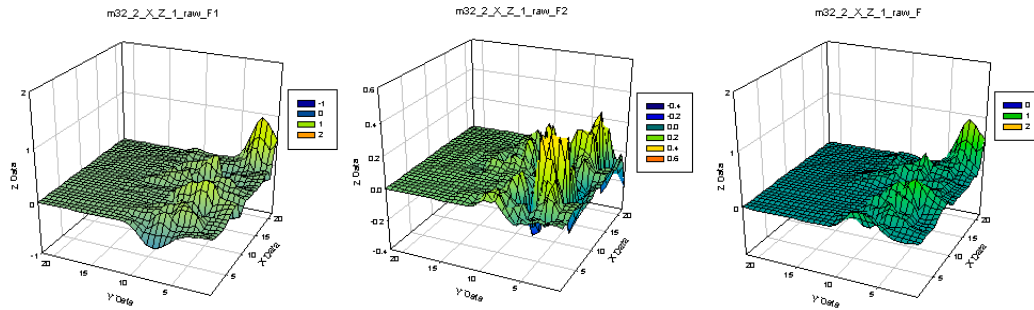
57	58	59	60	61	62	63	64
49	50	51	52	53	54	55	56
41	42	43	44	45	46	47	48
33	34	35	36	37	38	39	40
25	26	27	28	29	30	31	32
17	18	19	20	21	22	23	24
9	10	11	12	13	14	15	16
1	2	3	4	5	6	7	8

Fig. 4.9: Schematic Descriptive Block diagram for the “Set 1” experiment after processing with the color scheme. All vector field diagrams showed no apparent/consistent pattern, thus strongly suggesting a false alarm test case.

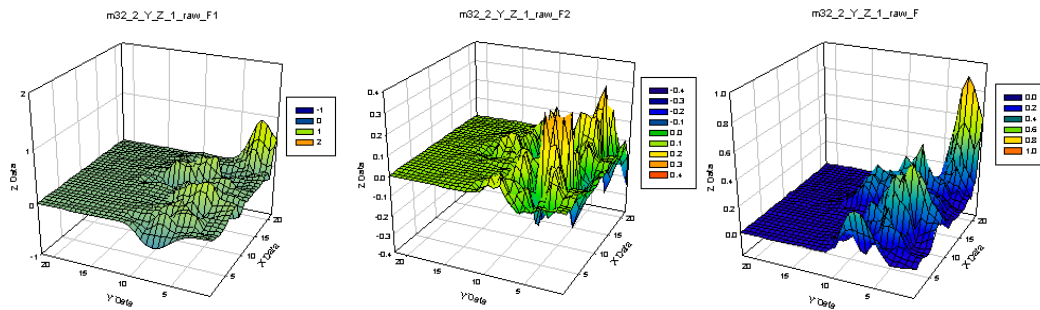
- Mode 1 (X – Y):



- Mode 1 (X – Z):



- Mode 1 (Y – Z):



- Mode 2 (X – Y):

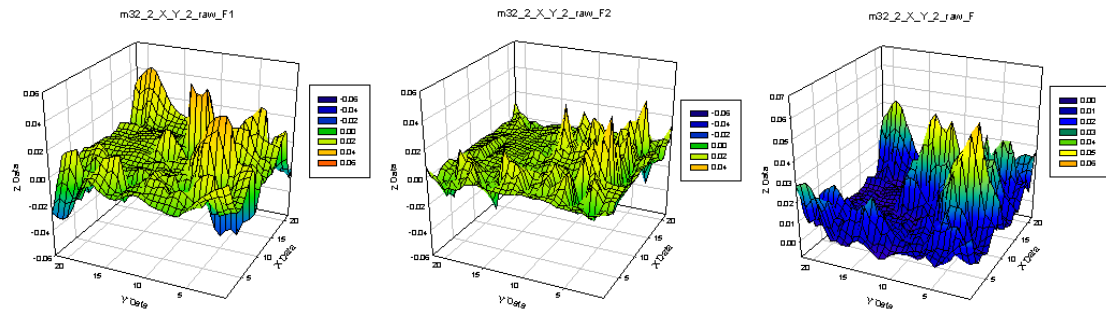
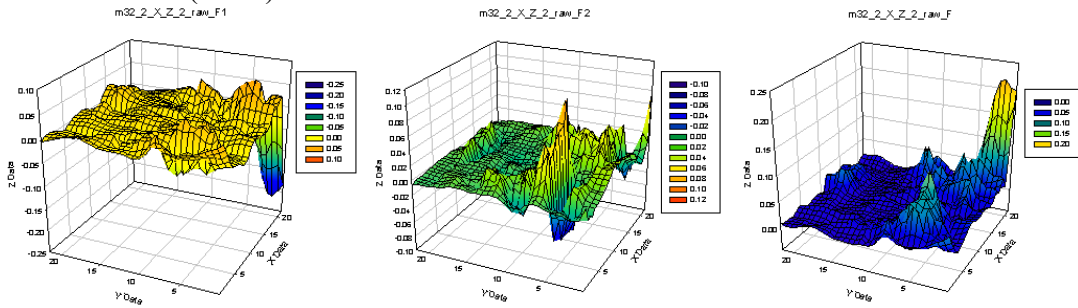
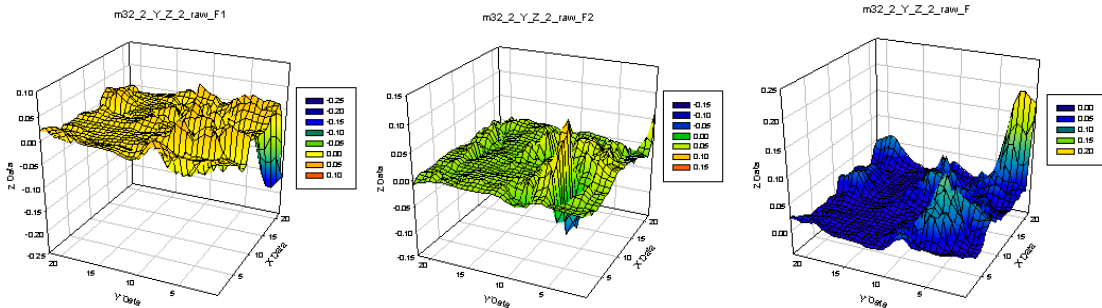


Fig. 4.10: “Set 2” – Spatial distribution of the defect energy force parameter for modes 1 to 3 showing the F_1 , F_2 and F (resultant) Force Diagrams (columns 1, 2 and 3) for the raw spatial distribution of states “X” “Y” and “Z” experiments.

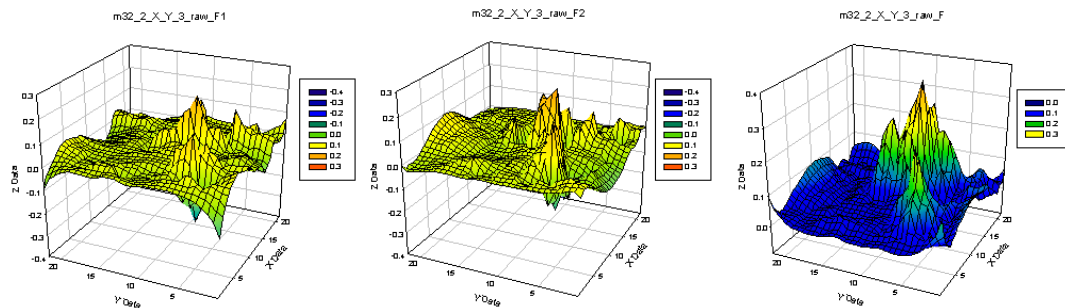
- Mode 2 (X – Z):



- Mode 2 (Y – Z):



- Mode 3 (X – Y):



- Mode 3 (X – Z):

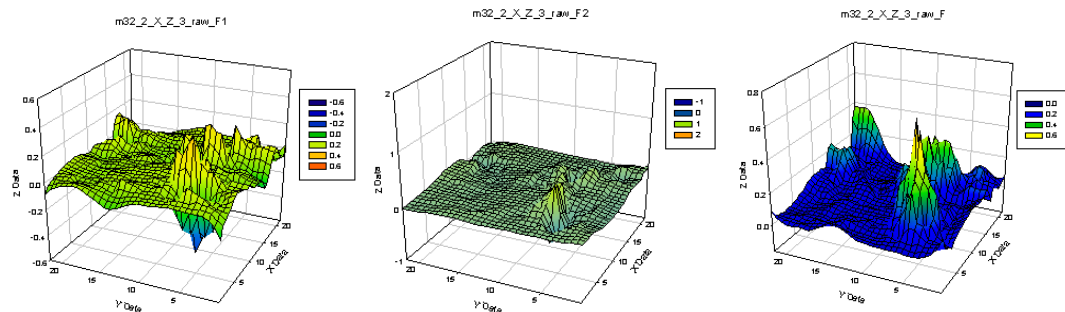


Fig. 4.10 (Continued): Set 2 – Spatial distribution of the defect energy force parameter for modes 1 to 3 showing the F_1 , F_2 and F (resultant) Force Diagrams (columns 1, 2 and 3) for the raw spatial distribution of states “X”, “Y” and “Z” experiments.

- Mode 3 (Y – Z):

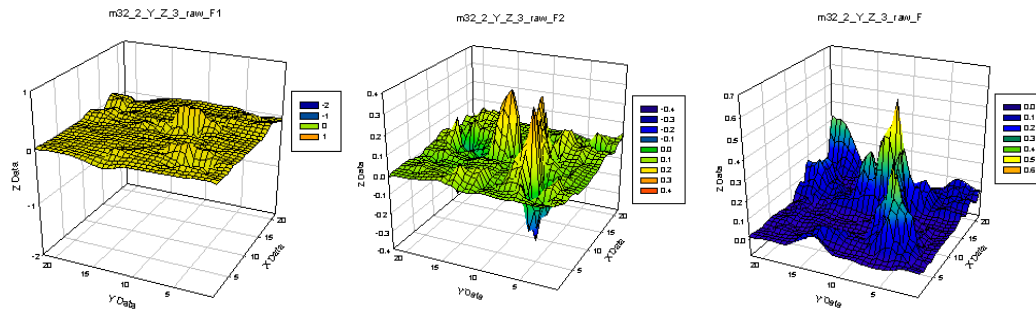
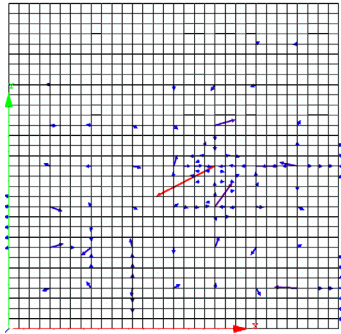


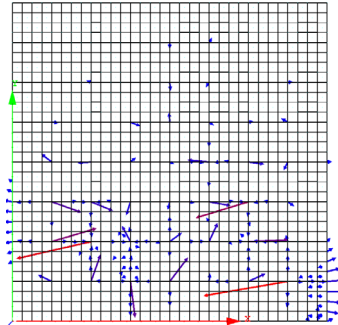
Fig. 4.10 (Concluded): “Set 2” – Spatial distribution of the defect energy force parameter for modes 1 to 3 showing the F_1 , F_2 and F (resultant) Force Diagrams (columns 1, 2 and 3) for the raw spatial distribution of states “X”, “Y” and “Z” experiments.

- **Mode 1:**

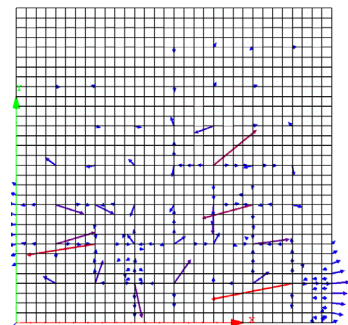
X-Y



X-Z

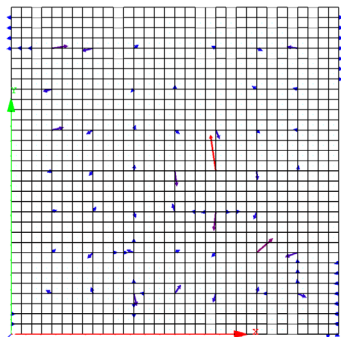


Y-Z

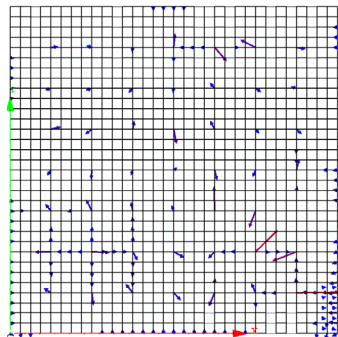


- **Mode 2:**

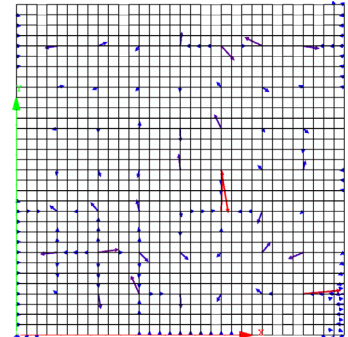
X-Y



X-Z

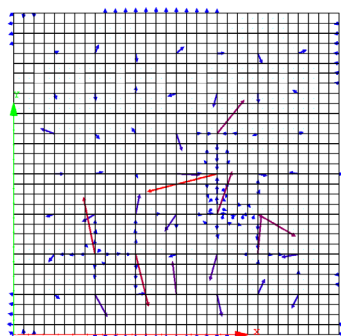


Y-Z

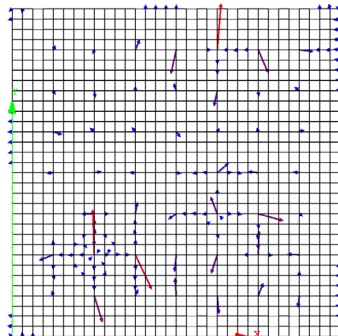


- **Mode 3:**

X-Y



X-Z



Y-Z

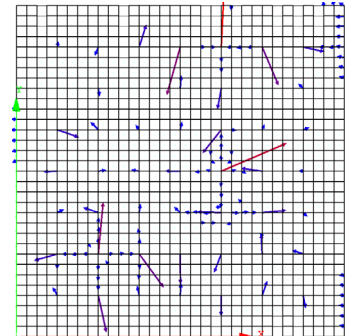
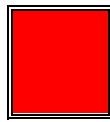
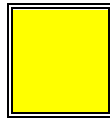


Fig. 4.11: Energy Vector Field Diagrams for “Set 2”, modes 1 to 3 for states “X”, “Y” and “Z” experiments.

Color Scheme



= Highest probability of damage at most 80% certainty
relative to noise levels in Set II “Xa” and “Xb”



= Less probability of damage (no more than 10% certainty)

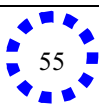
57	58	59	60	61	62	63	64
49	50	51	52	53	54		56
41	42	43	44	45	46	47	48
33	34	35	36	37	38	39	40
25	26	27	28	29	30	31	32
17	18	19	20	21	22	23	24
9	10	11	12	13	14	15	16
1	2	3	4	5	6	7	8

Fig. 4.12: Schematic Block diagram for the “Set 2” experiment after processing with the color scheme (The actual location of the damage is shown in dotted circles). Together with the vector field plots in Fig. 4.11, the strong indication exists for a single - location damage near shaded blocks 30, 31, 38 and 39.

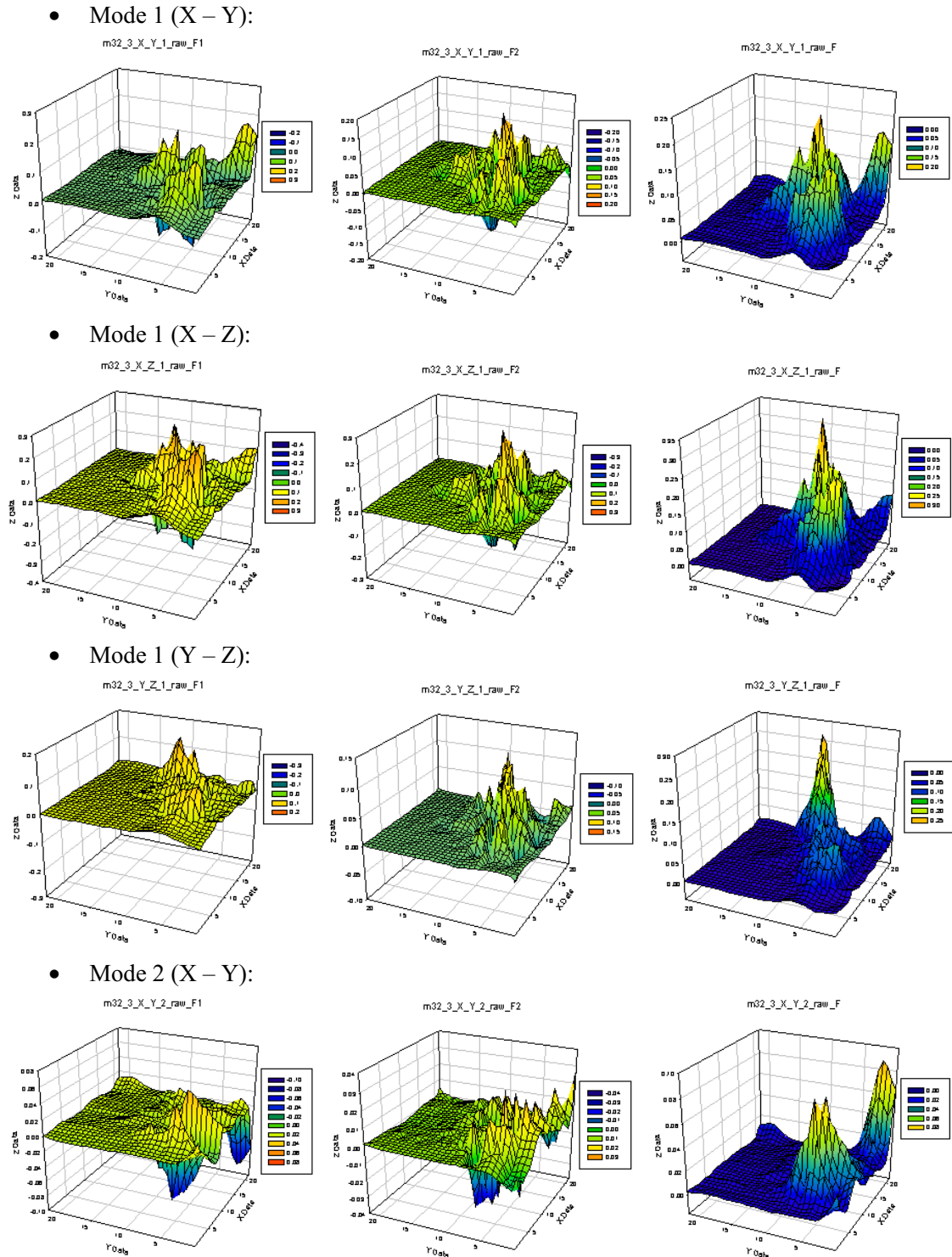


Fig. 4.13: “Set 3” – Spatial distribution of the defect energy force parameter for modes 1 to 3 showing the F_1 , F_2 and F (resultant) Force Diagrams (columns 1, 2 and 3) for the raw spatial distribution of states “X”, “Y” and “Z” experiments.

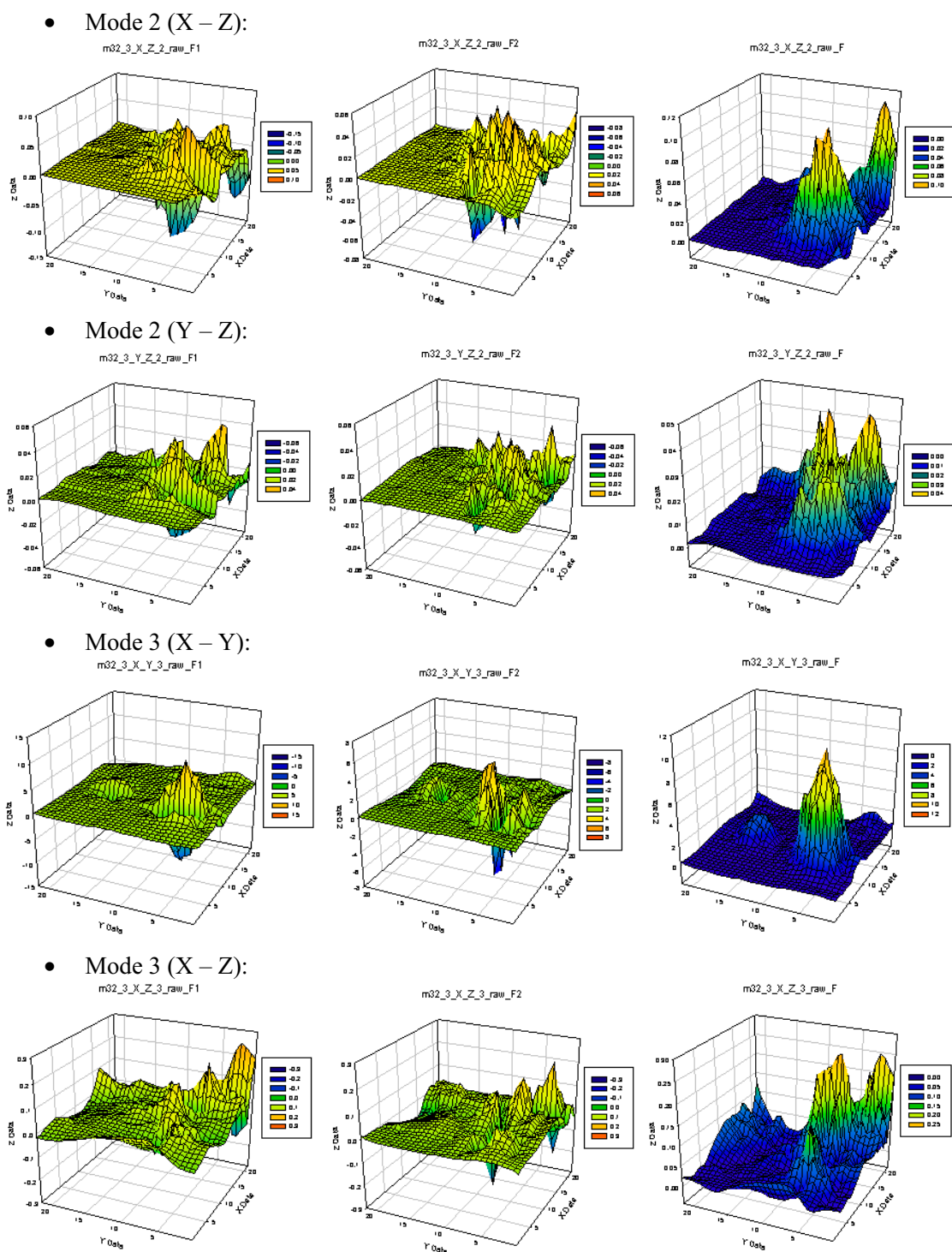


Fig. 4.13 (Continued): “Set 3” – Spatial distribution of the defect energy force parameter for modes 1 to 3 showing the F_1 , F_2 and F (resultant) Force Diagrams (columns 1, 2 and 3) for the raw spatial distribution of states “X”, “Y” and “Z” experiments.

- Mode 3 (Y – Z):

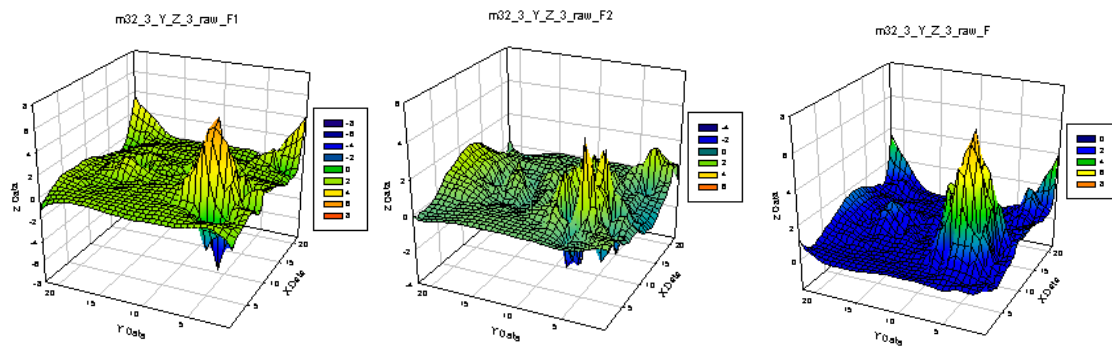
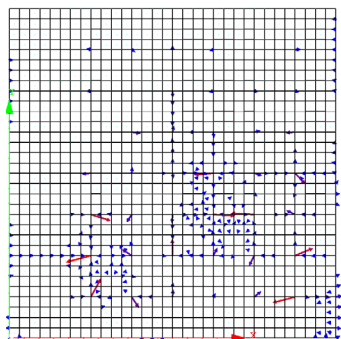


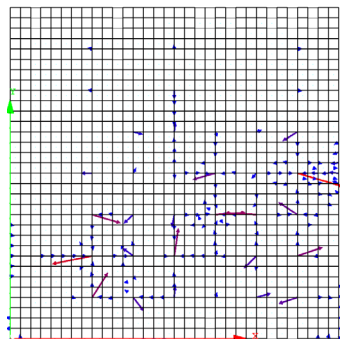
Fig. 4.13 (Concluded): “Set 3” – Spatial distribution of the defect energy force parameter for modes 1 to 3 showing the F_1 , F_2 and F (resultant) Force Diagrams for (columns 1, 2 and 3) the raw spatial distribution of states “X”, “Y” and “Z” experiments.

- **Mode 1:**

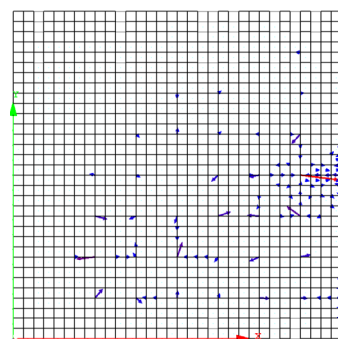
X-Y



X-Z

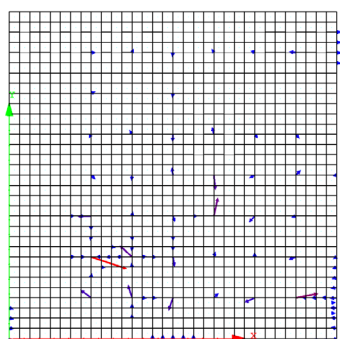


Y-Z

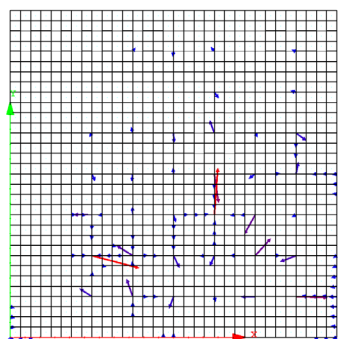


- **Mode 2:**

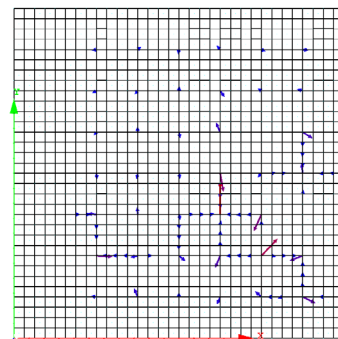
X-Y



X-Z

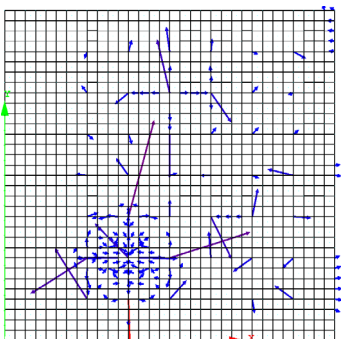


Y-Z

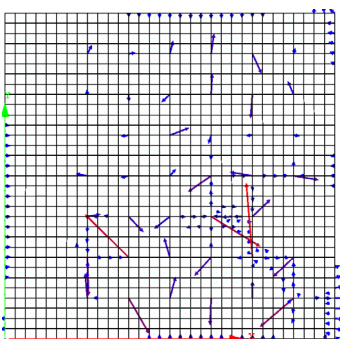


- **Mode 3:**

X-Y



X-Z



Y-Z

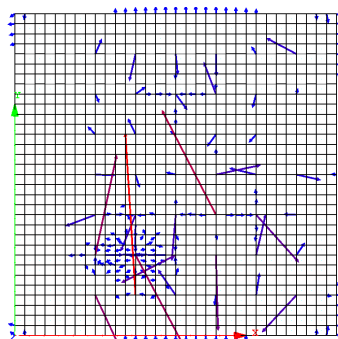
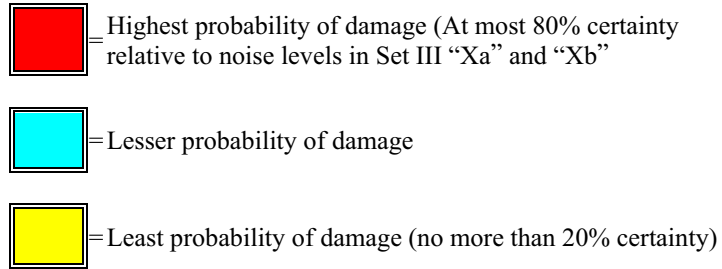


Fig. 4.14: Energy Vector Field Diagrams for “Set 3”, modes 1 to 3 for states “X”, “Y” and “Z” experiments.

Color Scheme



57	58	59	60	61	62	63	64
49	50	51	52	53	54	55	56
41	42	43	44	45	46	47	48
33	34	35	36	37	38	39	40
25	26	27	28	29	30	31	32
17	18	19	20	21	22	23	24
9	10	11	12	13	14	15	16
1	2	3	4	5	6	7	8

Fig. 4.15: Schematic Block diagram for the “Set 3” experiment after processing with the color scheme (The actual location of the damage is shown in dotted circles). Together with vector field plots of Fig. 4.14, a strong indication exists for multiple-location damages near shaded blocks 22 to 29 and 12 to 35.

4.6 Conclusions of the Experimental Verification

“Set 1”: This was a repeat of the vibration signatures of the same state of damage but at different collection times. In this case, no change in conditions between states “X” and “Y” is observed. Thus, there is no damage indicated here. It was found that this case was a representation of the thermal effects in the laboratory. A time difference of one day existed between states “X” and state “Y”. The specimen remained in the test fixture during this time but no additional damage was imposed. The schematic block diagram in Fig. 4.9 essentially reflects the presence of extensive noise in this “false – alarm” case

“Set 2”: This case indicates a single damage site that was introduced between accelerometers 15, 16, 23 and 24 see Fig. 4.1. The baseline state “X”, did not have any damage. The state “Y” had a damage of size 1.125” diameter as shown in Fig. 4.5. In state “Z” the hole imposed in state “Y” was increased to 1.6875 in. There was a strong indication (with the Highest certainty) of a damage located on the plate sector defined between accelerometers 30, 31, 32, 38, 40, 46, 47 and 48, also refer to blocks 30, 31, 38 and 39 in Fig. 4.12. This location was clearly in the correct quadrant of the plate though it was slightly lower than the actual damage location. There is some damage detected with less certainty in the area bounded by blocks 11, 12, 19 and 20 in Fig. 4.12.

“Set 3”: Here the same diameter hole that was present as in “Set 2”, state “Z” between accelerometers 15, 16, 23 and 24 existed in the state “X” as the baseline condition. A new damage site was then introduced at accelerometer locations 29, 30, 37 and 38 of size 1.6875 in. diameter and for state “Y”. In state “Z”, two more holes were made simultaneously of diameter 1.375” and 1.6875”. The first of these holes was introduced was introduced between accelerometers 32 and 40 and the other between accelerometers 55, 56, 63 and 64. Our conclusion stated that this set was certainly a case of multiple damage shown at two locations even though three more holes were induced. Note that the baseline state “X” which had the damage, this information was unknown at the time of the analysis. The first position is strongly indicated (highest possibility of a damage) at or around the location of block 12. The location of the second damage is bounded by the sites of blocks 22, 23, 30, 31, 38 and 39 as in Fig. 4.15.

These results were officially submitted to NASA Glenn and were found to be in close proximity with the actual experimental documentation. All the processing of the measured data was without any prior knowledge of the damage sites or sizes. The effort has shown that the damage detection method is proficient in detecting damage locations based on modal displacements. The focus of future work will be to obtain better determination of the site of the damage.

5.0 FULL FIELD EXPERIMENTAL INVESTIGATIONS—THE USE OF ELECTRONIC SPECKLE INTERFEROMETRY TECHNOLOGY AND EXTENSIVE PATTERN RECOGNITION TECHNIQUES FOR DEFECT LOCALIZATION

5.1 Introduction

Several newly emerging technologies are being investigated in recent years, with emphasis on providing full – field measurements of the complex mechanical response signatures of continuous systems. An example of this is provided by the so – called Electronic Speckle Pattern/Shearing Interferometry (ESPI and ESSPI). The data obtained from these technologies provide an excellent vehicle to assess the defect detection/localization capabilities of the global scheme under study in the present report. To this end, this chapter presents results of a detailed investigation of this type, i.e., utilizing the case of vibrating cracked plate, where the damages are actually produced by the crack propagation along the length of the fixed boundary of the plate (the problem has three sides free and the remaining fourth straight boundary of the plate is totally “clamped”). The complexity of this problem stems from two main factors. Firstly, with one of changed damage conditions of the plate corresponding to only the coordinates of the targeted damaged locations being frozen with the progression of the single line crack, methods utilizing solely the frequency changes to localize damage will basically fail here. Furthermore, any of the existing detection schemes using such notions as changes in “isolated” slopes, curvatures, flexibility of a mode shape will also have extreme difficulties (if at all possible) since (as will be shown later) the significant effects of a propagating crack along a single support line will trigger very large changes in the individual modes *almost everywhere* (and not only at the location of the increased damages only) and this will occur essentially with a random character, i.e., regions far away from the true propagating crack may be affected most depending on the particular mode being interrogated. The study of vibration behavior of plates with a crack is a problem of great practical significance, especially for the experimental verifications of theoretical proposals. Indeed, we note here that only a few papers have been published on the vibration analysis of a “finite-domain” cracked plate.

The traditional way of measuring vibration frequencies and damping of a single-degree-of-freedom (SDOF) system is by using a contact-type instrument, such as an accelerometer, to give time histories of the vibration signals. For a multiple-degree-of-freedom (MDOF) system such as a continuous plate, if the natural frequencies are well separated (without too much mode coupling interaction), the same method can be applied.

As far as the modal analysis is concerned some of the disadvantages of using accelerometer-based measurements are:

- Contact and point wise - the point-by-point measurement takes time, thus there is always an uncertainty of whether there is a change of vibration behavior of the structure during the modal testing.
- The finite size of the accelerometer instrument would also limit the dimensions of the tested structure.

Electronic speckle pattern interferometry (ESPI) is a full field non-contact method capable of analyzing the vibration of complex mechanical structure. This emerging new technology has many advantages over the conventional contact accelerometer method, including the following:

- Resonant frequencies and the corresponding mode shapes can be obtained simultaneously from the experimental measurements.
- Non-contact technique for measuring vibration of structures in hazardous conditions, e.g., elevated temperature, high voltage, and specimens subjected to toxic reactions, etc.
- Tremendous reduction in the environmental and experimental machinery noise measurements.
- Short duration of the actual experiments in the order of two hours.

Contour maps of vibration mode shapes can be measured and plotted by time average of ESPI, or their vibration amplitude gradients can be measured by time average of ESSI (Electronic Speckle Shearing Interferometry) that has a similar principle as compared to the ESPI. This method has the advantage of being insensitive to rigid body vibration modes. In structures subjected to complex loading it might be necessary to use both these sets of measurements. The only limitation is the lead time needed to set up the equipments for measuring these details. However, once operational, this set up can provide for very fast and large-area scans of accurate measurements. (e.g., in the order of a micrometer of translations of rather elaborate structural deformation modes) in a matter of minutes or at most very few hours.

Yang et al. [56] presented the development of this method both in technique and theory. The optical setups for measuring in-plane and out-of-plane displacements and strains, as well as their applications were shown by applying phase shifting techniques. The technique proposed by them gave wider and more controllable range sensitivity, thus allowing the measurements of displacement gradients corresponding to larger deformation.

Wong et al. [57] used a time-averaging electronic speckle shearing interferometer (ESSI) for modal damping measurements. They compared the damping factor of a cantilever beam by the ESSI method and the accelerometer technique. The main advantage of this method was the simplicity of the experimental setup and the

measurement procedure. They had proposed the use of three interferograms whereas hundreds were said to be required in the methods proposed earlier. The limitation of their method was that the relative phase between the points in a complex mode is depending on the spatial domain, thus causing some uncertainties in resolving the direction sensitivity.

Fringe patterns depicting the out-of-plane displacements and slope of deformed objects are obtained using digital speckle pattern and digital speckle shearing interferometer respectively. Ng [58] showed that the original design for digital speckle shearing interferometry was able to measure the objects subjected to complex loads necessary to produce both the data as stated above. With small modifications he also showed the out-of-plane displacement measurements.

To increase the visibility of the fringe pattern and to reduce the environmental noise simultaneously, an Amplitude Fluctuation electronic speckle pattern interferometer (AF – ESPI) was proposed by Wang et al. [59] for out-of-plane measurements. This was used by Ma et al. [60] and showed the resonant properties of a rectangular cantilever plate with cracks. The advantage of using the AF – ESPI method is that resonant frequencies and the corresponding mode shapes can be obtained simultaneously from the experimental measurement.

5.2 Principles of the Method—Fringe Formulation in ESPI and ESPI

When a speckle pattern produced by a diffusing object surface interferes with a reference light wave or with another speckle pattern, a random interference pattern is produced. The intensity distribution $I(x, y)$ of the interference pattern is given as

$$I(x, y) = I_o [1 + \gamma \cos \phi(x, y)] \quad (5.1)$$

where I_o represents the average intensity of the two light beams γ represents the modulation of the interference term and $\phi(x, y)$ represents the random phase angle before deformation of the object. When the object is deformed, an optical path change occurs due to the surface displacement of the object. Thus, the intensity distribution $I(x, y)$ of the interference pattern is slightly altered and now represented by

$$I(x, y) = I_o [1 + \gamma \cos \phi'(x, y)] = I_o \{1 + \gamma \cos [\phi(x, y) + \Delta]\} \quad (5.2)$$

where $\phi'(x, y)$ represents the random phase angle after deformation of the object and Δ represents the relative phase change due to the object deformation, which can be described by

$$\Delta = \phi'(x, y) - \phi(x, y) \quad (5.3)$$

In *electronic* SPI and SPSI, i.e., ESPI and ESPSI, the two intensity distributions $I(x, y)$ and $I'(x, y)$ before and after deformation are digitized and stored in two frames. Subtraction of the two frames yields a fringe pattern. Since intensity of an image cannot be negative, absolute values of the subtraction will be displayed. Now the eye sees the average of the absolute values of the subtraction over an elementary area and therefore,

$$\begin{aligned} I_{av} &= \frac{1}{2\pi} \int_0^{2\pi} |I(x, y) - I'(x, y)| d\phi \\ &= \frac{4}{\pi} I_o \left| \sin \left(\frac{1}{2} \Delta \right) \right| \end{aligned} \quad (5.4)$$

A visible fringe pattern is obtained on which the brightness is maximum when $\Delta = (2n+1)\pi$ and a minimum when $\Delta = 2n\pi$, n being the fringe order. In the real-time method, the first intensity distribution is stored in one frame while a real-time frame grabber stores the second image and the resultant image of the above subtraction observation is displayed also in the real-time frame grabber and hence fringes can be observed real-time on the monitor.

The phase shifting technique is used to determine the phase distribution in interferometric fringes. When this technique is used in SPI and SPSI, the relative phase change corresponding to the object surface displacements (in SPI) or the object surface displacement gradients (in SPSI) due to object deformation can be determined automatically and precisely by calculating the phase distribution from the measured intensities. Generally speaking there are three unknowns in the intensity distribution of Eq. (5.1). They are the average intensity I_o , the modulation of the interference term γ and the phase distribution ϕ of the interference pattern. In order to calculate the phase ϕ , it is necessary to record at least three intensity distributions corresponding to different amounts of phase shift. Here, the situation of recording only three intensity distributions is discussed. For each recording of intensity an additional phase shift of 120° for one beam in the interferometer is used. Digitizing three intensity patterns provides three equations like Eq. (5.1)

$$\begin{aligned} I_1(x, y) &= I_o \{1 + \gamma \cos[\phi(x, y)]\} \\ I_2(x, y) &= I_o \{1 + \gamma \cos[\phi(x, y) + 120^\circ]\} \\ I_3(x, y) &= I_o \{1 + \gamma \cos[\phi(x, y) - 120^\circ]\} \end{aligned} \quad (5.5)$$

The phase angle is then calculated at each detected point in this interference pattern as

$$\phi = \arctan \frac{\sqrt{3} (I_3 - I_2)}{2I_1 - I_2 - I_3} \quad (5.6)$$

After the object is deformed, three more frames of intensity data are taken while shifting the phase with the same amount as for the first set of data. The phase distribution ϕ' of the interference pattern after deformation can also be calculated, as was obtained previously for ϕ . The time for the acquisition of one frame image is usually 40 μ s and the calculation of the phase distribution ϕ or ϕ' can be finished within one second. Once these data are taken, the relative phase change can be calculated simply by subtracting ϕ from ϕ' according to Eq. (5.3).

5.3 General Experimental Set-up and Measurements

Electronic Speckle Pattern Interferometry is a method of producing interferograms without using a traditional holographic technique. The image data are digitized by a video camera and digital signal processors, because the interferometric image are recorded and updated by the video camera every $\frac{1}{30}$ sec, ESPI is faster in operation with the entire measurement completed in a couple of hours and more insensitive to environmental and machine noise compared to the conventional contact accelerometer techniques.

The out-of-plane and in-plane vibrating measurement by ESPI is shown schematically. If the image is taken after the specimen vibrates periodically, a charged coupled camera picks up the light intensity detected. A laser beam is used as the coherent light source, which is further being divided into two parts, the reference beam and the object beam by the beam splitter. The object beam travels to the specimen and then reflects to the CCD (charged coupled device) camera. The reference beam goes directly to the CCD camera via a mirror and a reference plate. The CCD camera converts the intensity distribution of the interference pattern of the object into a corresponding video signal at 30 frames/sec. The signal is electronically processed and converted to an image on the video monitor. The interpretation of the fringe image is similar to reading a contour map of the displacement field. A piezoelectric actuator that is attached to the specimen can excite the plate. To achieve the desired output of vibration frequency a digitally controlled function generator connected to a power amplifier is used. This entire experimental setup, as shown in Fig. 5.1 once setup in place doesn't require further human intervention to measure the mode frequencies and vibration of the structure. The accuracy obtained by using the ESPI full field method of experimental investigation is in the order of micrometer.

A similar setup can be used for measuring the slopes or changes in gradient in the structure. Although the time need for setup is more, the accuracy and the images obtained are in full completeness with respect to the space and content of the structure.

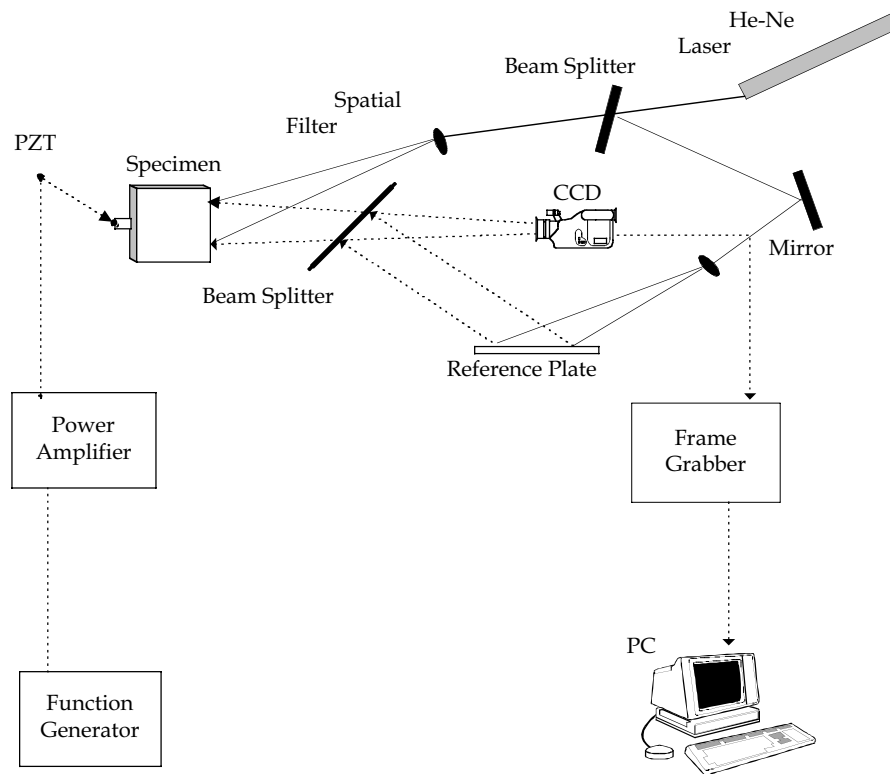


Fig. 5.1: Schematic Diagram of ESPI Experimental setup for out-of-plane measurement.

5.4 Specimen Description and Results

The material properties of the plate are mass density $\rho = 2700 \text{ Kg/m}^3$, Young's modulus $E = 70.9 \text{ Gpa}$ and Poisson's ratio $\nu = 0.33$. The location of the crack (represented as x) and the geometric dimensions of the plate are shown in Fig. 5.3, the thickness of the plate is 1 mm and crack length $a = 20, 35$ and 50 mm . These are the same as reported in reference [60].

The “independent” confirmations of the experimental AF – ESPI using finite element results are obtained by using ABAQUS, finite element modeling package in the above mentioned reference [60]. In all, a total of 1200 elements with eight-node two-dimensional shell elements (S8R5) were used in the analysis. This element approximates the Mindlin-type element that accounts for the rotary inertia effects and first-order shear deformations through the thickness. The same number of elements was used in order plot the mode shapes, the spatial distribution of defect energy force intensity parameter and nodal damage energy vector field diagram using the Damage Detection Code (DDC). The detailed of this latter code were described in the previous chapters (see Chapter III); for further details see also Saleeb et al. [53, 54].

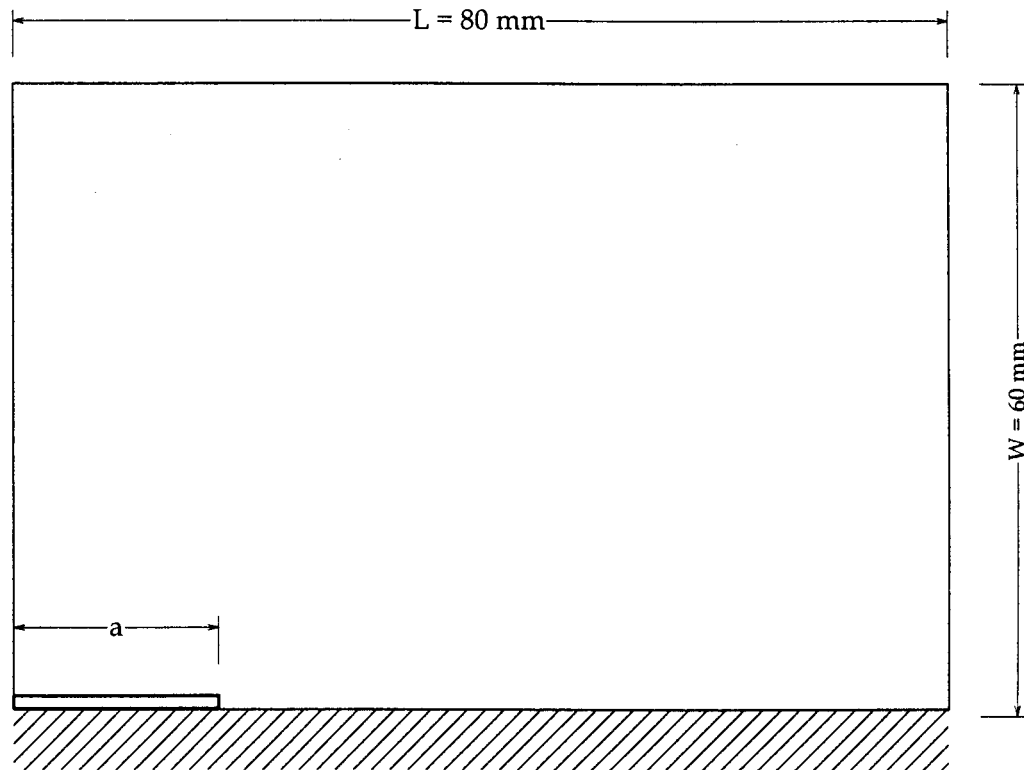


Fig. 5.2: Geometric dimensions and configurations of cracked rectangular plate.

Table 5.1 shows the results of the first 10 resonant frequencies for different crack lengths of 20 mm, 35 mm and 50 mm, obtained by the experimental AF – ESPI, Finite element method (Abaqus) and the DDC code. It is observed that the results are consistent and very close from all the methods which is remarkable considering the rather small number of total DOF's in meshes using the DDC (i.e., bilinear element basis in DDC as compared to biquadratic element in ABAQUS FE code. Due to the fact that in a real experiment the supports cannot be made ideally rigid, the values of the frequencies are much lower as compared to the Finite Element analysis or the DDC results (compare the three columns of each of the cases of Table 5.1). In Fig. 5.3, the 3D mode shapes of the damaged and the undamaged plate are shown for crack length 20 mm, 35 mm and 50 mm close to the support. The corresponding contours for the mode shapes are compared using the various methods as shown in Fig. 5.4, Fig. 5.5 and Fig. 5.6, for crack length 20 mm, 35 mm and 50 mm, respectively.

The mode shapes for each of the larger crack lengths (35 mm and 50 mm) showed significant changes in pattern for basically all the modes (from the first mode to the last mode), relative to the base reference case of 20 mm crack. For example, consider the mode shape numbers one and two together in Fig. 5.4 and 5.6, and then modes nine and ten in Fig. 5.4, and their counterparts in Fig. 5.5, i.e., to compare changes in pattern:

- i. From reference state (20 mm crack) to changed state of maximum (50 mm crack), and
- ii. From the reference versus the medium-size crack states (20 mm versus 35 mm), respectively

Considering case (i), for modes one of Fig. 5.4 and Fig. 5.6, significant variations for the slopes/curvatures of the mode – contour plots are visible all along the lower support line (including the actual damages but also quite apparent changes occur at the right lower quarter zone of the plate with no cracks existing there). Also, the most dramatic changes in these modes slopes/curvatures of modes two, in Fig. 5.4 and 5.6, are visible along the entire strip of the plate covering approximately one third of its horizontal dimension (i.e., not restricted to the nearly 30 mm length of the fixed support line, as would be ideally anticipated for damage-state changes produced from a crack length of 20 mm to its increased length 50 mm). Moving next to the comparisons of the higher mode numbers nine and ten in Fig. 5.4 (reference state) and Fig. 5.5 (medium crack-length damaged state), one essentially notices that the entire plate domain exhibits large pattern changes in these modes “slope/curvature” features. In conclusion, using the notions of differences in such simple measures (as slopes, etc.) of the mode shapes (even in their full – field format presented here) will (at best) lead to contradictory results as to the damage localization capabilities. This points out to the important fact that looking at the contour intensity of the mode shapes there is no consistency in the pattern in pointing out the location of the damage. The same conclusion applies for both the two damage scenarios, i.e., crack lengths of 35 mm and 50 mm, with the 20 mm crack serving as reference.

On the other hand, we have considered the following arguments to determine the effectiveness of the damage defect energy parameter and the vectorial fields of nodal damage forces (as outlined in Chapter III). The displacement results (no rotations) from the modes shapes of the “healthy” plate were considered as a 20 mm boundary crack vs. the “damaged” plate as a 35 mm and a 50 mm boundary cracks for the plate (Fig. 5.7 and Fig. 5.8, respectively). Both the energy vector field diagram and the contour intensity diagrams are plotted for the above cases. In the figures we have employed the following convention, i.e., the part (a) in each figure represents the energy vector field diagram and (b) represents its associated contour intensity plot, the latter thus providing a third alternative for further enhanced visualization. The (c), (d) and (e) represent the contour intensity plots for individual force components of the damage parameters respectively as was customarily used in Chapter III.

For all the cases to be reported here, only the data for the vertical displacements and frequencies (for all ten modes) were provided to the DDC code, as measured response (i.e., still lacking any rational DOF input to represent incomplete in data content, although it is worth mentioning that recent reporting in the literature on using ESPI/ESSI provide for both types of measurements. However, as will be subsequently demonstrated, excellent detection/localization results were obtained from the present global scheme. Of course, better resolutions are anticipated if the additional measurements of the rotation DOF are also incorporated in the processing of the data in the DDC code.

The final results obtained are depicted in Figs. 5.7 and 5.8, for the increased damage scenarios of crack lengths extending to 35 mm and 50 mm, respectively, from the baseline condition of a plate with a 20 mm crack length along the fixed support line. For all the modes considered, a very crisp and distinct pattern is clear in all the plots. The consistently – recognized vector field patterns, i.e., pointing outwardly from the damage inflicted regions, persisted in all the cases, thus “proving” all the theoretical features alluded to in Chapter III, i.e., dissipation – driven vector directions with increased true damages. As the crack propagates further, so will the length of significant, outwardly - pointing, vector fields that are plotted along the support line, with virtually zero interference from the other areas that are removed from the damage zone.

An accuracy of the above mentioned magnitude has never been exhibited (to this authors knowledge) by any of the earlier methods used by various researchers in damage detection. Indeed, the mere attempts to detect faults on the two dimensional surfaces (as in the domain of the present plate) are virtually nonexistent in the currently available literature on detection (mostly searches on “lines” were reported). Further, a crack in the boundary region usually involves a lot of self-induced noise that pollutes the real processing of data in any damage parameter, but the results obtained from the present DDC were very encouraging. The problem of measuring points on or near the boundary has always proved to be difficult due to the difficult accessibility for conventional/sensor like attachments in modal testing. The crack introduces a new free

boundary of the plate, the mode shape is quite complicated and different from that of a plate without a crack. Many researches have therefore restricted the scope of their detection demonstrating to cases involving damages located somewhere “inside” the test – object domain. This is an easier case, i.e., alleviating the potential extreme difficulty in applying, e.g., finite – differencing schemes, to obtain such measures as slope/curvatures of modes at a boundary point. Any such methods will most likely fall short when they reach the end or the edge of the domain. Judging by the obtained results here, the present scheme does not seem to be suffering from any such limitations.

Table 5.1: Comparison of the Frequencies for the first 10 resonant modes by AF-ESPI, FEM and DDC.

Frequencies (in Hz) for the modes									
Crack length	x = 20 mm			x = 35 mm			x = 50 mm		
	AF _ ESPI	Finite Element	Damage Code	AF _ ESPI	Finite Element	Damage Code	AF _ ESPI	Finite Element	Damage Code
Mode #									
1	196.00	224.00	218.17	167.00	188.00	199.72	124.00	140.00	145.23
2	397.00	418.00	418.27	322.00	344.00	413.34	244.00	268.00	399.34
3	964.00	1012.00	1051.00	711.00	754.00	1051.76	582.00	618.00	1019.69
4	1244.00	1393.00	1406.23	1140.00	1220.00	1359.42	1039.00	1106.00	1194.17
5	1454.00	1652.00	1688.21	1355.00	1558.00	1692.25	1287.00	1493.00	1649.34
6	2154.00	2329.00	2551.55	1912.00	2025.00	2531.57	1841.00	1918.00	2374.37
7	2544.00	2634.00	2635.33	2444.00	2564.00	2636.82	2084.00	2163.00	2541.21
8	2988.00	3133.00	3345.57	2958.00	2852.00	3370.77	2577.00	2661.00	2838.98
9	3969.00	4227.00	4218.15	3618.00	3842.00	4097.69	3170.00	3334.00	3641.33
10	4224.00	4508.00	4489.73	4050.00	4278.00	4472.69	3809.00	4143.00	4260.25

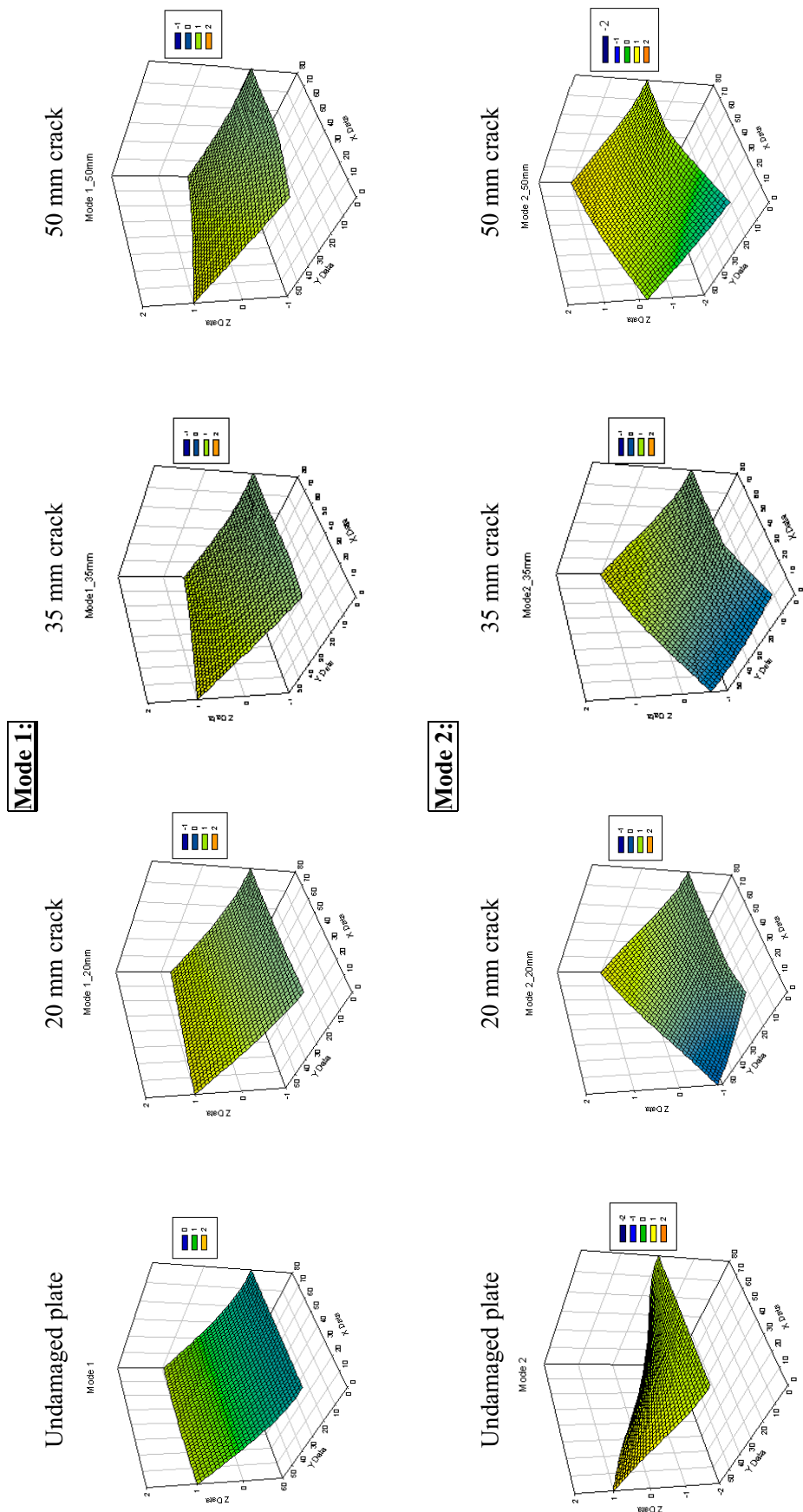


Fig. 5.3: Showing the 3D mesh plot of the first 10 mode shapes for boundary crack problem.

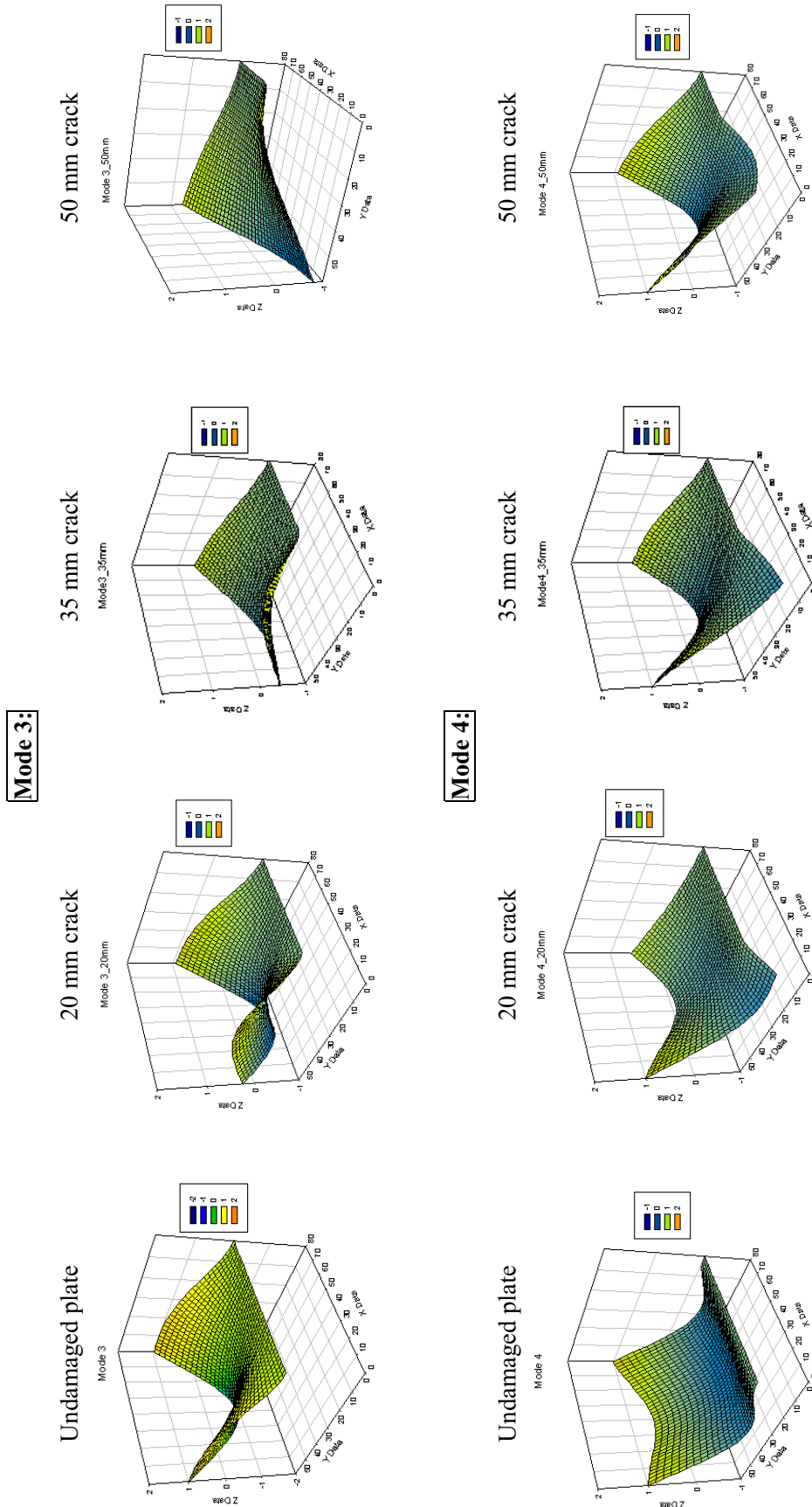
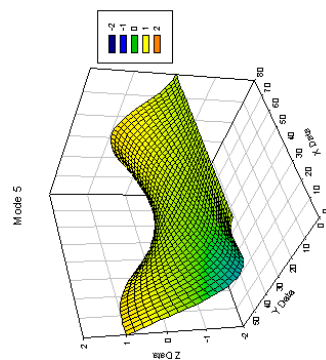


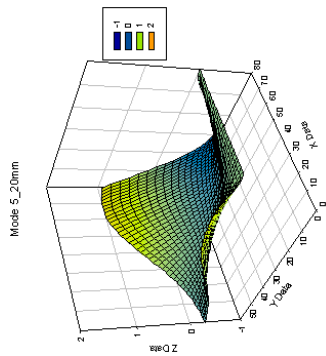
Fig. 5.3 (Continued): Showing the 3D mesh plot of the first 10 mode shapes for boundary crack problem.

Mode 5:

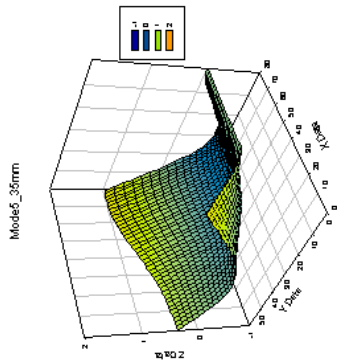
Undamaged plate



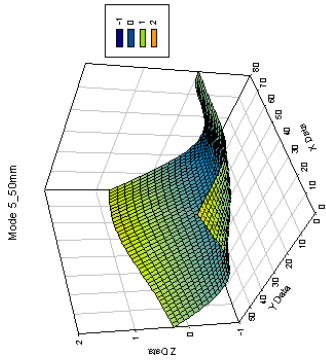
20 mm crack



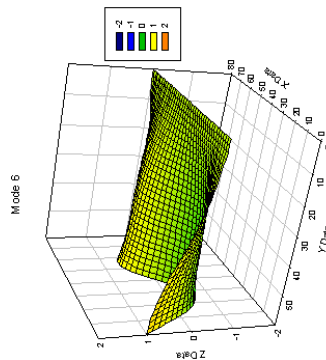
35 mm crack



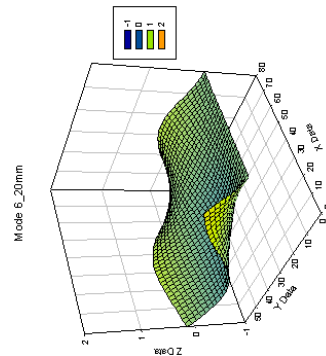
50 mm crack

**Mode 6:**

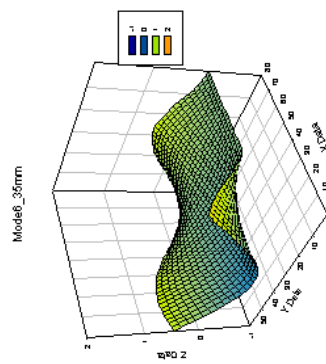
Undamaged plate



20 mm crack



35 mm crack



50 mm crack

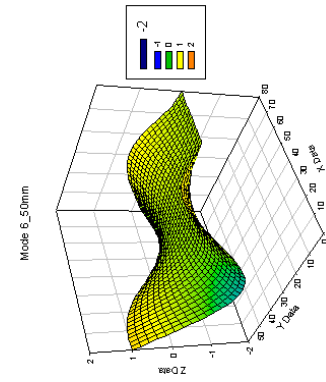


Fig. 5.3 (Continued): Showing the 3D mesh plot of the first 10 mode shapes for boundary crack problem.

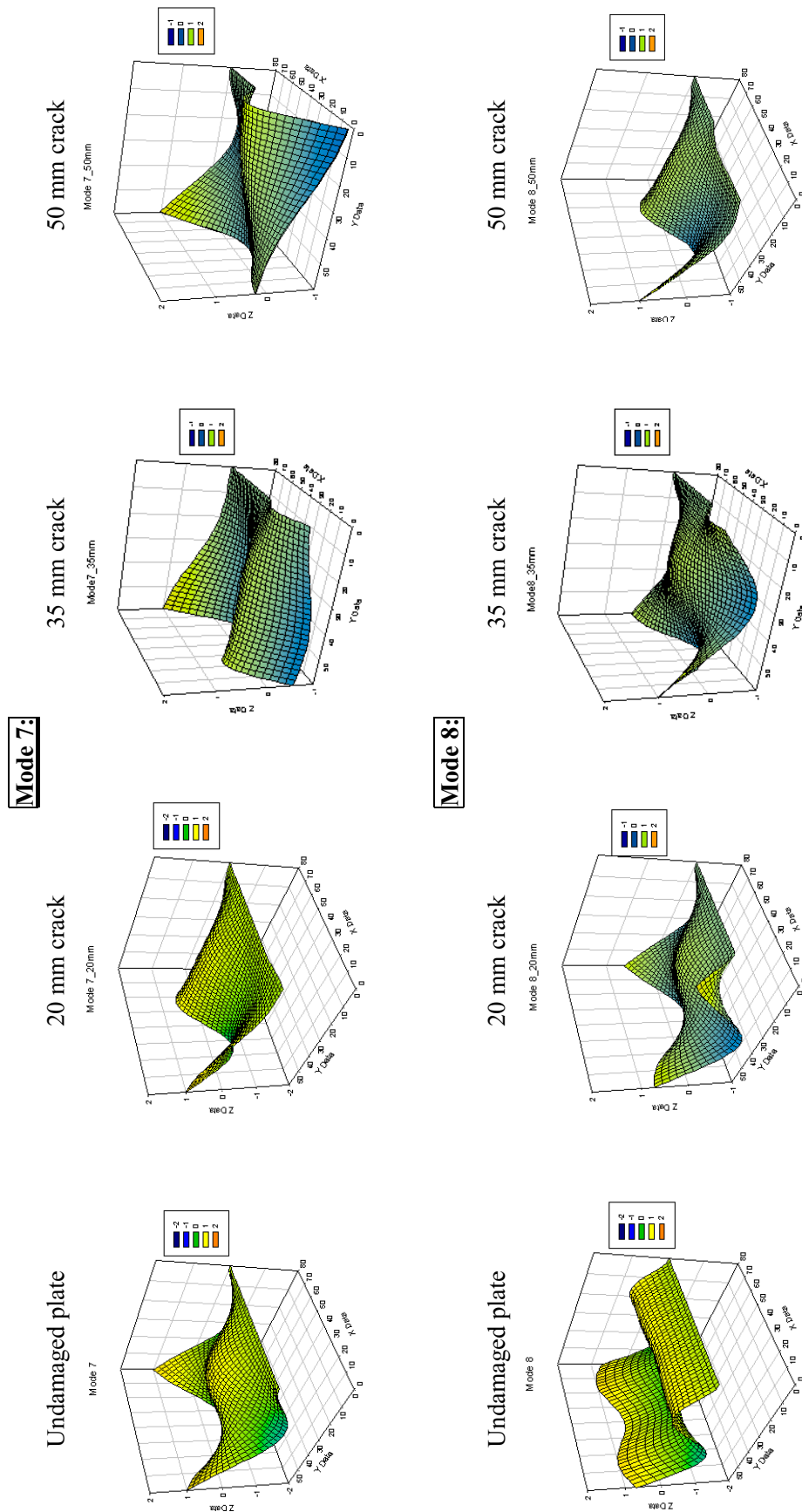
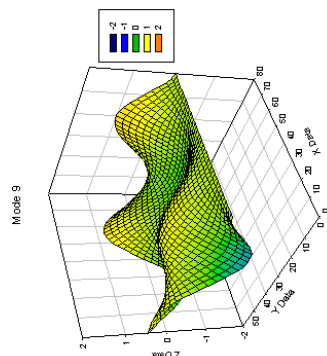


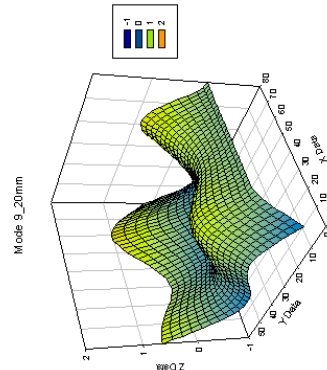
Fig. 5.3 (Continued): Showing the 3D mesh plot of the first 10 mode shapes for boundary crack problem.

Mode 9:

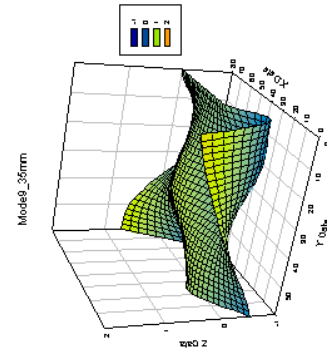
Undamaged plate



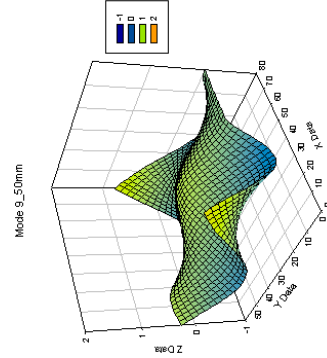
20 mm crack



35 mm crack

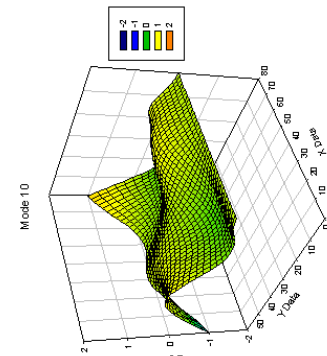


50 mm crack

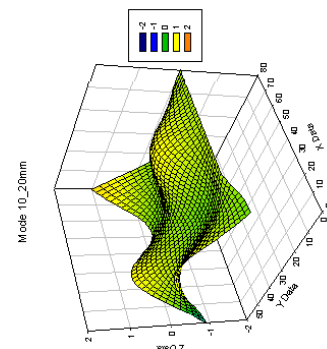


Mode 10:

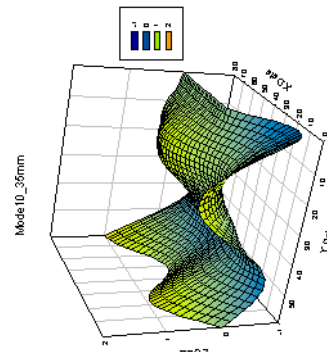
Undamaged plate



20 mm crack



35 mm crack



50 mm crack

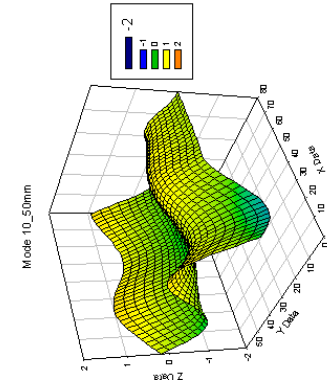
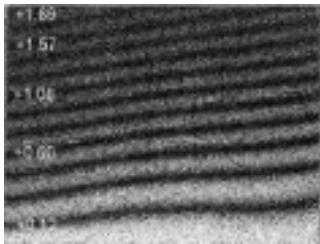


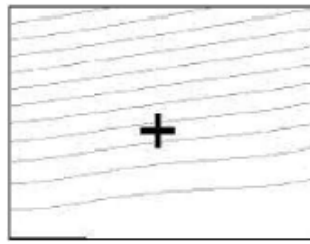
Fig. 5.3 (Concluded): Showing the 3D mesh plot of the first 10 mode shapes for boundary crack problem.

- **Mode 1:**

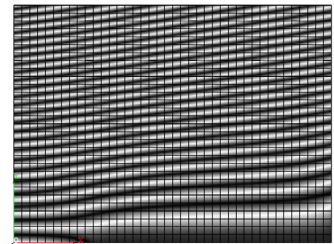
AF – EFSI



Finite Element Code

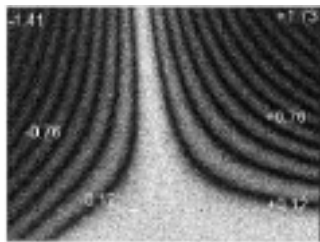


Damage detection code

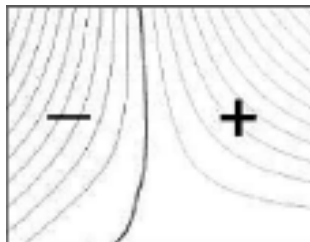


- **Mode 2:**

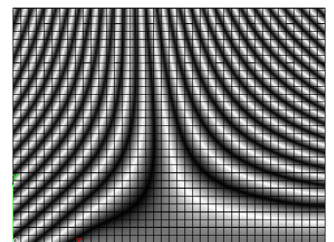
AF – EFSI



Finite Element Code

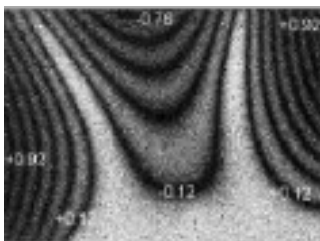


Damage detection code

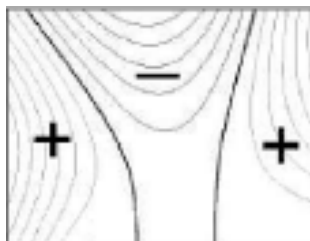


- **Mode 3:**

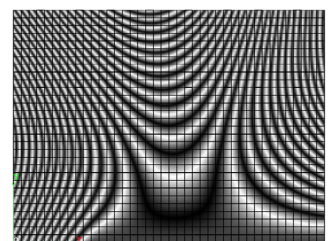
AF – EFSI



Finite Element Code

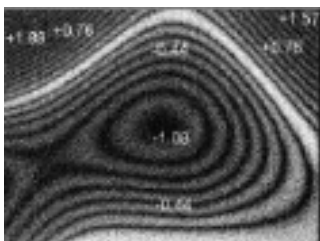


Damage detection code

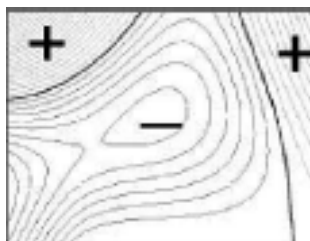


- **Mode 4:**

AF – EFSI



Finite Element Code



Damage detection code

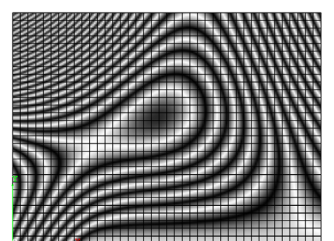


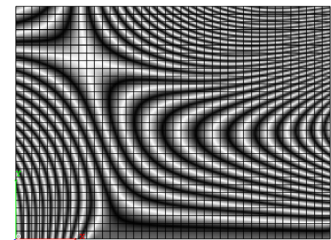
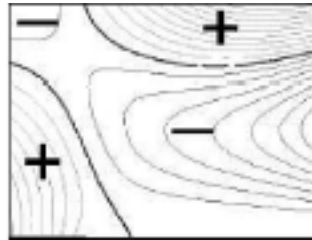
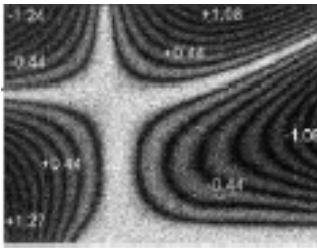
Fig. 5.4: Mode Shape contour plots using various methods for a = 20 mm crack.

- **Mode 5:**

AF – EFSI

Finite Element Code

Damage detection code

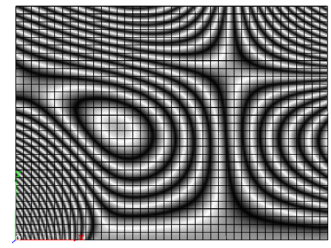
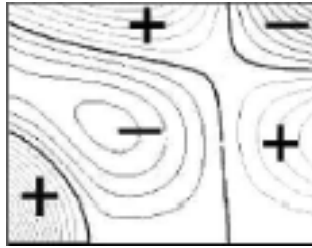
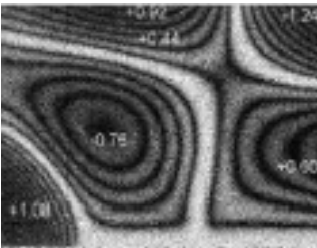


- **Mode 6:**

AF – EFSI

Finite Element Code

Damage detection code

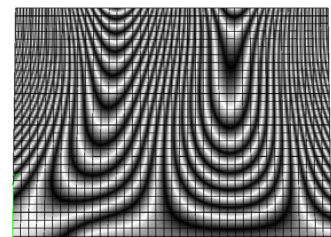
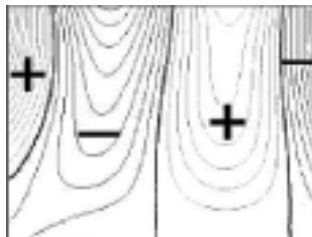
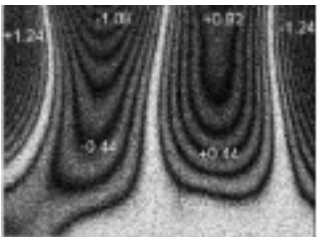


- **Mode 7:**

AF – EFSI

Finite Element Code

Damage detection code



- **Mode 8:**

AF – EFSI

Finite Element Code

Damage detection code

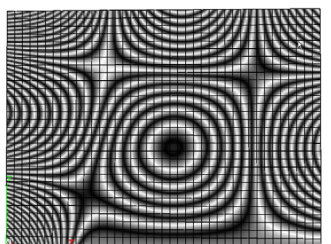
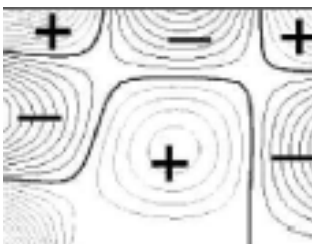
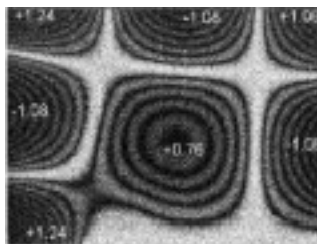


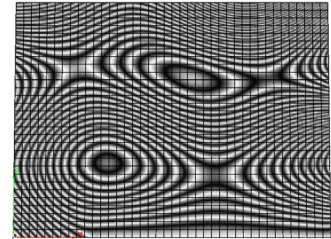
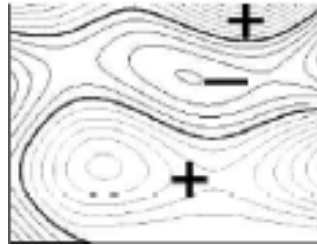
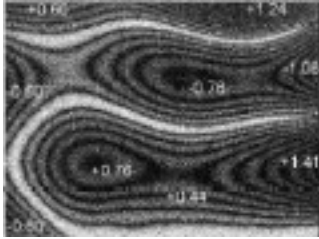
Fig. 5.4 (Continued): Mode Shape contour plots using various methods for a = 20 mm crack.

- **Mode 9:**

AF – EFSI

Finite Element Code

Damage detection code



- **Mode 10:**

AF – EFSI

Finite Element Code

Damage detection code

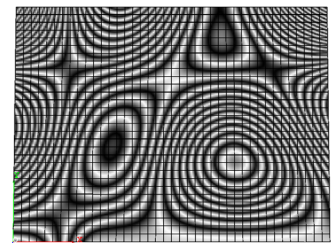
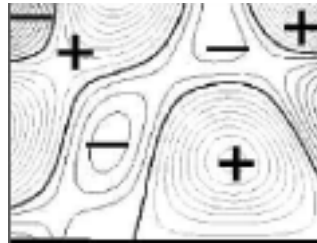
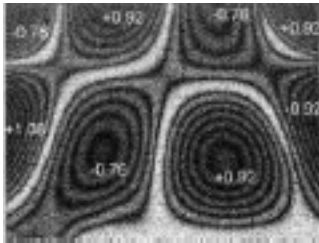
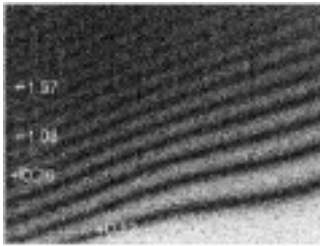


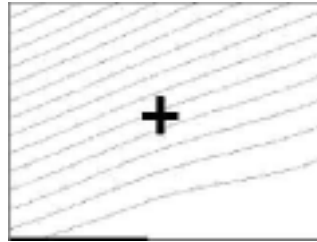
Fig. 5.4 (Concluded): Mode Shape contour plots using various methods for $a = 20$ mm crack.

- **Mode 1:**

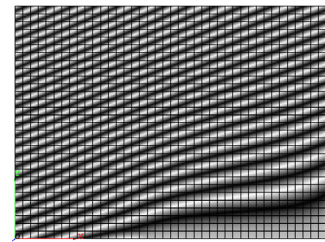
AF – EFSI



Finite Element Code

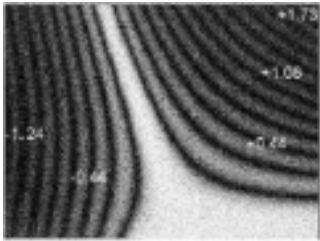


Damage Detection Code

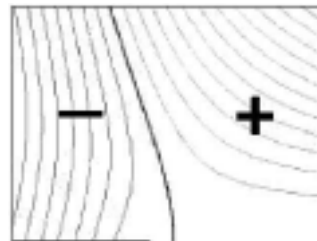


- **Mode 2:**

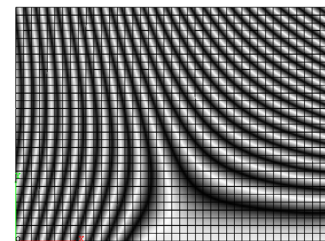
AF – EFSI



Finite Element Code

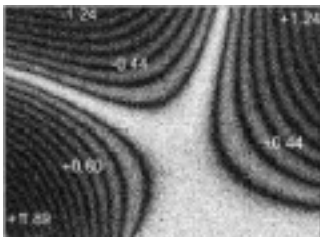


Damage Detection Code

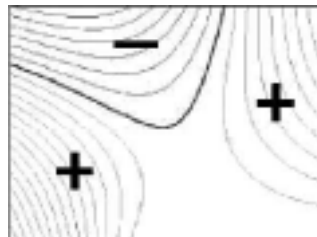


- **Mode 3:**

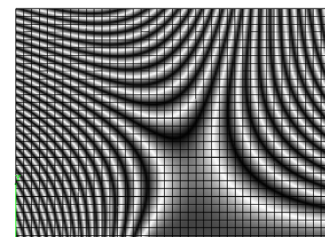
AF – EFSI



Finite Element Code

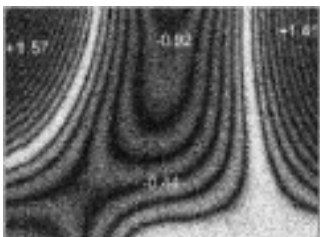


Damage Detection Code

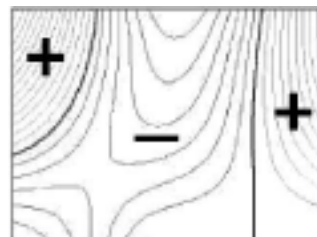


- **Mode 4:**

AF – EFSI



Finite Element Code



Damage Detection Code

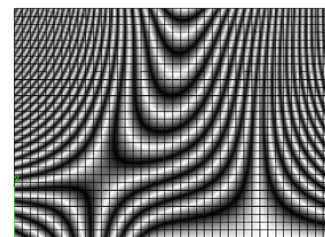
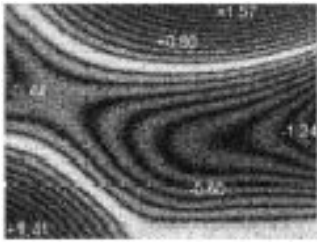


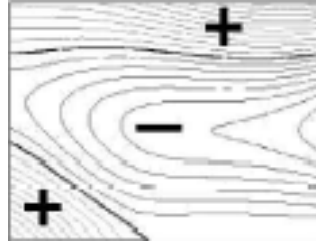
Fig. 5.5: Mode Shape contour plots using various methods for $a = 35$ mm crack.

- **Mode 5:**

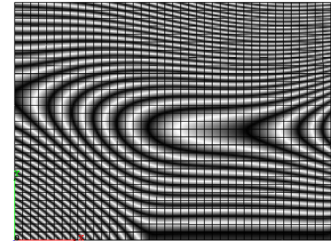
AF – EFSI



Finite Element Code

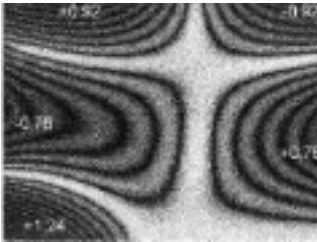


Damage Detection Code

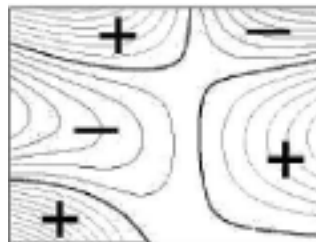


- **Mode 6:**

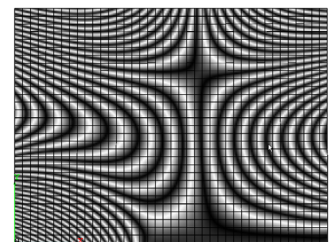
AF – EFSI



Finite Element Code

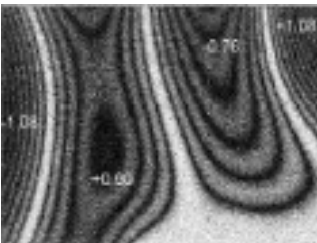


Damage Detection Code



- **Mode 7:**

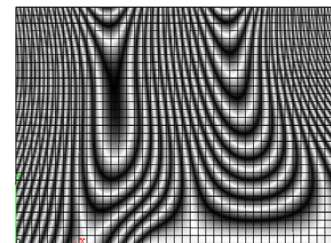
AF – EFSI



Finite Element Code

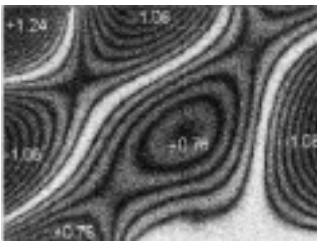


Damage Detection Code

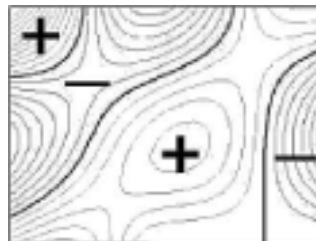


- **Mode 8:**

AF – EFSI



Finite Element Code



Damage Detection Code

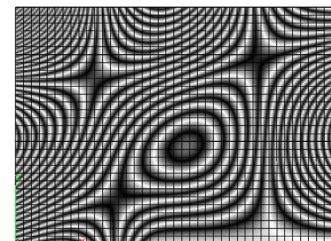


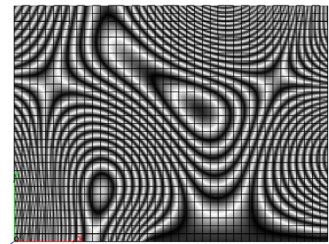
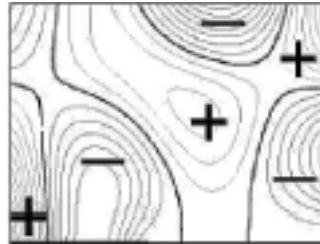
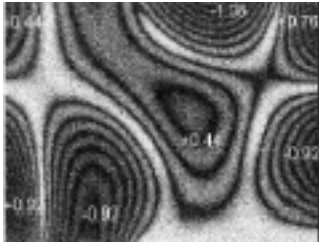
Fig. 5.5 (Continued): Mode Shape contour plots using various methods for a = 35 mm crack.

- **Mode 9:**

AF – EFSI

Finite Element Code

Damage Detection Code



- **Mode 10:**

AF – EFSI

Finite Element Code

Damage Detection Code

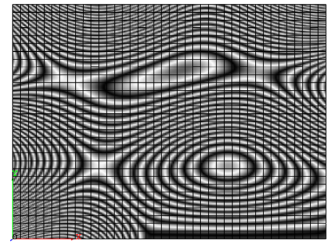
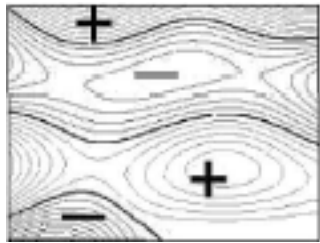
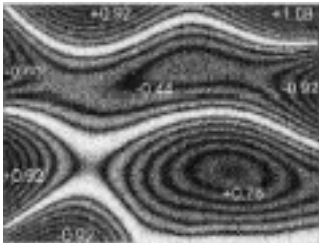
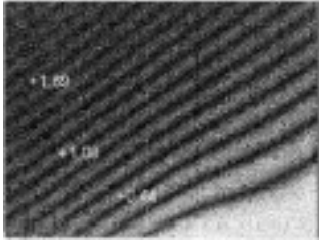


Fig. 5.5 (Concluded): Mode Shape contour plots using various methods for $a = 35$ mm crack.

- **Mode 1:**

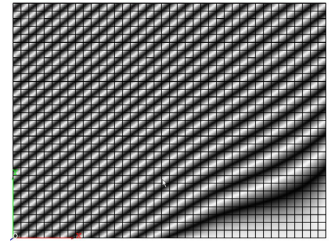
AF – EFSI



Finite Element Code

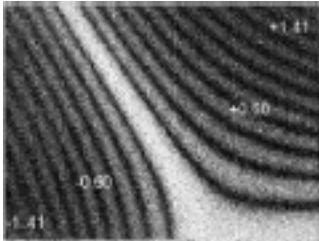


Damage Detection Code

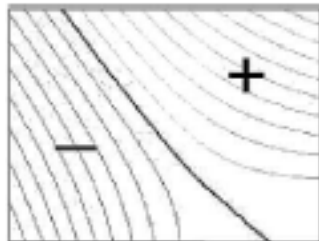


- **Mode 2:**

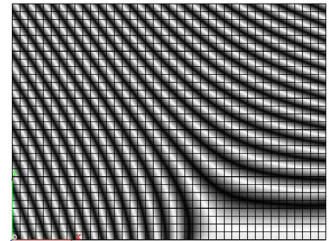
AF – EFSI



Finite Element Code

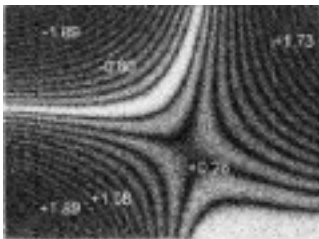


Damage Detection Code

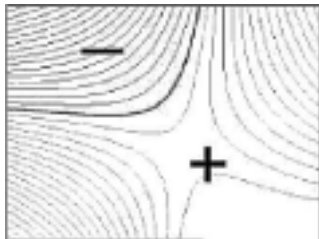


- **Mode 3:**

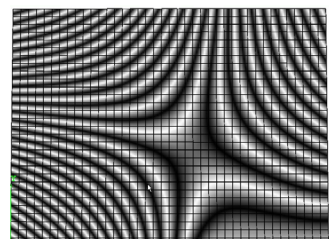
AF – EFSI



Finite Element Code

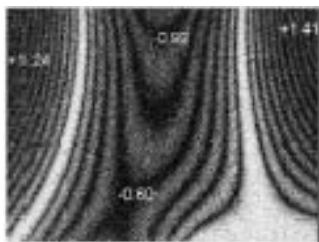


Damage Detection Code

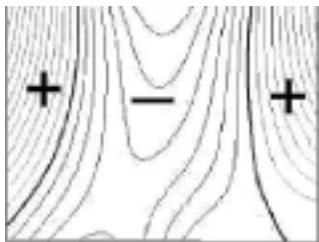


- **Mode 4:**

AF – EFSI



Finite Element Code



Damage Detection Code

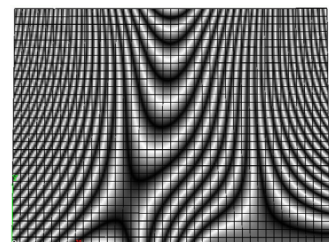
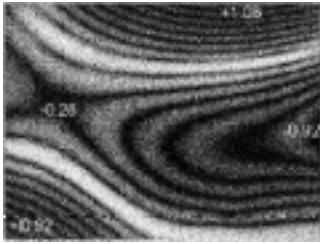


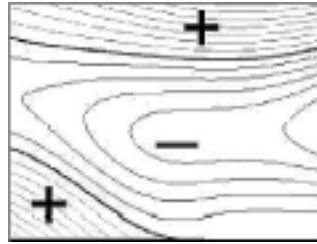
Fig. 5.6: Mode Shape contour plots using various methods for a = 50 mm crack.

- **Mode 5:**

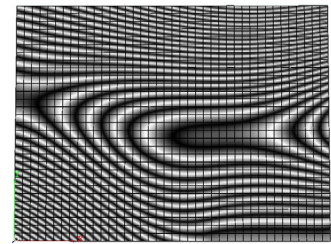
AF – EFSI



Finite Element Code

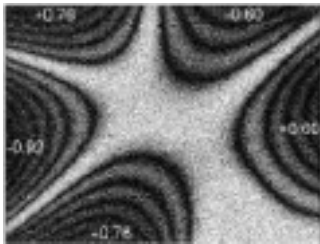


Damage Detection Code

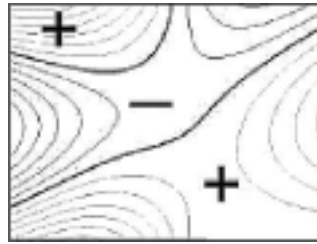


- **Mode 6:**

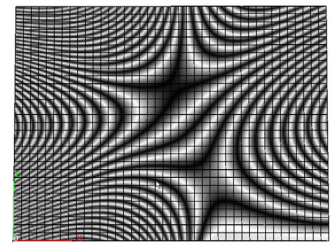
AF – EFSI



Finite Element Code

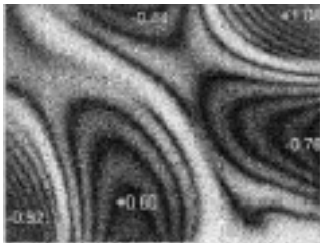


Damage Detection Code

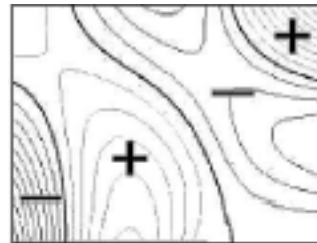


- **Mode 7:**

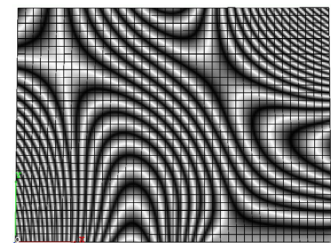
AF – EFSI



Finite Element Code

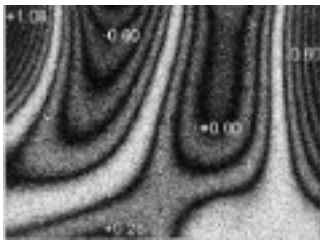


Damage Detection Code

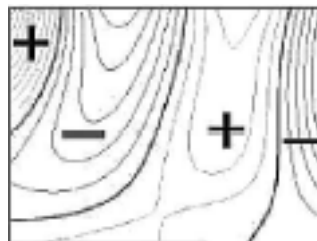


- **Mode 8:**

AF – EFSI



Finite Element Code



Damage Detection Code

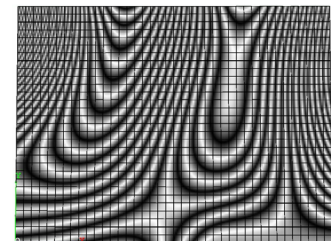
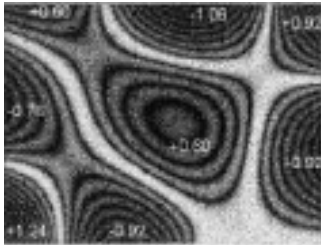


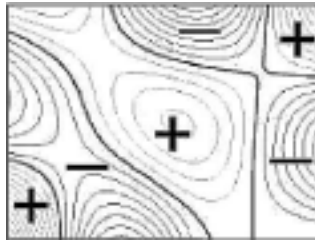
Fig. 5.6 (Continued): Mode Shape contour plots using various methods for a = 50 mm crack.

- **Mode 9:**

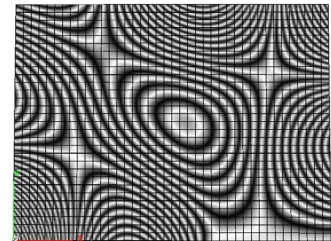
AF – EFSI



Finite Element Code

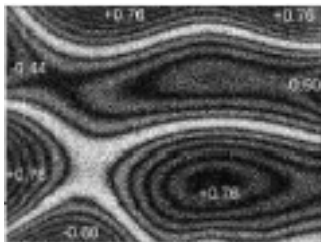


Damage Detection Code

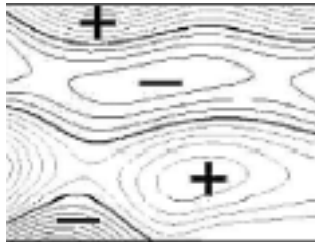


- **Mode 10:**

AF – EFSI



Finite Element Code



Damage Detection Code

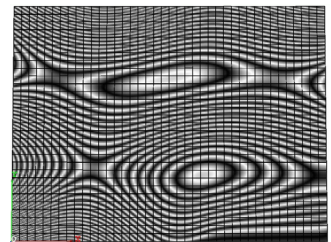
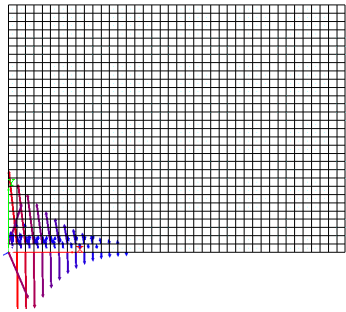
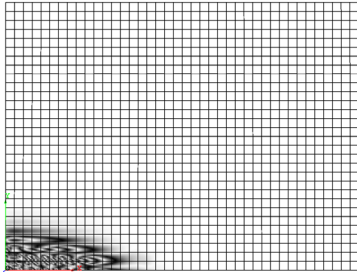


Fig. 5.6 (Concluded): Mode Shape contour plots using various methods for $a = 50$ mm crack.

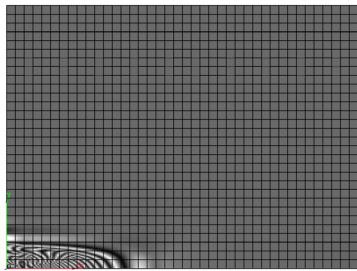
Mode 1:



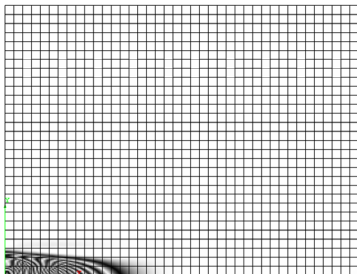
(a)



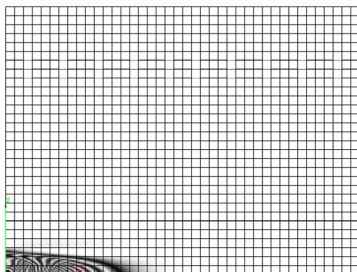
(b)



(c)



(d)



(e)

Mode 2

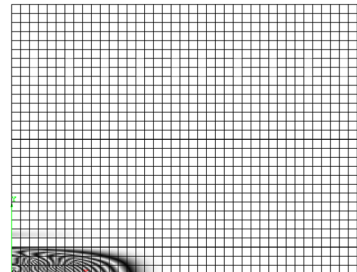
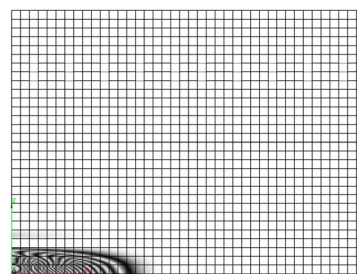
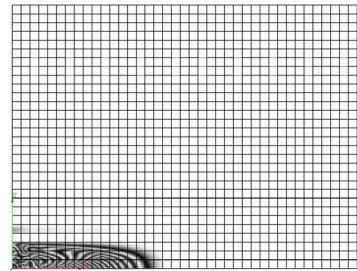
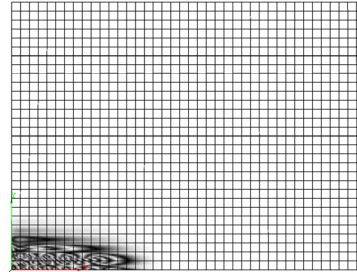
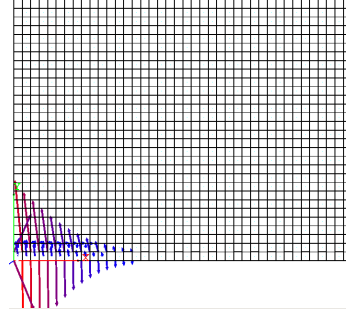
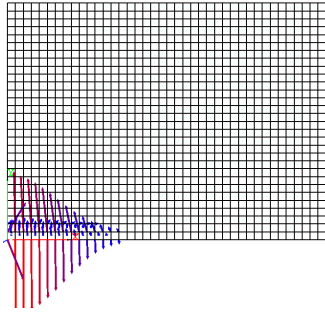
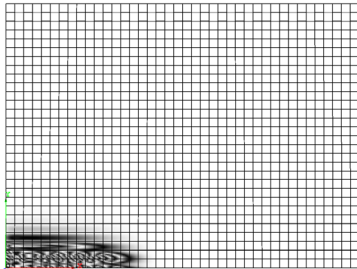


Fig. 5.7: Energy vector field plot, nodal damage intensity and damage defect Energy Parameter contour intensity for 20 mm boundary crack versus the 35 mm boundary crack.

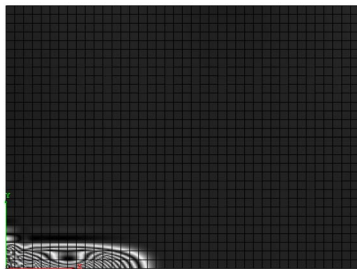
Mode 3:



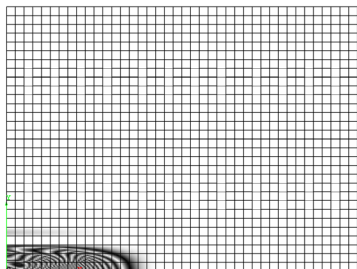
(a)



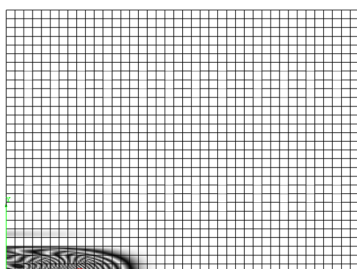
(b)



(c)



(d)



(e)

Mode 4:

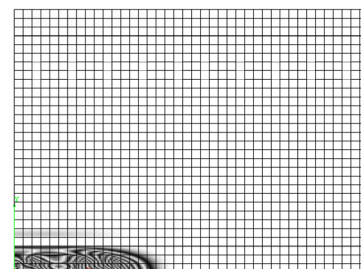
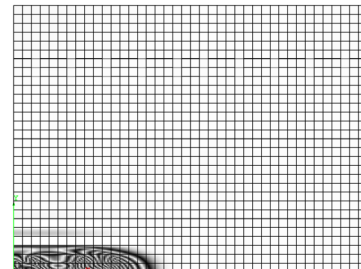
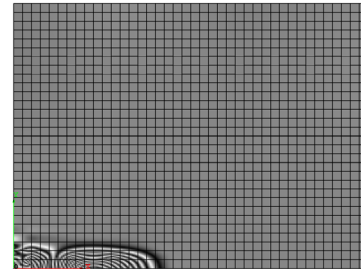
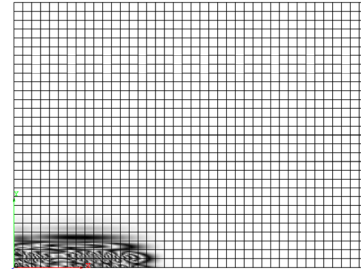
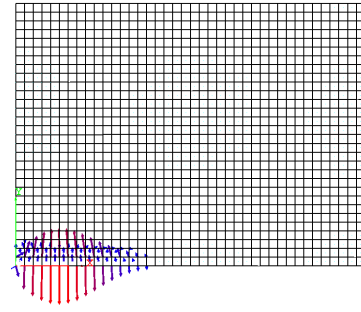
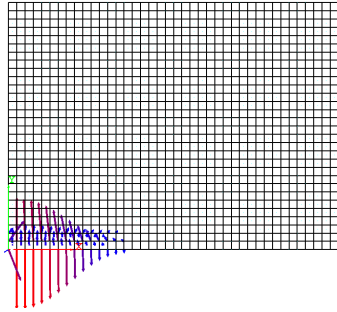
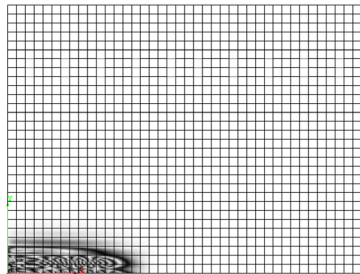


Fig. 5.7 (Continued): Energy vector field plot, nodal damage intensity and damage defect Energy Parameter contour intensity for 20 mm boundary crack versus the 35 mm boundary crack.

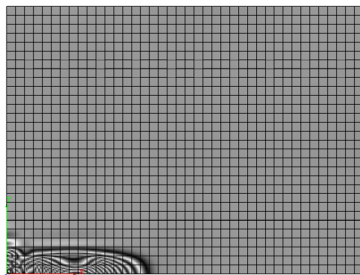
Mode 5:



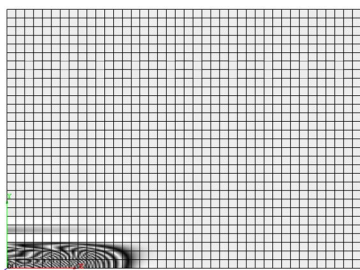
(a)



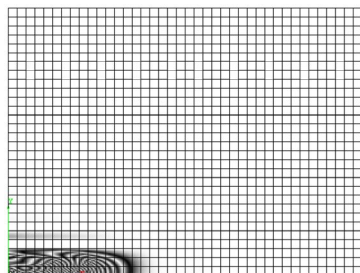
(b)



(c)



(d)



(e)

Mode 6:

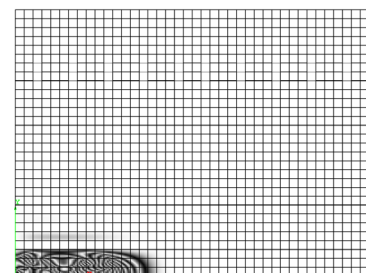
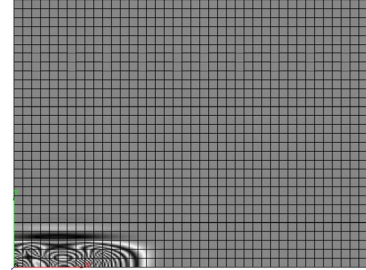
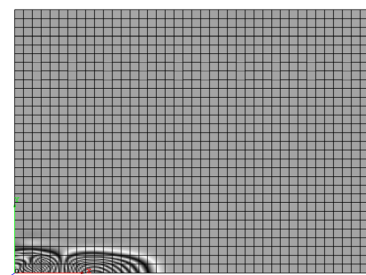
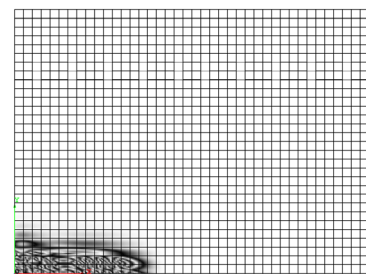
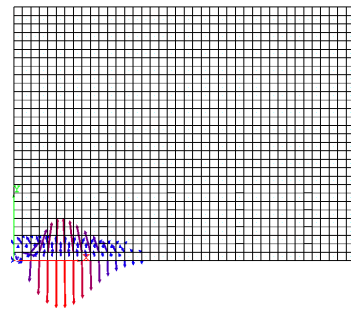
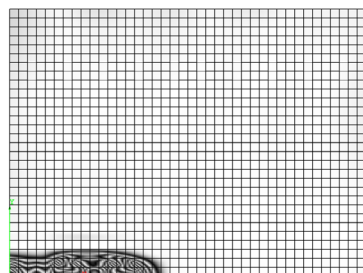
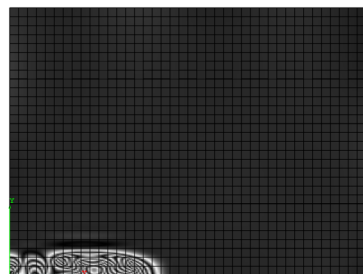
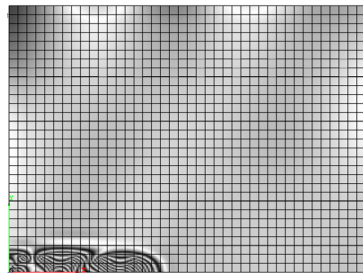
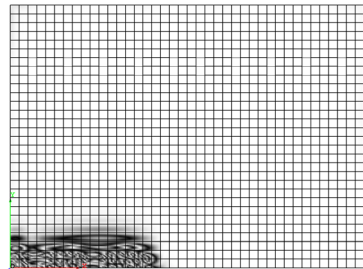
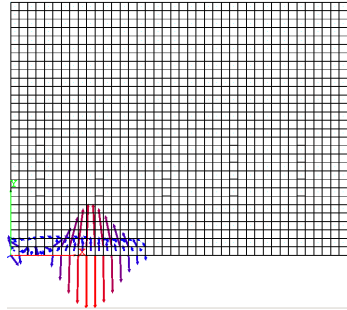
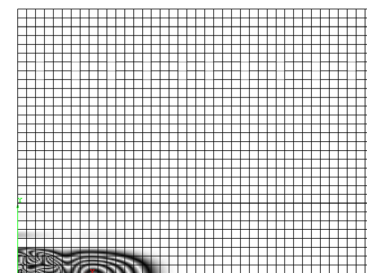
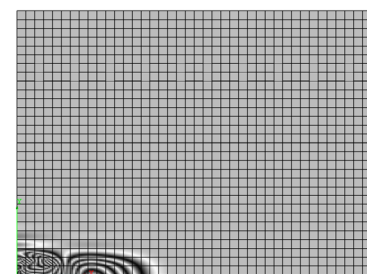
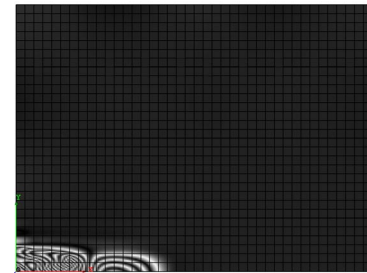
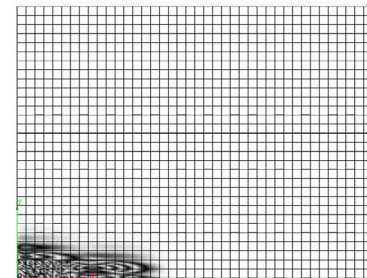
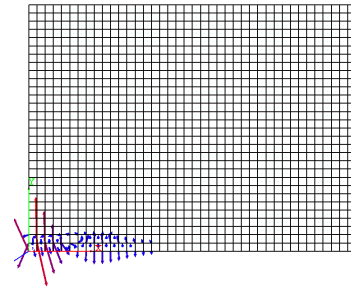


Fig. 5.7 (Continued): Energy vector field plot, nodal damage intensity and damage defect Energy Parameter contour intensity for 20 mm boundary crack versus the 35 mm boundary crack.

Mode 7:



Mode 8:



(a)

(b)

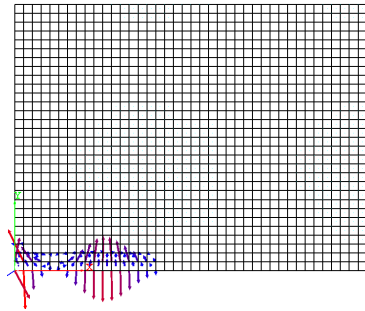
(c)

(d)

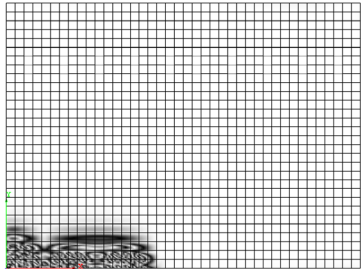
(e)

Fig. 5.7 (Continued): Energy vector field plot, nodal damage intensity and damage defect Energy Parameter contour intensity for 20 mm boundary crack versus the 35 mm boundary crack.

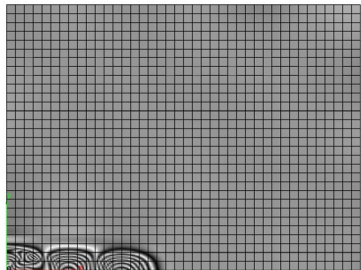
Mode 9:



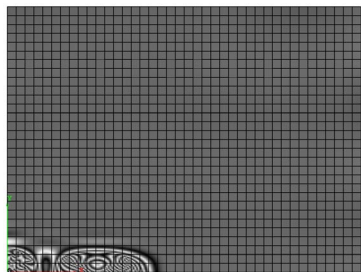
(a)



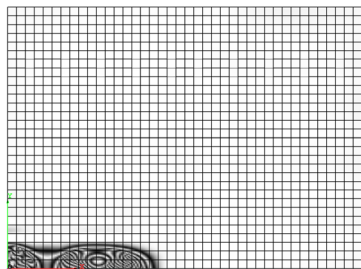
(b)



(c)



(d)



(e)

Mode 10:

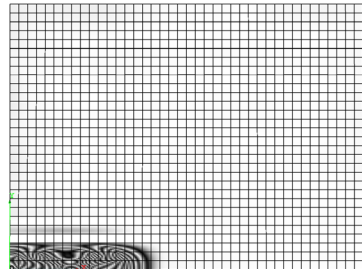
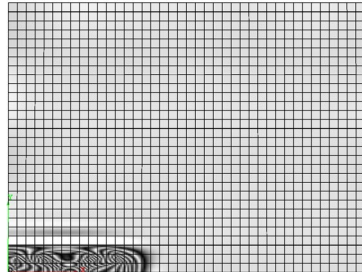
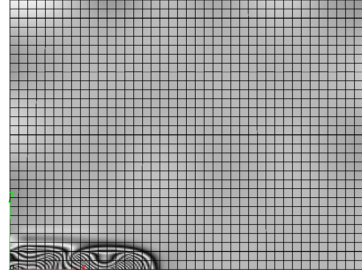
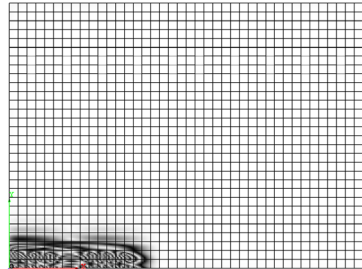
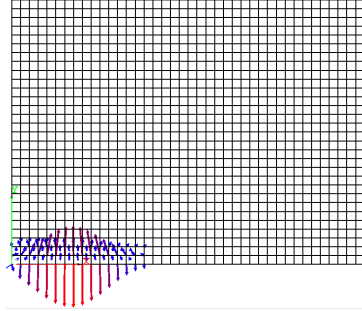
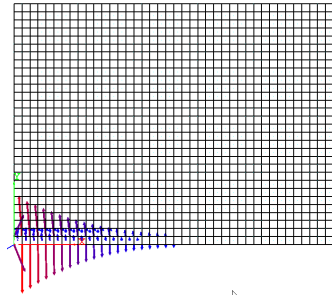
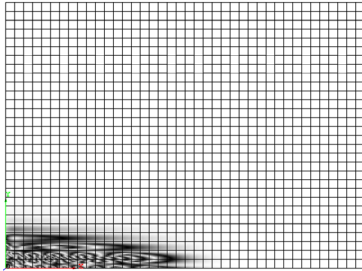


Fig. 5.7 (Concluded): Energy vector field plot, nodal damage intensity and damage defect Energy Parameter contour intensity for 20 mm boundary crack versus the 35 mm boundary crack.

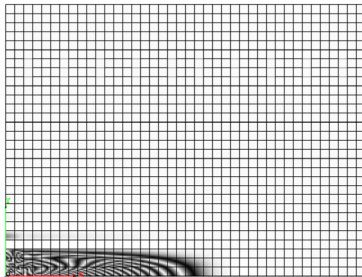
Mode 1:



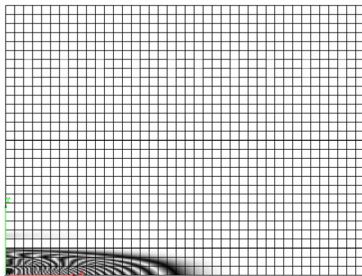
(a)



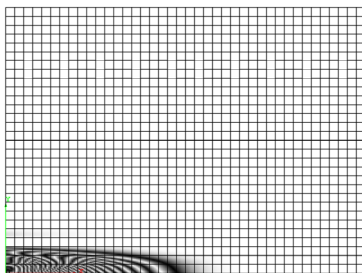
(b)



(c)



(d)



(e)

Mode 2:

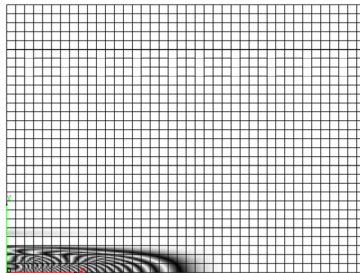
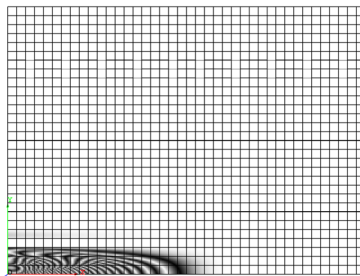
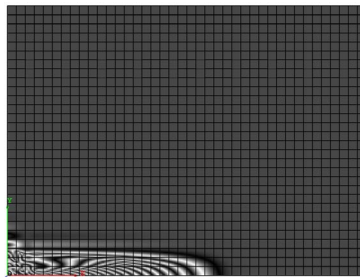
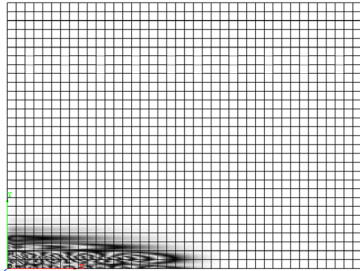
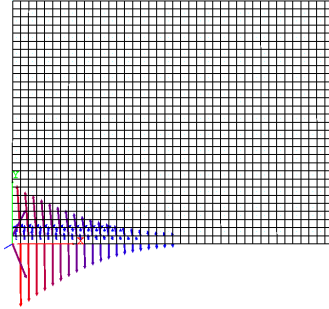
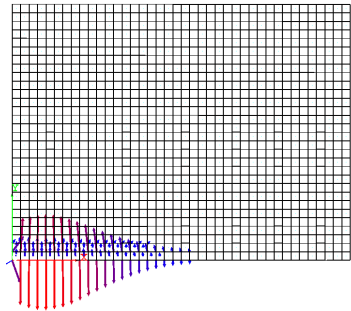
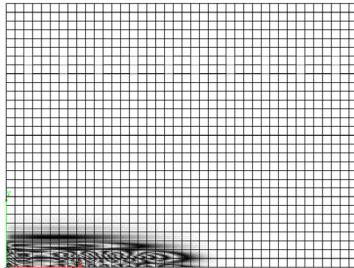


Fig. 5.8: Energy vector field plot, nodal damage intensity and damage defect Energy Parameter contour intensity for 20 mm boundary crack versus the 50 mm boundary crack.

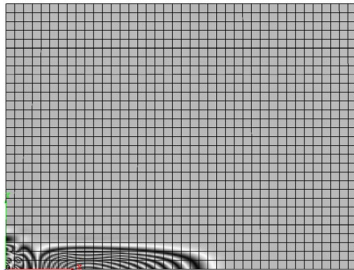
Mode 3:



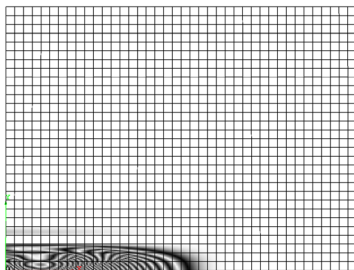
(a)



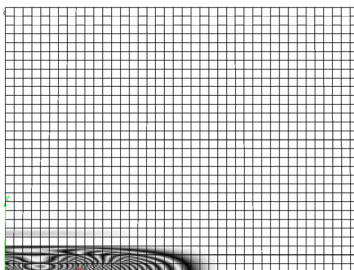
(b)



(c)



(d)



(e)

Mode 4:

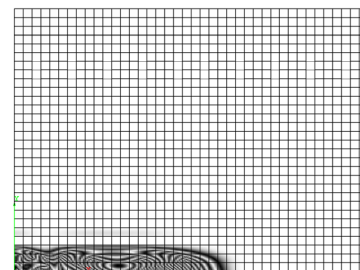
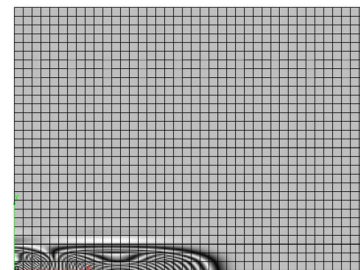
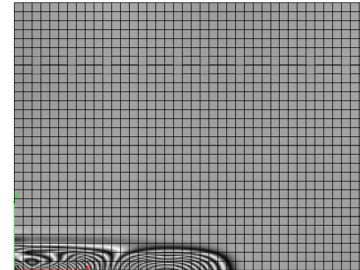
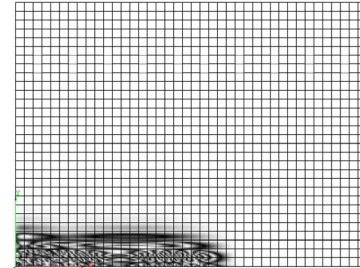
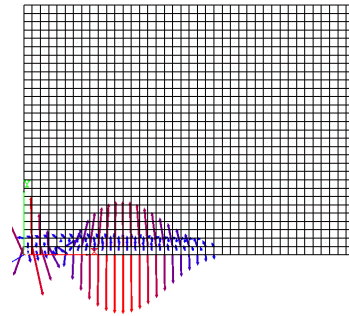
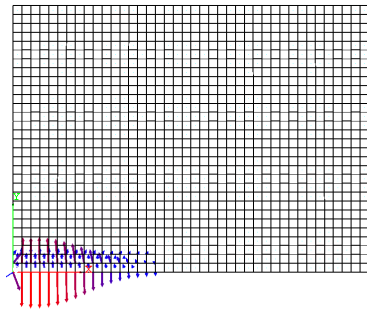
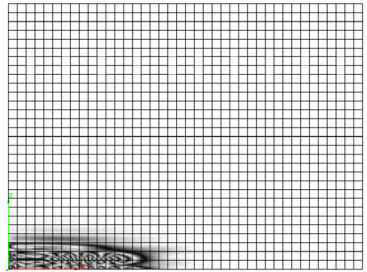


Fig. 5.8 (Continued): Energy vector field plot, nodal damage intensity and damage defect Energy Parameter contour intensity for 20 mm boundary crack versus the 50 mm boundary crack.

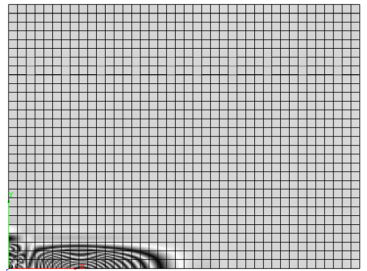
Mode 5:



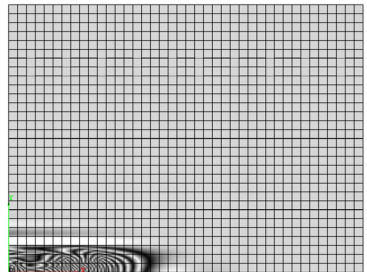
(a)



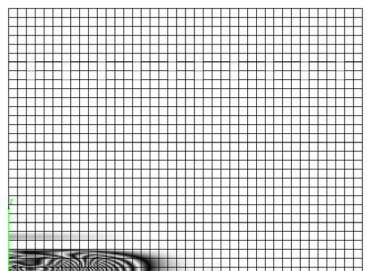
(b)



(c)



(d)



(e)

Mode 6:

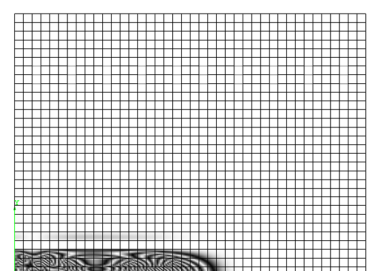
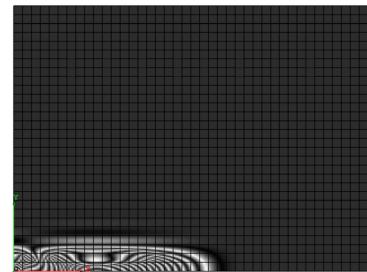
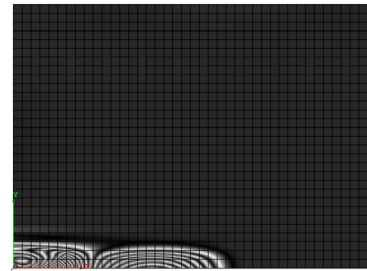
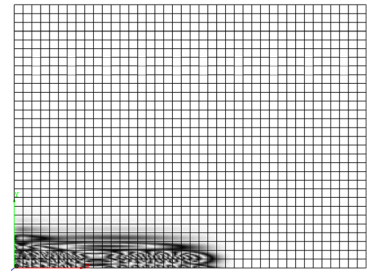
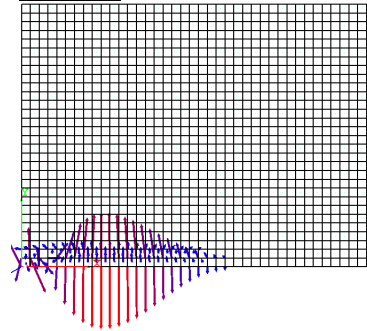
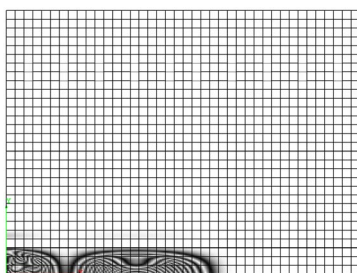
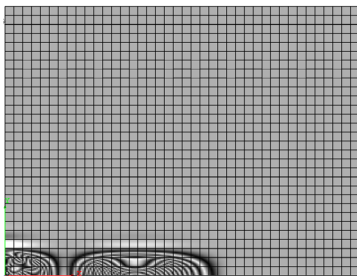
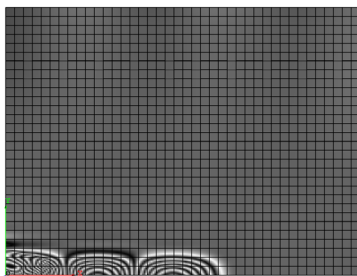
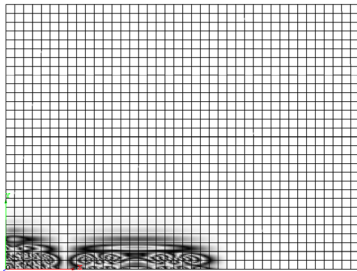
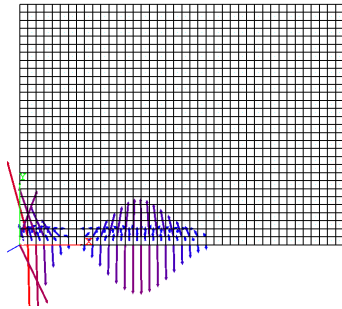
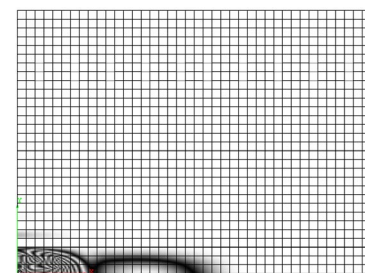
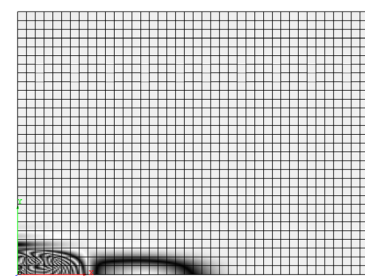
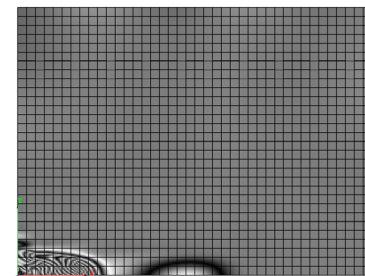
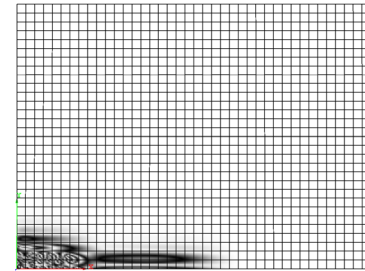
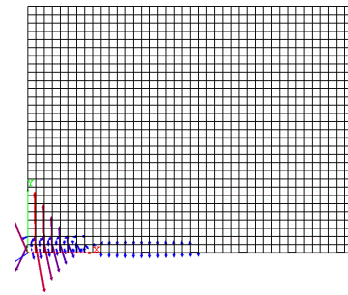


Fig. 5.8 (Continued): Energy vector field plot, nodal damage intensity and damage defect Energy Parameter contour intensity for 20 mm boundary crack versus the 50 mm boundary crack.

Mode 7:



Mode 8:



(a)

(b)

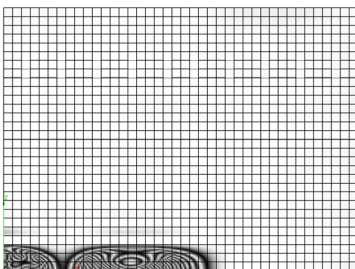
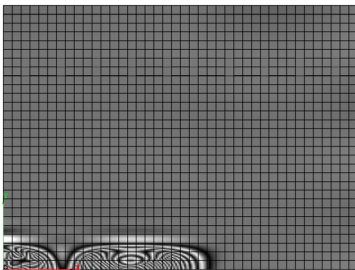
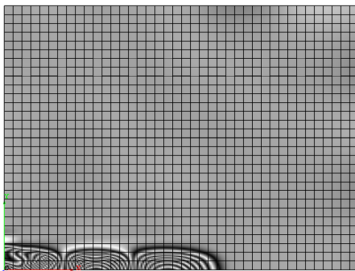
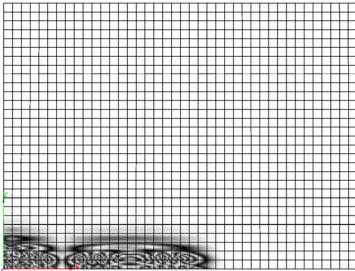
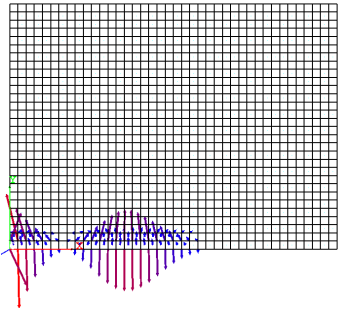
(c)

(d)

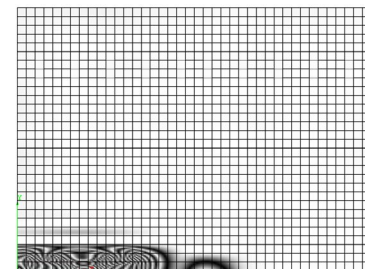
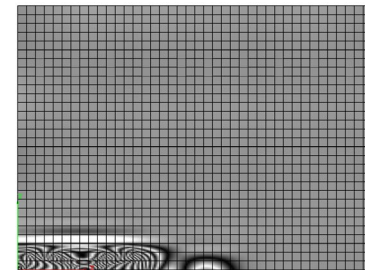
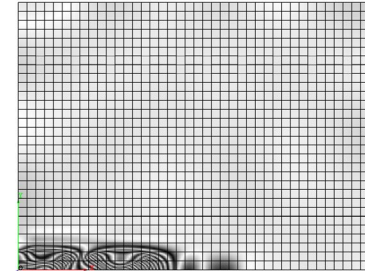
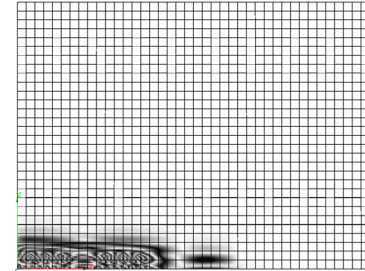
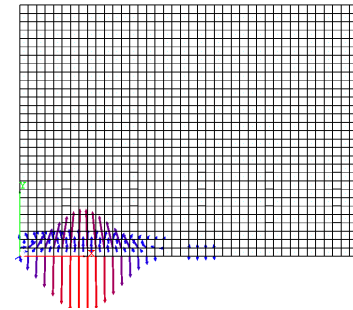
(e)

Fig. 5.8 (Continued): Energy vector field plot, nodal damage intensity and damage defect Energy Parameter contour intensity for 20 mm boundary crack versus the 50 mm boundary crack.

Mode 9:



Mode 10:



(a)

(b)

(c)

(d)

(e)

Fig. 5.8 (Concluded): Energy vector field plot, nodal damage intensity and damage defect Energy Parameter contour intensity for 20 mm boundary crack versus the 50 mm boundary crack.

5.5 Conclusions

A very important aspect that one has to consider from this chapter on full field investigation is that emerging new technologies such as ESPI and ESSI, are becoming available, which will provide all information and knowledge regarding the structural responses of complex configurations, (namely, frequencies, various modes, displacements, slope, etc.). The wealth of these accurate data can further be obtained without the harmful effects of the surrounding environment, in a short period of time and without human intervention or contact with the structural element under consideration. However, the full power of these experimental methods for detecting can only be realized if matched by robust detection/localization parameters that are able to reflect clear identifiable parts. For instance, using the contour plots only from the mode shapes, and comparing the patterns between the various cracked plate problems, it is seen that one can be easily misled in locating the damage, even if all the details of these modes are given. Therefore, we have emphasized before coming to the alternative viewpoint here by using the vector like indices which possess sufficiently general properties (both intensity and directions) to reveal crisp and distinct – persistent patterns for this purpose. In applications, the contour and vector plots for these were shown to be consistent across the entire spectrum of ten vibration modes considered.

6.0 SUMMARY AND CONCLUSIONS

6.1 Summary

The present study was conducted in conjunction with an ongoing research program dealing with the development of an integrated analytical/experimental NDE methodology for structural health/condition monitoring. The implementation of the overall procedure is formatted as a direct, global detection scheme. For this purpose the key ingredient is the use of a damage defect energy parameter, named the defect index. It provides the required sensitivity measure for detecting of localized damage/fault, on the basis of measured structural response signatures both static and dynamic.

From the viewpoint of practical utilization in structures, extensive testing for a valid assessment of any NDE technique becomes necessary, especially in view of the many complicating factors and the vast universe of damage detection scenarios that are likely to be encountered. To this end, the major problem addressed in this report has been concerned with the assessment of currently available experimental methods to be used in conjunction with the theoretical developments. With the further challenge stemming from the desire to search for damage locations over two-dimensional surfaces, two specific experimental investigations were conducted on the flexural/bending vibrations of plate. The first utilizes the more conventional approach in modal - testing, i.e., based on a coarse network of sensors (contacting accelerometers attached to the plate surface to measure vertical displacement amplitudes). This was conducted as part of the in-house developments at the funding agency (NASA Glenn

Center). The second investigation focused on results obtained from the newly emerging technologies, e.g., ESPI and ESSI, for full-field measurements.

6.2 Conclusion

Based on the presented results, the following conclusions may be made:

1. The spatial distribution of the damage defect energy parameter exhibited a distinctive pattern along the plate axes; i.e., calm with abrupt spikes or peaks after crossing the damage location. The simplicity of this intensity distribution renders the scheme very appealing when used in pattern recognition algorithms.
2. However, the use of only intensity (scalar – type) plots as in (1) above was found to be limited in applicability when false – alarm tests are included (e.g., due to environmental/operational changes but not actual defects. To this end, the complementing vector field plots were found to be essential, with their distinct directional properties (i.e., dissipation – driven vector field directions). The resulting multi-mode visualization scheme, i.e., intensity contours and vector plots, were shown to be very robust in all the cases, particularly in distinguishing true damage from false – alarm tests.
3. From the data of the experiments conducted by NASA and the processing of modal - testing results, the method for determining the damage using the above two visualization methods gave quite encouraging results. The method correctly identified a false – alarm case and damage sites in the two other true - defect scenarios were found. Despite the presence of a tremendous amount of variability/noise, in the experiments and with a rather limited number of points for measurements of the structural quantities (only vertical deflections were measured on a 8×8 grid). We specially identified the fact that *all* measurements for rotations were lacking contributed significantly to the inaccuracies and degradation of the current schemes ability to pinpoint damage sites.
4. As the culmination of the results in the report, the full – field measurements provided by the technique of ESPI experimentation, were utilized to show the full potential of the suggested NDE methodology. In particular, for all the ten modes of vibrations interrogated here for the difficult case of a one – edge supported plate with a propagating crack, both intensity contours and vector plots gave excellent results in all the cases.

6.3 Future Work

Collectively, the results obtained from work performed to date (including earlier theoretical and experimental studies), as well as the work in the present research will provide guidance in proposals for the three possible future work areas, including.

- (i) To conduct more extensive studies involving full – field measurements, also with static laboratory testing (to minimize noises possible).
- (ii) To demonstrate feasibility in field-testing. It requires a very carefully planned integration of hardware and software, for both calibration and portability requirements.
- (iii) A necessary and important corollary to item (ii) above concerns the inherent uncertainties implied in any experimental measurements on which the present (or any other) NDE scheme relies. This requires the use of sophisticated statistical tools for the ensuing statistical pattern recognition paradigm, i.e., involving extensive data compression, (as in principal component analysis, etc.), feature – extraction – and – discrimination (as emphasized in Chapters III to V here), and statistical modeling (for process control, regression, outlier detections, etc. Only then one can assure in a quantifiable manner that the measured changes in the response are indicative of true deteriorations/damages, as opposed to operational and/or environmental variabilities.

APPENDIX A

VARIABILITY/NOISE IN THE EXPERIMENTAL MEASUREMENTS

The measurements taken from the accelerometer for the plate modal displacements were checked for the presence of a pattern indicating the variation/noise. From the statistical analysis, using various methods as illustrated did not show any trend or a pattern but showed that the measurements were purely random noise.

A.1 Assumptions

- Each test in each mode is independent of the other.
- Relationship between modes is not considered. (Each mode is independent of the others.)
- Boundary and initial condition for both tests in each mode are the same, respectively.

A.2 Normality Test of Errors

- Find overall average error and standard deviation assuming normal distribution of points.
- Group the actual points from the test according to error.
- Use χ^2 test to confirm or reject normality assumption.

Random Tests

Chi Square Test Results			KS Test	
	P-value	Remarks	P-value	Remarks
Mode 1	0.505	Accept	< 0.01	Reject
Mode 2	0.015	Reject	< 0.01	Reject
Mode 3	0.853	Accept	0.054	Accept
Mode 4	0	Reject	< 0.01	Reject
Mode 5	0.035	Reject	< 0.01	Reject
Mode 6	0.381	Accept	< 0.01	Reject

A.3 Overall (System Wide) Displacement

Getting the difference in displacement (or error) between two tests for each point, and

- Run t – test to find
 - Mean and Standard deviation
 - Confidence interval at 95%, 99% levels.

	Mean	Std. Deviation	Confidence Interval	
			95%	99%
Mode 1	-0.78	0.744	(-0.99 , -0.57)	(-1.07 , -0.49)
Mode 2	-0.0818	0.2782	(-0.16 , -0)	(-0.19 , 0.025)
Mode 3	0.3138	0.2598	(0.239 , 0.388)	(0.214 , 0.413)
Mode 4	0.824	2.462	(0.117 , 1.531)	(-0.12 , 1.767)
Mode 5	-0.662	1.324	(-1.04 , -0.28)	(-1.17 , -0.16)
Mode 6	-1.27	8.62	(-3.75 , 1.2)	(-4.58 , 2.03)

A.4 Overall (System Wide) Displacement Using Relative Error

- Relative error = Error for each point/average magnitude.
- Defined as “Average magnitude” is defined as the absolute value for each displacement, then adding together and dividing by 2.

	Mean	Std. Deviation	Confidence Interval	
			95%	99%
Mode 1	-0.02997	0.0288	(-0.03821 , 0.0217)	(-0.041 , -0.01893)
Mode 2	-0.1382	0.3816	(-0.2478 , -0.0286)	(-0.2844 , 0.008)
Mode 3	0.0518	0.0711	(0.0314 , 0.0723)	(0.0246 , 0.0791)
Mode 4	0.1903	0.4014	(0.075 , 0.3056)	(0.0365 , 0.3441)
Mode 5	-0.1253	0.4038	(-0.2413 , -0.0093)	(-0.28 , 0.0294)
Mode 6	-0.19	1.262	(-0.552 , 0.173)	(-0.673 , 0.294)

A.5.1 Regression analysis of errors versus average magnitude (Linear equation)

- Linear Error = f (average magnitude)
- Linear Graph $y = c + (m x)$ where y = error in experiment and x = average magnitude as shown in Fig. A.1.

	c	m	R - sq (%)
mode 1	0.176	-0.0368	45.4
mode 2	-0.189	0.0407	7.3
mode 3	0.171	0.015	16.5
mode 4	-0.895	0.487	12
mode 5	-1.39	0.029	8.5
mode 6	0.08	-0.202	0.6

A.5.2 Regression analysis of errors versus average magnitude (non-linear—quadratic equation)

- Non – Linear Error = f (average magnitude)
- Linear Graph $y = f(x)$ where y = error in experiment and x = average magnitude as shown in Fig. A.2

Regression Analysis Quadratic Curve Graph ($y = c + b x + a x^2$)

y = error in the experiment
 x = average magnitude

	c	b	a	R - sq (%)
mode 1	-2.00E-03	-1.87E-02	-3.41E-04	46.3
mode 2	-2.80E-01	0.13024	-1.44E-02	9.9
mode 3	4.82E-02	5.45E-02	-1.82E-03	23.7
mode 4	2.22808	-1.8516	0.332162	24.9
mode 5	-2.4221	0.14728	-2.40E-03	21.6
mode 6	-1.6789	0.303721	-2.94E-02	0.9

The Higher the value of R-sq the better the result

Fig. A.1: Linear Regression analysis of errors versus average magnitude.

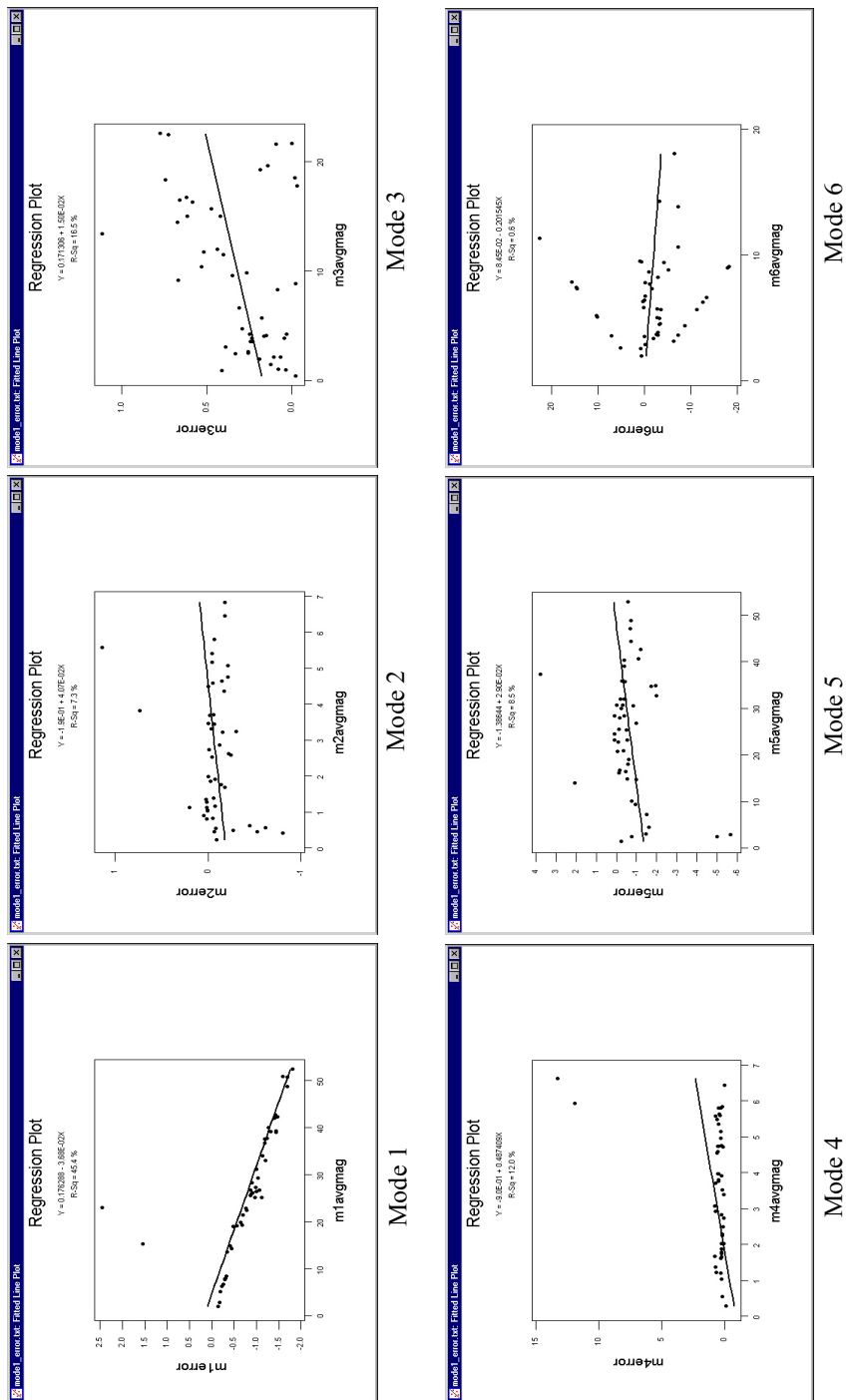
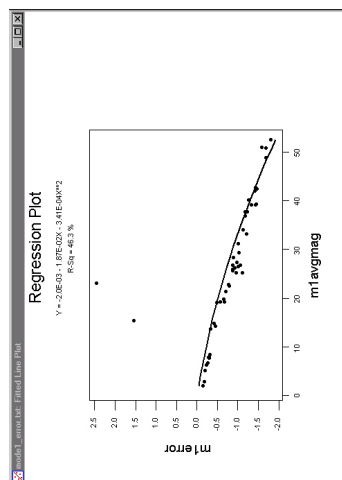
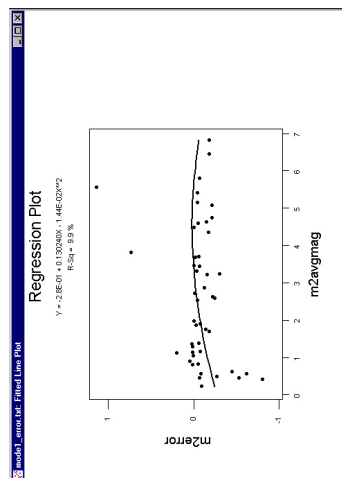


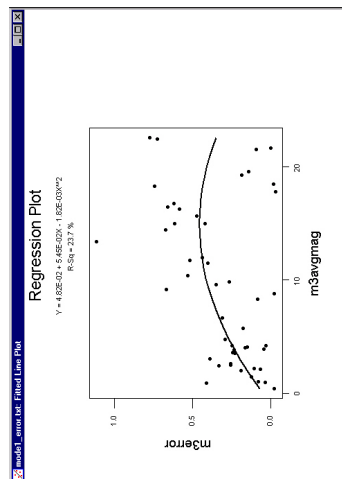
Fig. A.2: Non-Linear Regression analysis of errors versus average magnitude.



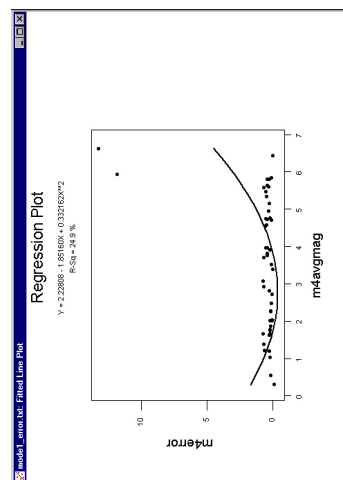
Mode 1



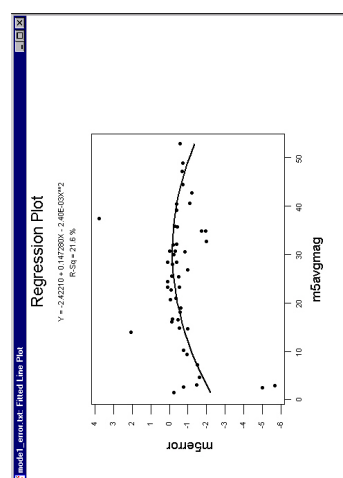
Mode 2



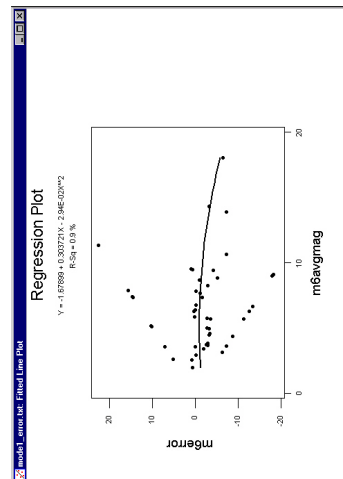
Mode 3



Mode 4



Mode 5



Mode 6

A.5.3.1 Regression analysis of error versus distance from fixed end

- Error = y (horizontal distance to fixed end)
- The horizontal distance to the fixed end is up to the third column. Each side from the fixed end is treated individually and combined.
- Linear Graph $y = c + (m x)$ where y = error in experiment and x = horizontal distance from fixed end as shown in Figs. A.3, A.4 and A.5.

Left Distance from fixed end				Right Distance from fixed end			
	c	m	R - sq (%)		c	m	R - sq (%)
mode 1	-0.048	-0.225	4	mode 1	0.044	-0.462	72
mode 2	-0.043	0.0279	0.5	mode 2	0.0327	-0.0836	12.1
mode 3	-0.053	0.214	40.6	mode 3	-0.0532	0.13	31
mode 4	-0.48	1.01	5.3	mode 4	-0.022	0.136	38.6
mode 5	0.655	-0.538	7.4	mode 5	0.4797	-0.5816	20.5
mode 6	-3.337	0.428686	0.3	mode 6	-1.9429	-0.1588	0

Combined Distance from fixed end			
	c	m	R - sq (%)
mode 1	-0.0023	-0.3436	14
mode 2	-0.0052	-0.0279	0.7
mode 3	-0.0053	0.1717	31.4
mode 4	-0.025	0.574	3.2
mode 5	0.567	-0.5599	11.2
mode 6	-2.64	0.13	0

Fig. A.3: Regression analysis of error versus distance from fixed end Left Distance from Fixed End – Linear Equation

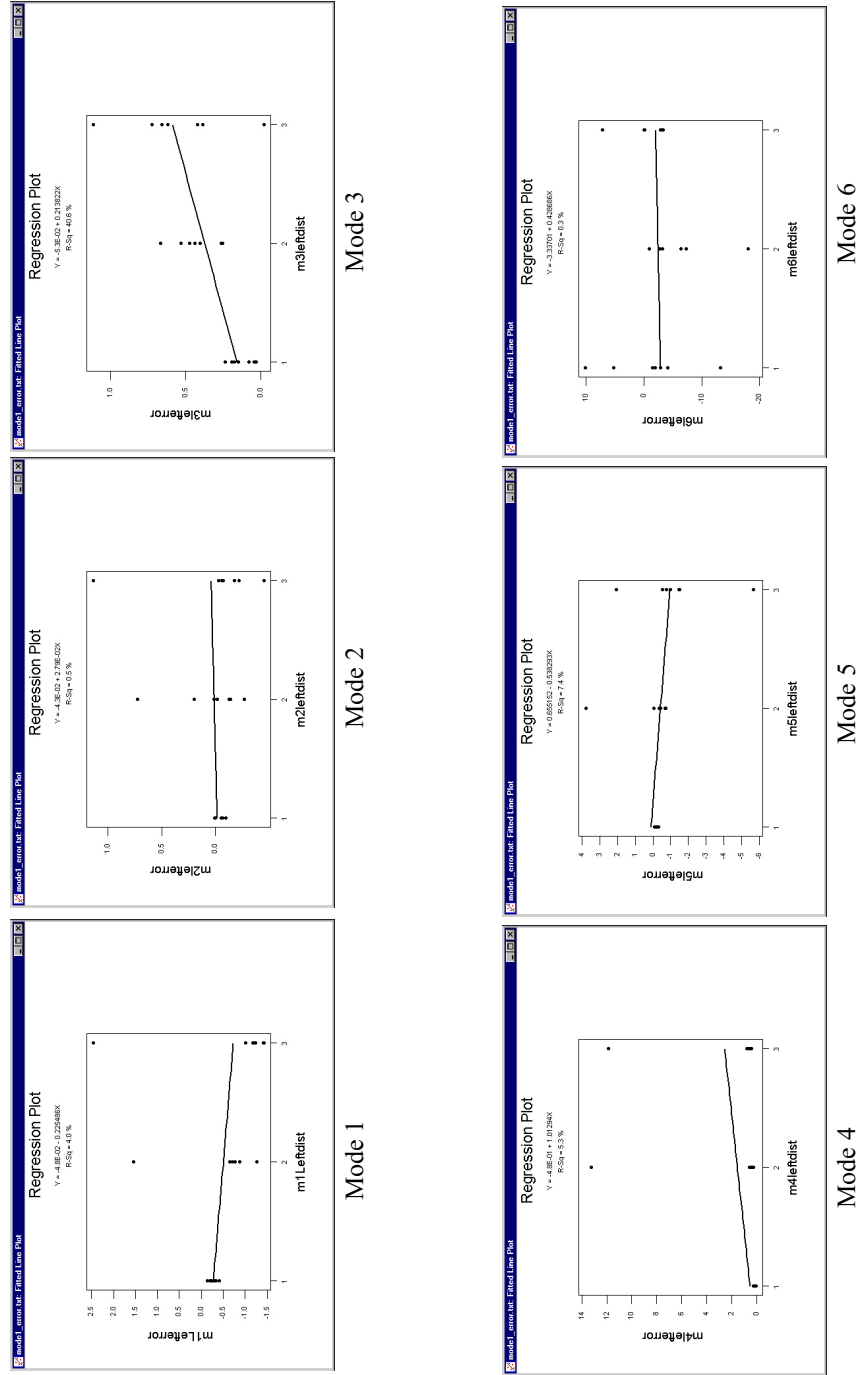


Fig. A.4: Regression analysis of error versus distance from fixed end Right Distance from Fixed End – Linear Equation

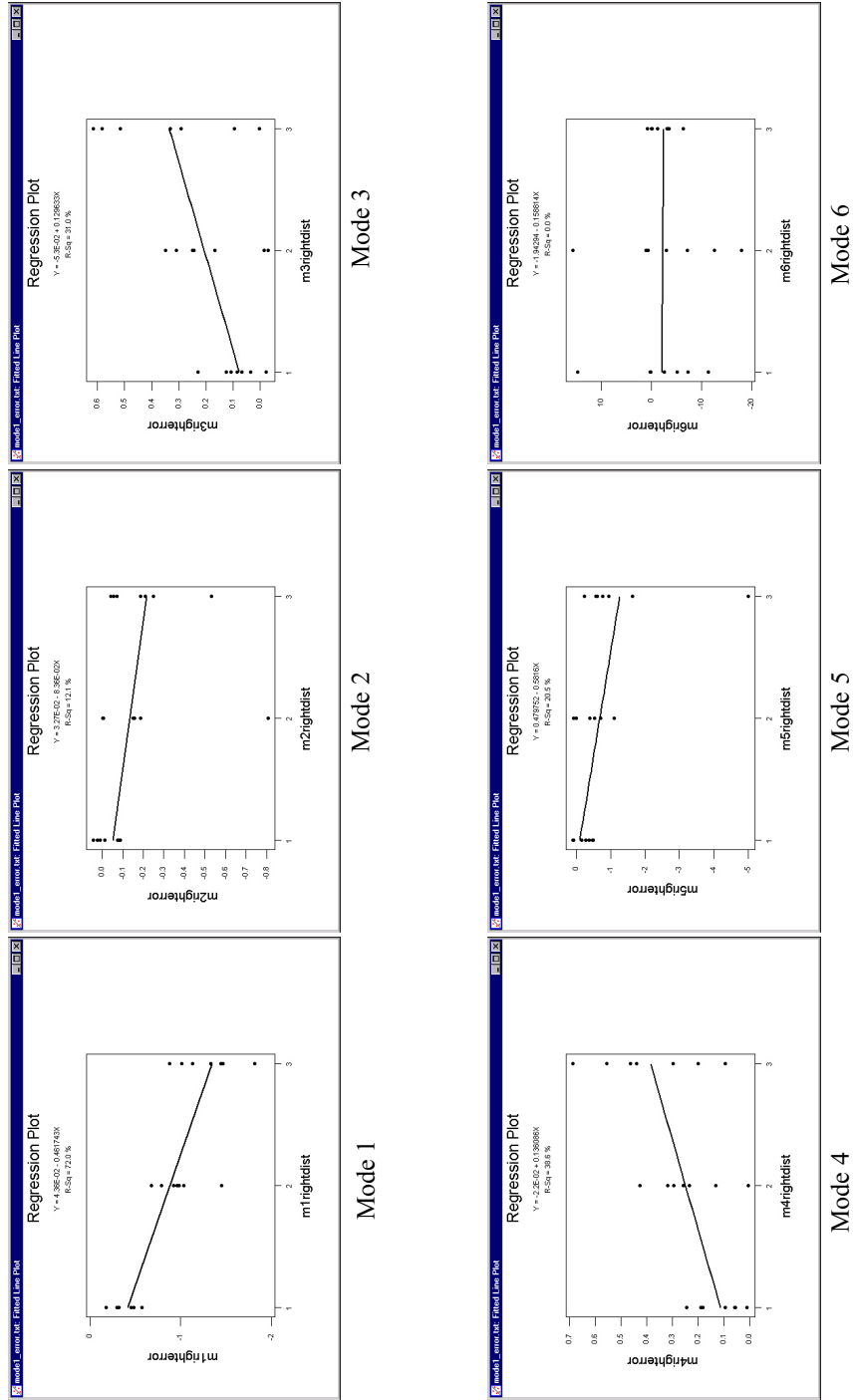
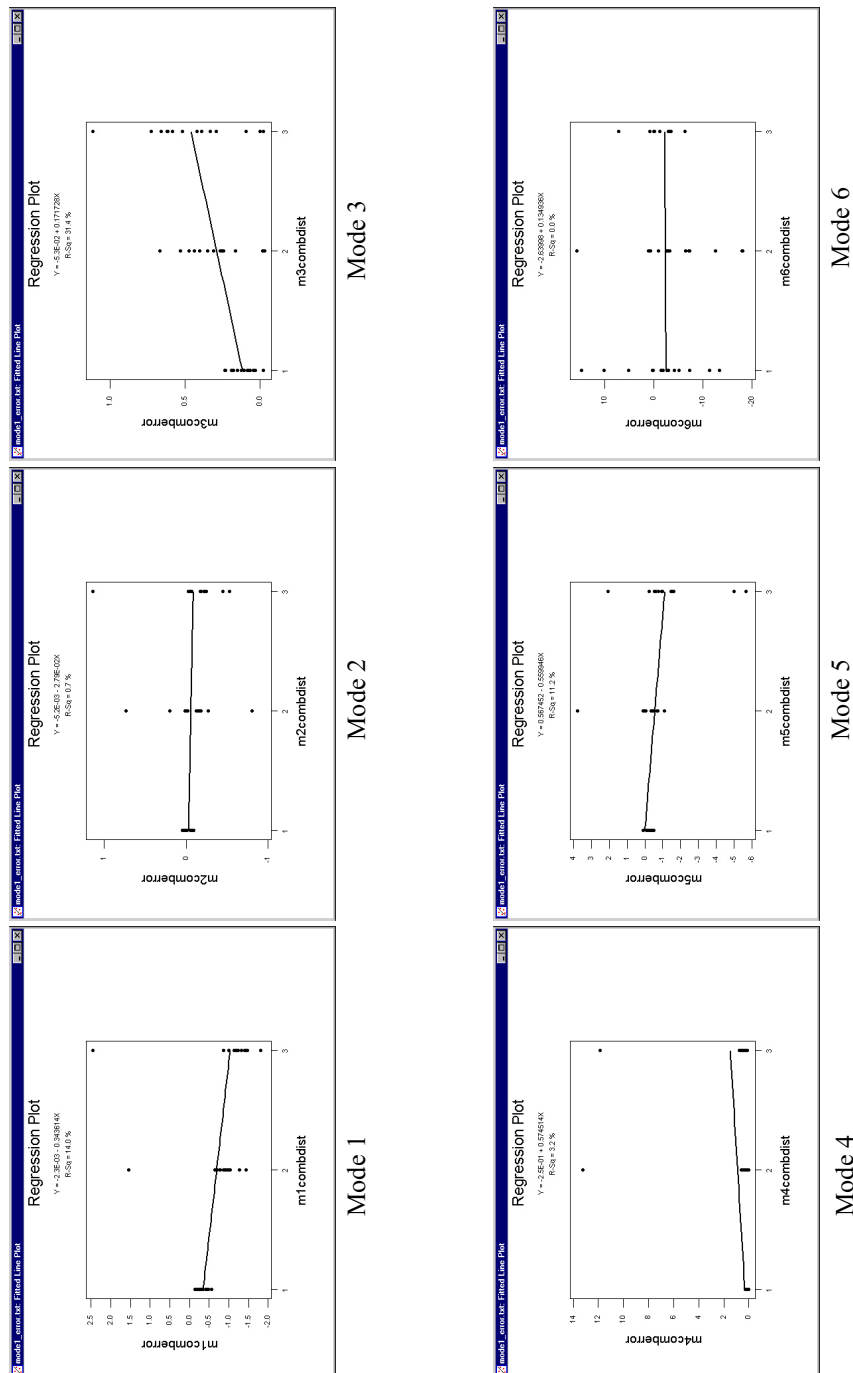


Fig. A.5: Regression analysis of error versus distance from fixed end Combined Distance from Fixed End— Linear Equation



A.5.3.2 Regression analysis of error versus distance from fixed end (Quadratic Graph)

- Error = y (horizontal distance to fixed end)
- The horizontal distance to the fixed end is up to the third column. Each side from the fixed end is treated individually and combined.
- Quadratic Graph $y = f(x)$ where y = error in experiment & x = horizontal distance from fixed end as shown in Fig. A.6, A.7 and A.8

Left Distance from fixed end					Right Distance from fixed end				
	c	b	a	R - sq (%)		c	b	a	R - sq (%)
mode 1	0.0239	-0.3120	0.0216	4.0000	mode 1	0.5080	-1.0190	0.1393	74.1000
mode 2	-0.2500	0.2777	-0.0625	1.3000	mode 2	0.2963	-0.3999	0.0791	15.7000
mode 3	-0.3500	0.5732	-0.0898	43.0000	mode 3	0.0696	-0.0177	0.0368	31.9000
mode 4	-4.1144	5.3797	-1.0917	7.4000	mode 4	0.0327	0.0698	0.0166	38.8000
mode 5	-2.2892	2.9949	-0.8833	14.0000	mode 5	-0.7700	0.9134	-0.3737	23.3000
mode 6	13.8175	-20.1560	5.1464	17.1000	mode 6	3.2319	-6.3686	1.5525	1.0000

Combined Distance from fixed end				
	c	b	a	R - sq (%)
mode 1	0.2660	-0.6655	0.0805	14.3000
mode 2	0.0225	-0.0611	0.0083	0.7000
mode 3	-0.0140	0.2777	-0.0265	31.6000
mode 4	-2.0408	2.7248	-0.5376	4.1000
mode 5	-1.5276	1.9541	-0.6285	15.9000
mode 6	8.5247	-13.2627	3.3494	5.5000

Fig. A.6: Regression analysis of error versus distance from fixed end – Quadratic Equation

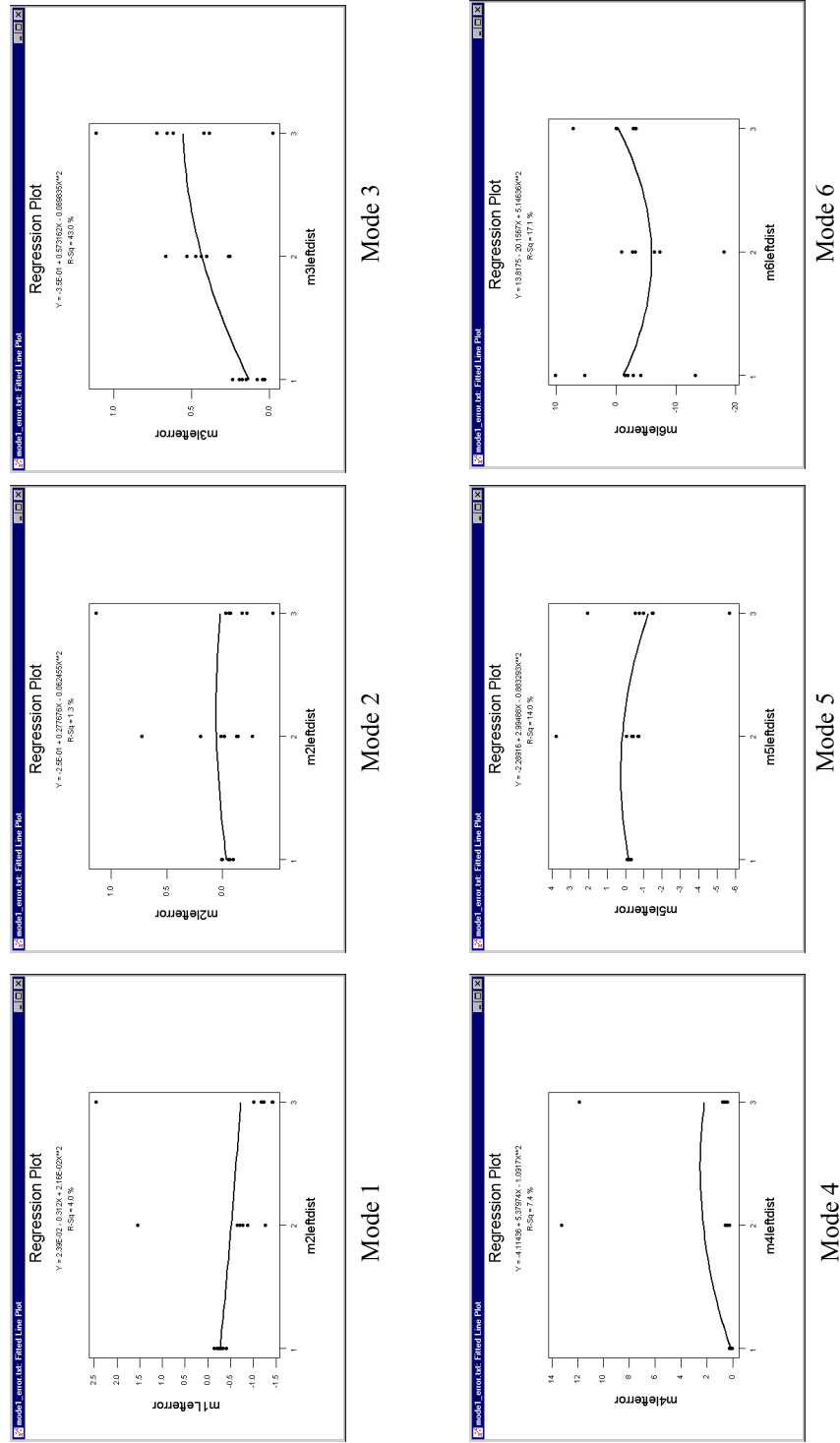


Fig. A.7: Regression analysis of error versus distance from fixed end Right Distance from Fixed End – Quadratic Equation

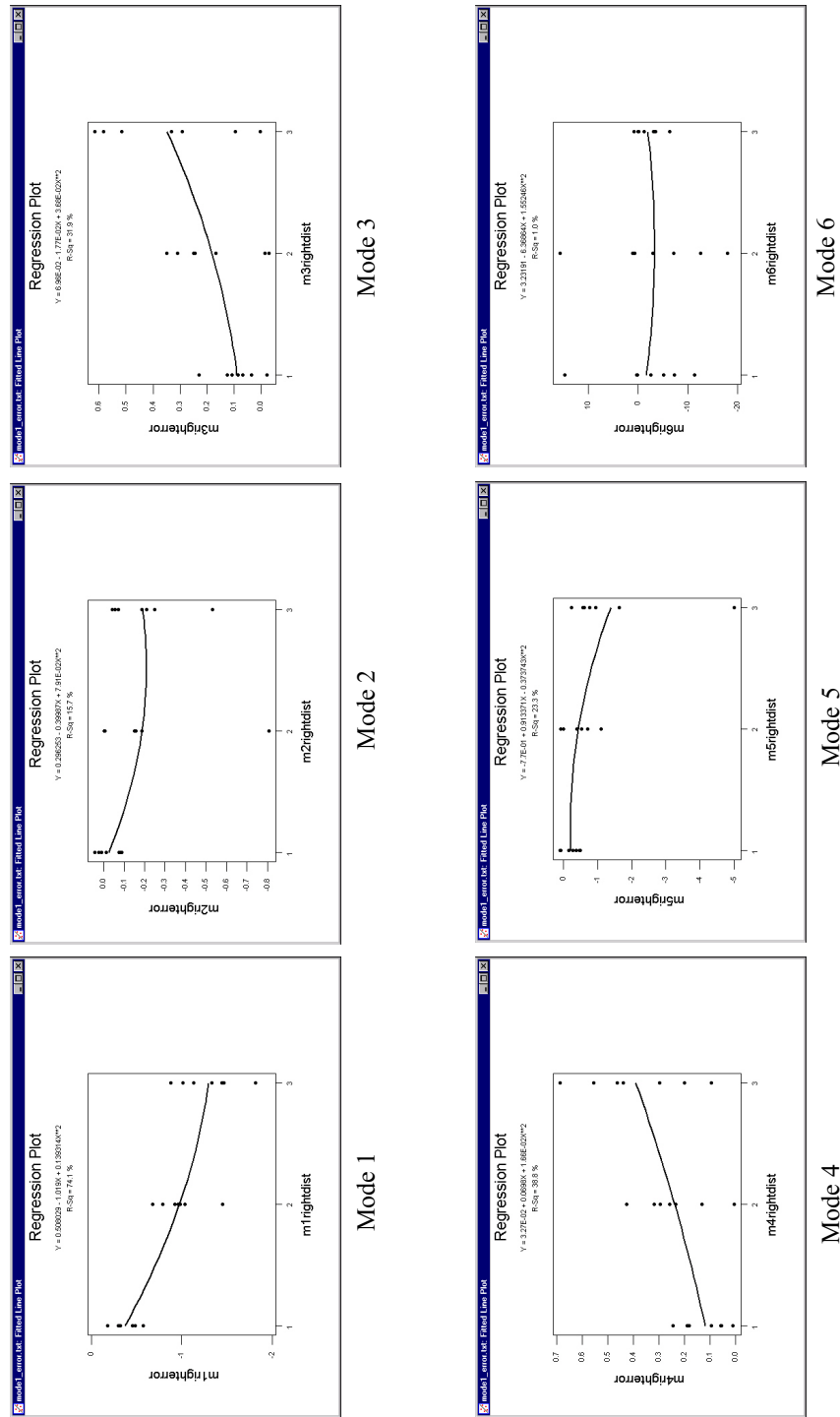
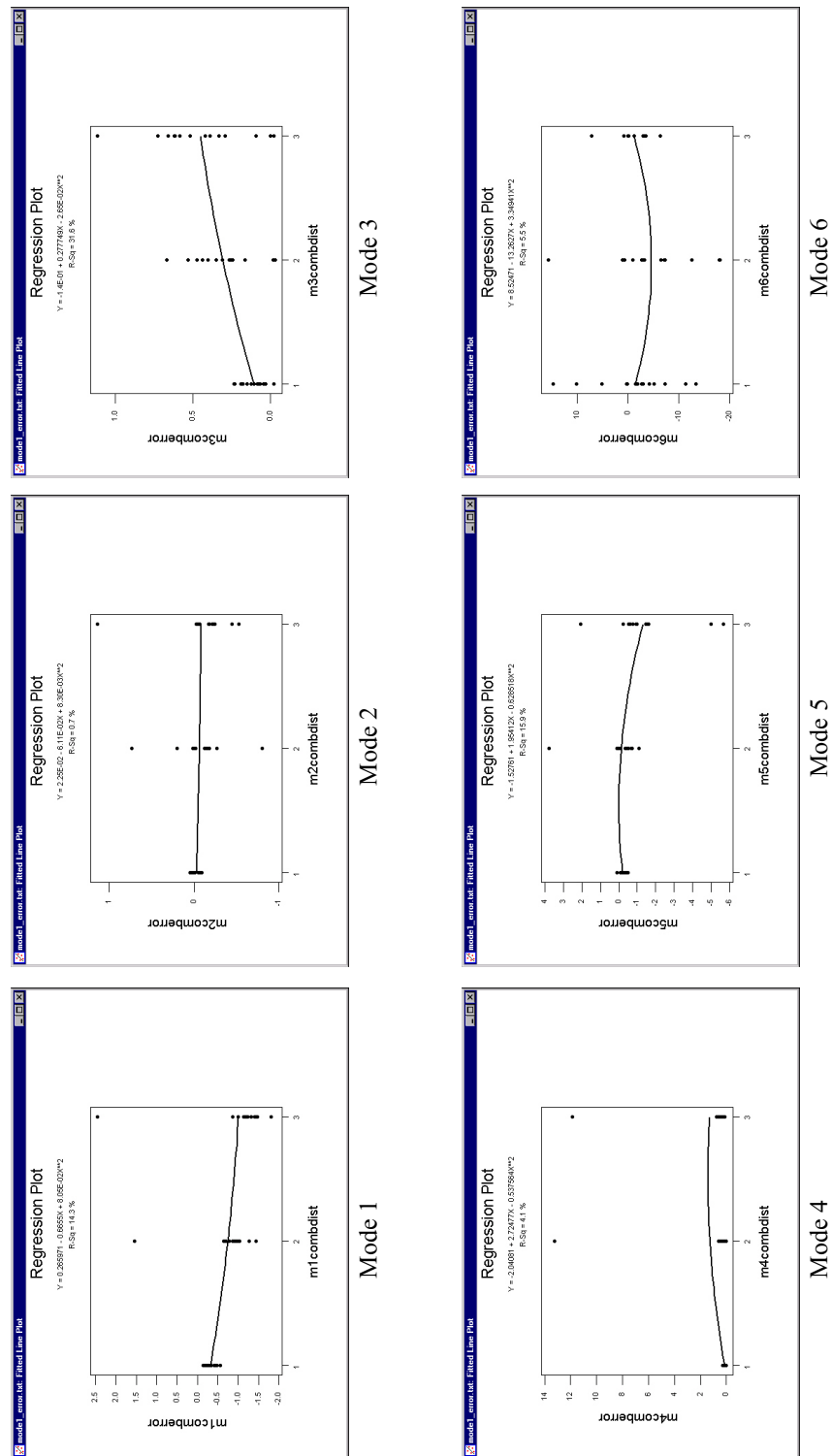


Fig. A.8: Regression analysis of error versus distance from fixed end Combined Distance from Fixed End – Quadratic Equation



A.5.4 Regression analysis of difference (in absolute values) in errors versus distance for each point

- Getting errors for each point. For each point, the difference of errors (using absolute values) from the adjacent points for one space and two spaces, for every point up to the third column.
- Run regression to see continuity of change of errors.

Diff. in errors = z (distance from point)

Left Distance from fixed end				Right Distance from fixed end				Combined Distance from fixed end			
	c	m	R - sq (%)		c	m	R - sq (%)		c	m	R - sq (%)
mode 1	-0.048	-0.225	4	mode 1	0.0436	-0.4617	72	mode 1	-0.0023	-0.3436	14
mode 2	-0.043	0.079	0.5	mode 2	0.0327	-0.0836	12.1	mode 2	-0.00523	-0.0279	0.7
mode 3	-0.053	0.2138	40.6	mode 3	-0.053	0.1296	31	mode 3	-0.053	0.1717	31.4
mode 4	-0.48	1.013	5.3	mode 4	-0.022	0.13608	38.6	mode 4	-0.25	0.5745	3.2
mode 5	0.655	-0.538	7.4	mode 5	0.4797	-0.5816	20.5	mode 5	0.597	-0.5599	11.2
mode 6	-3.337	0.42868	0.3	mode 6	-1.9429	-0.1588	0	mode 6	-2.63998	0.1349	0

Fig. A.9: Regression analysis of difference (in absolute values) in errors versus distance for each point Left Distance from Fixed End

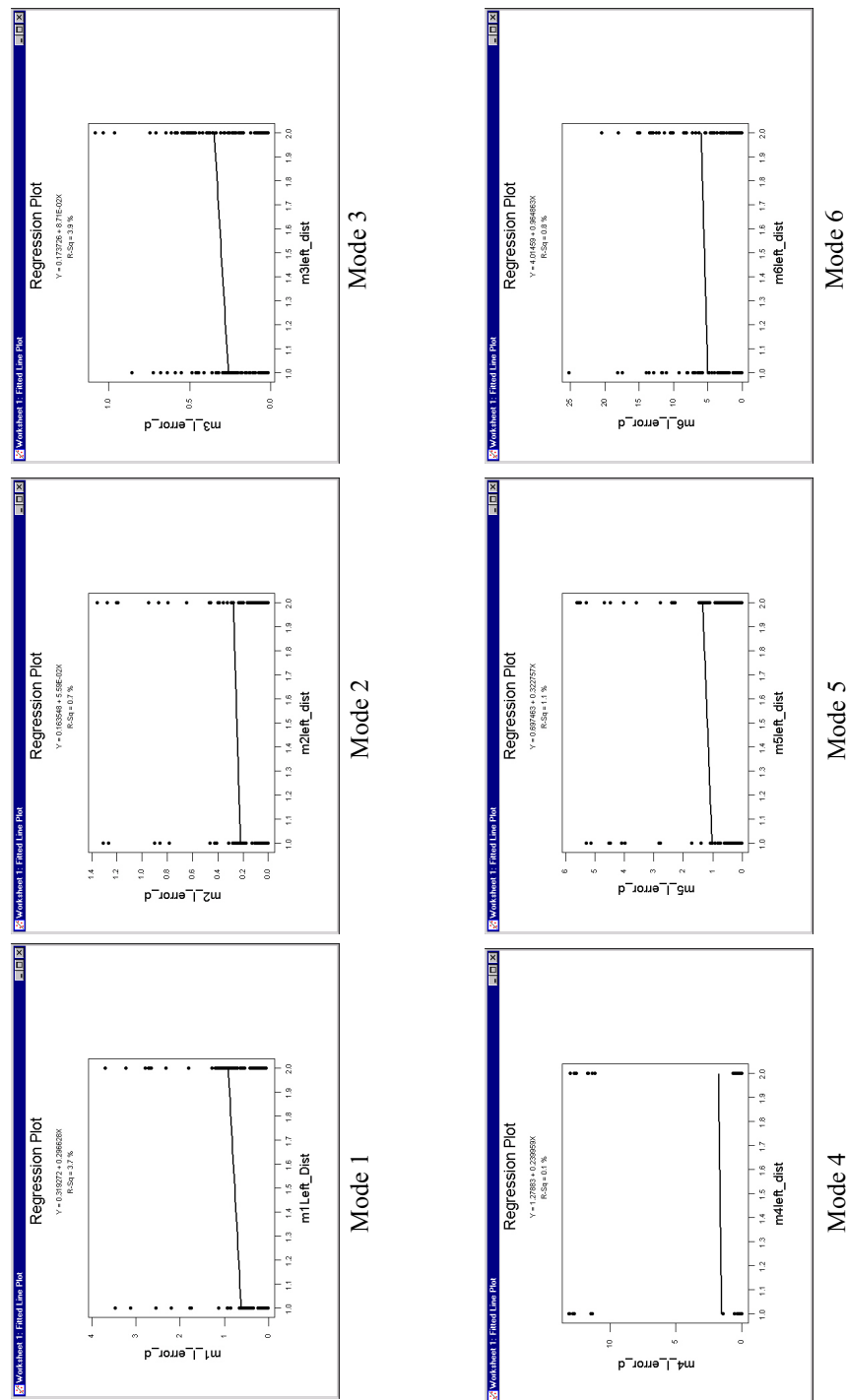


Fig. A.10: Regression analysis of difference (in absolute values) in errors versus distance for each point Right Distance from Fixed End

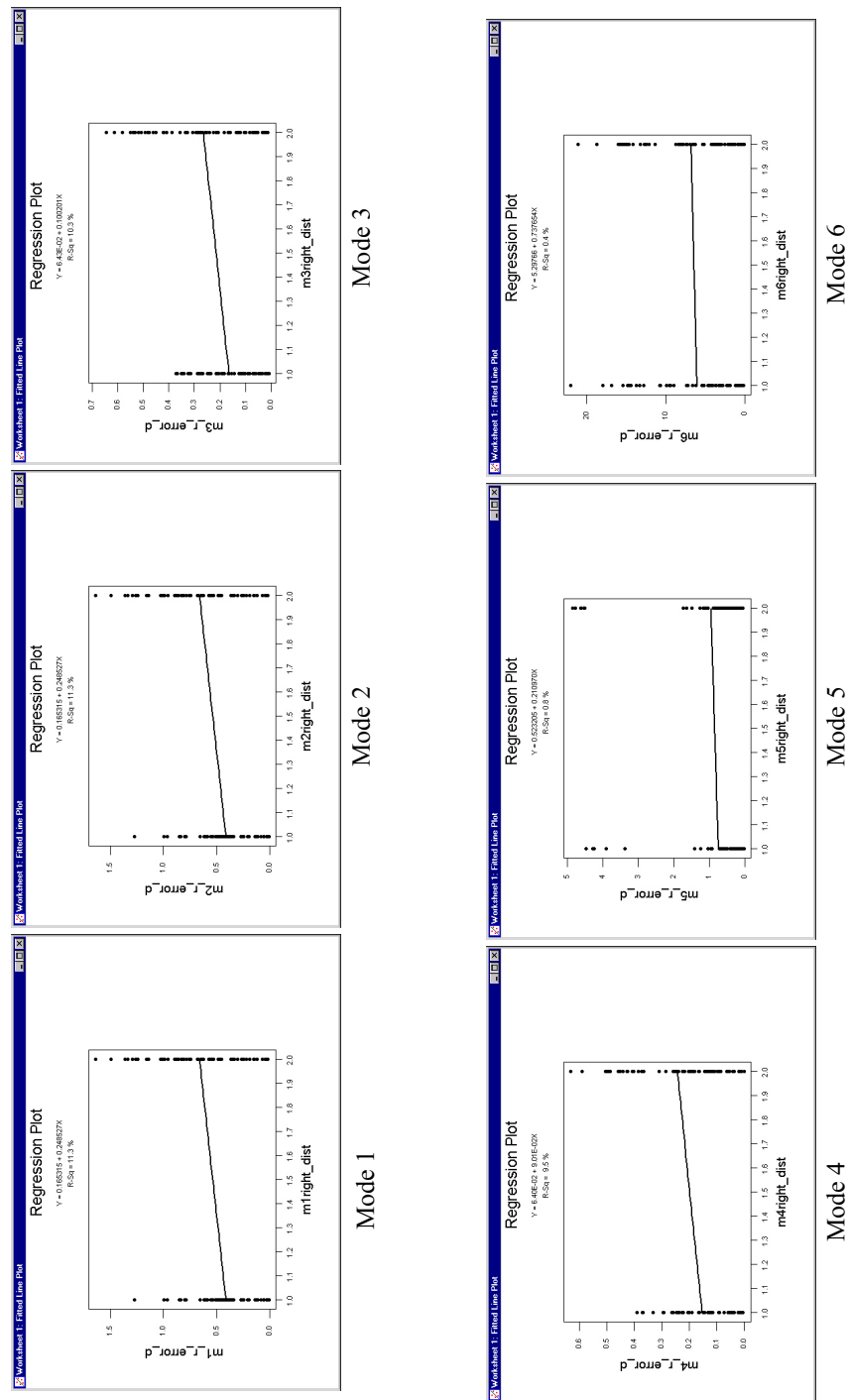
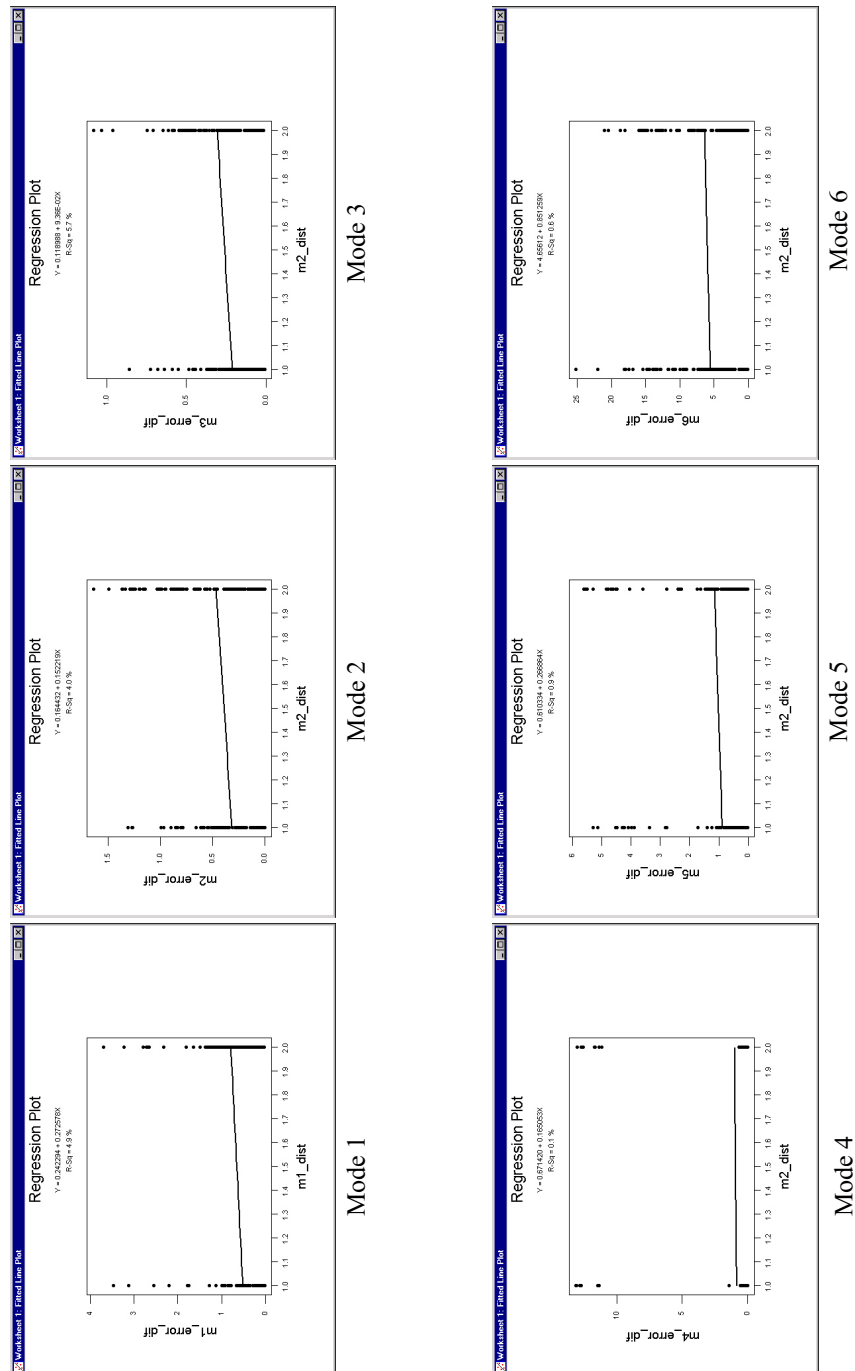


Fig. A.11: Regression analysis of difference (in absolute values) in errors versus distance for each point Combined Distance from Fixed End



REFERENCES

1. Stubbs, N., and Topole, K.G., 1995, "Non-destructive damage evaluation of a structure from limited modal parameters," *Earthquake Engineering and Structural Dynamics*, Vol. 24, pp. 1427–1436.
2. Stubbs, N., and Osegueda, R., 1990, "Global non-destructive damage evaluation in solids," *International Journal of Analytical and Experimental Modal Analysis*, Vol. 5, No. 2., pp. 67–79.
3. Biswas, M., Pandey, A.K., and Samman, M.M., 1990, "Diagnostic experimental epectral/modal analysis of a highway bridge," *The International Journal of Analytical and Experimental Modal Analysis*, Vol. 5, No. 1, pp. 33–42.
4. Wahab, M.M.A. and De Roeck, G., 1999, "Damage detection in bridges using modal curvatures: Application to a real damage scenario," *Journal of Sound and Vibration*, Vol. 226, No. 2, pp. 217–235.
5. Gattulli, V., and Rameo, F., 2000, "Integrated procedure for identification and control of MDOF structures," *Journal of Engineering Mechanics*, Vol. 126, No. 7, pp. 730–737.
6. Hajemstad, K.D. and Shin, S., 1996, "Crack identification in a cantilever beam from modal responses," *Journal of Sound and Vibration*, Vol. 198, No. 5, pp. 527–545.
7. Grahm, T., "Ultrasonic 2D SH crack detection in a layered anisotropic plate," *Journal of Nondestructive Evaluation*, Vol. 20, No. 1, 2001.
8. Dokun, O.D., Jacobs, L.J., and Haj-Ali, R.M., "Ultrasonic monitoring material degradation in FRP composites," 2000, *Journal of Engineering Mechanics*, Vol. 126, No. 7, pp. 704–710.
9. Sampaio, R.P.C., Maia, N.M.M. and Silva, J.M.M., 1999, "Damage detection using the frequency—response—function curvature method," *Journal of Sound and Vibration*, Vol. 226, No. 5, pp. 1029–1042.
10. Thyagarajan, S.K., Schulz, M.J., Pai, P.F. and Chung, J., 1998, "Detecting structural damage using frequency response functions," *Journal of Sound and Vibration*, Vol. 210, No. 1, pp. 162–170.
11. DiPasquale, E., Ju, J.W., Askar, A. and Cakmak, A.S., 1990, "Relation between global damage indices and local stiffness degradation," *Journal of Structural Engineering*, Vol. 116, No. 5, pp. 1440–1456.
12. Ray, L.R., and Tian, L., 1999, "Damage detection in smart structures through sensitivity enhancing feedback control," *Journal of Sound and Vibration*, Vol. 227, No. 5, pp. 615–632.
13. Hou, Z., Noori, M. and St. Amand, R., 2000, "Wavelet - based approach for structural damage detection," 2000, *Journal of Engineering Mechanics*, Vol. 126, No. 7, pp. 677–683.
14. Stubbs, N., and Garcia, G., 1996, "Application of pattern recognition to damage localization," *Microcomputers in Civil Engineering*, Vol. 11, pp. 395–409.
15. Ren, Wei-Xin., and De Roeck, G., 2002, "Structural damage identification using modal data—I : Simulation verification," *Journal of Structural Engineering* Vol. 128, No. 1, pp. 87–95.

16. Ren, Wei-Xin., and De Roeck, G., 2002, "Structural damage identification using modal data—II : Test verification," *Journal of Structural Engineering*, Vol. 128, No. 1, pp. 96–104.
17. Stubbs, N. and Osegueda, R., "Global damage detection in solids: Experimental verification," 1990, *International Journal of Analytical and Experimental Modal Analysis*, Vol. 5, No. 2, pp. 81–97.
18. Sohn, H., and Law, K., 1997, "A Bayesian probabilistic approach for structure damage detection," *Earthquake Engineering and Structural Dynamics*, Vol. 26, pp. 1259–1281.
19. Sohn, H., and Law, K., 2001, "Extraction of Ritz vectors from vibration test data," *Mechanical systems and signal processing*, Vol. 15, No. 1, pp. 213–226.
20. Sohn, H., and Law, K., 2000, "Application of load-dependent Ritz vectors to Bayesian probabilistic damage detection," *Probabilistic Engineering Mechanics*, Vol. 15., pp. 139–153.
21. Sohn, H., and Law, K., 2001, "Damage diagnosis using experimental Ritz vectors," *Journal of Engineering Mechanics*, Vol. 127, No. 11, pp. 1184–1193.
22. Vestroni, F., and Capeecchi, D., 2000, "Damage detection in beam structures based on frequency measurements," *Journal of Engineering Mechanics*, Vol. 126, No. 7, pp. 761–768.
23. Gawronski, W., and Sawicki, J.T., 2000, "Structural damage detection using modal norms," *Journal of Sound and Vibration*, Vol. 229, No. 1, 194–198.
24. Chen, H.R., and Kiriakidis, A.C., 2000, "Stiffness evaluation and damage detection of ceramic candle filters," *Journal of Engineering Mechanics*, Vol. 126, No. 3, pp. 308–319.
25. Maeck, J., Waheb, M.A., Peeters, B. De Roeck, G., De Visscher, J., De Wilde, W.P., Ndambi, J.-M., and Vantomme, J., 2000, "Damage identification in reinforced concrete structures by dynamic stiffness determination," *Engineering Structures*, Vol. 22, pp. 1339–1349.
26. Yuen, M.M.F., 1985, "A numerical study of the Eigenparameters of a damaged cantilever," *Journal of Sound and Vibration*, Vol. 103, No. 3, pp. 301–310.
27. Dimarogonas, A.D., and Papadopoulos, C.A., 1983, "Vibration of cracked shafts in bending," *Journal of Sound and Vibration*, Vol. 91, No. 4, pp. 583–593.
28. Akgun, M.A. and Ju, F.D., 1987, "Diagnosis of multiple crack on a beam structure," 1987, *International Journal of Analytical and Experimental Modal Analysis*, Vol. 2, No. 4, pp. 149–154.
29. Akgun, M.A. and Ju, F.D., 1990, "Damage diagnosis in frame structures with a dynamic response method," *Mechanics, Structures & Machinery*, Vol. 18, No. 2, pp. 175–196.
30. Fritzen, C.-P., Jennewein, D., and Kiefer, T., 1998, "Damage detection based on model updating methods," *Mechanical Systems and Signal Processing*, Vol. 12, No. 1, pp. 163–186.
31. Tsai, T., Yang, J.C.S., and Chen, R.Z., 1985, "Detection of damage in structures by the cross random decrement method," *Proceedings of the 3rd International Modal Analysis Conference*, Orlando, FL., Vol. 2, pp. 691–700.

32. Yang, J.C.S., Chen, J., and Dagalaski N.G., 1984, "Damage detection in offshore structures by the random decrement technique," *Journal of Energy Resource and Technology*, Vol. 106, pp. 38–42.
33. Rizos, R.F., Aspragathos, N. and Dimarogonas, A.D., 1990, "Identification of crack location and magnitude in a cantilever beam from the vibration modes," *Journal of Sound and Vibration*, Vol. 138, No. 3, pp. 381–388.
34. Pandey, A.K., Biswas, M. and Samman, M.M., 1991, "Damage detection from changes in curvature mode Shapes," *Journal of Sound and Vibration*, Vol. 145, No. 2, pp. 321–332.
35. Pai, P.F. and Jin, S., 2000, "Locating structural damage by detecting boundary effects," Vol. 231, No. 4, pp. 1079–1110.
36. Pai, P.F. and Young, L.G., 2001, "Damage detection of beams using operational deflection shapes," *International Journal of Solids and Structures*, Vol. 38, pp. 3161–3192.
37. Sohn, H., Czarnecki, J.A. and Farrar, C.R., 2000, "Structural health monitoring using statistical process control," *Journal of Structural Engineering*, Vol. 126, No. 11, pp. 1356–1363.
38. Agbabian, M.S., Masri, S.F., Millar, R.K. and Caughey, T.K., 1990, "A system identification approach to the detection of structural changes," *Journal of Engineering Mechanics*, Vol. 117, No. 2, pp. 370–390.
39. Masri, S.F., Chassiaskos, A.G. and Caughey, T.K., 1993, "Identification of nonlinear dynamics systems using neural networks," *Journal of Applied Mechanics*, Vol. 60, pp. 123–133.
40. Wu, S., Ghaboussi, J. and Garrertt Jr., J.H., 1992, "Use of neural networks in detection of Structural Damage," *Computers and Structures*, Vol. 42, No. 2, pp. 649–659.
41. Masri, S.F., Smyth, A.W., Chassiakos, A.G., Caughey, T.K. and Hunter, N.F., 2000, "Application of neural networks for detection of changes in nonlinear systems," *Journal of Engineering Mechanics*, pp. 666–676.
42. Garcia, G., Butler, K. and Stubbs, N., 1997, "Relative performance of clustering—based neural network and statistical pattern recognition models for nondestructive damage detection," *Smart Materials and Structures*, Vol. 6, pp. 415–424.
43. Yao, J.T.P., and Natke H.G., 1994, "Damage Detection and Reliability Evaluation of existing Structures," *Structural Safety*, Vol. 15, No. 12, pp. 3–16.
44. Aktan, A.K., Hogue, T.D., and Hoyos, A., 1988, "Regional Identification of Civil Engineering Structures," *Proc., Dept. of Civil Eng., University of Southern Calif., Los Angeles, CA*, pp. 135–180.
45. Raghavendrchar, M., and Aktan, A.K., 1992, "Flexibility by Multireference Impact testing for Bridge Diagnostics," *Journal of Structural engineering*, Vol. 118, No. 8, pp. 2186–2203.
46. Saleeb, A.F., Tseng, S.M., and Gendy, A.S., 1997, "Development and evaluation studies on new NDE techniques for damage detection in Structures," Reprint.
47. Tseng, S.M., 1993, "Studies on global methods for localized - damage detection in large scale structures," *The University of Akron, Ph.D. dissertation*.

48. Ratanasumritkul, S., 1997, "Experimental investigation of a new global damage detection scheme," The University of Akron, Masters Thesis.
49. Mindlin, D., 1951, "Influence of rotary inertia and shear on flexural motions of isotropic elastic plates," *Journal of Applied Mechanics*, pp. 31–38.
50. Saleeb, A.F. and Gendy, A.S., 2000, "Nonlinear dynamics for mixed shells with large rotation and elasto-plasticity," *International Journal of Computational Engineering Science*, Vol. 1, No. 1, pp. 1–31.
51. Timoshenko, S.P. and Gere, J.M., 1972, "Mechanics of materials," D. Van Nostrand Reinhold Company, New York.
52. Hinton, E., Salonen, E.M. and Bicanic, N., 1978, "A Study of Locking Phenomena in Isoparametric Elements," 3rd MAFELAP Conf., Brunel University, Uxbridge.
53. Saleeb, A.F., and Chang, T.Y., 1987, "An efficient quadrilateral element for plate bending analysis," *International Journal for Numerical Methods in Engineering*, Vol. 24, pp. 1123–1155.
54. Saleeb, A.F., Chang, T.Y. and Graf, W., 1987, "A quadrilateral shell element using a mixed formulation," *Computers and Structures*, Vol. 26, No. 5, pp. 787–803.
55. Bathe, K.J., 1995, "Finite Element Procedure," Prentice Hall, Englewood Cliffs, N.J.
56. Yang, L.X., Steinchen, W., Schuth, M. and Kupfer, G., 1995, "Precision measurement and nondestructive testing by means of digital phase shifting speckle pattern and speckle pattern shearing interferometry," *Measurement (Journal of the International Measurement Confederation)*, Vol. 16, pp. 149–160.
57. Wong, W.O., and Chan, K.T., 1998, "Measurement of modal damping by electronic speckle shearing interferometry," *Optics & Laser Technology*, Vol. 30, pp. 113–120.
58. Ng, T.W., 1995, "Digital speckle pattern interferometer for combined measurements of out-of-plane displacement and slope," *Optics Communications*, Vol. 116, pp. 31–35.
59. Wang, W.C., Hwang, C.H. and Lin, S.Y., 1996, "Vibration Measurement by the Time-Averaged Electronic Speckle Pattern Interferometry Methods," *Applied Optics*, Vol. 35, No. 22, pp. 4502–4509.
60. Ma, C. and Hsieh, D., 2001, "Full-Field experimental investigations on resonant vibration of cracked rectangular cantilever plates," *American Institute of Aeronautics and Astronautics Journal*, Vol. 39, No. 12, pp. 2419–2422.
61. Arnold, S.M. and Samorezov, S., 2002, "Modal Vibration Signature Experimental Plan and Results for Validating a Defect Detection Algorithm Scheme," NASA Technical Memorandum.

REPORT DOCUMENTATION PAGE			Form Approved OMB No. 0704-0188	
Public reporting burden for this collection of information is estimated to average 1 hour per response, including the time for reviewing instructions, searching existing data sources, gathering and maintaining the data needed, and completing and reviewing the collection of information. Send comments regarding this burden estimate or any other aspect of this collection of information, including suggestions for reducing this burden, to Washington Headquarters Services, Directorate for Information Operations and Reports, 1215 Jefferson Davis Highway, Suite 1204, Arlington, VA 22202-4302, and to the Office of Management and Budget, Paperwork Reduction Project (0704-0188), Washington, DC 20503.				
1. AGENCY USE ONLY (Leave blank)		2. REPORT DATE August 2002		3. REPORT TYPE AND DATES COVERED Final Contractor Report
4. TITLE AND SUBTITLE Defect Localization Capabilities of a Global Detection Scheme: Spatial Pattern Recognition Using Full-Field Vibration Test Data in Plates			5. FUNDING NUMBERS WU-708-87-13-00 NCC3-808	
6. AUTHOR(S) A.F. Saleeb and M. Prabhu				
7. PERFORMING ORGANIZATION NAME(S) AND ADDRESS(ES) University of Akron Department of Civil Engineering Akron, Ohio 44325-3905			8. PERFORMING ORGANIZATION REPORT NUMBER E-13414	
9. SPONSORING/MONITORING AGENCY NAME(S) AND ADDRESS(ES) National Aeronautics and Space Administration Washington, DC 20546-0001			10. SPONSORING/MONITORING AGENCY REPORT NUMBER NASA CR-2002-211685	
11. SUPPLEMENTARY NOTES Project Manager, S.M. Arnold, Structures and Acoustics Division, NASA Glenn Research Center, organization code 5920, 216-433-3334.				
12a. DISTRIBUTION/AVAILABILITY STATEMENT Unclassified - Unlimited Subject Category: 39 Available electronically at http://gltrs.grc.nasa.gov/GLTRS This publication is available from the NASA Center for AeroSpace Information, 301-621-0390.			12b. DISTRIBUTION CODE	
13. ABSTRACT (Maximum 200 words) Recently, a conceptually simple approach, based on the notion of defect energy in material space has been developed and extensively studied (from the theoretical and computational standpoints). The present study focuses on its evaluation from the viewpoint of damage localization capabilities in case of two-dimensional plates; i.e., spatial pattern recognition on surfaces. To this end, two different experimental modal test results are utilized; i.e., (i) conventional modal testing using (white noise) excitation and accelerometer-type sensors and (ii) pattern recognition using Electronic speckle pattern interferometry (ESPI), a full field method capable of analyzing the mechanical vibration of complex structures. Unlike the conventional modal testing technique (using contacting accelerometers), these emerging ESPI technologies operate in a non-contacting mode, can be used even under hazardous conditions with minimal or no presence of noise and can simultaneously provide measurements for both translations and rotations. Results obtained have clearly demonstrated the robustness and versatility of the global NDE scheme developed. The vectorial character of the indices used, which enabled the extraction of distinct patterns for localizing damages proved very useful. In the context of the targeted pattern recognition paradigm, two algorithms were developed for the interrogation of test measurements; i.e., intensity contour maps for the damaged index, and the associated defect energy vector field plots.				
14. SUBJECT TERMS Experimentation; Modal testing; Detection; Health monitoring; Damage			15. NUMBER OF PAGES 164	
			16. PRICE CODE	
17. SECURITY CLASSIFICATION OF REPORT Unclassified	18. SECURITY CLASSIFICATION OF THIS PAGE Unclassified	19. SECURITY CLASSIFICATION OF ABSTRACT Unclassified	20. LIMITATION OF ABSTRACT	